Communauté UNIVERSITÉ Grenoble Alpes

THÈSE

Pour obtenir le grade de

DOCTEUR DE LA COMMUNAUTÉ UNIVERSITÉ GRENOBLE ALPES

Spécialité : 2MGE : Matériaux, Mécanique, Génie civil, Electrochimie

Arrêté ministériel : 25 mai 2016

Présentée par

Asif Iqbal BHATTI

Thèse dirigée par **Olivier LE BACQ**, Chargé de Recherche, CNRS

préparée au sein du **Laboratoire Science et Ingénierie des Matériaux et Procédés** dans **l'École Doctorale I-MEP2 - Ingénierie - Matériaux, Mécanique, Environnement, Energétique, Procédés, Production**

Calculs Ab-initio et simulations atomistiques des propriétés thermodynamiques et cinétiques de complexes de métaux de transition utilisés comme batteries

First principles and Atomistic simulation of the thermodynamical and dynamical properties of transition-metal complexes for battery application

Thèse soutenue publiquement le **20 décembre 2018**, devant le jury composé de :

Madame FANNIE ALLOIN (Présidente du jury)

Madame MARIE-LIESSE DOUBLET (Rapporteur)

Monsieur CHRISTOPHE BUCHER (Rapporteur)

Monsieur JOSE BOTTA WALTER (Examinateur)

Monsieur OLIVIER LE BACQ (Directeur de thèse)

Madame Marie-Bernadette LEPETIT (invitée)

The fate of our times is characterized by rationalization and intellectualisation and, above all, by the "disenchantment of the world"

Max Weber

Declaration

Asif Iqbal BHATTI
2018

Acknowledgements

No vocabulary/words exist to describe the Entity/Being that encompasses all the cryptic consciousness that garners the subtleties and intricacies of this multi-verse, You are the One and the Only. The mystery of this universe is that it is incomprehensible yet our brain tries to grasp the infinite. It is said it is hard to unlearn what we have learned; *wissenschaftlich* attitude had questioned all my inherent assumptions such as *creed*, *beliefs*, and *dogma* and shake the static ground on which all beliefs stands (*Crisis is a blessing in disguise*). How do we start to question the ultimate reality? The big question still is why?

First of all, I would like to deeply thank my thesis advisor Prof. Olivier Le Bacq for providing with all the opportunities for completing this work. His knowledge, care, intellectual humility, and inspiration for this work pushed me to expand my knowledge and develop independent research potential. I thank him for his contributions of time, ideas, wonderful discussion and funding to make my Ph.D. experience productive and stimulating. Also, I would like to thank Jean Claude Lepretre for all his help and Alain Pasturel for his careful reading of the thesis and constructive criticism.

I would like to thanks Fannie Alloin to be the president and Christophe Bucher and Marie-Liesse Doublet to be the referees of my thesis and a member of my jury. I am genuinely obliged to Marie-Liesse Doublet for her thorough reading, comments, and insight full remarks which greatly helped me to improve my manuscript. I am also obliged to other members for their contribution.

Next, I would like to thanks my parents, siblings, and friends especially Ahmed Nouri and Yashank Gupta I had a great time with them in Grenoble, France. Lastly, thanks to Rim El-ballouli, you will be missed.

Abstract

Standard redox potentials for mono and bi-nuclear transition metal (TM) complexes $[M\,(dmbpy)_3]^{n+}\,nCi^-$, have been investigated using First Principles Calculation. Three metal centers are investigated: Fe, Ru, and Cu. Our modeling is validated on mono-nuclear compounds. This approach consists in determining the best small polymer (bi-nuclear) made out of these monomers for a battery application. For that, we varied the three available degrees of freedom i.e., the nature of the central TM atom (Fe, Ru, and Cu), counter-ions $Ci = PF_6^-$, $TFSI^-$ and ClO_4^- in interaction with the polymer, and the alkyl chain $-(CH_2)_n-$ of length n that connects both mono-nuclear in the bi-nuclear compound. The Iron compound with $-(CH_2)_{n=6}-$ is found to be the best candidate. The $[Cu\,(dmbpy)_2]^{n+}\,nCi^-$ complex shows too much structure deformation upon loading, making it less reliable for cathode material. Moreover, we studied two XC functional, PBE and PBE0 and found, for three complexes PBE approximation retains the ligand field picture whereas PBE0 functional induces an exaggerated and unexpected band dispersion by dissolving the ligand field picture expected for the octahedral environment of the TM in the studied complexes. These findings validate that hybrid functional for which it was designed to localize and cancel self-interaction error does not work for all system. More particularly, the PBE0 approximation fails to model the three complexes (Fe, Ru, and Cu) in functional conditions (in the field made by the counter-ions).

Further, we have developed an atomistic potential relying on the Force Field scheme for the Iron complex in order to study the dynamical properties of this compound at larger simulation scale (3D reticulated polymerization made of our Fe complex monomers). We made intensive use of our DFT data (energies, geometries, spin-state configurations, and calculated vibrational properties) to develop the required parameters entering the model. Moreover, computational techniques (written python language) were developed specifically to create a 3D structure of transition metal complexes satisfying the condition to be fully reticulated. Bounding conditions had to be designed and a procedure aiming at fixing reliable and physical effective charges on each atom of the simulation cell (compatible with DFT results) were developed. Our first simulations in explicit acetonitrile solvents have been attached to calculate the diffusion coefficients of

the counter-ions in both the fully loaded and unloaded states. A more ambitious and realistic calculation aims at investigating the paths of the counter-ions when one single center starts to be loaded in an unloaded environment.

Keyword: Polymer chemistry, Electrochemistry, Battery, DFT, Force Field development, Coordination polymers, Atomistic modeling, Coordination chemistry, MOFs, polymer materials

Résumé

Ce travail théorique vise à étudier, via les méthodes Premiers Principes, les propriétés des complexes de métaux de transitions, $[M\,(dmbpy)_3]^{n+}\,nCi^-$ pour un usage en batterie. Pour cette étude ab-initio, les composés mono et bi-nucléaires ont été retenus. La pertinance de notre modélisation a été validée sur les composés mononucléaires. Nous nous sommes interessé au complexes de Fe, Ru et Cu pour lesquels une validation expérimentale était possible. Notre étude a principalement consisté à faire varier les degrés de liberté que nous possédons pour optimiser le voltage et la cinétique de chargement des batteries. Pour cela, nous avons fait varier le TM = Fe, Ru, et Cu, la nature des contre-ions $Ci^- = PF_6^-$, $TFSI^-$ et ClO_4^- en interaction avec le polymère lors du processus de charge, ainsi que la longeur de la chaîne alkyl qui sépare les deux monomers dans le cas des composés binucléaires. Le composé à base de Fe avec une chaîne $-\,(CH_2)_{n=6}\,-$ a été retenu comme le meilleur candidat pour une application batterie. Le composé à base Ru montre un comportement proche de celui du Fe, quant-au complexe de Cu, il présente des changements de géométrie locale sous chargement trop importants, le rendant peu apte à conduire à une cinétique efficace. Cette étude nous a permis de déterminer que l'approximation PBE était le meilleur choix possible pour modéliser nos complexes dans les conditions de fonctionnement en batterie (dans le champ créé par les contre-ions) et que l'approximation PBE0, généralement utilisée dans la littérature, ne pouvait rendre compte de la physico-chimie de nos composés dans de telles conditions.

De surcroît, nous avons dévelopé pour le complexe de Fe, un potentiel atomistique de type "Champ de forces" de manière à pouvoir aborder les aspects dynamiques impliquant de plus grandes tailles de boîte de simulation. Ici, nous modélisons une structure 3D, totalement réticulée à partir de nos monomères à base de Fe. Nous nous sommes servi de la base de donnés DFT que nous avions généré (énergies, géométries, état de spin et fréquences vibrationnelles calculées) pour ajuster les paramètres entrant dans l'écriture du modèle. La construction de la géométrie initiale du polymère 3D a nécessité l'écriture d'un code de calcul visant à produire un arrangement complétement réticulé et à assigner les charges effectives issues des calculs DFT. Ce modèle nous a permis de déterminer les coefficients de diffusion des contre-ions pour les états totalement chargé et non-chargé. Un calcul plus ambitieux vise à déterminer les chemins de diffusion des contre-ions lors d'un processus de chargement en considérant un seul centre de degré d'oxydation 3+ au centre du polymère 3D, pour lequel les centres actifs possèdent un degré d'oxidation 2+. Les contre-ions assurent la neutralité globale.

Keyword: Polymer chemistry, Electrochemistry, Battery, DFT, Force Field development, Coordination polymers, Atomistic modeling, Coordination chemistry, MOFs, polymer materials

Contents

List of Figures

List of Tables

Chapter 1

The batteries and their modeling at the atomic scale

The purpose of this chapter is to provide the readers with the essential background knowledge of polymeric cathode materials and discuss a new class of cathode materials such as metal bipyridine and Metal-organic frameworks (MOFs). Further, provide a new concept in modeling the material by incorporating counter-ions instead of considering metallic cations. Since this research involves the study of cathode materials and counter-ions, we will focus our discussion on coordinating transition metal compounds for battery applications and beyond. Our discussion will be focused on understanding the role played by the counter-ions (high dissociation electrolyte) during the charge and discharge process in the battery and beyond. Moreover, theoretical tools that are used to model this material will be discussed. In the end, the motivation for this study and the goals what we ought to achieve will be presented.

1.1 Polymer material for cathode

1.1.1 Organic polymer in general

In literature, many types of organic materials have been developed as electronic conductive polymers [1, 2]. Some of the examples are nitroxide, phenoxide radical based polymers, conjugated carbonyls or carboxylate and quinone based material [3–5]. The advantage of using redox organic cathode materials is that they are abundant, non-toxic, and inexpensive. For some of the materials (as shown in Figure 1.1) it provides higher energy density, faster redox reactions with minimum structure deformations upon loading and unloading [6], are lightweight, and environmental friendly [7–9]. Moreover, this

case can be ideal for Na ion whose radius is larger than the one of Li for insertion or de-insertion. In polymers, Na is expected to suffer less from entrapment in the structure.

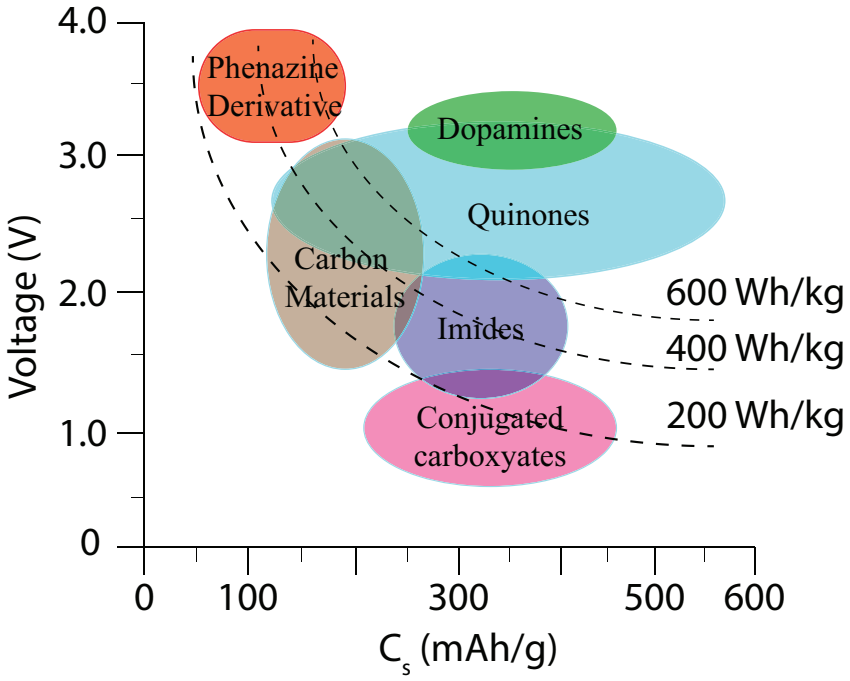

Figure 1.1: A comparison of discharge voltage, specific capacity and energy density distribution of organic materials for Li-ion batteries [10].

Electroactive Conducting Polymers (ECPs) in this class provides an alternative way to treat polymers as cathode materials such as polypyrrole (PPy), polyaniline (PANI), polythiophene and their derivatives. Figure 1.2 shows the chemical structure of these conducting polymers. These polymers have shown high electronic conductivity and reversible redox chemistry [11, 12]. In one of the studies of polypyrrole (PPy), the calculated open circuit voltage is about 2–4 V vs. Li^+/Li reference and a charge capacity of 133 mAh per gram [13, 14]. Despite their similarity to oxides for some organic materials, they lack the mechanical strength, low redox potential, poor rate capabilities, chemical bond during lithiation/delithiation and self-discharge. However, some of the challenges have been tackled one of them being the discharge rate. This is actively curbed by incorporating redox-active unit into a polymeric backbone [15].

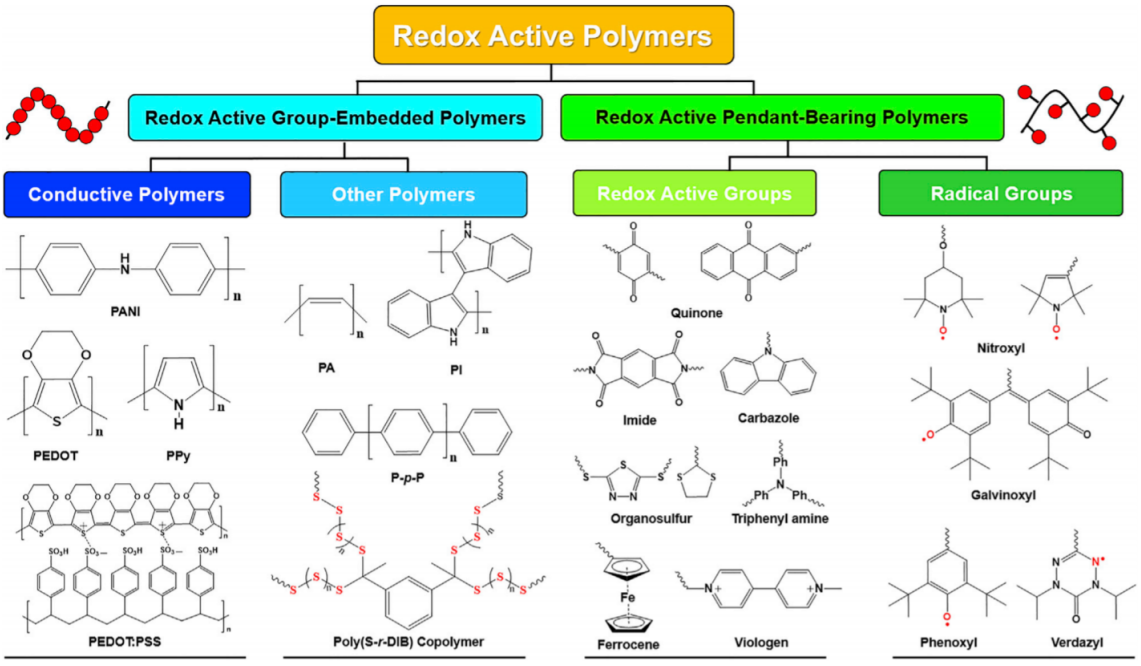

Figure 1.2: Classification and chemical structure of Redox Active Polymers. Image adapted from [16].

Further, among this class of materials are the organic radical battery (ORB) [17]. ORB radicals are stabilized by steric or resonance effect. Most of the radicals that have been studied are alicyclicnitroxyl such as 2,2,6,6-tetramethylpiperidine-1-oxyl (TEMPO) and 2,2,5,5-tetramethylpyrrolidine-1-oxyl (PROXYL), and among nitroxyl radical polymers are poly(2,2,6,6-tetramethylpiperidine-4-yl-1-oxylmethacrylate) (PTMA) and poly (2,2,6,6-tetramethylpiperidine-4-yl-1-oxylvinylether) (PTVE) [18]. The last two shows reversible redox reaction in aprotic solution, with high stability, voltage, and specific capacity. The nitroxyl radical polymers are rated to be 3.5 V with 147 mAh per gram which is comparable to that of $LiCoO_2$ (140 mAh per gram). However, these batteries have the low volumetric energy density, they are not suitable as the main battery in mobile phones or laptop computers but can be used as smart card power. Other than ORB's types of battery are the conjugated carbonyls or carboxylate [5] and quinone [19] materials.

1.2 Coordination polymers

As mentioned before these organic molecules suffer from mechanical stress, low cycling life and are prone to easy deformation. This can be avoided by introducing coordina-

tion compounds. Hence, long range coordination polymers can be built. Coordination complexes provide a path to increase or decrease the potential by tuning the metal center with appropriate ligands [20–23]. These materials, besides electron transfer, also exchange anions, which gives great flexibility for ionic conductivity. Transition metal polymer complex has an intermediate behavior in between crystalline and amorphous phase and provides multi-step oxidation along with low molecular weight.

1.2.1 Coordination complex as a cathode material for our battery

Most of the studies in literature that have been done is to study the redox properties and excited state energy of transition metal complexes [23–31] but not in the context of battery modeling. In this section, we will describe these materials for battery applications and beyond and define the new terminology associated with it.

To construct these complexes, transition metal elements are linked with ligands. With the choice of the ingredients, chemical and physical properties of the compounds can be altered by varying the oxidation states of metal ions or changing the number of ligands or incorporating counter-ions. In general, to apply these redox complexes as an active cathode material few criteria needs to be satisfied:

1. Firstly, the redox reactions should be chemically reversible and should operate under a large voltage window.

2. Secondly, it should display high chemical, electrochemical, and cell-component stabilities.

3. Thirdly, the structure should be stable and soluble upon multiple charge (oxidation) states and

4. Lastly, the material should be inexpensive, and widely available.

Few examples of transition metal complexes are acetylacetonate, metallocene derivatives, Metal organic frameworks (MOFs), dithiolate vanadium complexes, metal bipyridine and phenanthroline adducts complexes. Most complexes meet many, but not all, of the above criteria. For instance, an alkylammonium ferrocene derivative of metallocene undergo reversible redox reactions and exhibit high solubility (1.7 M in alkylcarbonate solvent mixtures). However, this material is limited to a single redox event ($n = 1e^{-}$) at 3.49 V versus Li/Li^{+}, thus requiring the use of a low-potential redox active partner (often

Li-metal), which leads to an increase in the complexity of the system and membrane design [32].

In Ligand field theory, *bpy* displays its effects in between weak and strong scale. A partial spectrochemical series of ligands from small Δ to large Δ is shown in Figure 1.3 (Δ is a splitting parameter between the t_{2g} and e_g states). Cabrera *et. al.* have studied the application of metal coordination complexes for redox flow batteries (RFB). They used Chromium complex to show when bipyridine (*bpy*) ligands are facilitated with substituent within the electrochemical window of acetonitrile redox couples position and reversibility are impacted. Furthermore, they showed solubility is also affected by changing both the ligand substituent and metal oxidation state [33].

Similarly, $[Ru(bpy)_3]^{2+}$ complex (which is a widely studied system and we have opted here as a potential battery material) when coordinated to *bpy* ligand display large chemical stability, excited state reactivity, luminescence (phosphorescence and fluorescence) and long excited state lifetime. Due to its excited state properties (metal to ligand charge transfer (MLCT) process), it is used as a dye because the energy gap between the t_{2g} and e_g states fall within the visible and ultraviolet regions [34, 35]. The estimated reduction potential calculated also lie in a reasonable voltage range that is +1.25 V to +1.30 V vs NHE (Normal Hydrogen Electrode).

$$I^- < Cl^- < F^- < CH_3CN < py\,(pyridine) < bpy$$

$$< phen\,(1,10-phenanthroline) < NO_2^- < CN^- < CO$$

Figure 1.3: In this spectrochemical series ligands on the left end are considered as weak fields and on the right end are stronger fields. Weak field results in high spin states (π-donors) whereas, stronger field results in low spin states (π-acceptors) [36].

For our case we have decided to study *bpy* (Its isomers exist in many configuration that is 2,2´-bipyridine (*bpy*) and 4,4´-dimethyl-2,2´-bipyridine (*dmbpy*) [37, 38]) as a ligand. It has the advantage that it is neutral, display robust redox stability, functionalization is easy and provides easy complexation with metal ions. Thus, it forms charged complexes and can be used to build coordination polymers with tunable properties.

To model the coordination complex we have chosen three (Fe, Ru, and Cu) metal elements with *bpy* ligand and defined this compound as mono-nuclear as shown in Figure 1.4. Further, we extended this definition to construct bi-nuclear and poly-nuclear compound as shown in the Figure 1.5. The former construction is formed by assembling two mono-nuclear units linked via the Linker. The Linker in our case is the

alkyl chain, $-(CH_2)_n-$. The later construction in literature falls under the category of Metal-organic frameworks (MOFs). A subclass of coordination networks (a subset of coordination polymer) with potential voids often attributed with porosity.

The theoretical molecular design shown in the Figure 1.5, is one of the typical case of MOF-polymer with architectural different porous size (by varying alkyl chain length) and one of the unique model for our system and a new contribution to coordination polymer, and battery community. Generally, MOFs compounds exists in various dimensions [39–41]. These porous compounds are extended through repeating coordination entities with cross-links between two or more individual chains, loops, or spiro-links [42]. The porosity open up a wide opportunity for intercalation of Li or counter-ions. For certain MOF, the pores are stable during the expulsion or insertion of solvents or ions which indicates there is a weak influence on structural deformity, a property which is very unique for practical applications.

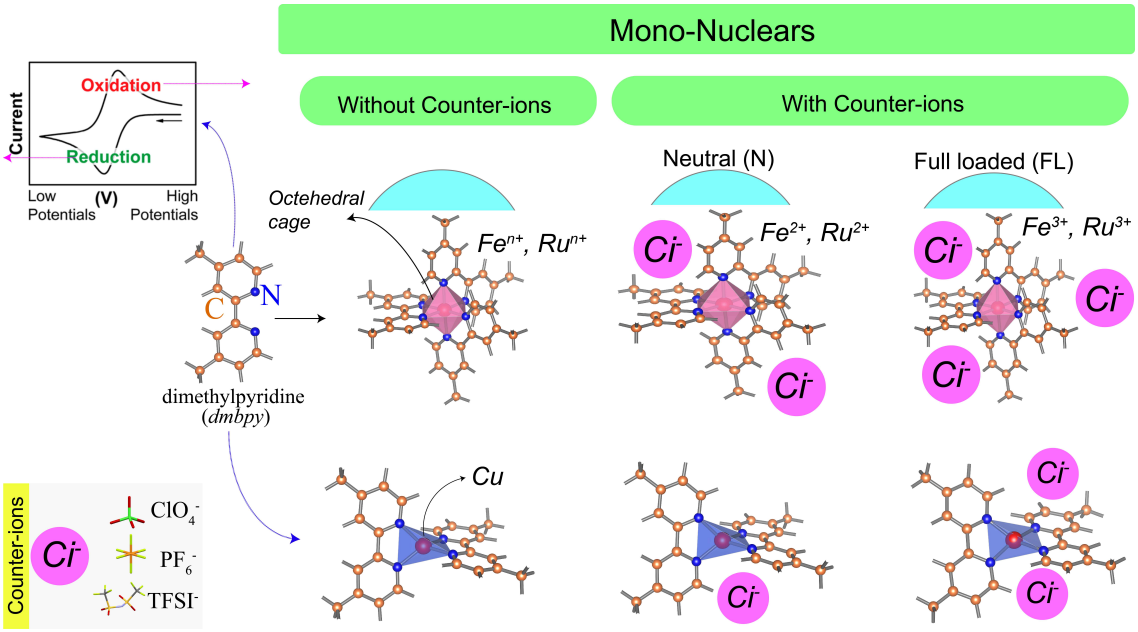

Figure 1.4: Schematic representation of the coordination complexes that is used to model as an active materials for cathode electrode. Two cases are considered with and without counter-ions. The Neutral state is termed when the compound is in the degree of oxidation 2+ and Full loaded when it is in the degree of oxidation of 3+ surrounded by counter-ions, Ci^-.

Although MOF posses unique topology, large pore volume, high specific surface area, accessible metal sites and adjustable functional linker its realization for practical applications is still under study and further being developed [40, 41]. To name a few applications where MOFs or MOF-derived materials have been employed are LIBs, SIBs,

$Li-O_2$ batteries, $Li-S/Se$ batteries, and supercapacitors. Other applications include purification of a gas, like separating gas, in catalysis, storage of gases such as hydrogen and carbon dioxide [43]. Some of the structure[1] used for this applications are shown in Figure 1.5 (a), (b), (c), and (d).

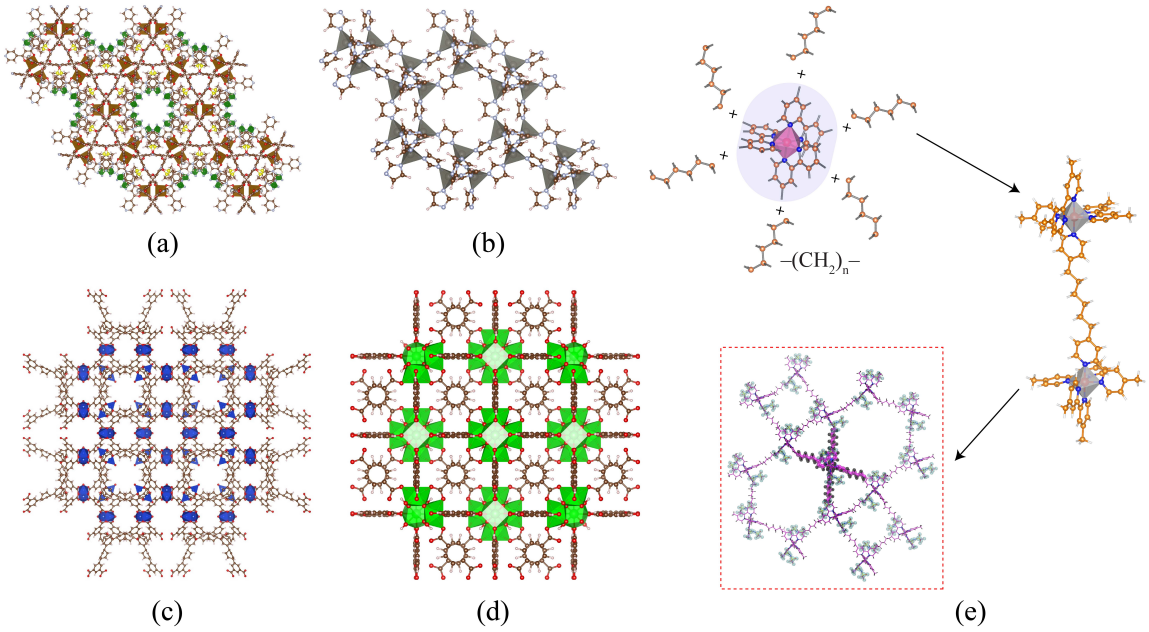

Figure 1.5: An example of Metal-organic framework (MOF) compounds consists of metal ions coordinated to organic ligands to form three-dimensional structures. (a) $[AgFe(dppd)_3]BF_4$ is a mixed metal made up of iron and silver nodes with dppd (1,3-di(4-pyridyl)propane-1,3-dionato) linkers, (b) ZIF-8 (Zeolitic Imidazolate Framework) made up of zinc ions coordinated to four imidazolate rings (c) Cu_2O_{10} nodes with 1,3,5-tris(3',5'-dicarboxy[1,1'-biphenyl]-4-yl)benzene linkers, (d) UiO-66 (Universitetet i Oslo) made up of $[Zr_6O_4(OH)_4]$ clusters with 1,4-benzodicarboxylic acid struts, and (e) Our 3D poly-nuclear compound made up of $[Fe(bpy)_3]^{2+}$ cluster with $-(CH_2)_n-$linkers (Named as UGA-01).

1.2.2 Functioning of polymer batteries

Figure 1.6, shows the working mechanism of battery composed of transition metal (TM) complex as a cathode electrode. The charge and discharge relies on the same mechanism as the general battery that is during discharge Li-ions move towards the cathode where they are intercalated into the cathode and during charge Li-ions migrate to the anode. The two electrodes are separated by a porous plastic film (separator) to restrict the contact of the electrode. The conductive medium which facile the diffusivity of ions is

[1] http://www.chemtube3d.com/solidstate/MOF-home.html

composed of liquid electrolytes. It contains a mixture of salts and organic alkyl carbonate solvents. Apart from the movement of Li-ion here we propose the fast kinetics of counter-ions is essential for a fast charging/discharging process and, the weak interaction of the anions with such complexes, opens up a wide range of possibilities to find an alternative to Li ion. For example, the replacement of Li ion by Na ion, which is found more abundant and environment friendly.

In our model we have ignored the contribution coming from the Li^+ ion because we assume due to positive charge they lies in the outer sphere whereas, counter-ions by virtue of their negative charge are in the inner sphere and contribute directly during the charge and discharge process. This is schematically shown in the inset dotted window in Figure 1.6 (e). In literature, first realization of this compound as a fuel cell have been discussed in the paper by Zheng *et. al.*, [44]. They synthesize the $[Fe(bpy)_3](BF_4)_2$ complex and reported the discharge voltage of about 4 V (vs Li/Li^+). They also investigated the discharge voltage of 2.2 V when coupled to $Li_4Ti_5O_{12}$ anode with Coulombic efficiency and energy/voltage efficiencies above 99% and 92%/93%, respectively.

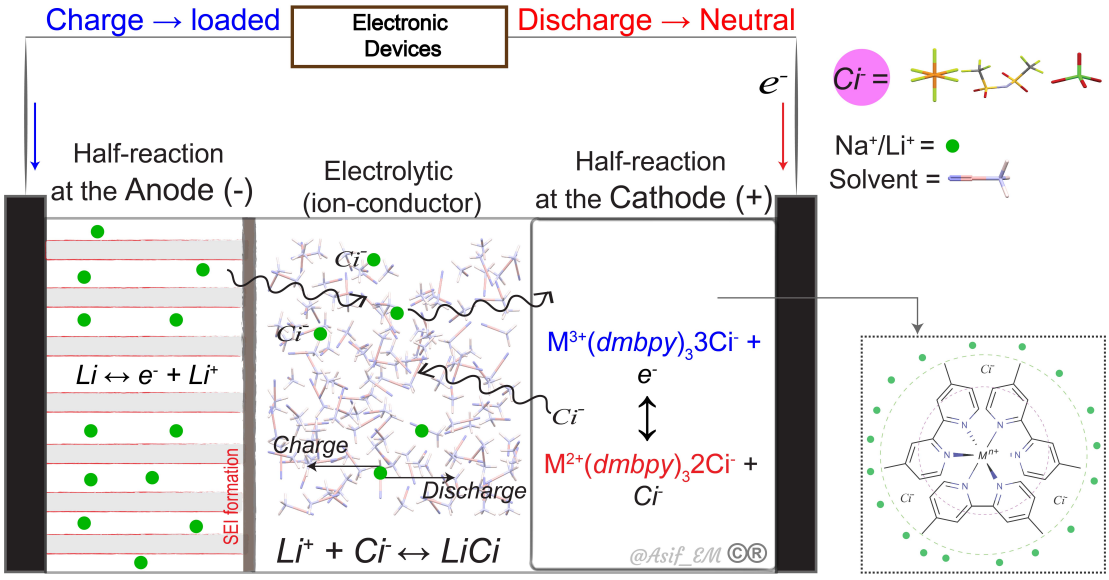

Figure 1.6: Schematic illustration of the working principle of the proposed transition metal based lithium battery during the charge/discharge process. The cathode electrode is made up of Fe or Ru complex and the active medium is composed of electrolytic material.

1.3 Thermodynamics of redox complexes

1.3.1 Ab-initio Redox Potentials: The Born-Haber Cycle

Many theoretical methods exist in literature to calculate the Redox potentials in solution phase [45, 46]. In this thesis, we will use the standard approach that is the Born-Haber cycle for the calculation of redox potential without considering the solvent effects. Figure 1.7, shows the schematic representation of Born–Haber thermodynamics cycle.

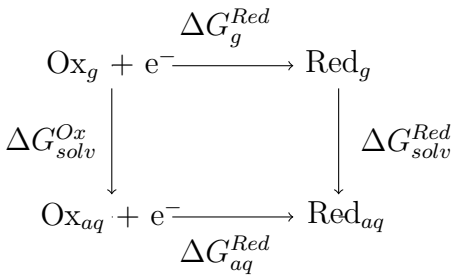

Figure 1.7: Born–Haber thermodynamics cycle.

The standard Gibbs free energy of redox half reaction, ΔG, consists of the free energy change in the gas phase and the solvation free energies of the oxidized and reduced species. From these values we calculate the overall reaction of the standard Gibbs free energy,

$$\Delta G_g^{Red} = \Delta G_{aq}^{Red} - \Delta G_{solv}^{Red} + \Delta G_{solv}^{Ox} \tag{1.1}$$

From the Nernst equation one determines the standard redox potentials,

$$V = -\frac{\Delta G^{Red}}{n\mathcal{F}} \tag{1.2}$$

Where $\mathcal{F}$ is the Faraday's constant $(1\ eV)$ and n is the number of electrons oxidized. ΔG^{Red} is calculated assuming the whole reaction process occur at the anode and the cathode as shown in Figure 1.6. The spontaneous reaction is characterized by negative Gibbs free energy and positive voltages. To calculate the thermodynamic properties Gibbs free energy is approximated in DFT calculations as it is often reduced to the total energy of the system. The energy expression is given by,

$$\Delta G^{Red} = U - T\Delta S + p\Delta V \approx U \tag{1.3}$$

Where the Enthalpy, U, is approximated with the internal energy, E, at temperature T as $E = E_{DFT} + E_{ZPE} + E_{Thermal}$. Where E_{DFT}, E_{ZPE}, and $E_{Thermal}$ are the total energy, zero point energy, and thermal correction made to the Gibbs free energy at temperature T. In our study, we will ignore the last two contributions and the solvation phase contribution. In Chapter 2 and 3, we will further develop the thermodynamic reaction cycle in the context of coordination polymers.

1.4 Electrolytic medium

Counter-ions/Anions in a electrolyte are synthesized with organic solvents to provide less resistance to ionic conductivity (rate capability) in addition to that it also provide high thermal stability, less degradation over many cycles, non-reactive with the battery components and large electrochemical stability window [6, 47–50]. As generally thought in literature the high conductivity of metal cations, ϱ_i, between the electrodes depends on the number of parameters such as a large number of ions, n_i, with charge q_i and high mobility, υ_i, but this is not the whole case as reviewed by the author [51].

$$\varrho_{ion} = \sum_i n_i q_i \upsilon_i \tag{1.4}$$

Under the external field, lithium-ions in its sphere drags around the solvent/Anions molecules held by weak coordination hence considerably limiting the cation mobility or in other words, the anion transport mobility affects the charge and discharges during the battery operation. In this section, we will discuss types of electrolytes along with its strengths and weaknesses from the perspective of battery applications. The discussion of lithium salts will be treated in a historical context.

1.4.1 Types of electrolytes

In literature, many types of electrolytic materials have been classified. Commonly, used electrolytes are *liquid electrolytes*, which are composed of a lithium salt dissolved in a liquid organic solvent. The most common electrolytes are a mix of carbonate species such as Ethyl(EC), Propyl(PC), DiMethy(DMC) or DiEthyl Carbonate (DEC) and salts such as $LiTFSI$ or $LiPF_6$, with a concentration ranging from 0.5 to 1 mol/L, to achieve a conductivity of around 1 mS/cm at room temperature depending on the application [52, 53]. Apart from liquid electrolyte, a few *aqueous electrolyte*s have also been proposed (due to low cost and the ability to withstand overcharge) but its commercial utilization has been limited due to their reactivity towards Li metal [54]. On the other

hand, *polymer electrolytes* has gone through various stages of development from dry solid polymer to gelled electrolyte system [55, 56] and polymer composite. The advantage and disadvantage of each one are,

- Dry polymer: it uses a solid type of material for the movement of ions. The ion conductivity is very poor at room temperature and requires more than 60 ^oC to be operational. The cyclability of polymer electrolyte with lithium metal electrodes is on the order of 200–300 cycles [56].

- Gel polymer: electrolyte which lies between solid and liquid phase [57] possess both cohesive properties of solids and the diffusive property of liquids. It consists of a substance called polyethylene oxide (PEO) which has the benefit which is Li metal as an anode can be used without worrying about the formation of dendrite growth.

- Composite electrolyte: comprises of a matrix polymer filled with non-reacting high surface area particles fillers such as ZrO_2, TiO_2, Al_2O_3 with hydrophobic fumed silica. This complex formation of matrix enhances the ionic conductivity at low temperatures and improve the stability of the interface with electrodes [57–63].

The advantage of polymer materials is that it can be formed in many shapes for portable devices as compared to Li-ion battery, which requires rigid casing. Lithium polymer offers (i) slightly higher specific energy (ii) high ionic conductivity at room temperatures (iii) good mechanical strength (iv) appreciable Ion transport number (v) thermal and electrochemical stabilities (vi) better compatibility with electrodes internal shortage, (vii) no internal leakage and non-combustibility [64, 65]. The major challenge for this type of electrolytes is to achieve higher conductivity, which would enable their utilization at room temperature instead 70 °C as currently employed. In order to tackle this issue and improve the mechanical properties plastic gel electrolytes have been devised [52]. Such electrolyte is composed of a co-polymer (PVDF-HFP) capable of trapping large amounts of liquid electrolytes within its amorphous domains, while the crystalline ones provide a good mechanical integrity.

In the classification of electrolytes, Dudley *et al.* [66], have studied non-aqueous electrolytes for Li-ion battery composed of a solution of 150 electrolyte solute mix with twenty seven solvents and five Lithium salts to find the optimal condition. They find for designing an electrolyte medium a compromise has to be made. For example, the solubility of Li^+ with Cl^- or F^- is very low but could be increased by Br^-, I^-, or S^{2-} but that would readily oxidize cathode materials at $< 4.0\ V$ vs. Li^+/Li. The

search of electrolyte that would not readily oxidize and would remain stable under room temperature and follows the above properties have been studied by many researchers [6, 64, 66–77]. Looking at the ionic studies of solutes in various solvents one can deduce two factors upon which conductivity of ions depends [78]
Average ion mobility:

$$LiBF_4 > LiClO_4 > LiPF_6 > LiAsF_6 > LiTf > LiTFSI \tag{1.5}$$

Dissociation constant:

$$LiTf < LiBF_4 < LiClO_4 < LiPF_6 < LiAsF_6 < LiTFSI \tag{1.6}$$

From the above relation, one can observe while selecting anions with appropriate requirements and well-behaved solvents the compromised has to be made. In this thesis, we have chosen to study following electrolytes $LiTFSI$, $LiPF_6$ and $LiClO_4$. These are common in the industry and readily applicable in the lab. For modeling our complexes, we will integrate these anions to our model and study their effects during the charge/discharge process. Lets briefly discuss these counter-ions in terms of their historical context.

1.4.2 Lithium salts

As discussed in the previous section, conducting medium is responsible for the internal transport of lithium ions to carry enough charge between both electrodes. The combination of selecting the best counter-ion to metal cation depends again on the application. Complexities that could arise from this are the interplays of the counter-ion with metal cations, solvent molecules, electrodes, and the current collectors. From the perspective of practical application usually compromise is made in this respect. In the following sub-sections, several properties of selected counter-ions are reviewed with its main disadvantage and advantages.

Lithium Perchlorate

Lithium Perchlorate, $LiClO_4$ (shown in Figure 1.8 (a)) is a highly soluble material and demonstrates high conductivity (for example $\approx 9.0\ m/\Omega cm$ in EC/DMC solvents at 20 $^{\circ}C$) and stability against anodic materials. The electrolytic window fall in the range of 5.1 V against spinal cathode [79]. The formation of phase at the anode electrode is also of low impedance, relatively less hygroscopic and is stable to ambient moisture. However, the high oxidation state of chlorine (VII) in perchlorate makes it a strong oxidant,

which readily reacts with most organic species in violent ways. And, under certain conditions such as high temperature and high current charge [80] makes it impractical as an electrolyte solute for industry purposes nevertheless, it is still frequently used as in various laboratory tests because it is easy to handle and economical.

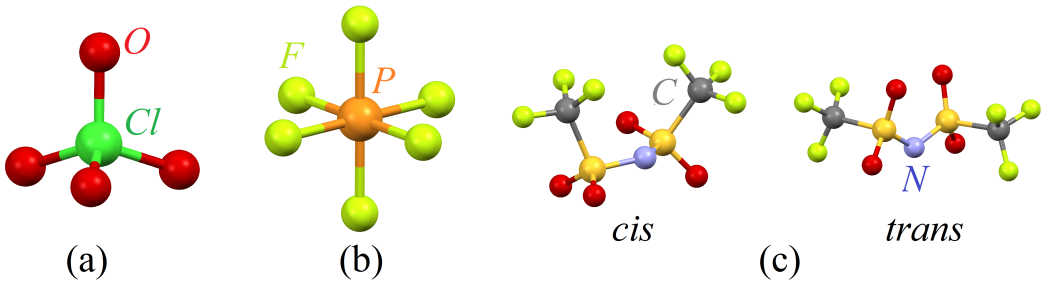

Figure 1.8: Types of (a) ClO_4^- and (b) PF_6^- and (c) $TFSI^-$counter-ions.

Lithium Hexafluorophosphate

Lithium Hexafluorophosphate, or $LiPF_6$, shown in Figure 1.8 (b) is the de-facto in the industry as an electrolyte material for a battery application. The high purity synthesis of this sample usher the industrialization of Li-ion battery by removing LiF ($LiPF_6(s) \rightleftharpoons LiF(s) + PF_5(g)$) and hydrogen fluoride (HF) at ambient temperature, which previously was responsible for reacting with solvents [81]. The chemical, physical, and thermal properties show it fulfills many conditions simultaneously. For example, in a carbonate solvent, it shows low:

- conductivity than $LiAsF_6$ [82]. For example, in EC/DMC (1:1) the conductivity is 10.7 $m/\Omega cm$, slightly less than $LiAsF_6$
- dissociation constant than $LiTFSI$ [78]
- ionic mobility than $LiBF_4$
- thermal stability than most of the other salts
- anodic stability than $LiAsF_6$ and $LiSbF_6$ [83] and
- chemical stability toward ambient moisture than $LiClO_4$, $LiTFSI$, and $LiTf$ ($Li(CF_3SO_3^-)$) [84].

and resist oxidation potential up to 5.1 V, thus enabling fairly large electrolytic window. Owing to many compromising advantages, $LiPF_6$ loses 50% of its weight at $> 200\ ^\circ C$,

but in non-aqueous solutions, the deterioration occurs at substantially lower temperatures, for example, as low as 70 $°C$. Moreover, $P-F$ bonds elongate by the presence of moisture in non-aqueous solvents, producing a series of corrosive products. Interestingly, $LiPF_6$ also decomposes at the positive side on the surface of the current collector. Usually, Aluminum is used as a current collector other electrolytes corrodes the surface with a passage of time but with $LiPF_6$ it get passivated [85].

Lithium bis(trifluoromethanesulfonyl)imide

Lithium bis(trifluoromethanesulfonyl)imide, or $LiTFSI$, is a hydrophilic salt with the chemical formula $Li(CF_3SO_2)_2N$ stabilized by two trifluoromethanesulfonyl (triflic) groups [86]. Thermodynamically, $TFSI^-$ is a flexible molecule with two most observed common conformation, *cis* and *trans*, as shown in Figure 1.8. This flexibility entails the internal degree of freedom around the $S-N-S$ axis moreover, the electronic properties shows the electrons from triflic groups are delocalized and the structure resonates between many states as shown in Figure 1.9. However, two metastable states are observed at room temperature [87]. The usage of this electrolyte in Li-ion batteries have shown an advantage over others salts with regards to (i) solubility in organic non-polar solvents (ii) Li cycling in $TFSI^-$ based electrolytes (iii) thermal stability, and (iv) high conductivity (melting point 236 $°C$ and decomposition at 360 $°C$) [88]. Despite all these merits, one of the disadvantages is the Al metal substrate gets corroded at the cathode, forming $Al(TFSI)_3$.

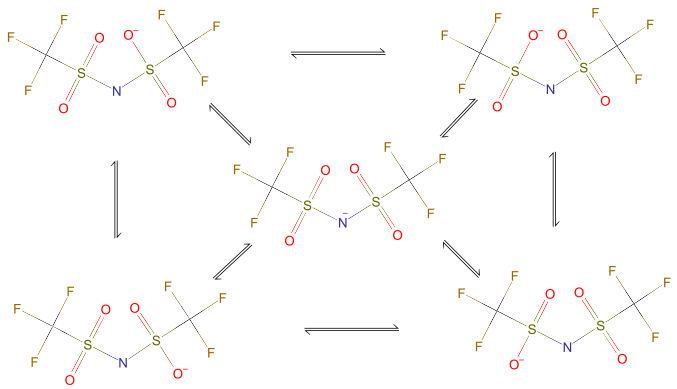

Figure 1.9: Resonance states of the $TFSI^-$ anion. Electronic density is delocalized.

Nonetheless, it provides higher conductivity than $LiTf$, and less hazardous than $LiClO_4$, thermally stable than $LiBF_4$ and $LiPF_6$, less toxic than $LiAsF_6$ and an oxidation limit lower than $LiBF_4$ and $LiPF_6$ but still high enough to be practical [83, 89, 90].

Efforts have been made to curb or modified with other metals, for example, one strategy has been devised is to passivate Al substrate with other salts or structurally modified $TFSI^-$ anion with perfluorinated alkyl chain, but this has produced low ionic conductivity. For industry applications and portable devices, Al has several advantages one of them being it is light-weight metal, stability to oxidation at a high potential, excellent processability, and low cost [91]. Many studies in recent years have been shifted in understanding and using $LiTFSI$ as an electrolyte solute for polymer based Li-ion batteries [52].

1.5 Experimental references to our study

Experimentally, the electrochemical studies were carried out at Electrochimie et physicochimie des matériaux et des interfaces (LEPMI) lab. In this section, we summarize their finding which will be a validation point for our theoretical modeling of these complexes.

The standard absolute voltage and standard rate constant were determined by Cyclic Voltammetry (CV) in three different electrolytic media with acetonitrile (ACN) as a solvent. All measurements were performed at room temperature (25 ± 20^o C). The experimental voltage and electron transfer kinetics are given in Table 1.1. The low k^o value for $LiTFSI$ compared to other electrolytes shows the intercalation or deintercalation is slower for Fe and Ru complexes due to the steric effects ($TFSI^-$ is a voluminous molecule). Whereas, for $LiPF_6$ and $LiCO_4$ it is considerably higher. For Cu, the kinetic rate is slower for every counter-ions so that substantial conformational changes upon loading and unloading are expected. A great part of our calculations will be devoted to this phenomena. Fe and Ru are coordinated with three ligands forming an octahedral environment provided by the *dmbpy* molecules with no room left for counter-ions to participate in the coordination. On the other hand, Cu coordination is somewhat more flexible and have been discussed in the literature [92–94]. The coordination is believed to vary from four to six depending upon the ligand. Our collaborators were able to synthesize these latter with two coordinated *dmbpy*, allowing the compound to see its voltage in an adequate window of potential for practical use.

Table 1.1: The $E^o(V)$ values have been measured vs. the Li^+/Li reference electrode and the kinetic rate $k^o(cm/s)$ have been determined according to the nature of the anion (from the electrolyte).

	$[Fe(dmbpy)_3]^{2+}$		$[Ru(dmbpy)_3]^{2+}$		$[Cu(dmbpy)_2]^{2+}$	
	E^o	k^o	E^o	k^o	E^o	k^o
$LiClO_4$	4.18	0.0450	4.39	0.05	3.15	0.00033
$LiPF_6$	4.20	0.0365	4.40	0.035	3.13	0.00033
$LiTFSI$	4.21	0.0096	4.40	0.0033	3.07	0.00014

In Table 1.1, mono-nuclear voltage and kinetics rate have been displayed. These results allow us to qualify the influence of the counter-ions on the electrochemical properties of the complexes. These data will be used to validate our calculated voltages. The $TFSI^-$ counter-ion appears as the least appropriate anion because it always leads to the lowest k^o values. This significant decrease, close to a factor four, can be attributed to the large volume of $LiTFSI$, which does not allow the rapid clearing of the complex in the loading process. For the Cu complex, the kinetic rate is low for every counter-ions, and the voltage found quite independent of the choice of the counter-ion. This kinetic behavior suggests it constitutes a poor candidate for a fast-charging battery.

As regards to the standard potentials, E^o, the system Ru^{2+}/Ru^{3+} displays higher potential values with respect to Fe^{2+}/Fe^{3+} system ($\approx$ 200 mV). The carbonate-based electrolytes are stable up to 4.2/4.4 V. Under these conditions, the use of Ru^{2+}/Ru^{3+} complex (E^o = 4.4 V vs. Li^+/Li) may lead to a higher parasitic oxidation. In the case of Fe^{2+}/Fe^{3+} complexes, this contribution should be negligible. In Table 1.2, measured kinetic rate and voltages are given for Fe bi-nuclear complex with chain, $-(CH_2)_n-$, of length n in the $LiClO_4$ medium. For a chain length, $n = 6$, the voltages and kinetic rate are found similar to the ones of the mono-nuclear compounds, whereas, for $n = 2$, it differs by an amount of 0.10 V. The difference between the two chains is 0.12 V. Thus, it appears that the bi-nuclear compound behaves more and more as an independent mono-nuclear compound as the size of the chain is increased. In general, the kinetic rate for the shorter chain is smaller than for the longer chains. These experimental results show that, although these counter-ions do not contribute directly to the coordination of the TM ions, they induce noticeable effects on the kinetic rate and voltages of our compounds. The theoretical work in this thesis will try to qualify these effects at the atomic scale.

Table 1.2: The $E^o(V)$ values have been measured vs. the Li^+/Li reference electrode and the kinetic rate $k^o(cm/s)$ have been determined in $LiClO_4$ medium. L here is the linker chain length.

	$[Fe^2(Lbpy)_3]^{4+}$	
L	E^o	$k^o(\pm 10\%)$
$-(CH_2)_2-$	4.29	0.028
$-(CH_2)_6-$	4.17	0.050

1.6 Ab-initio approach in modeling batteries

To model the above complex, we will use Kohn-Sham Density functional theory (DFT) to investigate the geometry, energetics, and thermodynamic properties. We will present the general theory that is behind the DFT codes. For more and in detail theoretical discussion, the reader can consult the vast amount of literature [95, 96].

1.6.1 Density functional theory

The exact Hamiltonian $\hat{H} = \hat{T}_e + \hat{T}_n + \hat{V_{N-e}} + \hat{V_{e-e}} + \hat{V_{N-N}}$ is a many body problem and poses immense complexity to solve exactly. With Born Oppenheimer (BO) approximation, the complexity of the Hamiltonian is reduced to a many electrons problem. The nuclear part is treated as a classical particle and is added to electronic energy, calculated from Quantum mechanics. It is possible to solve it exactly, but for very small systems. The theory of Hohenberg and Kohn (HK) recasts the problem into a mono-electronic one. It relies on two theorems:

Theorem 1. *The total energy, is a unique functional of the electron density* $\rho(\boldsymbol{r})$.

The first theorem states that no two external potential, $V_{ext}(\mathbf{r})$, exists which give rise to the same density $\rho(\boldsymbol{r})$, so each $V_{ext}(\mathbf{r})$ must be a unique. Hence, the corresponding Hamiltonian, wavefunction, and potential is a unique functional of electron density. This theorem establishes the uniqueness of electron density. The second theorem runs on the line of variational theorem to find the best density that minimizes the Hamiltonian.

Theorem 2. *The groundstate energy can be obtained variationally: the density that minimizes the total energy is the exact groundstate density.*

This theorem states that, if we have trial electron density $\tilde{\rho}(\boldsymbol{r})$, then this will be an upper bound to the true ground state density, $\rho(\boldsymbol{r}) < \tilde{\rho}(\boldsymbol{r})$. With this two theorem the

complexity of 3N particle wavefunctions is reduced to a three variable particle density [97, 98]. The functional form of energy given by HK is,

$$E_{HK}\left[\rho\left(\boldsymbol{r}\right)\right]=T_{e}^{int}\left[\rho\left(\boldsymbol{r}\right)\right]+V_{e-e}^{int}\left[\rho\left(\boldsymbol{r}\right)\right]+\int v_{ext}\rho\left(\boldsymbol{r}\right)d^{3}\boldsymbol{r}=F_{HK}\left[\rho\left(\boldsymbol{r}\right)\right]+\int v_{ext}\rho\left(\boldsymbol{r}\right)d\boldsymbol{r} \tag{1.7}$$

with density given by $\rho\left(\boldsymbol{r}\right)=\sum_{i}^{N}\left|\phi_{i}\left(\boldsymbol{r}\right)\right|^{2}$. On the right side of the Equation 1.7, there are three terms that contribute to the HK total energy. The first term represents the kinetic energy of the interacting electrons. The second term electron-electron repulsion interactions and the third term Nuclear-electron interaction (sometimes also called external potential). This functional is a complicated interacting system and still unsolvable. Kohn and Sham (KS) [97, 98] suggested this functional could be re-written as an independent particle system and the approximation to the ground state density will be exactly same as for the interacting system, if we have the exact exchange-correlation (XC) functional.

$$E_{KS}\left[\rho\left(\boldsymbol{r}\right)\right]=T_{s}\left[\rho\left(\boldsymbol{r}\right)\right]+\int v_{ext}\rho\left(\boldsymbol{r}\right)d\boldsymbol{r}+E_{H}\left[\rho\left(\boldsymbol{r}\right)\right]+E_{XC}\left[\rho\left(\boldsymbol{r}\right)\right] \tag{1.8}$$

Where $T_{s}\left[\rho\left(\boldsymbol{r}\right)\right]=\sum_{i}^{N}<\phi_{i}|-\frac{\hbar}{2m}\nabla^{2}|\phi_{i}>$ and $E_{H}\left[\rho\left(\boldsymbol{r}\right)\right]=\frac{1}{2}\int\int\frac{\rho(\boldsymbol{r}')\rho(\boldsymbol{r})}{|\boldsymbol{r}-\boldsymbol{r}'|}d\boldsymbol{r}'d\boldsymbol{r}$ is independent particle kinetic energy operator. With four terms contributing to the total energy. The first term represents the kinetic energy of the non-interacting electrons. The second term represents the Nuclear-electron interaction. The third term represents the Hartree interactions and the fourth exchange and correlations term where all the approximation are stuffed up. In purposing this formulation the dynamical correlation of electron is lost yet the Pauli exclusion principle is forced to be satisfied. In this mean field approximation, the electrons moves in an effective potential (electrons moves in average potential). Where $v_{eff}\left(r\right)$ is given by,

$$v_{eff}\left(\boldsymbol{r}\right)=v_{ext}(\boldsymbol{r})+\int\frac{\rho\left(\boldsymbol{r}'\right)}{\left|\boldsymbol{r}-\boldsymbol{r}'\right|}d\boldsymbol{r}'+\frac{\delta E_{XC}\left[\rho\left(\boldsymbol{r}\right)\right]}{\delta\rho\left(\boldsymbol{r}\right)} \tag{1.9}$$

With this effective potential, the KS Hamiltonian becomes an eigenvalue problem, and most of computational time is spend on diagonalizing this matrix

$$\left(-\frac{\hbar^{2}}{2m}\nabla^{2}+v_{eff}\left(\boldsymbol{r}\right)\right)\phi_{i}\left(\boldsymbol{r}\right)=\varepsilon_{i}\phi_{i}\left(\boldsymbol{r}\right) \tag{1.10}$$

where ε_{i} are the eigen values, and ϕ_{i} are the single-electron wave-functions usually expressed in basis sets. Types of basis sets varies according to DFT codes. In physics

planes waves are used whereas, in quantum chemistry Gaussian or Slater type orbitals are preferred. When expressed in this fashion, it turns the partial differential equation into Matrix form. Than this expression is minimized subject to orbitals orthogonality and are solved by varying $\rho(\boldsymbol{r})$ and $v_{eff}(\boldsymbol{r})$ until self consistency with respect to the energy, forces etc. within a specified tolerance is achieved. In Figure 1.10, pictorial representation of the steps involved in solving KS equations are shown.

1.6.2 Exchange Correlation (XC) functional

If we could exactly represent this XC functional, the difference of behavior between interacting and non-interacting electrons could be vanished, and the KS theory should become exact. However, this is a bottleneck in the DFT and over the last years, many functional have been proposed to approximate this functional as exactly as possible. Nevertheless, a series of approximations have been derived, allowing to model complicated systems with enough accuracy. To approximate this functional, we separate the exchange-correlation energy, E_{XC}. By comparing Equation 1.8 and 1.7 we get an expression for E_{XC},

$$E_{XC}[\rho] = \left(T_e^{int}[\rho(\boldsymbol{r})] - T_s[\rho(\boldsymbol{r})]\right) + \left(E_{e-e}^{int}[\rho(\boldsymbol{r})] - E_H[\rho(\boldsymbol{r})]\right) \tag{1.11}$$

The most common approximations for E_{XC} are the local density approximation (LDA) and generalized gradient approximation (GGA). In LDA, E_{XC} is derived from the exchange-correlation energy of a uniform electron gas which tends to give good results for slowly varying densities. The exchange-correlation approximation based on LDA can be expressed as,

$$E_{XC} \approx E_{XC}^{LDA}[\rho(\boldsymbol{r})] = \int \rho(\boldsymbol{r})\,\epsilon_{XC}(\rho(\boldsymbol{r}))\,d\boldsymbol{r} \tag{1.12}$$

Where ϵ_{XC} is the XC energy density per particle. For LSDA the density could be replaced with $n(\boldsymbol{r}) = n^{\uparrow}(\boldsymbol{r}) + n^{\downarrow}(\boldsymbol{r})$. One step up is the GGA also called semi-local functional, which includes the local variation in density.

$$E_{XC} \approx E_{XC}^{GGA}[\rho(\boldsymbol{r})] = \int \rho(\boldsymbol{r})\,\epsilon_{XC}(\rho(\boldsymbol{r}), \nabla\rho(\boldsymbol{r}))\,d\boldsymbol{r} \tag{1.13}$$

There are wide varieties of GGA functional based on the characteristics of gradients in the electron density most of them have been implemented in computational codes. For solid state materials Perdew-Wang functional (PW91) [99] and the Perdew-BurkeErnzerhof functional (PBE) [100] are the most widely used functionals.

1.6.2.1 Hybrid functional

Local or semi-local functionals tend to delocalize electron and hence results in weak bonds, on the other hand, non-local functional localizes which is important for the transition metal [101]. In constructing functional, a compromise is usually made to cancel this self-interaction error (SIE) as much as possible. In Chapter 2, we will show an example for Fe complex, where a ligand field picture is vanished even within this approximation. The general formulation proposed by Becke [102] is to include a fraction of HF exchange energy in E_{XC} functional:

$$E_{XC} = aE_X^{HF} + (1-a)E_X^{DFT} + E_C^{DFT} \tag{1.14}$$

The parameter a is chosen on the basis of functionals approximation or usually it is fitted with the available training data sets. For the functional of hybrid type, like PBE, a is reasoned theoretically to be 0.25 [100, 103]. This functional in various code is known as PBE0, PBE1PBE1 or PBEh. Due to orbitals dependency, non-local functionals do not suffer from self-interaction error (SIE). On the hand, the correlation part is dependent on total electron density and its gradient suffers from self-interaction error (SIE). Other than this, there are other hybrid functionals one of them is B3LYP which has the form,

$$E_{XC}^{\mathrm{B3LYP}} = E_X^{\mathrm{LDA}} + a_0(E_X^{\mathrm{HF}} - E_{\mathrm{X}}^{\mathrm{LDA}}) + a_{\mathrm{X}}(E_{\mathrm{X}}^{\mathrm{GGA}} - E_{\mathrm{X}}^{\mathrm{LDA}}) + E_{\mathrm{C}}^{\mathrm{LDA}} + a_{\mathrm{C}}(E_{\mathrm{C}}^{\mathrm{GGA}} - E_{\mathrm{C}}^{\mathrm{LDA}})$$

where $a_0 = 0.20$, $a_{\mathrm{C}} = 0.81$ and $a_{\mathrm{X}} = 0.72$ have also been found successful for certain simple TM oxides [104]. Variation of this includes B3PW91. The other is TPSSh which includes 10% HF exchange term [105]. Besides general-purpose hybrids (such as PBE0) there are specialized hybrids intended for a particular narrow purpose. Jensen *et al.,* studied the first-row transition elements with GGA and hybrid functional and found that they are much more sensitive to the system being studied [106]. Ioannidis *et al.*, have reported with the increase in Hartree-Fock exchange term there is effective delocalization of charge to ligands and the shift in predicting the spin state ordering of the system [30, 107, 108]. This finding is also observed in this work for Fe complex, with and without the external field made by the counter-ions, and shows no sign of ligand field effect. In this work, we will test PBE0 (25%), B3PW91 (20%), and PBE functionals to calculate the fundamental properties of our compounds and will present the most important functional in the main discussion.

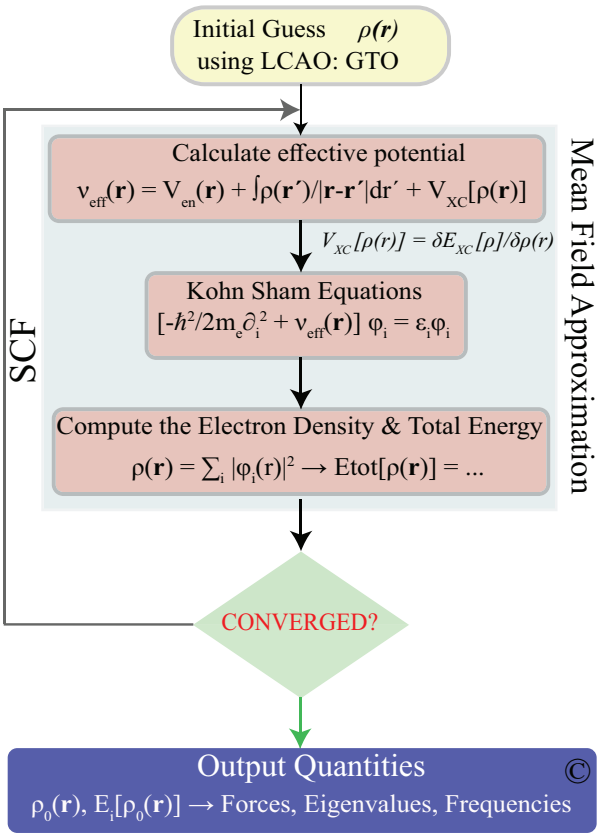

Figure 1.10: Flowchart for the self-consistent solution of the KS equation. The initial density is usually taken to be the superimposition of atomic orbitals and then effective potential is calculated by considering the variation of the total energy functional with respect to electron density.

1.7 Atomistic modeling for large scale system

To explore larger systems and timescales, we are forced to lower the degree of complexity of our models by abandoning the exact treatment of the electronic states provided by the very time-consuming Quantum Mechanical techniques. In other words, an alternative to DFT methods has to be considered by making use of some approximated Hamiltonian, constructed from ab-initio or experimental results. In Figure 1.11, timescales for different methods are shown, ranging from the atomic scale to the micro scale.

Molecular dynamics package (To name a few: AMBER[2], LAMMPS[3], and NAMD[4]) offers various types of ensembles which can be used to study the model realistically. In

[2]http://ambermd.org/
[3]https://lammps.sandia.gov/
[4]https://www.ks.uiuc.edu/Research/namd/

Atomistic MD simulation, rather than calculating the exact description of the system, we rely on computing the statistical averages over a long timescale. The system properties are simulated via exploring the configuration space at room temperature using canonical/isobaric (NVT/NPT) ensemble. In the following section, some of the theory behind MD simulations is outlined. For more complete description the readers can consult the literature [109].

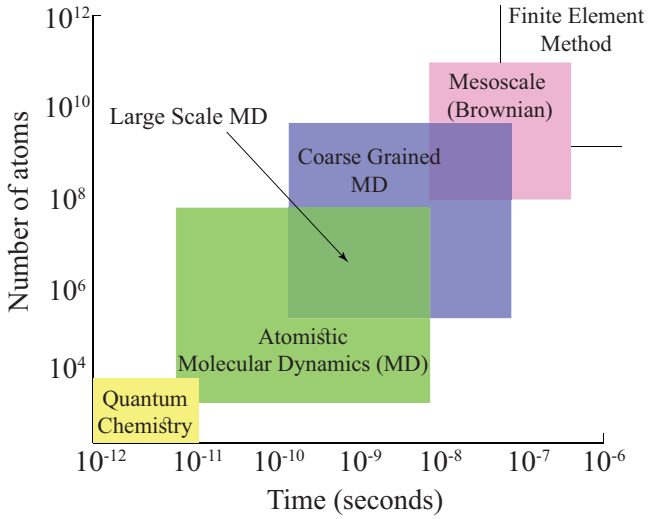

Figure 1.11: Timescales ranging from atomic level to micro level. The approximation shows the technique employed for simulating organic and inorganic materials [110]. In this picture we are at the Atomistic Molecular Dynamics timescale.

1.7.1 Molecular Dynamics (MD) simulation

The molecular dynamics simulation method is based on classical mechanics where the quantum effects are completely ignored by invoking the Born-Oppenheimer approximation. This approximation is justifiable due to the large mass difference between electrons and the nucleus resulting in a ratio of velocities $v_{electron}/v_{nucleus} \approx 10^4$. With that, the nuclei move in an effective potential where the coordinates of the electrons are treated as parameters. Hence the position of the atoms are treated as point particles on a coarse-grained level.

The ensemble in which we have obtained results is the NVE ensemble where the number of particles, volume and energy is constant. The Hamiltonian for this simple ensemble is given by, $\mathcal{H} = K + V(\boldsymbol{r})$, where r is a 3N dimensional vector describing all atomic positions and $V(\boldsymbol{r})$ is the potential energy function which comprises of bonded and non-bonded interactions. K is the kinetic energy given by $K = \sum_{i=1}^{N} m_i \boldsymbol{v}_i^2/2$, where

$\boldsymbol{v}_i$ and m_i are the velocity and mass of the i'th particle, respectively. The instantaneous temperature, T, can be calculated from the equipartition theorem, $K = 3Nk_BT/2$, without constraints on dimensionality. k_B is Boltzmann's constant. Further, time dependence of particle positions ($\boldsymbol{r}$), velocities ($\boldsymbol{v}$) and forces ($\boldsymbol{F}$) are determined from the relation, $\boldsymbol{F}_i = -\nabla_{\boldsymbol{r}_i} V(\boldsymbol{r})$. Usually, in almost all MD simulations the initial positions and velocities for all particles i are determined from Maxwell distribution.

Many algorithms exist in literature for integrating the equations of motion all of them have merits and demerits here we are going to touch a few of them. The differential equation is solved by numerical methods, most common are leap-frog and velocity Verlet integration schemes. The velocity Verlet and the leap-frog integrator are two common algorithms that are used by AMBER software. Leap-frog scheme, a modification of Verlet method, starts with positions $\boldsymbol{r}$ at time t and velocities $\boldsymbol{v}$ at time $t + 1/2\Delta t$ where Δt is the timestep. Then it updates the positions according to velocities, evaluates the potential and acquires acceleration in the next time point and updates the velocities. On the other hand, with velocity Verlet positions, velocities and accelerations at time $t+\Delta t$ are obtained from the same quantities at time t and continues. We have presented the simple expression, $\mathcal{H}$, for NVE ensemble. For complicated ensembles for example like isothermal-isochoric or isothermal-isobaric simulations, the expression for the total energy becomes more involved. For a more complete description of integrator and ensemble the readers can consult the literature [109].

1.7.2 Force Fields and the Potential Energy Function

As described above, the potential is responsible for propagating the system in time. In order to calculate the forces on each atoms we fist compute the potential energy function, $V(\boldsymbol{r})$. The force field (FF) potential consists of interatomic interaction functions whose parameters are tuned in order to describe the properties of the systems. These parameters are typically obtained from a large set of data obtained from ab-initio or by fitting to experimental data such as NMR, Infrared, Raman, or neutron spectroscopy, etc. A relatively huge number of sets of parameters exist and each parameter set has a name and provides parameters for certain types of molecules. For example, peptide, protein, and nucleic acid parameters are provided by parameter sets (*e.g.*, parm10, parm99, GAFF *etc.*) with names starting with "ff" and containing a two-digit year number, for instance, "ff99". General AMBER force field (GAFF) database provides parameters for small organic molecules to expedite simulations of drugs and small molecule ligands in conjunction with bio-molecules. Whereas, other parameters are fitted to the ab-initio calculation for specific systems. In this thesis, we have used Amber (Assisted Model

Building with Energy Refinement) potential. Parameters for this potential have already been developed in the context of drugs discovery, biology, and soft matter in which we can have our market. But we actually had to develop our home-made parameters for some specific bond and local arrangements. The simplistic five component picture of the potential energy that most molecular dynamics programs describe is,

$$V(r_N) = \sum_{bonds} k_b(l - l_0)^2 + \sum_{angles} k_a(\theta - \theta_0)^2 + \sum_{dihedrals} \frac{1}{2}\nu_n[1 + \cos(n\varphi - \gamma_{eq})]$$

$$+ \sum_{i<j} 4\varepsilon_{ij}\left[\left(\frac{A_{ij}}{r_{ij}}\right)^{12} - \left(\frac{B_{ij}}{r_{ij}}\right)^{6}\right] + \sum_{i<j}\frac{q_i q_j}{r_{ij}} \tag{1.15}$$

Above Eq. 1.15, consists of two parts; bonded and non-bonded schematically shown in Figure 1.12. The bonded part comprises of bond stretching, angle bending and dihedral torsion terms. In this description, the first term represents the energy between covalently bonded atoms based on ideal spring approximation. This approximation is satisfactory near the equilibrium bond length but becomes poor when distances go too far from the ground state. The second term represents the change in energy as a function of the angles between the various chemical bonds. The third term represents the energy needed to rotate around the bonds.

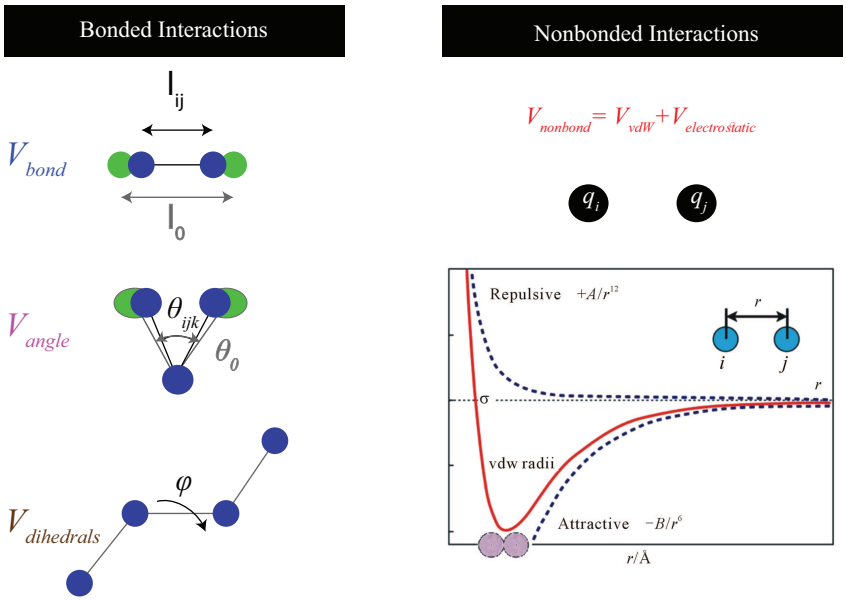

Figure 1.12: Schematic representation of Amber potential interactions terms.

The second part consists of van der Waals (vdW) and Coulomb interactions. With van der Waals interaction term, atoms with no net electrostatic charge will still tend to attract each other at short distances or tend to repel each other when they get too close. The form of the van der Waals (vdW) energy is calculated using the equilibrium distance (r_{ij}) and well depth (ϵ_{ij}). The constants A and B depend on the atom types and are derived from experimental data. In electrostatic interactions terms, opposite charges attract and like charges repel each other. These interactions are a long range, therefore, evaluating this with current methods has $O\left(NlogN\right)$ or $O\left(N\right)$ asymptotic complexity. Still, it remains the most demanding part of the calculation. Having laid out the description of the terms that are essential to model realistic system in Chapter 4 we will develop further in the context of Amber potential.

1.8 Aim of this research

The topic which we have opted was motivated by studying a different class of materials to model cathode electrode. In this regards, our attention was diverted to study organic system incorporating transition metal atoms and constructing long-range polymers. The introduction of transition metal complex, brings a larger mechanical stability to the system (metal-ligand coordination provides a way to enhance the bonding via co-valency) and lowering the problem of dissolution. However, in literature, most of the studies that have been done with these complexes do not include full-scale modeling. For example, they are modeled without counter-ions and have considered only the oxidation states. A truly experimental system comprises complexes with counter-ions and solvent molecules. To model these systems realistically we need to include counter-ion and report the voltage, geometry, and configuration of these systems and to show these can be modeled with current DFT. However, this will require an immense amount of work (we will ignore implicit solvent scheme from DFT calculation but will incorporate in a more realistic MD simulation) to explore large potential energy surface and immensity will further increase by exploring bi-nuclear states with different alkyl chain size. This will allow us to understand the effects of mono-nuclear sites within a bi-nuclear structure for cathode material design and to our knowledge, no computational data exist to study these as a function of chain length. We hope to induce some deep insights from this study and can be useful for the battery community.

This difficult task will be answered by the state of the art Density functional theory which at a theoretical level does not involve any assumption and is accurate. However, the choice of XC functional for these complex poses an extremely difficult task in select-

ing an appropriate approximation for these systems. With this in mind our first priority will be to study all these functionals and compute the voltage, geometry and coordination picture that is relevant in Ligand field theory to truly describe the coordination complexes. Among these chosen functional the best voltage and geometry and coordination picture will give us the most appropriate approximation for these complexes. In this study, we will analyze three complexes (Fe, Ru, and Cu) in the context of battery applications and demonstrate which complex is mostly appropriate.

As mentioned, with current DFT methods we are constrained by CPU time and memory and moreover, we cannot simulate up to thousands of atoms we need to resort to another approximation. We will opt MD approach with potential governed by our parameters fitted to DFT calculations. We have to mention this is a delicate and sensitive subject where no literature data exist and we rely on the experimental groups for their inputs. In this regards, the second phase of thesis will be devoted to construct and investigate fully reticulated poly nuclear 3D compounds (we have to mention this approach does not exist in literature and this is the first study) and employ the Atomistic potential (based on our DFT calculations) to study the dynamic properties of more realistic cathode materials and hope to answer the questions such as the effect of solvents on counter-ions and its role on structure stabilization further the effect of chain length on the 3D complex.

To sum up, we are presenting here a theoretical work aiming at contributing to these efforts by designing a transition metal polymer for cathode materials. We will provide a theoretical explanation for the observed phenomenon's (fundamental aspects) and propose a strategy for the modification of polymers to improve their performance (design aspects) in working conditions. In this endeavor, we embark on the study of transition metal complexes; modeled with different electrolyte medium (*i.e.*, counter-ions) to comprehend the structural effects during loading and unloading and their corresponding thermodynamics properties. We will take the advantage of computational approaches to model cathode materials for the battery applications.

1.9 Thesis outline

The chapters in this thesis go by pairs. Chapter 2, and 3 are in tight connection. In these chapters, thermodynamic properties and configuration of the mono-nuclear and bi-nuclear complex are discussed within the framework of Density functional theory (DFT). Likewise, the next two chapters have to be considered as a consistent set. In chapter 4, force field for Iron complex is developed and its ability to model bi-nuclear compound is

validated. In chapter 5, the so-developed Atomistic model is used to study the dynamics of the 3D poly-nuclear at large spatial and temporal scales. And the last chapter is the general conclusion summarizing the findings, giving a few perspectives, and highlighting the contribution of this work to the lithium battery research community.

■

Chapter 2

Thermodynamics properties of mono-nuclear Fe, Ru and Cu complexes

This chapter is devoted to the elementary pattern of our polymer batteries: the monomer or mono-nuclear made of a transition metal ion (Fe, Ru, and Cu) complexed by three 2,2´-dipyridyl (*bpy*) but also 4,4´-Dimethyl-2,2´-dipyridyl (*dmbpy*) molecules in the case of Fe and Ru and two molecules of *bpy* or *dmbpy* for Cu. Figure 2.1, provides a schematic representation of these compounds that we are addressing. We have decided to duplicate our study devoted to *bpy* by a new one, using *dmbpy* as a ligand, in order to provide a first account of the effects that can cause a polymerization; the methyl fragments plugged in replacement of the H atoms in the *bpy,* mimic the tip of an alkyl chain connecting both mono-nuclears.

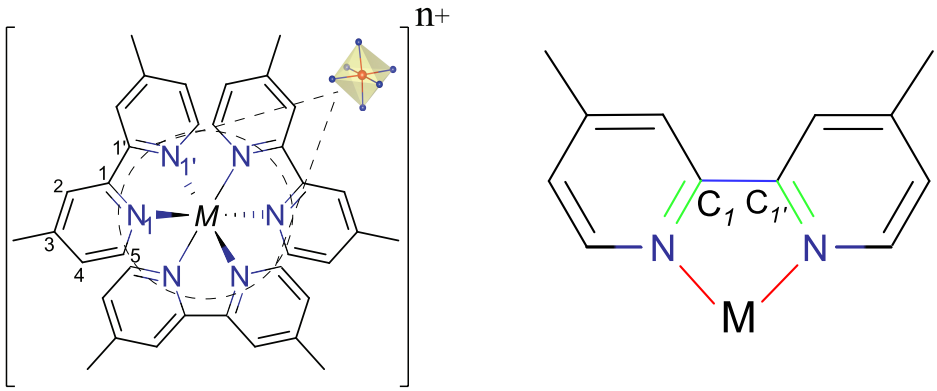

(a) **(b)**

Figure 2.1: (a) Schematic representation of the Transition metal complex with redox states. Here $M^{n+} = Fe$ and Ru where $n = 2$ or 3. (b) Selective bond lengths parameters in a complex are shown in color.

The characterization of the electronic properties, spin state ordering, geometry, and voltage of the mono-nuclears is an essential prerequisite before any attempt to model realistic polymerized batteries made of these elementary bricks. If literature is already abundant regarding the elucidation of these properties (gas phase, solid phase), many questions remain open, even for this single pattern, since all these independent studies were not particularly aiming at considering the complex for battery application: such a usage implies specific working conditions that we propose to investigate in the present work. More specifically, the process of charge of such a monomer consists in a change of the degree of oxidation of the transition metal ion by expelling a Li^+ (or Na^+) ion out of the cathode material, but leaving at its vicinity the counter-ions, denoted Ci^-, with which the Li^+ or Na^+ were associated in the electrolyte. These negatively charged ions are expected to affect in a non-negligible manner the properties of our positively charged complex. This approach is, to our knowledge quite unseen and is dictated by our will to model the electrochemical potential of our complex in the most realistic conditions as possible. At first, our strategy had consisted in neglecting the effects of the counter-ions to obtain a reference-calculation, in order to validate our settings by comparison with the independent calculations found in the literature. Then, we have added the counter-ions in order to appreciate their influence on the electrochemical properties of our systems. Rapidly, the problem of the choice of the most appropriate exchange correlation (XC) potential came up, and great attention will be brought in this chapter on this very sensitive issue.

2.1 Computational details

In this thesis, all calculations were performed using Gaussian09[1] program [111]. The optimization of the structure was investigated using DFT method by employing all-electron polarization basis set, def2SVP, of Ahlrich [112, 113] unless stated otherwise. The stability of the SCF solution was checked and Kohn-Sham (KS) orbitals were re-optimized (if unstable) using keyword *stable=opt*. In a few cases where geometry optimization was terminated due to convergence failure, converged KS orbitals were used as an initial guess (PBE0 orbitals in case of PBE and vice versa). Default integration grid was used for all the calculations. Several commonly used DFT functionals were tested. For example, Local Spin Density Approximation (LSDA), and among Generalized Gradient Approximation (GGA) functional family PBE [99] exchange-correlation (XC) form was tested. Moving up in the third and higher Jacob's ladder, PBE0 [100] (25), B3LYP (20) and TPSSh (10%) were also tested. The percentage shown in brackets is the Hartree-Fock (HF) exchange contribution. Because of computational limitations and huge size of our systems, double hybrid functionals were not tested. We studied our system with different functionals and determined the appropriate XC functionals (PBE and PBE0) which capture the condition thermodynamically and structurally closer to experiments.

All calculations were carried out in a vacuum with three anions (ClO_4^-, PF_6^-, and $TFSI^-$). Default criterion for the self-consistent field (SCF) and gradient were used. The geometry was optimized until the forces on each atom were less than 1×10^{-5} Ha/Bohr (Default). Moreover, to find out if the obtained structure is at local minima we did the vibrational analysis with the most stringent option such as *opt=tight* and ultrafine grid for integration. In all calculations, symmetry was turned off by using the keyword *nosymm* to lower system energy by breaking the molecular symmetry. For closed shell systems, it was not necessary to use unrestricted spin formalism because all electrons are paired up whereas, for open shell systems one electron is usually not paired for this reason it is vital to use unrestricted spin formalism together with the keyword *guess=mix*. This keyword allows the initial guess taken from the initial density matrix and requests the HOMO and LUMO be mixed so as to destroy spin and spatial symmetries and to produce the UDFT wavefunction for singlet states.

In choosing XC functional, other essential factors that have to be taken into consideration are the choice of basis sets to describe the wavefunction accurately. This choice always involves a balance between accuracy and computational cost. Many basis set options exist such as the famous split-valence Pople basis sets (6-31G, 6-311G etc.) which

[1] http://gaussian.com/

have the added value of assigning diffusive function on top of polarization but for our purposes it does not support second row transition elements and mixing and matching basis sets from different families can lead to problems. For this reason, we have chosen to stick with one family of basis sets. The Ahlrich def2 basis set family covers most of the periodic table. Two basis sets Def2SVP and Def2TZVP are considered with Def2TZVP giving us the added "polarization functions" which enhances the flexibility of atoms to form chemical bonds in any direction and hence improve calculated molecular structures. However, the Gaussian09 program does not support the diffusive basis in this family so we use the currently implemented basis sets. Generally, we calculated the voltage with these two basis sets and found the voltage to be almost similar. Finally, our choice turned to def2SVP basis: all the details regarding our technical choices are gathered in Appendix B. For electronic structure analysis, we used the GaussSum code to generate the density of state (DOS) and partial density of plot (PDOS) using Mulliken population analysis [114]. The technical details of this code have been given in the Appendix A (*see section* A.2).

2.2 Redox complex without counter-ions

In this section, we are aiming at calculating the ground state of our complex without considering the counter-ions. This approach coincides with what it is traditionally encountered in literature and instead has to be considered as a calculation of the energy of first ionization of the compounds than a real modeling of the loading process of our battery in working conditions, for which, negatively charged molecules of the electrolyte (counter-ions) come and surround the complex. The field created by these counter-ions is however expected to affect the total energies and consequently the voltages. We shall consider this more accurately and propose a model in the next section. This assumption has to be viewed as a starting point in our attempt to model the charging/discharging process at the cathode and for which numerous points of validation are available to check out the settings of our calculations. For this first study, we have used Fe and Ru transition metal ions complexed by three *dmbpy* molecules. Figure 2.1 (a), shows the 3D geometry of our complex of coordination: three *dmbpy* arrange themselves around the metallic site so that an octahedral cage of nitrogen encloses the transition metal ion.

2.2.1 Ground state structure of Fe and Ru complex

Figure 2.2, shows the deformation of the structure during loading and unloading. This deformation is observed clearly for all three parameters as shown in Table 2.1. The experimental bond lengths for the *bpy* molecule in the complex are shown in Table 2.1 and 2.2. Moreover, all calculations in this thesis have been done for the *dmbpy* ligand. For specific complex experimental data for the Metal complex with *dmbpy* ligands are not available so, for validation purposes, we are comparing our results for complex without methylation. In doing so, we can also study the effect of methylation on the structural properties.

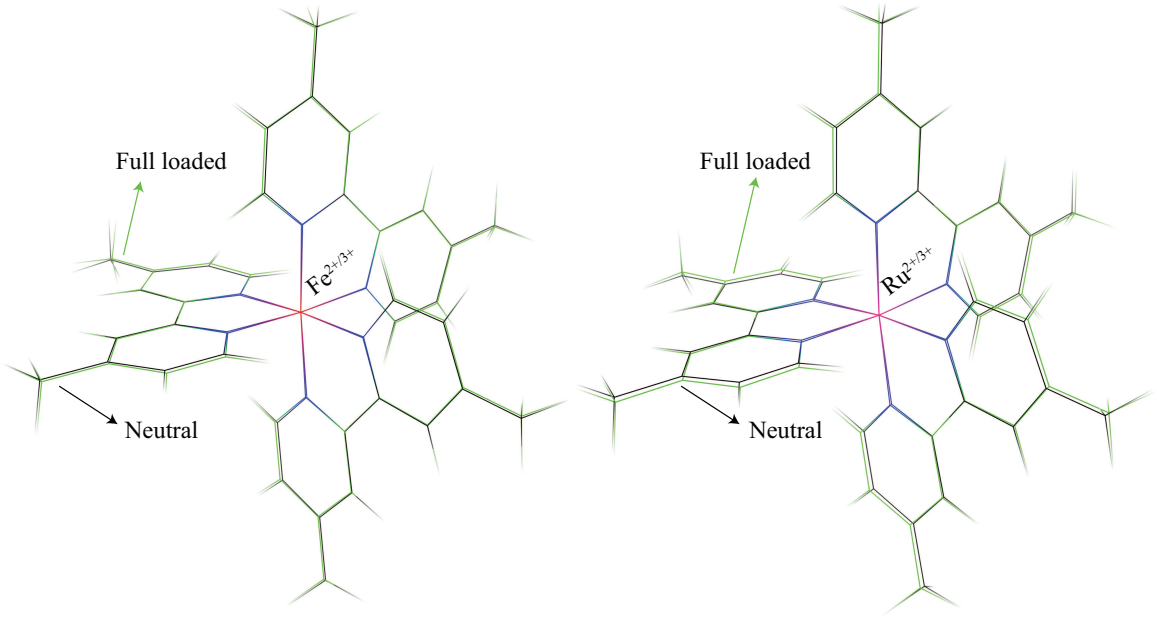

Figure 2.2: Comparison of ground state structure deformation from $[M(dmbpy)_3]^{2+}$ $\rightarrow$ $[M(dmbpy)_3]^{3+}$ at PBE0/PBE//Def2SVP level of theory. Hydrogen atoms have been omitted for clarity reason.

We analyze the system with various spin multiplicities to find the lowest energy. Moreover to find the Metal spin state, Mulliken net spin polarization was performed. For $[Fe/Ru\,(dmbpy)_3]^{2+}$ the net spin polarization shows zero electron on metallic site. On the basis of Mulliken net spin analysis we have shown for $[Fe/Ru\,(dmbpy)_3]^{3+}$ complex an unpaired electron resides on the metallic center, which shows the oxidation is taking place at the metallic center and *dmbpy* ligands are neutral. Similarly, England *et. al.*, investigated the $[Fe\,(bpy)_3]^{3+}$ complex and they showed no assignment of oxidation was taking place at the *bpy* ligand [24]. Scarborough *et al.*, have studied a number of complexes and study the oxidation level of *bpy* when coordinated to metal sites. The

criterion they used to establish the spin state of the metallic site is by $C1-C1'$, $N-C1'$, and $M-N$ (Iron and nearby Nitrogen atoms), bond lengths [25]. Moreover, they observe by Mulliken net spin density analysis no oxidation or reduction is taking place at the ligands. England *et al.*, have performed the DFT calculation without considering counter-ions and found BP86 functional (family among gradient corrected functional) better describes their systems [24]. They establish the low spin (LS) by comparing the bond lengths parameter with the experimental structure.

For comparison purposes, experimental bond lengths for complexes are reported in a crystal phase for PF_6^- and ClO_4^- counter-ions and acetonitrile (ACN) solvent. Also, between these two counter-ions, $C1-C1'$ bond lengths vary on the order of 0.001 Å. The $M-N$ bond lengths calculated for $[Fe\,(dmbpy)_3]^{n+}$ complex for $n=2$ shows the variation on the order of 0.03 Å with respect to PBE0 functional and for $n=3$, 0.01 Å is observed. Whereas, for Ru, the variation is about 0.01 and 0.02 Å for $n=2$ and 3 respectively. For other parameters such as, $C1-C1'$, we did not observe any significant difference, however, for $Ru^{3+}$with respect to two functional, we observe a difference of 0.02 Å. It might be due to the crystal structural data were obtained at 105 K and no data exist in literature at 300 K to our knowledge. Likewise, for $N-C1$, a small difference of 0.01 Å is observed. Hence, from all this discussion we notice both these approximations work nice and describe the bond lengths parameters well when compared to experimental data.

Table 2.1: Selected average experimental bond lengths for $[M(bpy^0)_3]^{2+}$ (*Neutral*) and $[M(bpy^0)_3]^{3+}$ (*Full Loaded*) complex are compared to the minimized structure obtained at PBE/PBE0//Def2SVP level of theory. For Fe: experimental parameters for *Neutral* are given for methylation and for *Full loaded* without methylation. All bond lengths are given in **Å**.

	$[Fe(dmbpy)_3]^{2+}$			$[Fe(dmbpy)_3]^{3+}$		
	Opt		Exp [24, 115]	Opt		Exp [116]
	PBE	PBE0		PBE	PBE0	
$Fe-N$	1.96	1.99	1.965(3)	1.98	1.97	1.96(3)
$C1-C1'$	1.470	1.474	1.473(3)	1.471	1.471	1.472(6)
$N-C1$	1.363	1.344	1.350(0)	1.370	1.354	1.350(0)

Table 2.2: Selected average experimental bond lengths for $[M(bpy^0)_3]^{2+}$ (*Neutral*) and $[M(bpy^0)_3]^{3+}$ (*Full Loaded*) complex are compared to the minimized structure obtained at PBE/PBE0//Def2SVP level of theory. For *Ru*: experimental parameters for *Neutral* and *Full loaded* system are given without methylation, respectively. All bond lengths are given in **Å**.

	$[Ru(dmbpy)_3]^{2+}$			$[Ru(dmbpy)_3]^{3+}$		
	Opt		Exp [117]	Opt		Exp [117]
	PBE	PBE0		PBE	PBE0	
$Ru-N$	2.066	2.065	2.054 [117, 118]	2.077	2.071	2.056
$C1-C1'$	1.473	1.473	1.474(7) [25]	1.475	1.473	1.450
$N-C1$	1.365	1.348	1.351	1.375	1.357	1.353

2.2.2 Electronic structure for Fe and Ru compounds

2.2.2.1 Results within the PBE0 approximation

From the paper of [107], the PBE0 approximation appears to be the most appropriate approximation for the exchange and correlation (XC) potential to cope with systems made of transition metals surrounded by *bpy* ligands, in particular, the Fe complex. This is quite natural, that is our first calculations attempt to model this system making use of this approximation. However, this approximation remains in many aspects unclear as we shall explain in the followings via the careful analysis of the density of states and, sometimes, in contradiction with its nature (delocalization effects instead of expected localization ones) as already noticed by the authors of the original paper [107].

Figure 2.3 and 2.4, show the electronic levels of $[Fe\,(dmbpy)_3]^{n+}$ ($n = 2$ and 3) as well as a corresponding density of states (for which we found the visual more adequate enough to discuss and comment our results). This latter was generated from the data of the electronic energy levels by applying the Hermite-Gaussian smearing method of unit height one, if the orbital energy levels are near the height goes according to the sum of Gaussians [114]. In the plot, broadening of the peaks is controlled by the parameter $w_{1/2}$= 0.1 eV. It denotes the full width at half maximum (FWHM). The HOMO and LUMO states are spotted on each plot. In the followings, we shall locate and name a given peak with respect to the HOMO level, such that the first peak encountered below the HOMO level is HOMO-1, the next one HOMO-2, and so on $\cdots$. For $n = 2$ (Figure 2.3), the HOMO state mostly interests the d states of Fe (blue curve) and a very weak hybridization is found with its six N neighbors so that the six valence electrons of Fe^{2+}

correspond to the HOMO level. We, however, notice that the ligand field picture is not strictly observed since one single peak is obtained instead of both e_g and t_{2g} levels expected in the octahedral environment. This lack of degeneracy can be explained by the very weak hybridization with the nitrogen atoms: such a ligand field scheme is recovered when more covalent chemical bonds are developed. The present calculation shows that the PBE0 approximation tends to award a too ionic character to the transition metal. In the case of $n = 3$, the d-band of Fe^{3+} contains five electrons and emptying of the HOMO level was expected.

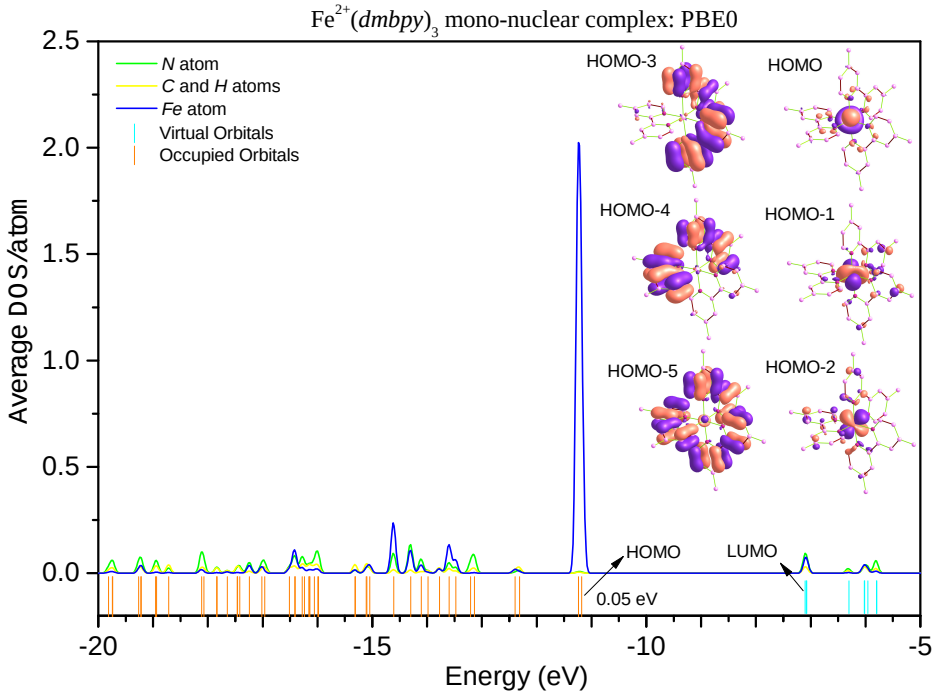

Figure 2.3: Average partial density of states (PDOS) calculated within the PBE0 approximation for the $[Fe(dmbpy)_3]^{2+}$ complex. It is built upon the data of the electronic levels using Hermite-Gaussian smearing method with a smearing parameter of $w_{1/2} = 0.1$ eV. We have added the partial DOS corresponding to Fe, the sum of carbon and hydrogen contributions from the *dmbpy* (in yellow) and the sum of the six nitrogen contributions from the *dmbpy* in green. The occupied orbital electronic levels are reported in orange color at the bottom.

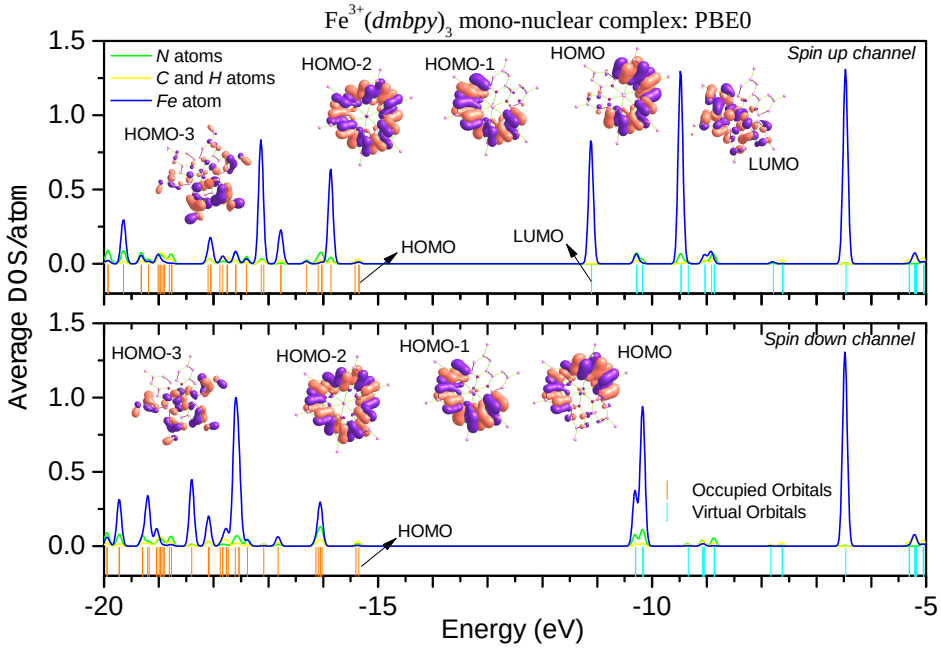

Figure 2.4: Spin-polarized average partial density of states (PDOS) calculated within the PBE0 approximation for the $[Fe(dmbpy)_3]^{3+}$ complex. It is built upon the data of the electronic levels using a Hermite-Gaussian smearing method with a smearing parameter of $w_{1/2} = 0.1$ eV. We have added the partial DOS corresponding to Fe, the sum of carbon and hydrogen contributions from the *dmbpy* (in yellow) and the sum of the six nitrogen contributions from the *dmbpy* in green. The occupied electronic levels are reported in orange color at the bottom.

Figure 2.4, actually reveals that the d level of Fe^{3+} does not contribute any more to the HOMO level of the compound (mainly C and H states does) but, instead, hybridizes strongly with the N levels over a long series of hybridization states. Despite this PBE0 approximation were found adequate in literature since it provides an exact magnetic state (as provided by the experiments) as well as accurate geometries for the compounds, we object that (i) the expected ligand field picture is fully invalidated (we do really expect that d states continue to contribute to the HOMO level) but also that (ii) the PBE0 approximation leads here to the formation of much delocalized band instead of an amplification of the localization phenomenon as its Hartree-Fock part suggests. Let's remind, here, that these calculations are our first guess to model our compounds and only reproduce the calculation of ref [107].

To conclude this paragraph, we display in Figure 2.5 and 2.6 our study devoted to the Ru complex within the same approximation. The results are found to be similar to the ones we obtained for Fe. They are however a little bit more in agreement with the ligand field picture, despite quite insufficiently: for $n = 2$, a degeneracy into e_g and t_{2g}

parts start to be noticeable, and for $n = 3$, a residue of d states of Ru remains in the HOMO level but in such a small amount that the hybridization effects of the d levels of Ru with the N levels below the HOMO level still have to be considered as the majority event.

For PBE0 functional, it can be seen from the Table 2.2, the average distance between the $Ru^{2+} - N$ is 2.065 **Å** which compared to experimental values vary by 0.01 **Å** whereas, for $Fe^{2+} - N$ it varies by 0.02 **Å**. We believe improvement of Ru^{2+} DOS plot over Fe^{2+}, is due to the hybridization with the Nitrogen octahedral cage which is substantiated by the geometrical parameters as compared to the Fe^{2+} complex.

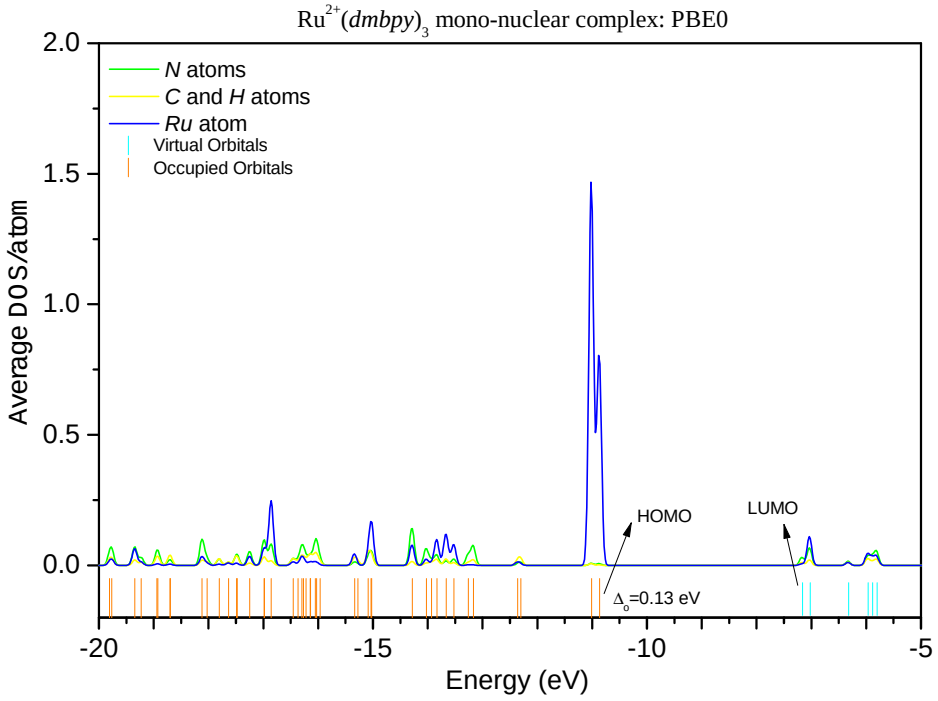

Figure 2.5: Idem as Figure 2.3 but for $[Ru(dmbpy)_3]^{2+}$ complex.

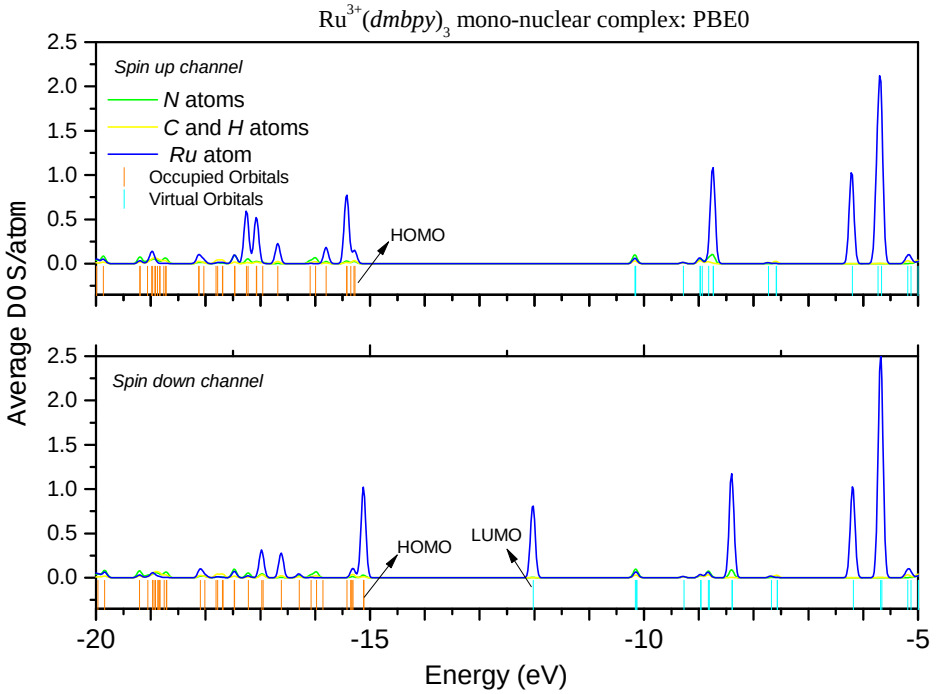

Figure 2.6: Idem as Figure 2.4 but for $[Ru(dmbpy)_3]^{3+}$ complex. Each spin channel has been plotted on the same axis.

2.2.2.2 Results within the PBE approximation

As already mentioned, the PBE approximation was providing similar results as the PBE0 approximation for the geometry of our compounds so that nothing fundamentally forbids us at present to pursue our investigations within this approximation. Thus, let's examine in this paragraph if the electronic structure using this latter XC approximation is found in better agreement with our ligand field picture for the transition metal in an octahedral environment of nitrogen. In Figure 2.7, 2.8, 2.9, and 2.10, we report the plots of the partial DOS for both the M^{2+} and M^{3+} valence state within the PBE approximation for $M = Fe$ and Ru, respectively. They appear quite different with respect to PBE0 and corresponds in a very satisfactory way to the ligand field scheme, which is expected commonly for systems with the octahedral environment. Moreover, during the oxidation process, our Mulliken charge analysis reveals that one electron leaves the HOMO level as expected. We consider these latest results as major improvements with respect to the PBE0 case. More specifically, for Fe and Ru complex in the case $n = 2$, both e_g and t_{2g} peaks may be distinguished. For $n = 3$, for both Fe and Ru, the HOMO states displays in majority a d character, even if the open shell of the transition metal invariably leads to a larger hybridization between nitrogen and metal states than in the case of $n = 2$.

The open shell electronic structure favors such a behavior since the relative shift of spin up and down bands (both result and cause of the magnetism of the metal of transition considered at this degree of oxidation) provides an additional degree of freedom to mix the bands, and consequently to find a state of lower energy by hybridization. However, at this stage, the choice for the XC correlation potential (between PBE and PBE0) remains quite subtle. The study devoted to the calculation of the voltage, the addition of counter-ions all around the compounds, but also in the next chapter, the behavior of both these approximations with respect to polymerization of these elementary patterns, will continue to affine and fix our final decision regarding the proper description of the XC potential in our compounds.

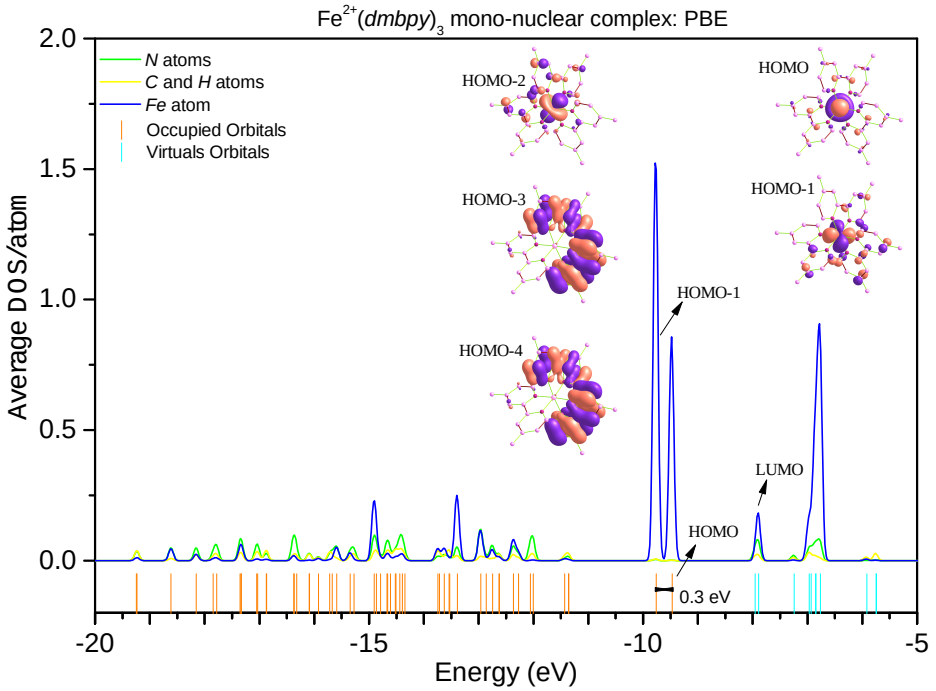

Figure 2.7: Idem as Figure 2.3.

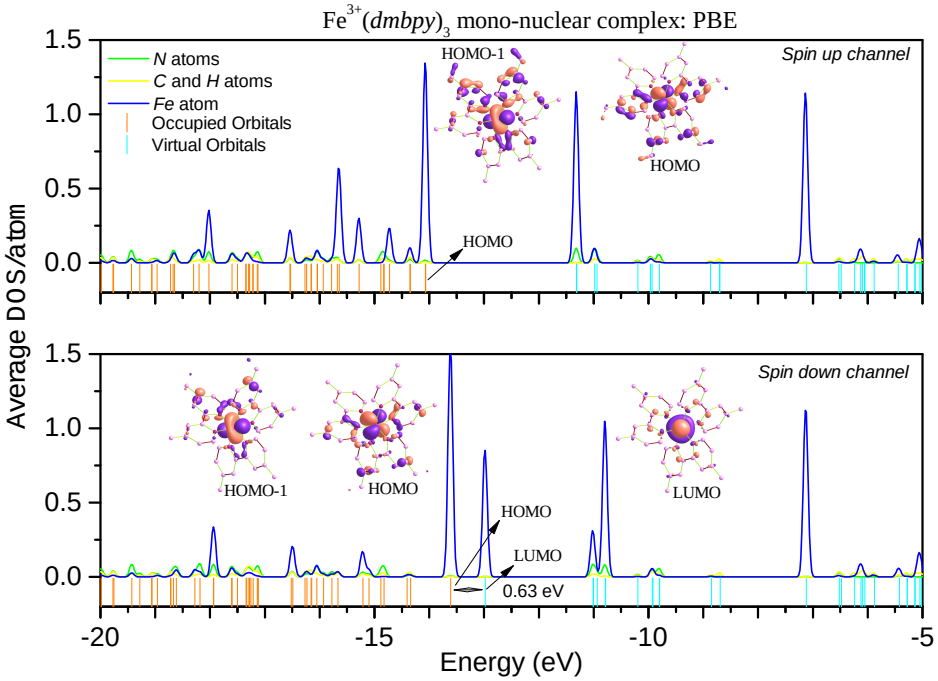

Figure 2.8: Idem as Figure 2.4. Each spin channel has been plotted on the same axis.

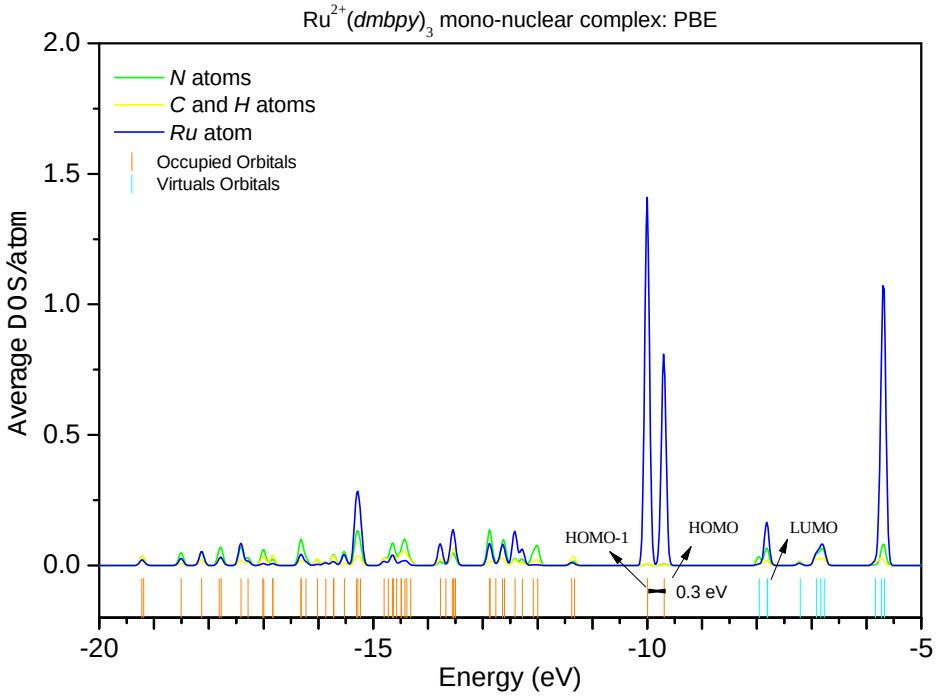

Figure 2.9: Idem as Figure 2.3 but for $[Ru(dmbpy)_3]^{2+}$ complex.

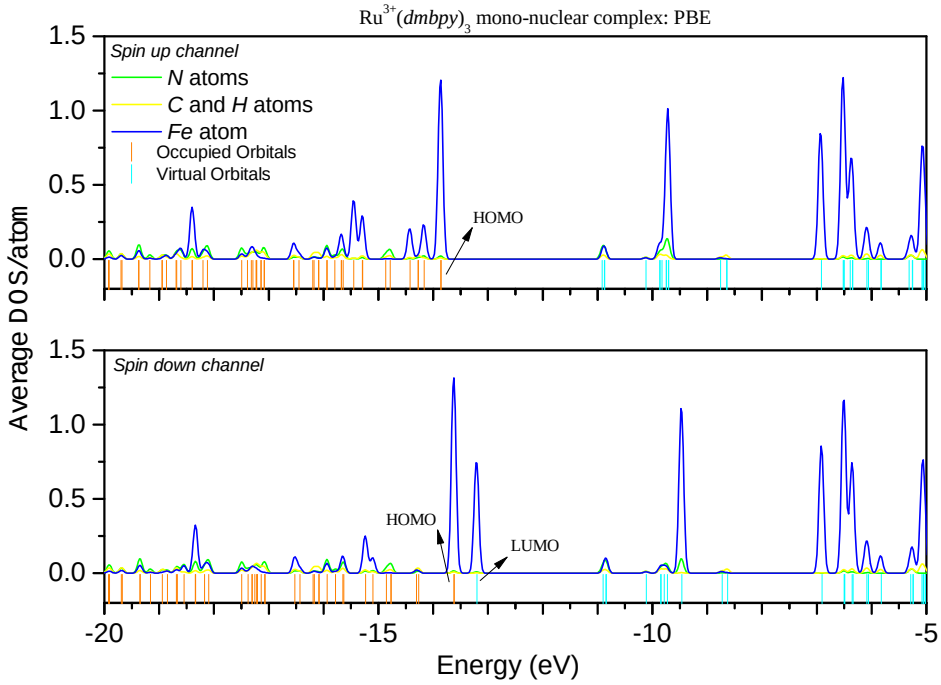

Figure 2.10: Idem as Figure 2.4 but for $[Ru(dmbpy)_3]^{3+}$ complex. Each spin channel has been plotted on the same axis.

2.3 Cu complex

The case we have discussed before (Fe and Ru compounds) are characterized by their ability to form coordination in which the octahedral geometry predominates. For Cu complex, the case is a little bit different so that we consider it apart. Hathaway *et al.*, have reviewed Copper(ll) complexes and classified different stereochemistries according to coordination. Unlike the first-row transition metals where they can coordinate in a wide range that is in octahedral, tetrahedral and square-coplanar geometries, Cu ion, on the other hand, shows reluctance in forming up a regular octahedral or tetrahedral stereochemistries. This usually comes from the $3d^9$ outer electronic configuration which lacks cubic symmetry, and hence coordination of four, five or six is observed with structure distortions in its geometry through bond-length or bond-angle [92]. Moreover, the experimental group at LEPMI lab has synthesized the Cu complex coordinated by two *dmbpy* for a battery application. That is the compound we had decided to study (schematically represented in the Figure 2.11) is in tight connection with the experiments. In that case, Cu ion is coordinated by four Nitrogens.

Here, we are presenting a very brief description of our results for the Cu complex since this case of study (the molecule considered without counter-ions) represents a very

poor description of our compound in functioning conditions (battery applications): as we shall see in the next section, the role played by counter-ions is crucial given the very deep changes of conformation they induce. We had this present calculation only to complete our series (Fe, Ru, and Cu) to allow the first comparison with experimental data. Let's, however, comment the so-obtained geometries.

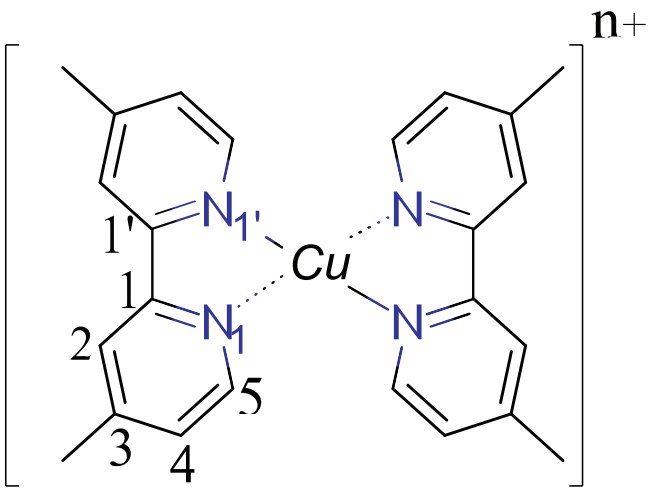

Figure 2.11: Schematic representation of the Cu Transition metal complex with redox states $n = 1$ and 2.

Figure 2.12 (a) presents the relaxed geometry of the compound for $n = 1$: a distorted tetrahedral geometry is obtained. In Figure 2.12 (b), we have superimposed the geometry of the previous compound ($n = 1$) with the optimized geometry of our compound for $n = 2$. We have shifted and rotated this second molecule such that one chosen *dmbpy* ligand in each compound exactly match so that we can assess the displacement of the second one as n pass from 1 to 2. As oxidized ($n = 2$), significant rotation of φ_0 is observed for the second *dmbpy* with respect to the corresponding one considered at $n = 1$: an almost square planar is obtained. Such a reorganization of the ligands all around the Cu ion, as oxidized, is a deep drawback for battery applications since such effects slow down the charge/discharge kinetics of the compound. This effect was expected and in agreement with the experiments (see section 1.5 for more detail). The DOS (not represented) display the same features as the ones encountered for Fe and Ru complex, but with variations of shape due to the change of local geometry (distorted tetrahedral $\rightarrow$ "square planar"). From these calculations, total energies for $n = 1$ and $n = 2$ are obtained allowing us to calculate the voltage we need to allow our first comparison to the experiments. The case of the Cu-based complex will be further developed in the

more realistic conditions of simulation considered in the next section taking into account the field created by the counter-ions.

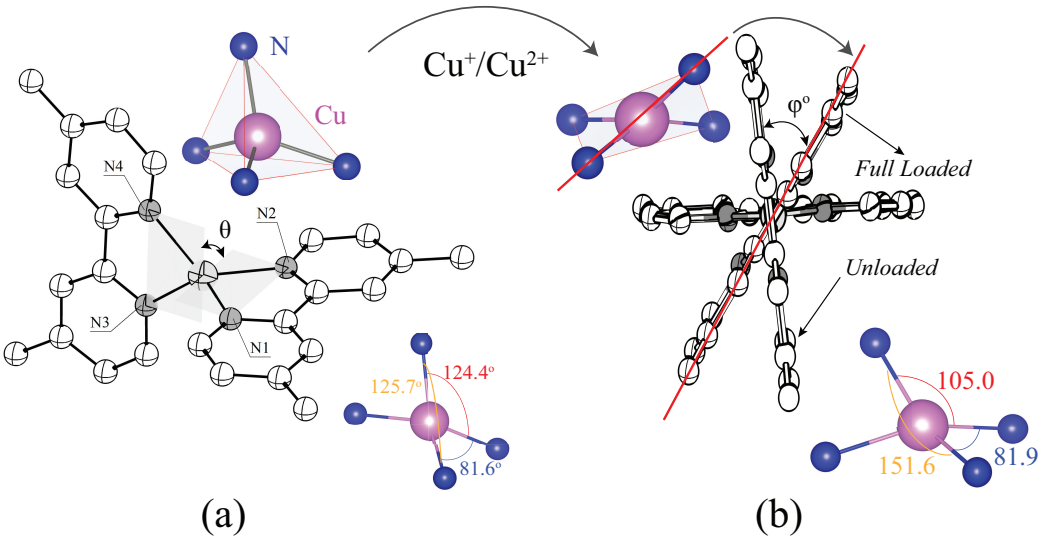

Figure 2.12: (a) Ground state structure of $[Cu(dmbpy)_2]^+$ complex (b) Superimpose optimized structure of $[Cu(dmbpy)_2]^{2+}$ on $[Cu(dmbpy)_2]^+$ complex. Hydrogen atoms have been omitted for clarity reason. θ^o is the angle between two *dmbpy* plane. φ^o is the rotation angle resulted from oxidation.

2.3.1 Calculation of the voltage

We are presenting here what can be considered as the degree zero of approximation to calculate the voltage of a candidate-battery: the difference of total energies between the compounds considered in two different degrees of oxidation, which instead identify to the energy of first ionization rather than a voltage in functioning conditions. This approach is a common one and we have reported results in this paragraph for Fe, Ru and Cu complex.

Table 2.3: Absolute value identified as the first approximation to the ionization energy. Ground state energy has been calculated for methylated compound.

E_M	$\approx E^N - E^{FL}$ (eV)	
	PBE	PBE0
E_{Fe}	-11.20510649	-11.12205402
E_{Ru}	-11.45626036	-11.43517778
E_{Cu}	-8.68679291	-8.50746271

In addition, we have also reported in the table the difference of voltages (the absolute voltage of Fe being considered as the reference). This is the formulation we will adopt in the following of this thesis as far as counter-ions will be taken into account. We add them here for further direct comparison with our results including counter-ions effects. In Table 2.4, the relative voltage difference has been calculated for both PBE and PBE0 functionals. Moreover, the reported voltage in literature has been computed considering implicit solvents whereas experimental voltages in electrolytic medium (solvents, ions, *etc.*) [24]. The voltage reported for V_{Ru-Fe} in our calculation without any external field agrees well with the experiments and DFT calculations. In Table 2.4, relative voltages are given with and without methylation. In Table 2.5, ground state multiplicity along with Mulliken net spin on Metal sites are shown. Our calculation agrees with DFT as well as experimental values. The effect of methylation on voltages can be observed by a difference of 0.24 for Cu/Fe and 0.01 for Ru/Fe. For Fe and Ru, the voltage corroborates with the experimental values whereas, for Cu, they are off by $\sim$ 1.5 V. Such a huge error on the voltage for the Cu complex was expected. However, as already mentioned, the role played by the counter-ions, bringing an additional negative center at the vicinity of the positively charged complex, combined to the ability for the compound to easily vary its coordination is expected to curb this problem.

Table 2.4: Relative voltages calculated for mono-nuclear complex using Def2SVP basis set. For completeness purposes we have included voltage for non-methylation.

	Non-methyl		Methyl		
	PBE	PBE0	PBE	PBE0	Exp
$V_{Ru-Fe}(V)$	+0.25	+0.30	+0.25	+0.31	+0.20 [24]
$V_{Cu-Fe}(V)$	-2.75	-2.82	-2.51	-2.61	-1.03

2.4 Spin contamination problem and magnetism

For transition metal complex, DFT poses a spin contamination problem. Therefore, for these systems, we investigated the contamination at ground state geometry. For closed shell system, the system does not show any contamination even if the calculations are spin polarized, however, for open shell $< \hat{S}_2 >$ deviates from $S_z\,(S_z + 1)$. Where $S_z = 1/2$, the difference between up and down spin of the system. This contamination arises from unrestricted Kohn-Sham (UKS) formalism where Slater determinant is not an

eigenfunction of the spin operator. In literature, it is commonly argued this value could be ignored, however, some studies have argued it is the reason which leads to mixed state and should be treated. As, a general rule if the difference between $S_z\,(S_z+1)$ and $<\hat{S}_2>$ is less than 10% it could be safely ignored [119]. In literature, for hybrid functional, this contamination leads to optimized geometry in high spin state hence giving erroneous energy [120, 121]. On the other hand, semi-local functional tends to give low spin state [26]. Here, we have investigated both and observe the contamination values falls below the above threshold. The initial value of the spin state is a very sensitive parameter to determine the exact ground state. We prepared various spin multiplicities to find the lowest energy of our systems and performed the Mulliken net spin polarization analysis to check out the so-obtained spin states and orbital occupancies.

Table 2.5: Ground state magnetic states calculated for mono-nuclear complexes with and without methylation. S is the spin ground state of the system. M is the net Mulliken spin polarization on transition metal site in a cluster.

Net spin on sites (μ_B)					
Complexes	Methyl		Non-Methyl		Ground state
	PBE	PBE0	PBE	PBE0	
	M				S
$[Ru(dmbpy)_3]^{2+}$	0	0	0	0	0
$[Ru(dmbpy)_3]^{3+}$	0.91	1.01	0.91	1.01	1/2
$[Fe(dmbpy)_3]^{2+}$	0	0	0	0	1
$[Fe(dmbpy)_3]^{3+}$	1.08	1.14	1.08	1.14	1/2
$[Cu(dmbpy)_2]^{+}$	0	0	0	0	0
$[Cu(dmbpy)_2]^{2+}$	0.5	0.68	0.5	0.68	1/2

2.5 Complexes in the field of counter-ions

Our preliminary study opens more questions than it actually solves it. The choice of the proper approximation for the XC potential remains uncertain since the geometries and differences of the voltage obtained by both these approximations are very similar. The case of the Cu complex is pathologic for both approximations, so does the requirement for an increase in our level of modeling. Adding the counter-ions to the vicinity of the complex appears as an appropriate improvement. This addition will further create electrostatic effects which are sensitive enough to induce the cation center and its environment but also induce the change in the potential of the local geometry. Moreover,

steric effects are also likely to change the total energies and geometries of the compounds as the complex change their degree of oxidation by re-approachement of such counter-ion coming from the electrolyte. This cannot be without consequences on the calculation of the voltages. In this section, we will repeat the approach of the previous section and emphasize the intakes brought by the introduction of counter-ions found in usual electrolytes, namely ClO_4^-, PF_6^-, and $TFSI^-$.

2.5.1 Why introducing counter-ions and how?

As stated in the first chapter, most studies found in literature have been done assuming only solvation effects to mimic the experimental conditions. In this thesis, we have considered the counter-ions to study the battery in working conditions, rather than adding solvent molecules and Li^+ or Na^+ ions. This deserves some explanations. Understanding Polymer-batteries from the point of view of oxides or intercalation compounds-batteries should be a dead end. In the case of intercalation compounds, the change in the electrochemical potential finds its origin in the insertion of Li^+ ions inside octahedral and tetrahedral sites of the host structure, leading to local deformation of these patterns. The more these deformations are limited, the better the performance of the battery is. Our polymer-batteries are made of chains of polymers bathing into a mixture of solvent molecules and high conductive ions coming from the electrolyte. In such a mixture, the Li^+ ions and their counter-ions are fully dissociated and surrounded by solvent molecules. The electrostatic potential created by the solvated Li^+ ions is screened by the solvent. In addition, presenting the same sign as the transition metal of the complex, this effective medium (namely Li^+ surrounded by solvent molecules attenuating the + charge) are supposed to be expelled far away from the electrochemical center (Fe^{2+}, Ru^{2+} or Cu^+). Only the counter-ion which were initially associated with the Li^+ ion in the electrolyte, charged negatively, is found to be a relevant parameter for our study. Quite certainly, our calculations will overestimate the effects due to the counter-ions since we do not screen these latter by solvent molecules (these calculations are out of the scope of this Ph.D. work), but as we shall develop all along this section, such a screening were not found mandatory to recover an excellent agreement between our calculated voltages and the available experimental ones. Moreover, let us mention that our system has to be regarded as soft matter. If local deformations can be noted in oxides during an event of Li insertion; our complex which is more flexible in nature than oxides can also induce effects brought by these negatively charged counter-ions. They are expected to induce more drastic changes in the configuration of our complex than insertion does in oxides and are assumed to be the majority phenomenon during a loading cycle of the battery

made out of our compounds with respect to the effects that could induce a fully solvated Li^+ ion, for example.

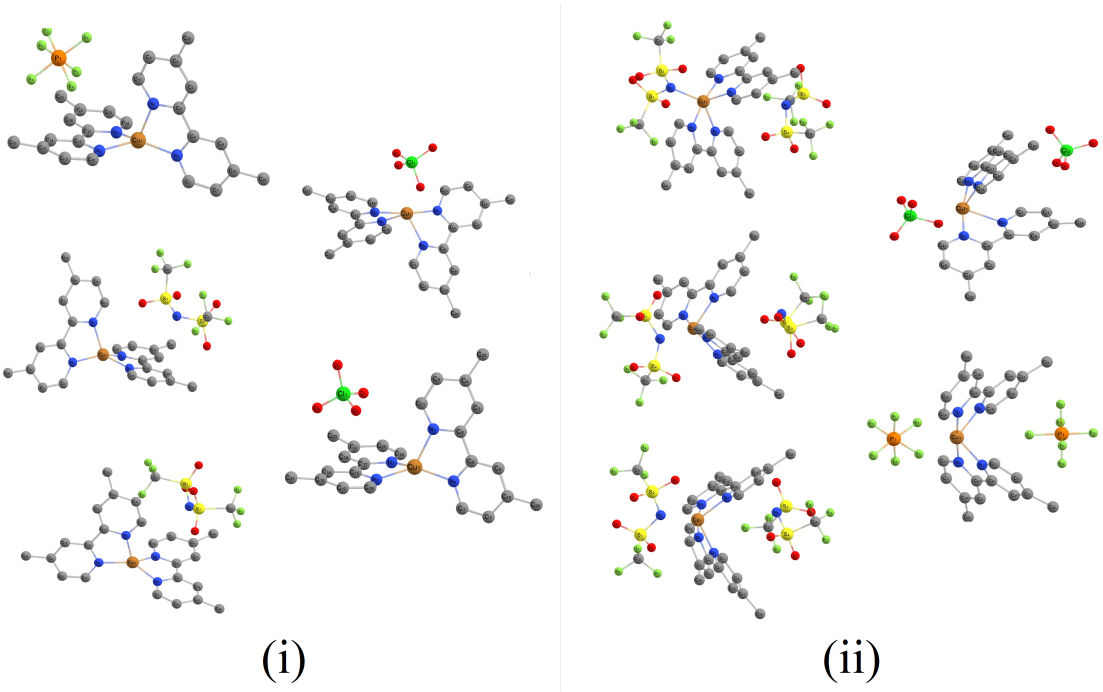

Figure 2.13: Metastable configurations obtained for (i) $[Cu(dmbpy)_2]^+ Ci^-$ and (ii) $[Cu(dmbpy)_2]^{2+} 2Ci^-$ compounds at various initial locations.

To conclude, let's mention a few words about the challenging technical problems that raises such an introduction of the counter-ions in our DFT calculations. They reside in the huge amount of initial locations that had to be attempted to explore the full potential energy surface of our problem. The obtaining of the ground state were found very sensitive to the locations of the counter-ions according to their nature: a voluminous $TFSI^-$ ion will not locate at the same position as a ClO_4^- ion. Moreover, even for the same counter-ion, an inappropriate initial location can lead to ghost ground states. This was particularly sensible in the case of the Cu complex, for which the complication by only two *dmbpy* molecules, increases the number of guess locations in the space of the configuration. We illustrate this point in Figure 2.13. Finally, great care has to be brought to the conformation of the counter-ion itself. We devote the next section to this point.

2.5.1.1 Weakly coordinating anions

Before caring about our global analysis of the geometry of the whole complex, a series of points and difficulties inherent to the counter-ions themselves must be addressed. The anion known as $TFSI^-$ is a flexible molecule around its $S-N-S$ center and many initial conformations were computed to get its ground state geometry in the gas phase. In the Figure 2.14, we provide both metastable ground states. These two states are commonly observed experimentally. They correspond to the C_1 symmetry (*cis*) and C_2 symmetry (*trans*), respectively.

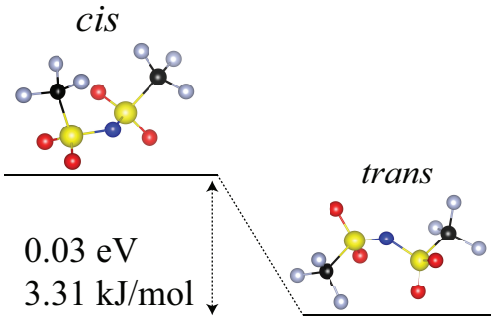

Figure 2.14: Calculated structure of $TFSI^-$ anions in the gas phase: two conformations are investigated the *cis* and the *trans* ones. *Trans* conformation is found to be the ground state by an amount of 3.31 kJ/mol. This small barrier entails the internal flexibility.

The energy difference between these two conformers is found to be 0.035 eV (namely 3.31 kJ/mol for PBE and PBE0) and the comparison of their total energies allows to predict that the *trans* configuration is the global minima in agreement with the literature [122, 123]. Such energy is not negligible since three $TFSI^-$ molecules come and surround the complex: an accumulated miss in the determination of the lowest energy conformation could modify the total energy by an amount of about 0.1 eV and induce the same mistake in the calculation of our voltage.

The Mulliken charge analysis, calculated with both functionals, shows the charge distribution is the same for both conformers. No charge localization is observed on the Nitrogen atom but distributed over all oxygen and N atoms [122]. Dipole moment calculated for *trans* and *cis* are 0.083 and 3.45 Debye, respectively. This, was also observed in [124]. This is explained by its larger dipole moment, smaller molecular volume and by a better satisfaction of the steric effects in *trans* configuration. This point will be further discussed in the context of external perturbation, in the next section.

On the other hand, due to their high symmetrical nature PF_6^-, and ClO_4^- (Figure 1.8 (a) and (b)) counter-ions do not raise such difficulties. The calculated bond distance for $P_1 - F_i$ at PBE and PBE0 are 1.644, 1.618 and for $Cl_1 - O_i$ 1.473, 1.444 respectively. Resolution of the diffraction pattern gave $P - F$ bond lengths of 1.601 and 1.568 Å [125]. We only observe a slight variation of the bond lengths when these counter-ions are embedded in a complex. Due to their high electronegative nature, it is recommended to use basis sets which include diffusive and polarization functions. Among def2 family of basis sets, many basis sets are available but we chose to use Def2SVP and Def2TZVP [112, 113] to study. In Appendix B, we have shown using Def2TZVP basis sets does not bring any huge difference to the reported voltage and geometry. In the proceeding sections, all results will be with Def2SVP basis sets.

2.5.2 Thermodynamics and voltage within the field of counter-ions: formalism

In this paragraph, we briefly derive the expression of the voltage of our battery when the counter-ions, denoted Ci^-, are directly taken into consideration in the process of charging or discharging of the batteries. The half-reaction at the cathode (here, written for Fe) reads,

$$[Fe\,(dmbpy)_3]^{3+}\,3Ci^- + e^- \rightharpoonup [Fe\,(dmbpy)_3]^{2+}\,2Ci^- + Ci^- \tag{2.1}$$

Where Ci^- stands for the counter-ions, *i.e.*, Ci^- can either be $TFSI^-$, PF_6^- or ClO_4^-. Typically, the formula $[Fe\,(dmbpy)_3]^{3+}\,3Ci^-$ corresponds to the Fe^{3+} ion surrounded by three *dmbpy* ligands and three Ci^- counter-ions at its immediate vicinity. This pattern corresponds to the charged monomer and our DFT calculations are, from now on, attached to calculate the total energies of this full pattern but also the one of $[Fe\,(dmbpy)_3]^{2+}\,2Ci^-$ (with the same notation) that we shall refer as the unloaded or discharged pattern (or monomer). They directly take into consideration the interactions between the Ci^- ions and the complex. At the Li anode, the half-reaction reads.

$$Li^+ + Ci^- \rightleftharpoons LiCi \tag{2.2}$$

$$Li \rightleftharpoons e^- + Li^+ \tag{2.3}$$

They convey the phenomena of dissociation of the $Li - Ci$ molecules into a Li^+ and

Ci^-anion in the electrolyte (Eq. 2.3, as well as the adsorption of the Li^+ ion on the surface of the anode. This latter finally contribute to form an adlayer of metallic bcc-Li at the surface of the anode, making use of the electron coming from the cathode (Eq. 2.4). Thus the balanced equation for the full cycle reads after simplifications.

$$[Fe\,(dmbpy)_3]^{3+}\,3Ci^- \rightharpoonup [Fe\,(dmbpy)_3]^{2+}\,2Ci^- + LiCi - Li(bcc)$$

The corresponding Gibbs free energy is given by,

$$\triangle G_{Fe} = E^{\left[Fe(dmbpy)_3\right]^{2+}2Ci^-} + E_0 - E^{\left[Fe(dmbpy)_3\right]^{3+}3Ci^-} \tag{2.4}$$

where the total energy corresponding to $LiCi$-Li(bcc) is noted E_0. This energy is a constant for our problem and the same value has to be used whatever the transition metal (Fe, Ru, Cu) is considered. In our calculations, the Gibbs free energy, $\Delta G = U - T\Delta S + p\Delta V$, will be approximated by the internal energy, U, which corresponds to our first-principles total energies, since the contributions of entropy and variations of the volume of the cell are very small (< 0.01 V): these terms can be ignored. Given that the voltage associated with the chemical reactions reads,

$$V = -\frac{\triangle G}{n\mathcal{F}} \tag{2.5}$$

After substitution of Eq. 2.4 in Eq. 2.5, we get

$$V = -\frac{E^{\left[Fe(dmbpy)_3\right]^{2+}2Ci^-} + E_0 - E^{\left[Fe(dmbpy)_3\right]^{3+}3Ci^-}}{n\mathcal{F}} \tag{2.6}$$

or, alternatively by introducing a reference potential, $V_0 = E_0/nF$,

$$V^{Fe} = -\frac{E^{Fe^{2+}(dmbpy)_3 2Ci}}{n\mathcal{F}} - \frac{-E^{Fe^{3+}(dmbpy)_3 3Ci}}{n\mathcal{F}} - V_0 \tag{2.7}$$

This V_0 potential gathers all the various energies not directly connected with the total energies of our compounds in the degree of oxidation 3+ and 2+. It contains all the terms that can hardly be calculated within the framework of our methods (solvated $Li-Ci$, the calculation of the total energy of bcc-Li using the Gaussian code is delicate as any calculations concerning condensed phase with this code, work of extraction of the electrons, and so on $\cdots$). As commonly met in literature, we present our results with respect to one selected voltage (for us, the one of Fe): we are comparing the calculated differences of voltage, $\delta V = V^M - V^{Fe}$, where $M = Ru$ and Cu, with respect to their corresponding experimental data. Thus, V_0 is vanished in the expression of δV, avoiding

to introduce too many additional errors arising from our approximate knowledge of V_0.

2.5.3 Ground state structure of Fe and Ru redox complex

According to the reaction mechanisms using these two XC functionals, we obtained the minimized geometry with counter-ions around it in the gas phase and each structure was ranked according to energetics this is schematically shown in Figure 2.15. In Figure 2.15, the minimized position of counter-ions is shown after scanning all the locations. Figure 2.15 (a), shows the neutral case where we have obtained the position of counter-ions after exploring many locations. This trend is observed for both Fe and Ru based complex. It can be seen counter-ions are not consistent and vary by its nature. For PF_6^- and ClO_4^- which we have labeled L_1, shows the minima position is opposite to each other (This state we termed as *free*). Whereas, for $TFSI^-$ which we have labeled L_2 the minima position is on the different location with *cis* conformation.

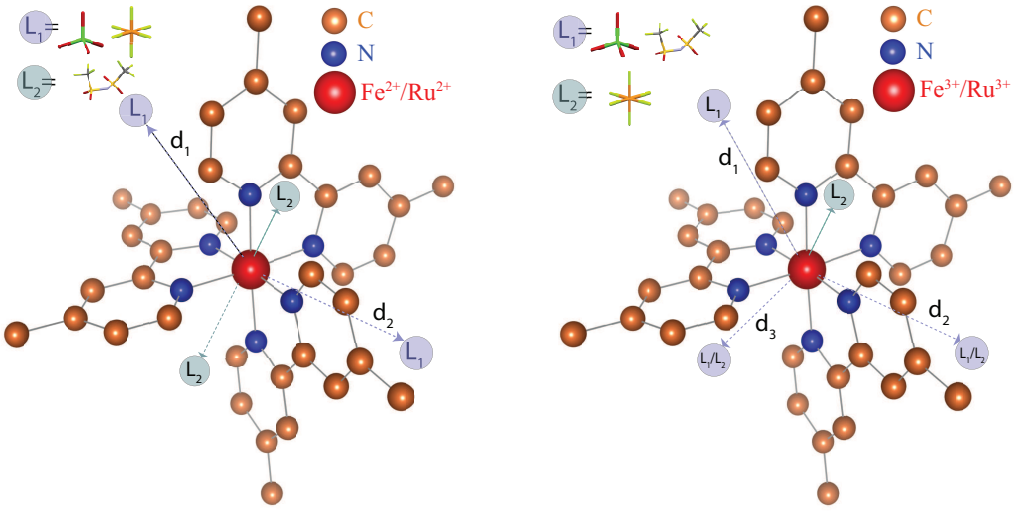

(a) **(b)**

Figure 2.15: Schematic representation of $[M(dmbpy)_3]^{n+}$ nCi^- complex for (a) $n = 2$ (b) $n = 3$ with $M = Fe$ and Ru outlining the location of the counter-ions after relaxation of the geometry. In (a) L_1 label spot the smallest and symmetric counter-ions, namely PF_6^- and ClO_4^- whereas L_2 label stands for the most voluminous $TFSI^-$ counter-ion: the location of the counter-ion depends deeply on steric effects (see text) similarly, in (b) but with different counter-ions position labeling. Hydrogen atoms are omitted for clarity.

It is interesting to see in the Figure 2.15 (a) the L_2 location is somewhat *caged* by the atoms $N2 - Fe/Ru - N4 - N3$ as compared to L_1. It shows the steric effect deeply plays a role in finding the minima position. On the other hand, 2.15 (b), gets a little bit more complicated to understand. In our understanding, if we have already obtained the neutral compound, now we have to add one more counter-ions and find the minima position relative to this state. However, our analysis shows the position is completely altered when three counter-ions are accounted. It can be seen clearly from the Figure 2.15 (b), with the same labeling scheme the counter-ions location varies. For ClO_4^- and $TFSI^-$ which we have labeled now L_1, is a mixture of *free* and *caged* state. Whereas, L_2 has taken the position of Neutral in Figure 2.15 (a). This show exploring all the location to find the local minima requires immense work and analysis. We would like to point out the configuration given below were explored with PBE0 functional whereas, for PBE we also observe the same configuration. With PBE0 hybrid functional one would observe the elongation of bonds due to HF exchange terms. However, due to steric and electrostatic effects, counter-ions produce external perturbation to the system which forces the system to compact itself around Metal ions.

Here, one thing to bring in notice is the geometry obtained with two functionals shows the same location of counter-ions irrespective of the functional used. So, we have decided to show for one functional only. For PF_6^- and ClO_4^- counter-ions. The conformational space is simplified by ignoring the internal high molecular symmetry whereas, for $TFSI^-$ it amounts to exploring each complex with different states and here we found $TFSI^-$ in a *cis* state to be lower in energy than *trans* state by 0.29 eV for $[Fe\,(dmbpy)_3]^{2+}$ $2TFSI^-$ and 0.28 eV for $[Fe\,(dmbpy)_3]^{3+}$ $3TFSI^-$ with PBE functional. It might be due to large dipole moment or lesser molecular volume. Watkins *et al.*, have also reported the same observation via Raman spectroscopy with the magnesium complex dissolved in n-butyl-N-methylpyrrolidinium bis(trifluoro-methylsulfonyl)imide (BMPyrTFSI) room-temperature ionic liquid (RTIL). There findings reveals coordination with metal ion, $TFSI^-$ prefers to be in the *cis* state. They suggested this state is stabilized by the effect of RTIL cations in the second solvation sphere or it could be due to the greater dipole moment of the *cis* conformer [126].

Without loss of generality, we have chosen PF_6^- counter-ion for showing the electronic and structural effects during loading for both Fe and Ru based complex. We have also performed the calculation with other counter-ions but have not presented here nevertheless the behavior is same. It can be seen in Figure 2.16, the octahedral geometry is intact, but a displacement of the *dmbpy* molecule and a variation in bond lengths of counter-ions during loading is observed. The electrostatic effect between counter-ions

and complex causes the elongation of counter-ions bonds by 0.03 Å on average. In Table 2.7 and 2.9, average distance of counter-ions for both Neutral and Fully loaded complexes are shown. From the trend, it shows the position vary according to nature of counter-ions and less difference is observed among XC functionals. In increasing order of voluminous effect of counter-ions the $M-N$ length for $[Fe(dmbpy)_3]^{n+}\ nCi^-$ varies a little.

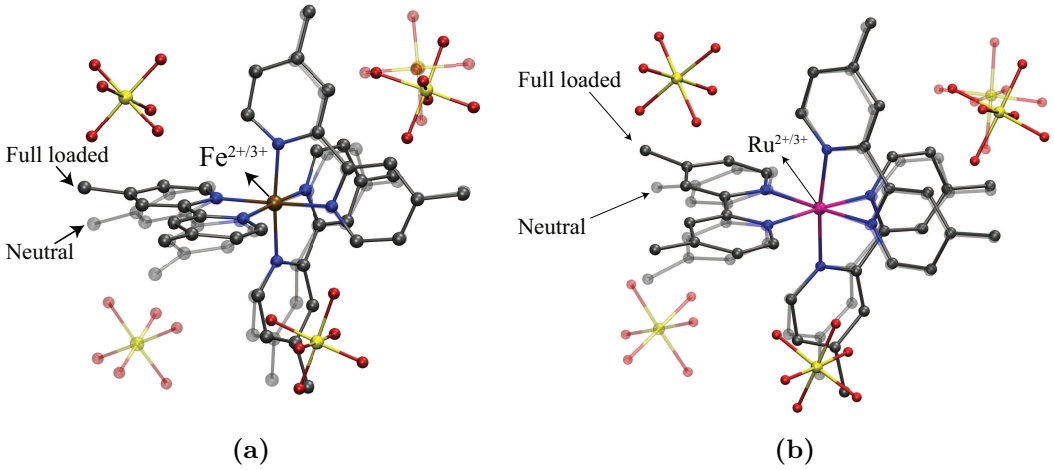

Figure 2.16: (a) Superposition of the relaxed geometry of$[Fe(dmbpy)_3]^{2+}\ 2Ci^-$ and $[Fe(dmbpy)_3]^{3+}\ 3Ci^-$ mono-nuclear complex within the field created by PF_6^- counter-ions. Counter-ions corresponding to the degree of oxidation $n=2$ are represented in light colors (they are labeled N, like Neutral or Not charged complex), the three counter-ions corresponding to $n=3$ are plotted in deepest colors and denoted FL, like Fully Loaded complex. This figure illustrates that the deformation of our pattern is weak during the loading process. However, the arrival of a new counter-ion induces a significant displacement of one former counter-ion. In (b) we report the same plot but for the Ru-based compound. It presents the same features.

For $[Fe(dmbpy)_3]^{2+}2PF_6^-$ complex in Table 2.6, the $M-N$ length agrees very well with the experimental values except for PBE0 which overestimates the length by 0.02 Å and regarding other parameters, we see a variation of ±0.01 Å. Moreover for $[Ru(dmbpy)_3]^{2+}2PF_6^-$ are nearly the same. Both these approximations work fine, but when we compare our data with the charged state as described in previous sections (In Table 2.1 and 2.2) we still see the values in the presence of external perturbation are more or less same. This shows the counter-ion although weak does not perturb the complex state, however, the steric effect induces changes in the conformation state. Overall, if we

see a big picture, it is observed Fe complex behavior is not consistent with Ru complex in terms of geometrical parameters.

Table 2.6: Selected experimental bond lengths (averaged) for $[Fe(dmbpy)_3]^{2+}\ 2PF_6^-$ (Neutral) and $[Fe(dmbpy)_3]^{3+}\ 3PF_6^-$ (*Full L*oaded) complex compared to the minimized structure obtained at PBE/PBE0//Def2SVP level of theory. For Fe: experimental parameters for *Neutral* are given for methylation and *Full loaded* without methylation. All bond lengths are given in Å.

	$[Fe(dmbpy)_3]^{2+}2PF_6^-$			$[Fe(dmbpy)_3]^{3+}3PF_6^-$		
	Opt		Exp [24, 115]	Opt		Exp [116]
	PBE	PBE0		PBE	PBE0	
$Fe-N$	1.960	1.986	1.965(3)	1.971	1.971	1.96(3)
$C1-C1'$	1.468	1.471	1.472(6) [25]	1.465	1.467	1.473(6)
$N-C_1$	1.371	1.351	1.350(0)	1.369	1.356	1.350(0)

Table 2.7: Average bond lengths computed for $Fe-N$ (Å) mono-nuclear complex in ClO_4^- , PF_6^- and $TFSI^-$ counter-ions medium. $Fe-X_i$ (Å) is the distance measured from metal to the center of counter-ions.

$[Fe(dmbpy)_3]^{2+}2Ci$							
	Exp[115]	PBE			PBE0		
		ClO_4^-	PF_6^-	$TFSI^-$	ClO_4^-	PF_6^-	$TFSI^-$
$Fe-N$	1.965	1.960	1.960	1.959	1.986	1.986	1.984
$Fe-X_1$		5.948	6.263	5.508	5.992	6.162	5.561
$Fe-X_2$		6.211	6.154	5.518	6.002	6.219	5.560

$[Fe(dmbpy)_3]^{3+}3Ci$							
	Exp[116]	PBE			PBE0		
		ClO_4^-	PF_6^-	$TFSI^-$	ClO_4^-	PF_6^-	$TFSI^-$
$Fe-N$	1.96(3)	1.966	1.971	1.967	1.969	1.971	1.966
$Fe-X_1$		5.234	5.388	5.303	5.124	5.362	5.293
$Fe-X_2$		5.195	6.188	5.313	5.124	6.061	5.276
$Fe-X_3$		5.201	5.897	5.300	5.129	5.821	5.274

Table 2.8: Selected Experimental bond lengths (averaged) for $[Ru(dmbpy)_3]^{2+}\ 2PF_6^-$ (Neutral) and $[Ru(dmbpy)_3]^{3+}\ 3PF_6^-$ (*Full L*oaded) complex compared to the minimized structure obtained at PBE/PBE0//Def2SVP level of theory. For Ru: *Neutral* and *Full loaded* are without methylation. All bond lengths are given in Å.

	$[Ru(dmbpy)_3]^{2+}2PF_6^-$			$[Ru(dmbpy)_3]^{3+}3PF_6^-$		
	Opt		Exp	Opt		Exp [117]
	PBE	PBE0		PBE	PBE0	
$Ru-N$	2.064	2.063	2.054 [117, 118]	2.069	2.063	2.056
$C1-C1'$	1.471	1.471	1.474(7) [25]	1.469	1.467	1.450
$N-C_1$	1.372	1.355	1.354 [25]	1.372	1.357	-

Table 2.9: Average bond lengths computed for $Ru-N$ (Å) mono-nuclear complex in ClO_4^- , PF_6^- and $TFSI^-$ counter-ions medium. $Ru-X_i$ (Å) is the distance measured from metal to the center of counter-ions.

	$[Ru(dmbpy)_3]^{2+}2Ci$						
	Exp[117, 118]	PBE			PBE0		
		ClO_4^-	PF_6^-	$TFSI^-$	ClO_4^-	PF_6^-	$TFSI^-$
$Ru-N$	2.054	2.063	2.064	2.060	2.062	2.063	2.060
$Ru-X_1$		6.084	6.276	5.510	6.035	6.222	5.558
$Ru-X_2$		6.084	6.302	5.511	6.032	6.250	5.558

	$[Ru(dmbpy)_3]^{3+}3Ci$						
	Exp[117]	PBE			PBE0		
		ClO_4^-	PF_6^-	$TFSI^-$	ClO_4^-	PF_6^-	$TFSI^-$
$Ru-N$	2.056	2.065	2.069	2.064	2.058	2.063	2.060
$Ru-X_1$		5.304	6.309	5.334	5.176	6.156	5.327
$Ru-X_2$		5.331	5.826	5.358	5.161	5.810	5.326
$Ru-X_3$		5.287	5.277	5.339	5.169	5.215	5.319

Now we will discuss the magnetic properties of these complexes. We computed different multiplicity (2S+1) of the system to find the lowest spin state of the system. For $[Fe/Ru(dmbpy)_3]^{2+}\ 2PF_6^-$ (*Neutral*) complex the ground state is found to be singlet which corroborated with the experimental and DFT calculation very nicely [25]. For full loaded system, $[Fe/Ru(dmbpy)_3]^{3+}\ 3PF_6^-$, lowest spin multiplicity was found to be the doublet. Similarly, for each counter-ions, we observed the same spin multiplicity that

is *fully loaded* system is accompanied by doublet ($S = 1/2$) state whereas *neutral* by singlet ($S = 0$) state irrespective of the external perturbation.

Moreover, Mulliken spin density analysis shows an electron resides on the metal center for loaded system whereas, on *dmbpy* and counter-ions it is zero despite the external perturbation. On the other hand, for the neutral system net spin density on metal center, *dmbpy* and counter-ions is zero which perfectly corroborates to the DFT and experimental studies [24, 25]. To see if the ligands have induced the ligand field effect we observe the splitting of Fe d-states. However, for the transition metal, Fe, a complex ligand field effect is distorted when switching functionals from gradient corrected to hybrid functionals. It has also been reported by [107, 121, 127] where they observe increasing Hartree-Fock (HF) exchange terms, reduces the charge on Fe center when coordinated to *bpy* ligands, hence depletion of charge to ligands. Contrary, to the belief that it was made to localize charge and cancel self interaction error (SIE) and give a correct prediction of spin state ordering of a system. With PBE0 (25% HF), we observe the similar effect via PDOS with and without external perturbation. In the next, section we will discuss the electronic structure in the presence of the counter-ions.

2.5.4 Electronic structure of Fe and Ru compounds

2.5.4.1 Results within the PBE0 approximation

Figure 2.17, 2.18, 2.19, and 2.20 shows the electronic structure of $[Fe/Ru(dmbpy)_3]^{n+}$ nPF_6^- complex as a series of energy levels and convoluted as a density of states curve. For $[Fe/Ru(dmbpy)_3]^{2+}$ $2PF_6^-$ complex, HOMO-2, HOMO-1 and HOMO level has the most Fe/Ru character and weak covalent interaction between Fe/Ru and N atoms. Additionally, both complexes display three doubly occupied d orbitals (84, 82, and 84% Fe; 77, 74, and 79% Ru) similar to the previous studies [24] but complex are with methylation. Consequently, as expected, the electronic structure of these di-cations are best described as $[Fe/Ru(dmbpy)_3]^{2+}$ $2PF_6^-$. Similarly, for $[Fe(dmbpy)_3]^{3+}$ $3PF_6^-$ complex, calculations are spin unrestricted and each spin channel has been plotted. HOMO-2, HOMO-1 and HOMO level has zero Fe character whereas, LUMO shows 83% $Fe - d$ orbital occupation. On the other hand for $[Ru(dmbpy)_3]^{3+}$ $3PF_6^-$ complex, HOMO-2, HOMO-1 and HOMO level has Ru character in the spin down channel with single d orbitals occupation (0, 56, and 57% Ru) whereas, LUMO shows 83% $Ru - d$ orbital occupation.

Analyzing the oxidation level of $[Fe(dmbpy)_3]^{3+}$ $3PF_6^-$ complex a shift of peaks by 3 eV is observed, but the HOMO level is no more of Fe character, mostly it has counter-ion

character. Despite the construction of hybrid functional to localize it shows delocalization in the energy window -8.5 to -13 eV compared to $[Fe(dmbpy)_3]^{2+}\, 2PF_6^-$. Hence, weak interaction between Fe and other atoms imply the reason for longer bond lengths. With regards to the introduction of external perturbation to the system in the form of counter-ions, it can be seen near the HOMO level no direct influence is observed at the metallic center and weak interaction exist with the metallic center. Whereas for Ru, we see significant interaction with nearby *dmbpy* molecules and we do not see considerable elongation of bond lengths as we saw for Fe case.

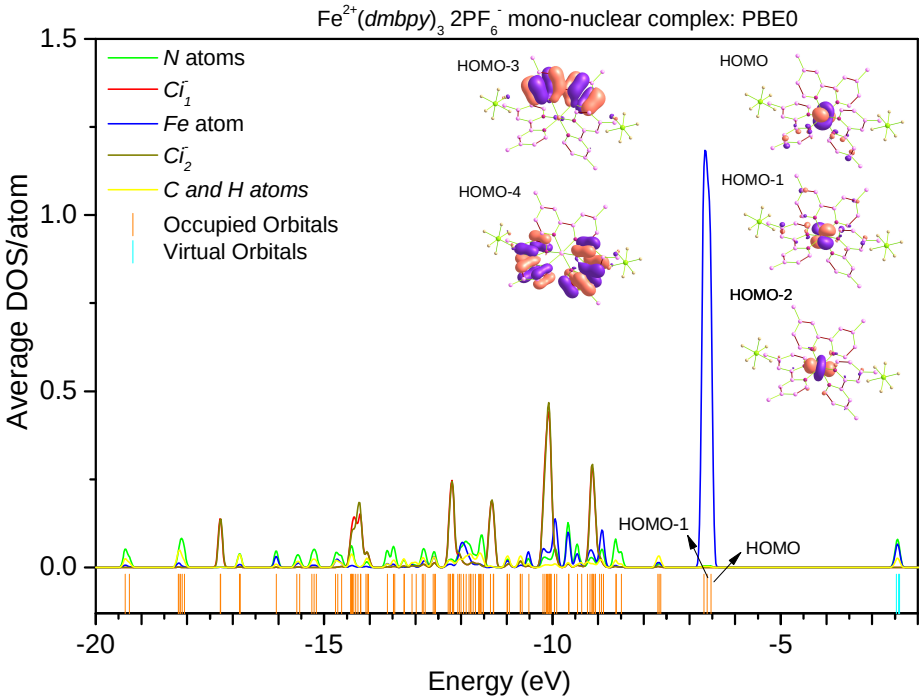

Figure 2.17: Average partial density of states (PDOS) calculated within the PBE0 approximation for the $[Fe(dmbpy)_3]^{2+}\, 2PF_6^-$ complex. It is built upon the data of the electronic levels using Hermite-Gaussian smearing method with a smearing parameter of $w_{1/2} = 0.1$ eV. We have added the partial DOS corresponding to Fe, the sum of carbon and hydrogen contributions from the *dmbpy* (in yellow) and the sum of the six nitrogen contributions from the *dmbpy* in green. The occupied electronic levels are reported in orange color at the bottom.

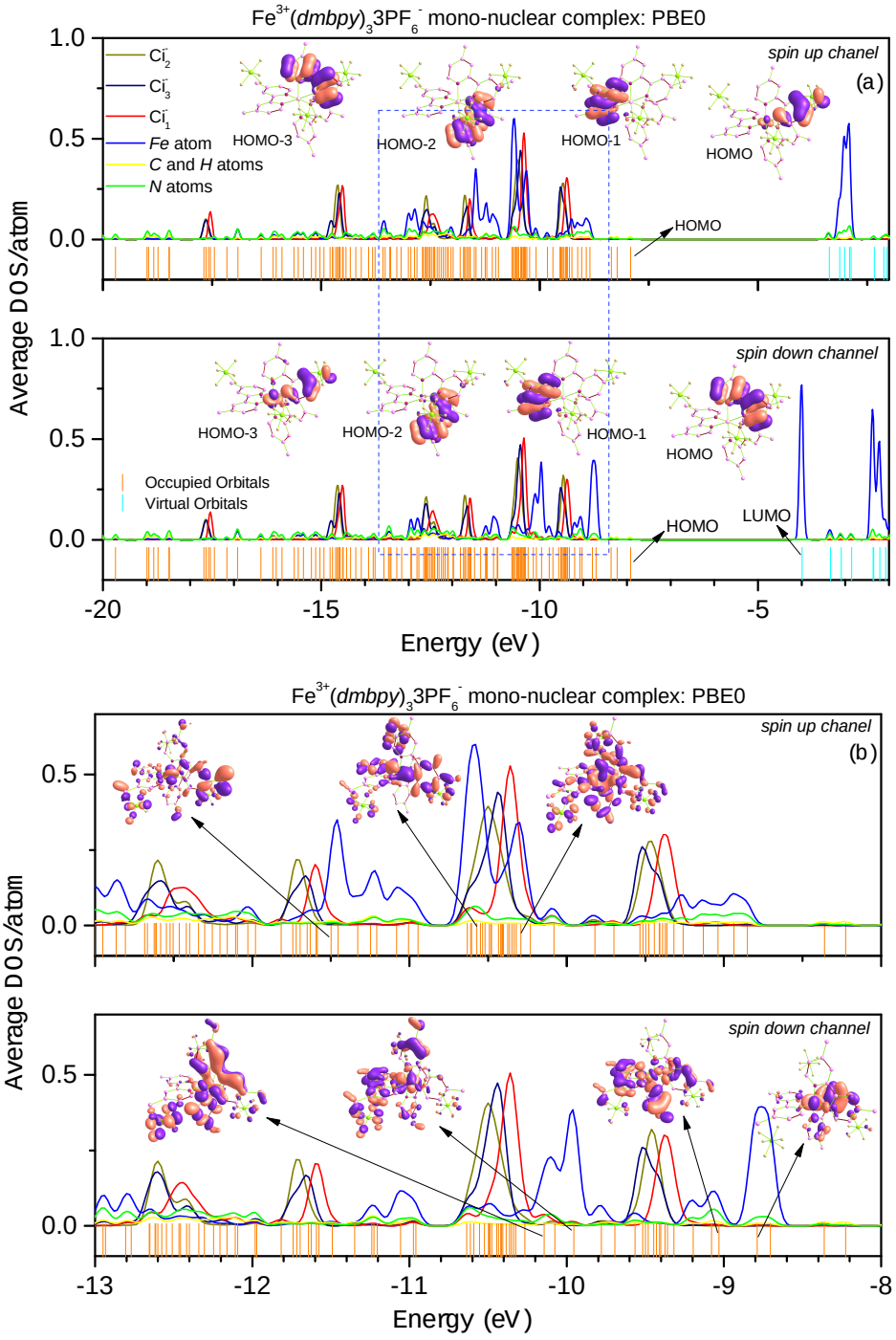

Figure 2.18: (a) Spin-polarized average DOS calculated within the PBE0 approximation for the $[Fe(dmbpy)_3]^{3+}\ 3PF_6^-$ complex. It is built upon the data of the electronic levels using Hermite-Gaussian smearing method with a smearing parameter of $w_{1/2} = 0.1$ eV. We have added the partial DOS corresponding to Fe, the sum of carbon and hydrogen contributions from the *dmbpy* (in yellow) and the sum of the six nitrogen contributions from the *dmbpy* in green. The occupied electronic levels are reported in orange color at the bottom. In (b) a scaled version of blue dot square region in (a) is shown to verify that there are no pure Fe-states.

On the other hand, for $[Ru(dmbpy)_3]^{3+}\,3PF_6^-$ complex, a shift of 3 eV is seen but the HOMO level is no more of Ru character mostly it has a $dmbpy$ character in the up channel. Whereas, in the down channel it has more Ru character. It can be seen during oxidation a large splitting between HOMO and LUMO is observed (with octahedral splitting parameter, $\triangle_o$, of around 3 eV). The DOS plot reveals a number of interesting points first the ligand field picture is intact for Ru (observed e_g and t_{2g} peaks) but for Fe it is destroyed which is what we observed in case without external perturbation and secondly, the external field does not influence the metal sites directly although through $dmbpy$ ligands.

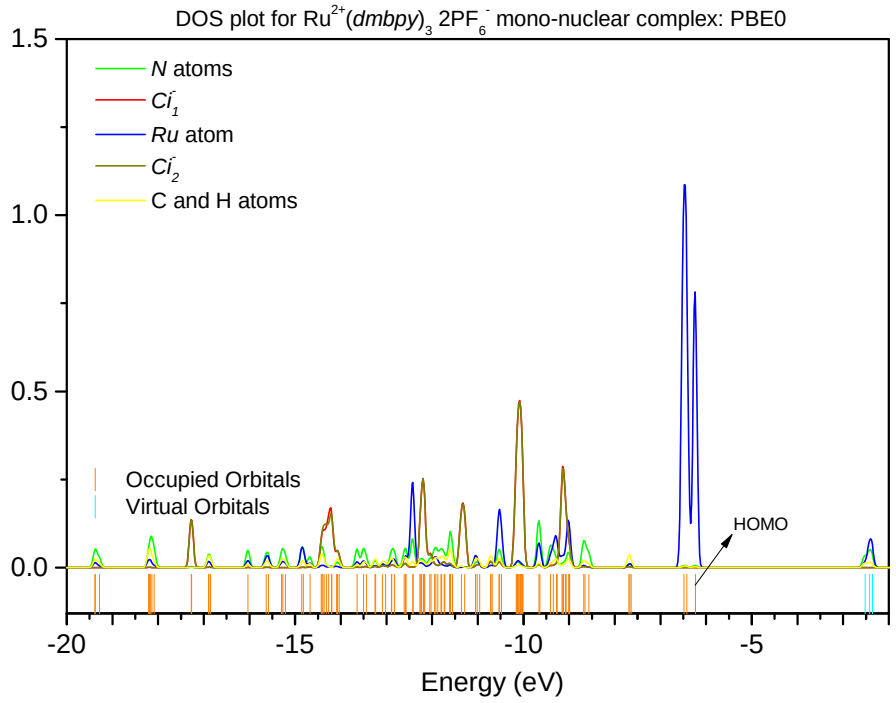

Figure 2.19: Idem as Figure 2.17 but for $[Ru(dmbpy)_3]^{2+}2PF_6^-$.

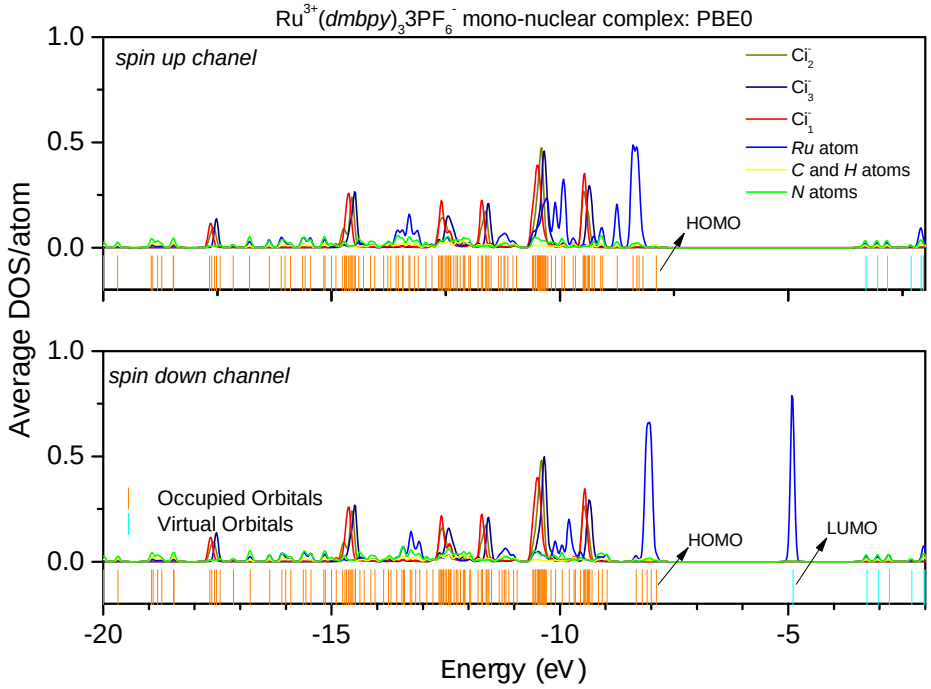

Figure 2.20: Idem as Figure 2.18 but for $[Ru(dmbpy)_3]^{3+}3PF_6^-$ complex. Each spin channel has been plotted on the same axis.

2.5.4.2 Results within the PBE approximation

Figure 2.21, 2.22, 2.23 and 2.24, shows the PDOS plot for PBE functional are quite different with respects to PBE0. For PBE functional, ligand field is intact which is common for the octahedral system and during oxidation one electrons is left and the shift in energy is observed. For $[Fe(dmbpy)_3]^{2+}\,2PF_6^-$ complex, HOMO-2, HOMO-1, and HOMO level has the most Fe character and weak covalent interaction between Fe and N atoms for both PBE and PBE0 functionals. Both complexes display three doubly occupied d orbitals (78, 78, and 86% Fe; 71, 71, and 81% Ru) similar to the previous studies [24] but our complex is with methylation. On the other hand, for $[Fe(dmbpy)_3]^{3+}\,3PF_6^-$ complex, HOMO levels comprised mostly of Fe character and compared to $[Fe(dmbpy)_3]^{2+}\,2PF_6^-$ there is a shift in peaks by 2.2 eV in the energy window of -4.5 to -7 eV. Whereas, for PBE0 functional a shift of 3 eV is seen but the HOMO level is no more of Fe character mostly it has counter-ion character. Both complexes display singly occupied d orbitals (68, and 68% Fe; 61, and 61% Ru) in spin down channel and LUMO comprises 85 and 76% respectively. In this case, both complexes retain the ligand field picture and e_g and t_{2g} peaks are observed.

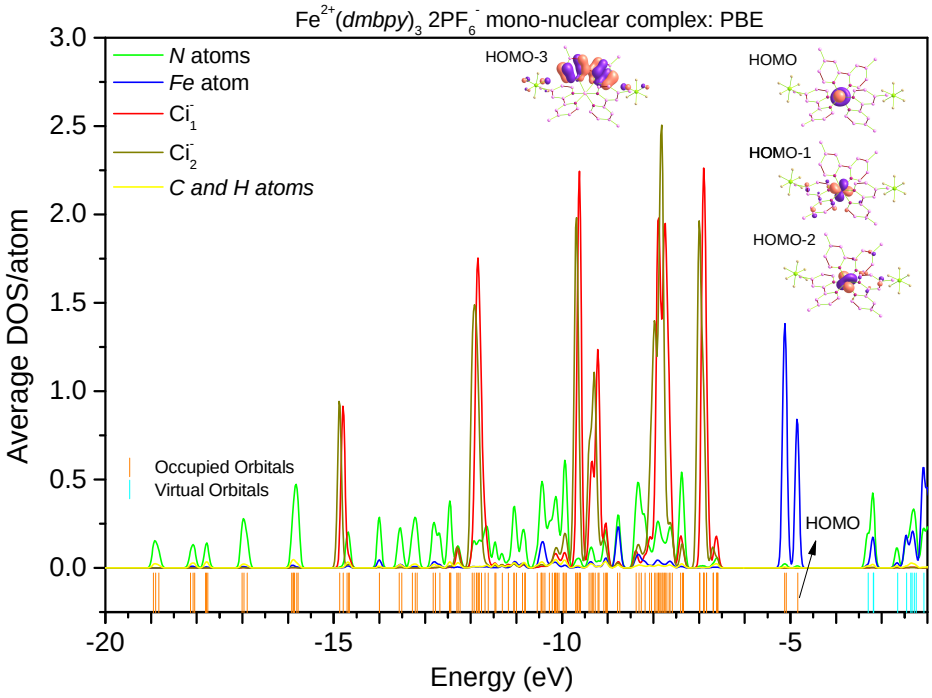

Figure 2.21: Idem as Figure 2.17.

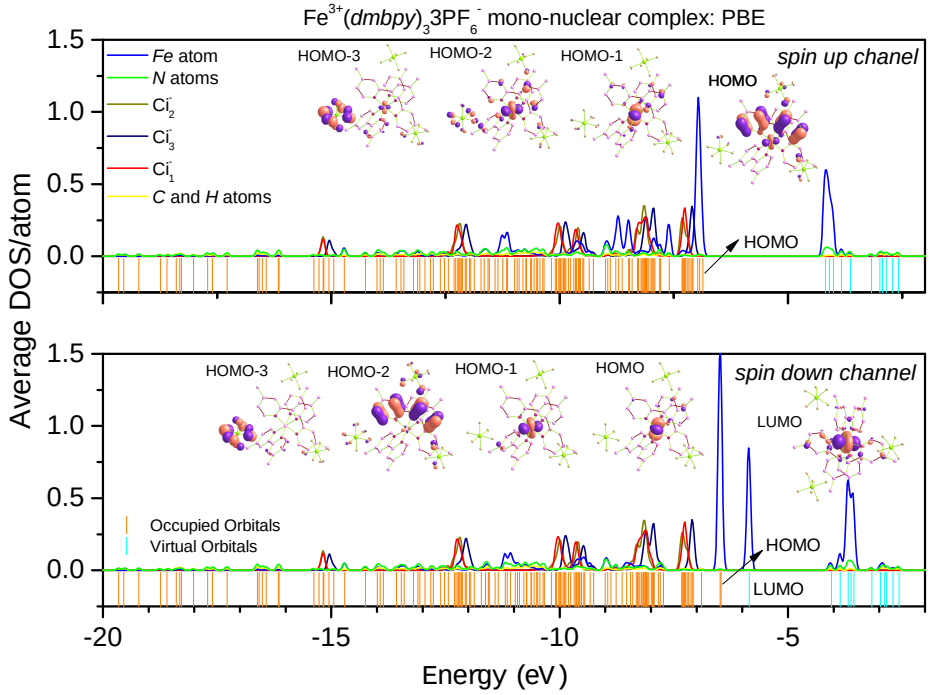

Figure 2.22: Idem as Figure 2.18. Each spin channel has been plotted on the same axis.

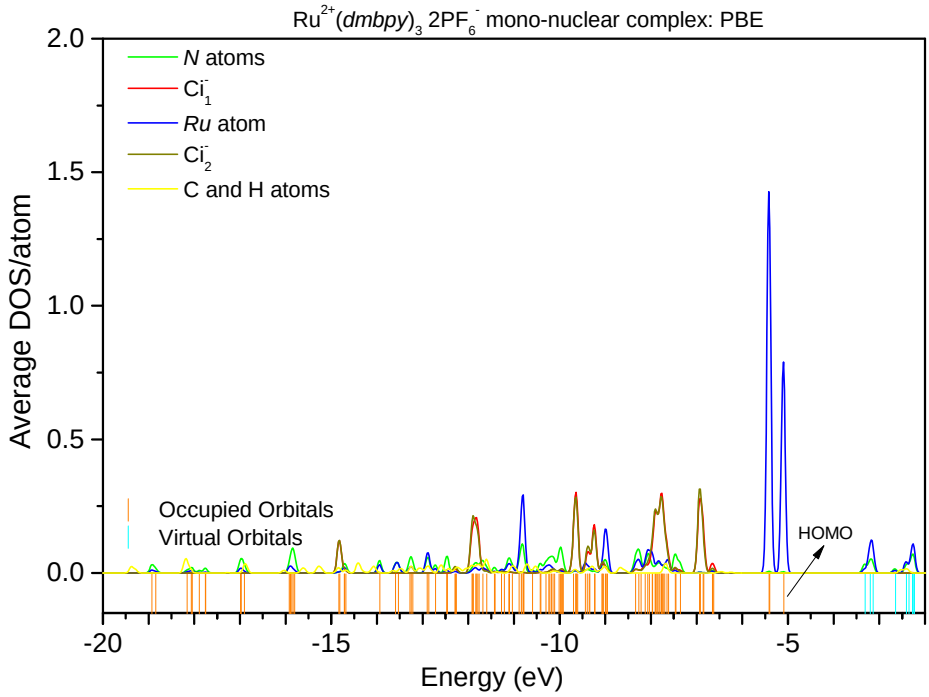

Figure 2.23: Idem as Figure 2.17 but for $[Ru(dmbpy)_3]^{2+}2PF_6^-$.

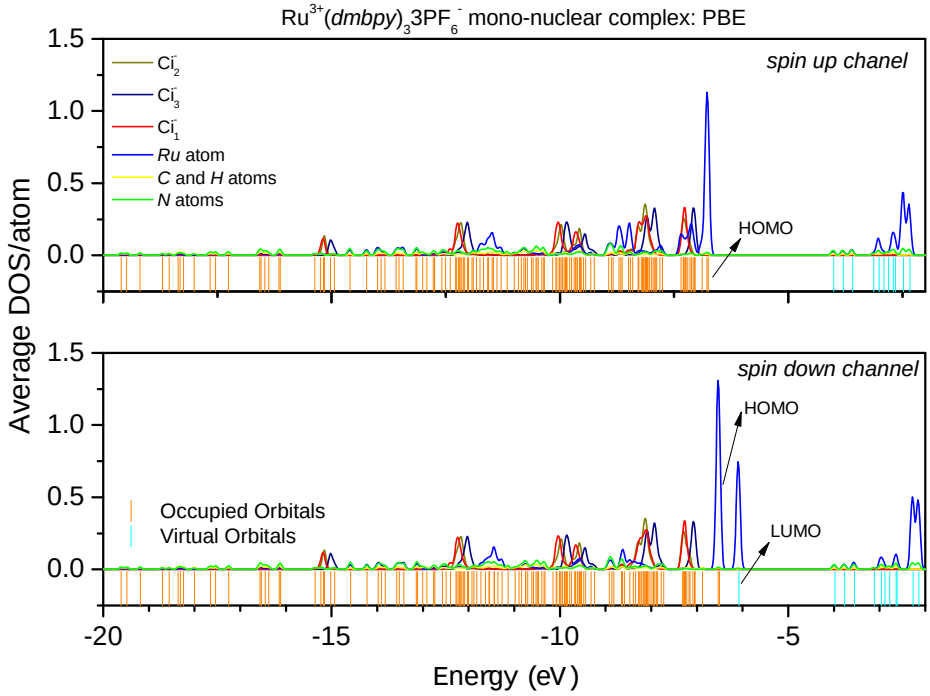

Figure 2.24: Idem as Figure 2.18 but for $[Ru(dmbpy)_3]^{3+}3PF_6^-$ complex. Each spin channel has been plotted on the same axis.

2.5.5 Cu redox complex

To model $[Cu\,(dmbpy)_2]^{n+}\ nCi^-$ complex two *dmbpy* are coordinated with Cu ion and counter-ions to maintain charge neutrality. We choose two *dmbpy* because the Gibbs free energy lies in the working voltage range without oxidizing the electrolytic medium. For calculating voltage, the reaction mechanism is the same as mentioned in section 2.5.2 but with substituted Cu. The reaction without derivation is,

$$V_{Cu} = -\frac{E^{[Cu(dmbpy)_2]^+Ci^-}}{n\mathcal{F}} - \frac{-E^{[Cu(dmbpy)_2]^{2+}2Ci^-}}{n\mathcal{F}} - V_0 \tag{2.8}$$

In section 2.3, we studied the oxidation of Cu complex without external perturbation. The deformation without counter-ions was clearly visible. It went through tetrahedral to square planar. In this section, we will see this planarity is even further distorted in the presence of counter-ions. Figure 2.25, shows the deformation of Cu complex for PF_6^- counter-ions. Ci_1 and Ci_2 shows the position of counter-ions for *neutral* and f*ully loaded* state respectively. In Table 2.10, average bond lengths of $[Cu\,(dmbpy)_2]^{n+}\ nCi^-$ complex in three medium are presented. The voltage and bonds are well described by the PBE and PBE0 functional and its value is close to experimental one. The change in bond lengths from $[Cu(dmbpy)_2]^+\ PF_6^-$ to $[Cu(dmbpy)_2]^{2+}\ 2PF_6^-$ varies on average by 0.04 Å and the structural deformation is shown in Figure 2.25.

In Figure 2.26 and 2.27, ground state structures obtained with two counter-ions are shown. It can be seen during the loading process the structure deforms. With one counter-ion the structure retains its tetrahedral coordination and with further loading process, it transforms into five coordinated complexes. PBE functional for $[Cu(dmbpy)_2]^{2+}$ $2ClO_4^-$ system poses severe electronic and geometry convergence problem. We tried many configurations for some it was successful but gives higher energy and for some other configuration it was lower, but the SCF electronic convergence fails. Compared to other counter-ions it might be due to the high electronegative nature of ClO_4^- which influences the structure at the core and also *dmbpy* ligands. We think the obtained structure is the local minima since we don't have the crystal structure for this complex. Moreover for other counter-ions like PF_6^-, crystal structure data are available but when that structure is optimized in gas phase the position of the counter-ions changes and the structure deforms whereas, in crystal shape it is bounded by the crystal symmetry and the position of counter-ions are clearly defined. We raised this discussion because the position of the ions alters the $Cu\,(II)$ complex. For $Cu\,(I)$ complex we have shown it maintains its tetrahedral geometry, but there is another position where it can coordinate with $Cu(I)$ directly giving it pentavalent coordination. Among all these possibilities our

criterion was to rank structure according to energetics.

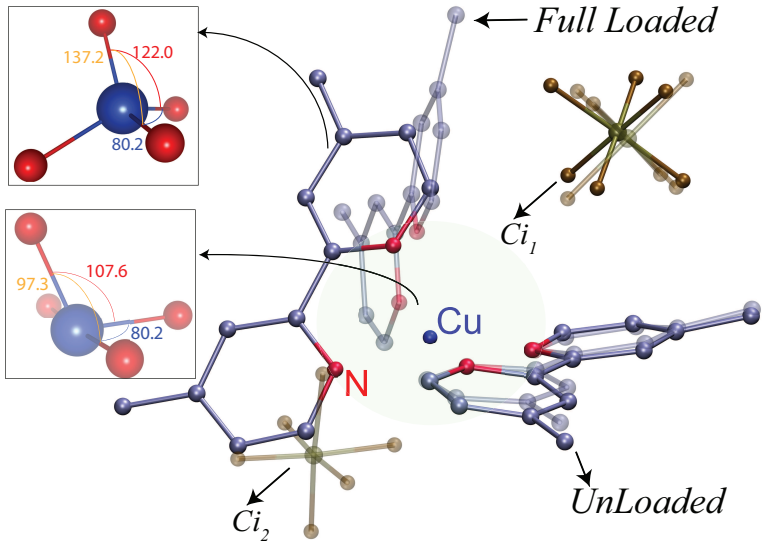

Figure 2.25: Superposition of the relaxed geometry of $[Cu(dmbpy)_2]^{n+}$ nCi^- mononuclear complex within the field created by PF_6^- counter-ions at the PBE0/Def2SVP level of theory. Both counter ions corresponding to the degree of oxidation $n = 1$ are represented in bold colors (they are labeled Neutral or Unloaded), the two counter-ions corresponding to $n = 2$ are plotted in light colors and denoted Fully Loaded complex. This figure illustrates that the deformation of our pattern is substantial during the loading process. However, the arrival of a new counter-ion induces a significant displacement of one former counter-ion. Hydrogen atoms are omitted for clarity reasons.

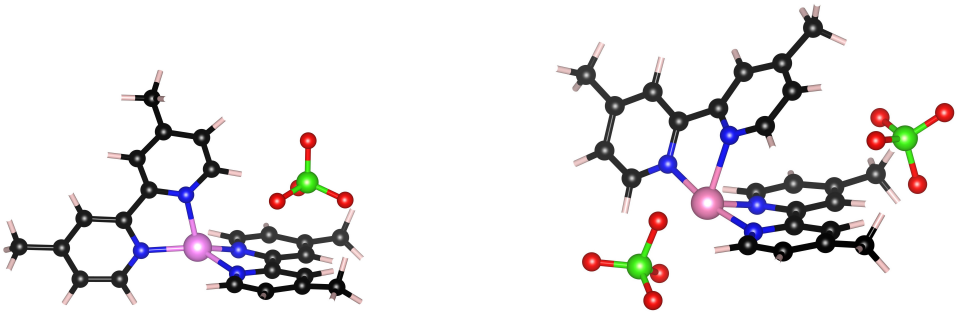

(a) **(b)**

Figure 2.26: Ground state structure of (a) $[Cu(dmbpy)_2]^+$ ClO_4^- and (b) $[Cu(dmbpy)_2]^{2+}$ $2ClO_4^-$ complex at PBE0/Def2SVP level of theory. Hydrogen atoms are omitted for clarity reasons.

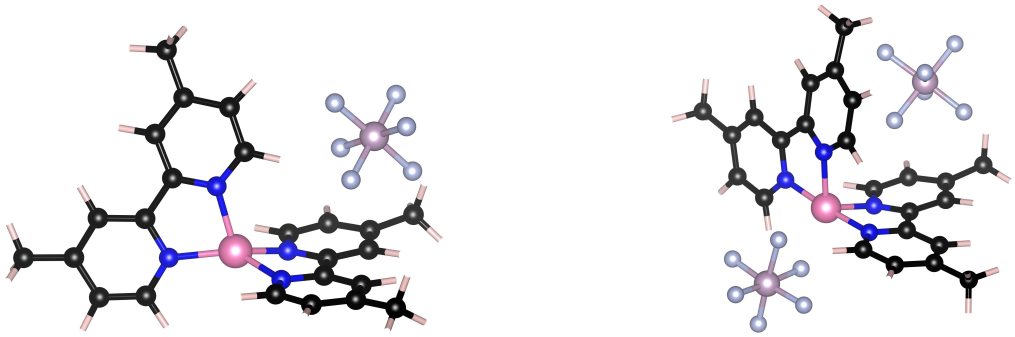

(a) (b)

Figure 2.27: Ground state structure of (a) $[Cu(dmbpy)_2]^+PF_6^-$ and (b) $[Cu(dmbpy)_2]^{2+}$ $2PF_6^-$ complex at PBE0/Def2SVP level of theory. Hydrogen atoms are omitted for clarity reasons.

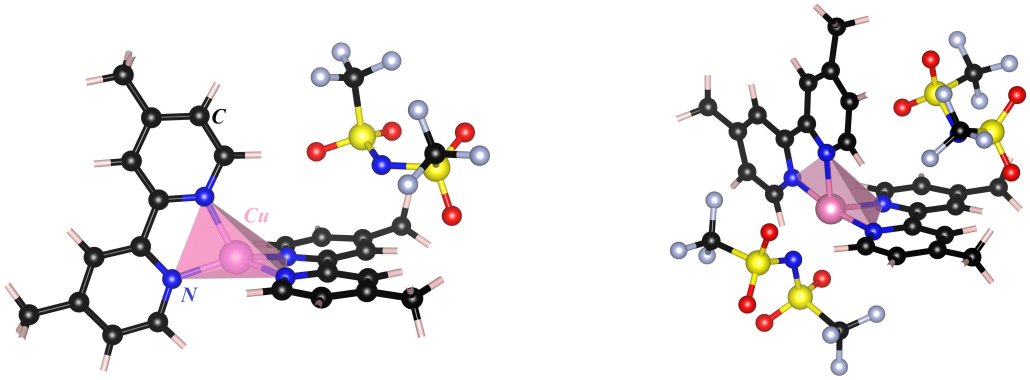

(a) (b)

Figure 2.28: Ground state structure of (a) $[Cu(dmbpy)_2]^+$ $TFSI^-$ and (b) $[Cu(dmbpy)_2]^{2+}$ $2TFSI^-$ complex at PBE0/Def2SVP level of theory. Hydrogen atoms are omitted for clarity reasons.

For this complex, the structure of di-cation $[Cu(dmbpy)_2]^{2+}$ $2PF_6^-$ in the crystal have been experimentally studied. Wang *et al.,* investigated the crystal structure to find neutrality of the ligands. The reported average intrachelate $C-N$ bond length is 1.348 Å and $C-C$ is 1.486 Å which is similar to the uncoordinated bpy^0 molecule and shows two ligands are neutral [128]. The obtained structure comprise of tetrahedrally geometry compressed with angle $\theta^o = 42.9$ between two coordination planes (atoms are fitted to bpy^0 planes maximally). For $[Cu(dmbpy)_2]^+$ PF_6^- there were no experimental data available so we assume that there would be not much variation with respect to $[Cu(dmbpy)_2]^{2+}$ $2PF_6^-$ complex. The measured angle reported here is between two

$M(dmbpy)$ chelate rings. As shown in Figure 2.26, *dmbpy* are not planar they deviate around the central carbon bonds in the presence of counter-ions and when no ions are present they lie in the same plane. This is what we have shown in the above previous sections where counter-ions were absent. Huge variation of θ^o with respect to experimental value shows the optimize structure in gas phase differs from the crystal structure. Sullivan and Murphy *et al.*, [129, 130] have investigated the structural and electronic pathways of $[Cu(bpy)_2Cl^-]Y$ crystal structure for different counter-ions and reported the stereo-chemistry and coordination of $Cu(II)$ complex. The coordination with Cl^- forms pentavalent coordination with one $Y = \left[PF_6^-\right] H_2O$ counter-ions to neutralize the system. The average bond length $Cu - N$ varies on the order of 2.04 – 2.10 Å for which they have also reported. Whereas, [128, 131] did the experimental study of the crystal structure and found the bond lengths to be on the order of 1.959 Å in the counter-ion PF_6^- medium.

Table 2.10: Average bond lengths computed for Cu^+ mono-nuclear complex in ClO_4^-, PF_6^- and $TFSI^-$ medium. Where X_i means the center of counter-ions from which the distance is measured. θ^o is the angle between two $M(dmbpy)$ chelate rings. All bond lengths are given in **Å**.

$[Cu(dmbpy)_2]^+Ci^-$							
		PBE			PBE0		
	Exp	ClO_4^-	PF_6^-	$TFSI^-$	ClO_4^-	PF_6^-	$TFSI^-$
Cu-N1	-	2.053	2.025	2.049	2.081	2.082	2.073
Cu-N2	-	2.007	2.019	2.013	2.049	2.026	2.044
Cu-N3	-	2.019	2.049	2.019	2.042	2.054	2.043
Cu-N4	-	2.031	2.005	2.020	2.033	2.047	2.045
$C1 - C1'$	-	1.485	1.485	1.484	1.484	1.484	1.485
$Cu - X_1$	-	5.00	5.382	5.130	4.900	5.443	5.531
θ^o	-	87.19	84.69	83.36	82.45	83.09	85.45

To compare our results we have taken the latter parameter and are listed in the Table 2.10 and 2.11. For this study, this deviation shows that Cu complex with coordination still deforms which renders it less reliable for the battery usage. As mentioned earlier during the loading process one counter-ions distance, $Cu - X_2$ is less than the $Cu - X_1$ and this is what makes the structure deform completely.

In Figure 2.28, a case for $TFSI^-$ is discussed. This case poses a little problem in finding the correct ground state. To check which conformation of $TFSI^-$ gives the

lowest structure we modeled with *cis* and *trans* configuration. For the PBE0 functional *cis* state is lower in energy by 0.12 eV and 0.02 eV for $Cu\,(I)$ and $Cu\,(II)$ complex respectively. On the other hand, for PBE functional we found *cis* to be the lowest configuration by 0.03 eV for $Cu\,(I)$ complex and *trans* by 0.05 eV for $Cu\,(II)$ complex. This difference when compared to the barrier between two rotamers of $TFSI^-$ in gas phase ($\approx$ 0.03 eV) shows in working battery condition two states are accessible during full loading.

Now we will discuss the magnetic properties of these complexes. We computed the different multiplicity (2S+1) of the system to find the lowest spin state of the system. For $[Cu(dmbpy)_2]^+\,PF_6^-$ (neutral) the ground state is found to be singlet and for $[Cu(dmbpy)_2]^{2+}\,2PF_6^-$ (fully loaded) it is doublet. Similarly, for each counter-ions, we observed the same spin multiplicity that is fully loaded system is accompanied by doublet ($S = 1/2$) state whereas, neutral by singlet ($S = 0$) state irrespective of the external perturbation. Moreover, Mulliken spin density analysis shows an electron resides on the metal center for loaded system whereas, on *dmbpy* and counter-ions it is zero despite the external perturbation. On the other hand, for the neutral system net spin density on metal center, *dmbpy* and counter-ions is zero.

To see if the ligands have induced the ligand field effect we observe the splitting of $Cu - d$ states. However, for Cu complex ligand field effect is distorted when switching functionals from gradient corrected to hybrid functionals. Again for this case, we have chosen PF_6^- counter-ions to study the electronic structure. For $[Cu(dmbpy)_2]^+\,PF_6^-$, we see for both XC functionals ligand field picture is intact but for $[Cu(dmbpy)_2]^{2+}\,2PF_6^-$ complex the bands are totally dispersed for PBE0 functional.

Table 2.11: Average bond lengths computed for Cu^{2+} mono-nuclear complex in ClO_4^-, PF_6^- and $TFSI^-$ medium. Where X_i means the center of counter-ions from which the distance is measured. θ^o is the angle between two $M(dmbpy)$ chelate rings. All bond lengths are given in **Å**.

$[Cu(dmbpy)_2]^{2+}2Ci^-$							
		PBE			PBE0		
	Exp[128, 131]	ClO_4^-	PF_6^-	$TFSI^-$	ClO_4^-	PF_6^-	$TFSI^-$
Cu-N1	1.959(2)	2.046	2.109	2.116	2.196	2.099	2.078
Cu-N2		2.017	2.002	2.023	2.067	1.997	2.023
Cu-N3		2.063	2.002	2.040	1.994	2.104	1.999
Cu-N4		2.274	2.111	2.121	2.041	1.997	2.213
$C1 - C1'$	1.486	1.484	1.481	1.481	1.480	1.479	1.480
$Cu - X_1$		6.461	5.418	5.051	5.618	5.433	6.655
$Cu - X_2$		2.950	3.253	2.085	2.920	3.210	3.663
θ^o	42.9	74.06	82.99	80.95	86.29	83.59	83.66

2.5.6 Electronic structure for Cu compounds

2.5.6.1 Results within the PBE0 & PBE approximation

Figure 2.29, 2.30, 2.31 and 2.32, shows the electronic structure of $[Cu(dmbpy)_2]^{n+}\ nPF_6^-$. DOS plot for PBE and PBE0 functional are displayed for $[Cu(dmbpy)_2]^{n+}\ nPF_6^-$ complex. In the plot, Carbon and Hydrogen atoms contribution has been omitted. For $[Cu(dmbpy)_2]^{+}\ PF_6^-$ complex, HOMO-2, HOMO-1, and HOMO level has the most Cu character and display three doubly occupied d orbitals (92, 75, and 67% PBE; 93, 76, and 74% PBE0) and considerable covalent interaction between Cu and N atoms exists for both PBE and PBE0 functional and ligand field picture is intact and during oxidation one electrons is left and the shift in energy is observed.

On the other hand, for $[Cu(dmbpy)_2]^{2+}\ 2PF_6^-$ complex, calculations are spin unrestricted and for PBE functional the HOMO level comprises mostly of Cu, C and H atoms character in the energy window of -5 to -9eV and compared to $[Cu(dmbpy)_2]^{+}\ PF_6^-$ there is a shift in peaks by 1 eV. Whereas, for PBE0 functional a shift of peaks is seen around $-8 - 13\ eV$ but the HOMO level is no more of Cu character mostly it has C and H atoms character. Despite the construction of hybrid functional to localize, it shows delocalization in the energy window -8 to -13eV compared to $[Cu(dmbpy)_2]^{+}\ PF_6^-$. It can be seen near the HOMO level weak interaction between Cu and N exists and diminishing ligand field effect is observed. For PBE functional, during the loading process metallic

center interacts with counter-ions. This external influence distorts the geometry forming distorted tetrahedral geometry.

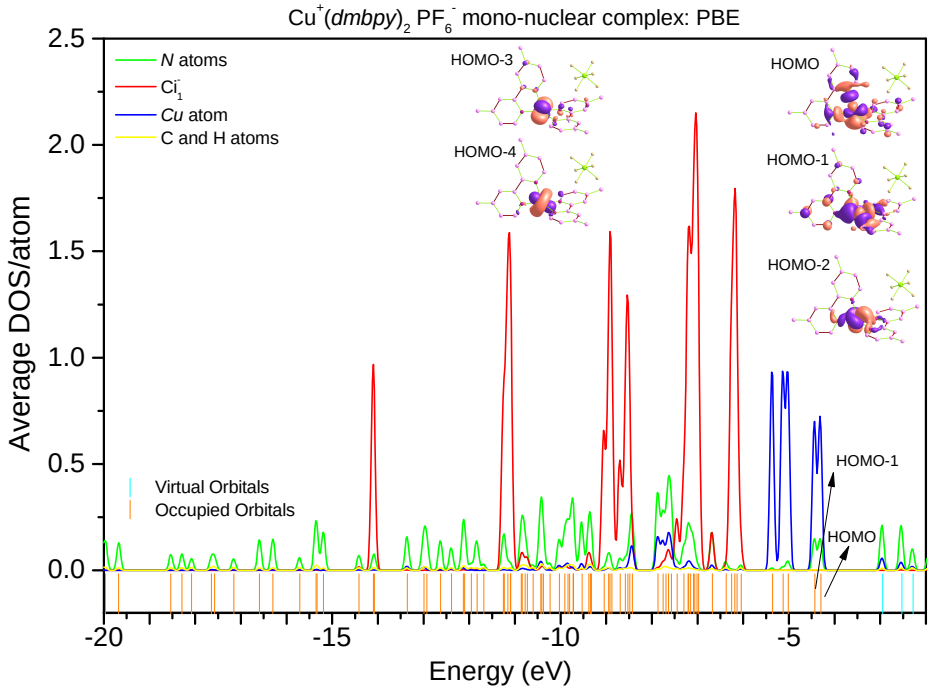

Figure 2.29: Idem as Figure 2.17 but for $[Cu(dmbpy)_2]^+ PF_6^-$ complex and at the PBE/def2SVP level of theory.

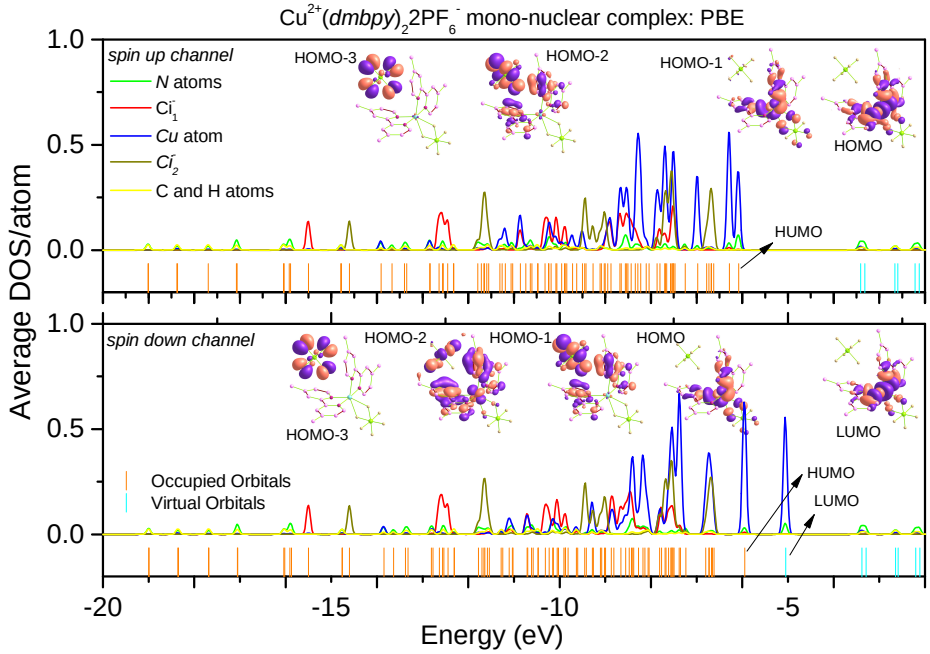

Figure 2.30: Idem as Figure 2.18 but for $[Cu(dmbpy)_2]^{2+}\,2PF_6^-$ complex and at the PBE/def2SVP level of theory. Each spin channel have been plotted on the same axis.

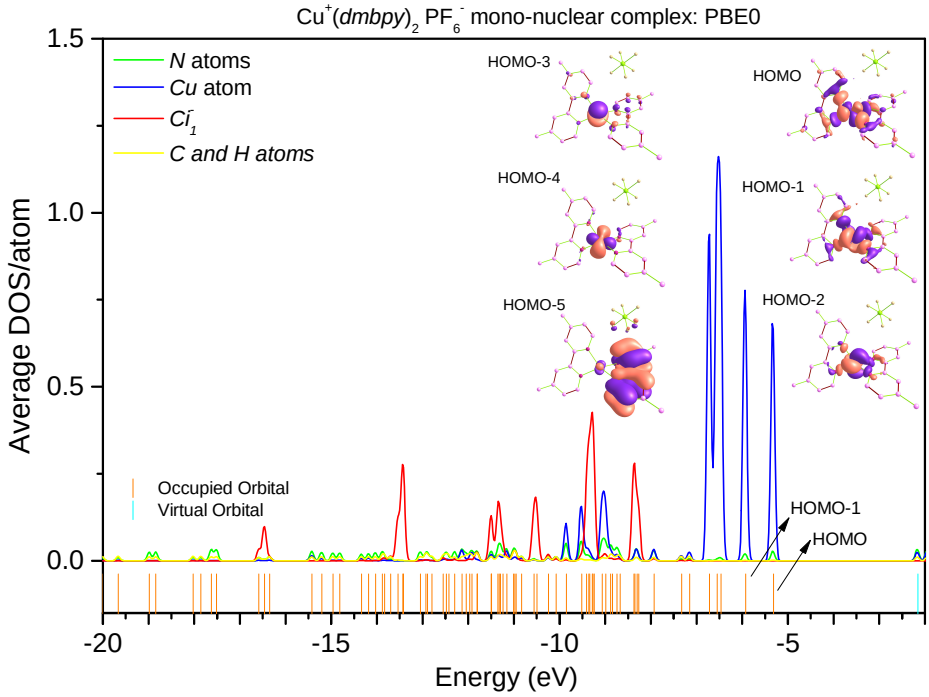

Figure 2.31: Idem as Figure 2.17 but for $[Cu(dmbpy)_2]^{+}\,PF_6^-$ complex and at the PBE0/def2SVP level of theory.

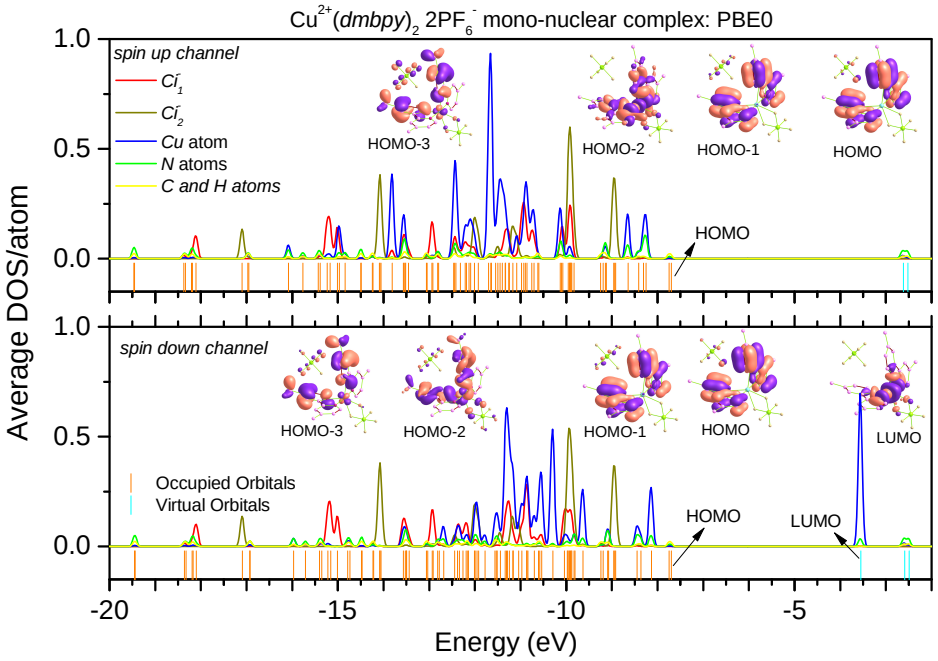

Figure 2.32: Idem as Figure 2.18 but for $[Cu(dmbpy)_2]^{2+}\,2PF_6^-$ complex and at the PBE0/def2SVP level of theory. Each spin channel have been plotted on the same axis.

2.5.7 Calculation of the mono-nuclear voltage

Experimentally, voltages obtained with three electrolyte fall in narrow range. In Eq. 2.7, additive constant V_0 approximates all the intricate terms such as Li^+ interaction with $TFSI^-$, PF_6^- or ClO_4^- and deposition of Li on the anode electrodes and other effects. This value fixes our voltages for mono-nuclear and will be used to compare with the bi-nuclear complex. In Table 2.12, the relative voltage difference for Cu and Ru mono-nuclear complex are compared to experiments. The experimental trend shows that, with increasing ions size, voltages decrease on average by 0.002 V for V_{Ru-Fe} and 0.06 V for V_{Cu-Fe}. The PBE0 functional were found more adequate in the case for V_{Cu-Fe} but for V_{Ru-Fe} PBE functional shows better agreement with the experimental trends. Since the voltage hardly varies within functional approximation we can take any counter-ion to model bi-nuclear complex. For all cases, the sign was found to be positive which indicates the reaction is spontaneous. The voltage reported in this work corroborates with experimental and theoretical studies. In Table 2.13, net Mulliken

spin polarization in the presence of each counter-ions are shown. It can be seen no net difference is observed between counter-ions.

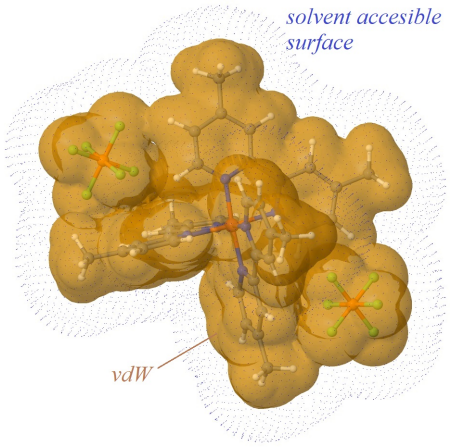

Figure 2.33: In this model, solute cavity is created by a set of overlapping spheres and the solvent is defined by some parameters such as dielectric constant, molar volume and polarizability.

For comparison purposes, we have performed one more calculation taking into account the effects caused by the implicit solvent model (schematically shown in Figure 2.33). For this calculation, default values were used and the geometry was optimized with the solvation model. Acetonitrile solvent was modeled by means of the self-consistent reaction field (SCRF) method based on the Polarizable Continuum Model (PCM) as implemented in Gaussian09 code. For PF_6^- counter-ion we did not observe any large variation on the voltage. Which explains there interaction are considered in the secondary sphere while counter-ions in the inner sphere resembles the model more realistically.

Table 2.12: Comparison of experimental and calculated relative voltage for mononuclear complex with two functionals.

	$V_{Ru-Fe}(V)$			$V_{Cu-Fe}(V)$		
Ci^-	ClO_4^-	PF_6^-	$TFSI^-$	ClO_4^-	PF_6^-	$TFSI^-$
PBE/PCM	0.17	0.28/0.24	0.31	-1.04	-0.68/-0.4	-0.85
PBE0/PCM	0.37	0.34/0.32	0.26	-0.97	-0.85/-0.5	-0.95
Exp.	0.208	0.201	0.198	-1.035	-1.075	-1.14

Table 2.13: Calculated magnetic state of the mono-nuclear complex. S is the spin ground state of the system, and Q is a total charge on a system and NS is the net Mulliken spin polarization on transition metal site in a cluster obtained at the Def2SVP level of theory.

	Net Spin (NS)						Q	S
	PBE			PBE0				
	ClO_4^-	PF_6^-	$TFSI^-$	ClO_4^-	PF_6^-	$TFSI^-$		
$[Ru(dmbpy)_3]^{2+}2C$	0	0	0	0	0	0	0	0
$[Ru(dmbpy)_3]^{3+}3C$	0.62	0.9	0.9	1.01	1.01	1.01	0	1/2
$[Fe(dmbpy)_3]^{2+}2C$	0	0	0	0	0	0	0	0
$[Fe(dmbpy)_3]^{3+}3C$	0.9	1.08	1.08	1.14	1.14	1.14	0	1/2
$[Cu(dmbpy)_2]^{+}C$	0	0	0	0	0	0	0	0
$[Cu(dmbpy)_2]^{2+}2C$	0.5	0.5	0.52	0.66	0.68	0.69	0	1/2

2.6 Conclusion

In this chapter, we demonstrated that the choice of the functional has a considerable effect on the description of electronic structure. To the opposite, structural parameters are hardly affected by this choice. The introduction of the counter-ions in the neighboring of the complex induces indirect effects, as revealed by our analysis of the PDOS and our study of the local geometry, thereby improving the voltage for the Cu complex. The voltage obtained within both functionals agrees nicely with the experimental values. However, further investigation is still needed to definitively validate our approximation for Bi-nuclear system. In the next section, we will further investigate the functional that is suitable by studying different oxidation states of bi-nuclear chains.

■

Chapter 3

Low-dimensional polymer batteries: the bi-nuclear complexes

In this Chapter, we tackle the problem of the bi-nuclear complex by introducing alkyl chain of length n between two mono-nuclear patterns in order to study their configuration, electronic properties, spin state ordering, geometry and voltage. More specifically, we will focus on the effects caused by the loading process on the local and global geometries as well as their implications on the electronic structure, these effects being crucial to qualify the ability of our compounds to present an efficient battery cycle life.

3.1 Problem encountered for the placement of bi-nuclear center

With bi-nuclear compounds, a first opportunity is given to introduce parameters to tune the properties of the batteries: indeed, electrochemical properties of compounds are expected to vary according to the length of the alkyl chain connecting both mono-nuclears. The question we address here is the determination of the optimal length of the alkyl chain regarding the usage of compounds for a battery application. Let us have the list of all the phenomena that can be affected by the length of the alkyl chain:

1. The average distance between two active centers will be varied according to the length. These latter being charged, the electrostatic repulsion between each other will depend on it and the process of loading of one site as the other is already loaded (we shall denote it as the half-loaded state in the following) will be affected in a different manner according to this distance.

2. The global geometry is expected to be different according to the flexibility of the alkyl chain. A more folded conformation will vary the local potential on one site and the electrochemical potential will vary adequately.

3. Changing this length will allow to vary the environment around the active centers: a small chain will introduce huge steric effects and the location of the counter-ions will be consequently modified. All these changes of conformations induce small variations of energy that are entirely reported on the voltage.

4. The electronic polarization in the chain is varied with its length and can eventually influence the electronic states of the *dmbpy* molecules. Such a re-polarization could affect the electrochemical potential of the central Fe since hybridization states between the nitrogens of the *dmbpy* and Fe atoms are observed. We expect that a small chain (2C) will really modify the electronic structure of the patterns and differ neatly from the case of mono-nuclear compounds. For larger size, our system should behave like independent mono-nuclears.

We have selected three lengths for the alkyl chain: 2, 4 and 6 carbon[1]. With six carbons, both monomers are separated enough to treat the limit case for which both mono-nuclears hardly affect each other, as a test using an eight carbons chain has revealed. The analysis of the local geometry, the electronic structure and the calculation of the voltage will allow us to assess what is the best match for the length of the alkyl chain.

To conclude, let us mention that, experimentally, the small bi-nuclear centers (2C) in a solution contains two type of polymers. The regular geometry consists in the connection of two mono-nuclear complexes by a single alkyl chain. The other one corresponds to a double connection. They are presented in the Figure 3.1. At room temperature, the regular case is ultra predominant and have been selected to model the bi-nuclear compounds. We, however, had a calculation on the second type of polymer but we didn't pursue on this molecule, because it does not represent the majority effects encountered in our battery.

[1]We will adopt the following convention in the rest of thesis for representing alkyl chains to avoid confusion. Alkyl chains, $-(CH_2)_n-$, corresponding to $n = 2$, 4, and 6 are represented by 2C, 4C, and 6C respectively.

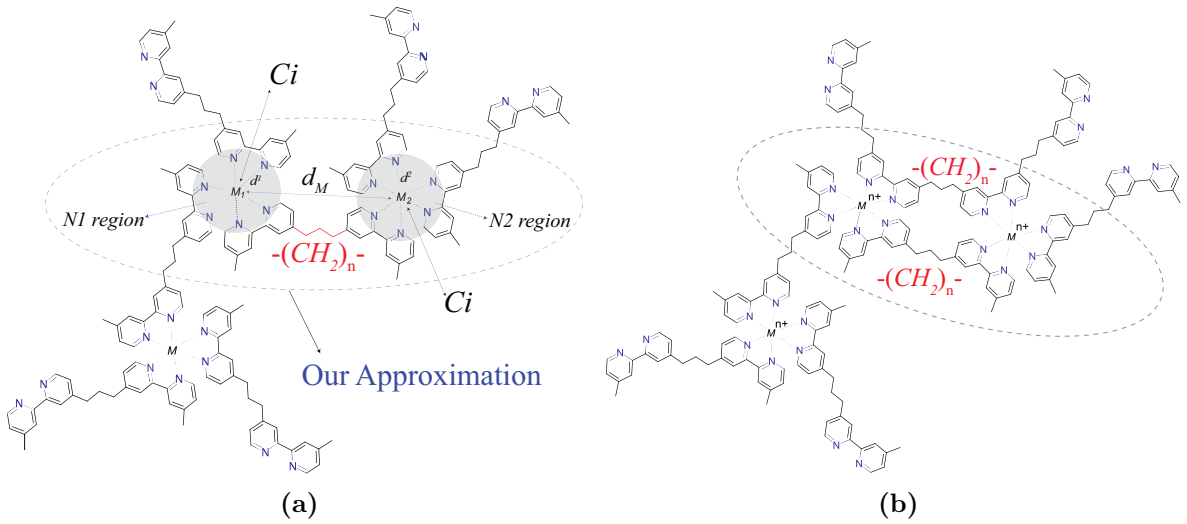

Figure 3.1: Approximation of the model considering $-(CH_2)_n- \equiv nC$ alkyl chain of length n. (a) Regular and (b) Strange bi-nuclear configuration. Identification of regions within a bi-nuclear system. *N1* and *N2* are the regions corresponding to the *Nitrogen* atoms and M_i is the metallic center for $M_i^{n+} = Fe$. The nearest distance between the Metal site and counter-ions are shown with $M_i - Ci$. Ci labels the counter-ions surrounding each active centers.

3.2 Thermodynamics and voltage within the field of counter-ions: formalism

In this paragraph, we adopt the expression of the voltage of the battery that we derived in the previous chapter to the case of the bi-nuclear compounds. Let's introduce more general notation for the dimer as follows:

$$D_{n_1,n_2} = [Fe\,(dmbpy)_3]^{n_1+}\, n_1 Ci + nC + [Fe\,(dmbpy)_3]^{n_2+}\, n_2 Ci \tag{3.1}$$

Which represents two mono-nuclear patterns connected by an alkyl chain $nC \equiv -(CH_2)_n-$ with n the size of chain. n_1 and n_2 are the degrees of oxidation of the first and second patterns, respectively. Ci labels the counter-ions surrounding each active centers. If n_1 and n_2 both equal 2, the polymer is unloaded. If $n_1 = 2$ and $n_2 = 3$, the polymer is said half-loaded and if $n_1 = n_2 = 3$, our polymer is fully loaded. Using the notational scheme, the balanced equation corresponding to a half loaded polymer reads,

$$D_{3,2} \rightharpoonup D_{2,2} + LiCi - Li(bcc) \tag{3.2}$$

The corresponding Gibbs free energy is approximated by,

$$\triangle G_{Fe} = E^{D_{2,2}} + E_0 - E^{D_{3,2}} \tag{3.3}$$

Where the total energy corresponding to $LiCi - Li(bcc)$ is noted E_0. $E^{D_{2,2}}$, and $E^{D_{3,2}}$ are the total energy of the dimers obtained by DFT calculations. The corresponding voltage is calculated by forming:

$$V_{HL} = -\frac{E^{D_{2,2}} + E_0 - E^{D_{3,2}}}{\mathcal{F}} \tag{3.4}$$

Where the label HL denotes that this voltage corresponds to the half-loaded compound. A reference potential, $V_0 = E_0/nF$, can be introduced as we made in the case of mono-nuclear compounds. The voltage corresponding to the fully loaded (FL) system is directly obtained through:

$$V_{FL} = -\frac{E^{D_{2,2}} + 2E_0 - E^{D_{3,3}}}{2\mathcal{F}} \tag{3.5}$$

3.3 Optimization of the conformation

3.3.1 Preliminary calculation: without counter-ions

First, we have undertaken a series of calculations consisting in obtaining a first optimized geometry for dimers without adding the counter-ions. In fact, optimizing the geometry of such soft and flexible molecules is a very costly job in terms of CPU time and an overall optimization of the molecule surrounded by the counter-ions presents too many internal degrees of freedom to hope to obtain the ground state from a single calculation. To avoid to be trapped into metastable states of conformation, we used the following approach:

1. At first, we have plugged an alkyl chain on a mono-nuclear pattern, whose optimized geometry was obtained in the previous chapter. The calculation revealed that the alkyl chain had a trend to bend.

2. Then a second mono-nuclear pattern were plugged at the other tip of the alkyl chain and a new optimization of geometry was performed. After optimization, our results have shown that the huge electrostatic interactions between both mono-nuclear centers (both transition metal ions are charged positively) forces the carbon atoms of the alkyl chain to recover a straight alignment.

This prototype of a molecule, presenting a straight alkyl chain was used as an initial guess and future optimizations will mainly focus on the exact location of the counter-ions around the active centers but also observing the influence on the curvature of the alkyl chain. Let us mention that these new optimizations of the geometry including the counter-ions will be global: no atom locations are kept fixed in the followings. The purpose of this work was only to prepare an initial state.

3.3.2 Introducing counter-ions

From previous calculations, bi-nuclear compounds are constructed. Due to the large system size, Def2SVP basis sets were employed with the two exchange-correlation functionals: gradient corrected functional PBE [99] and hybrid functional PBE0 [100]. This was done for Neutral ($2\left[Fe\left(dmbpy\right)_3\right]^{2+}4Ci$), Half loaded ($\left[Fe^{3+}Fe^{2+}\left(dmbpy\right)_3\right]5Ci$) and Full loaded ($2\left[Fe\left(dmbpy\right)_3\right]^{3+}6Ci$) systems, where counter-ions are noted $Ci = PF_6^-$, $TFSI^-$ or ClO_4^-. For comparison purposes with mono-nuclears, PDOS plot for bi-nuclear will be analyzed with $Ci = PF_6^-$. We have also performed the calculation with other counter-ions but have not presented here nevertheless the behavior is same. The determination of the spin multiplicity is vital for the correct prediction of the ground state. In the case of the mono-nuclear compound, fixing the correct spin ground state was an easy task since one single metallic center were considered. For bi-nuclear compound, two metallic sites pose a spin orientation problem. The system could be in the ferromagnetic or anti-ferromagnetic state. For Neutral, the system is a closed shell and the ground state for bi-nuclear is the sum of each mono-nuclear. For a fully loaded system, each mono-nuclear is an open shell system and the total spin magnetic moment can be either in two states, $S = 0$ or $S= 1$. For Fe complex, we found that $S = 1$ was the correct ground as it gives the lowest ground state energy.

To conclude this technical part, we report here that the PBE0 functional were always found suitable for the determination of the ground state, without any problems of convergence. However, as regards to PBE functional, we were not capable to found a converged ground state for the half-loaded system when the largest size of the alkyl chain is considered (six carbons). This point that can apparently be annoying since the PBE approximation were found to be our best approximation for the mono-nuclear compound) will be debated in the followings at the light of our study devoted to the electronic structure. We can however already states that for half loaded system, the system tunnels between two states, one with closed shell and the other with open shell so that the overall spin state of the system is observed to be $S = 1/2$. We understand that this can induce electronic convergence failure due to the observed trend of the PBE

approximation to obtain localized d-states, so pretty inappropriate to represent this tunneling of one electron from one site to the other. To the contrary, Hybrid functional (PBE0), as shown in the previous chapter, tends to delocalize the electronic states and they have all the material inside to represent this tunneling so that an easy convergence is obtained. However, the true question is to assess if such an average wavefunction, as provided by the excessive delocalization of the PBE0 approximation, is an acceptable description to represent this jump of the electron from one pattern to the other. The final section devoted to the calculation of the voltages will answer this question.

In this section, we will present the results corresponding to the PF_6^- counter-ions, since no major differences of behavior were noticed between our counter-ions. Moreover, as stated in the previous chapter, the voltage computed for mono-nuclear complex hardly varies with the nature of the counter-ions. We assume this will be also the case for bi-nuclear systems. Let's now turn to the obtained conformations. Here, we are attached to the global conformation (analysis of the alkyl chain curvature and counter-ions location), the local geometry all around the iron centers will be investigated in the next paragraph.

In Figure 3.2, we present the optimized structures for the neutral bi-nuclear compound (two counter-ions balance the Fe^{2+} charge for each pattern) for the three alkyl chains we have investigated ($n = 2$, 4 and 6) to connect them. In this neutral case, one counter ion is systematically rejected at the tip of the dimer whatever the size of the chain may be. The second counter-ion (for a given mono-nuclear) is found to lie in the region between both patterns. The largest the length of the alkyl chain is, the closest to the chain, this counter ion is. If we may conclude that the general arrangement of the counter-ions is the same for all the alkyl chains, steric effects induced by the shrinkage of the carbon chain expel the second counter-ions further away from the axis formed by the alkyl chain.

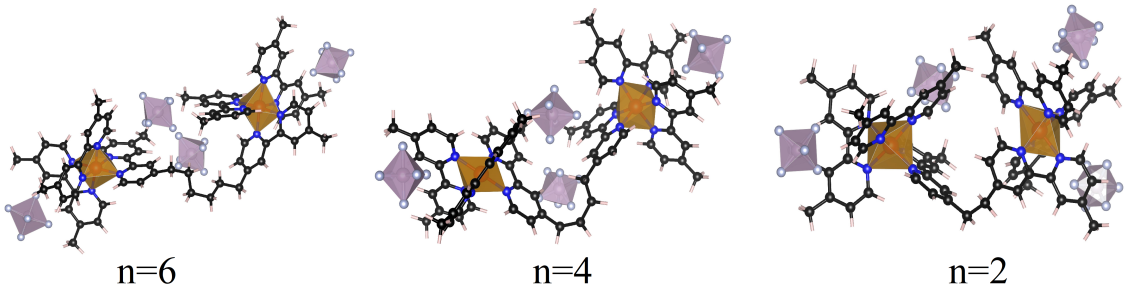

Figure 3.2: Minimized structure of Fe Neutral (N) complex for alkyl chain $-(CH_2)_n-$ of length n for $n = 6$, 4 and 2 at the PBE0/Def2SVP level of theory.

In Figure 3.3, the same series is shown but for the half loaded compound: one Fe

sees in degree oxidation 3+, the other remains 2+ so that only one counter ion is added. Here we have to distinguish between the longer ($n = 4$ and 6) and smaller ($n = 2$) chain lengths. For the longest, it is clearly noticeable that the carbon chain bends as this new counter-ion is added so that both patterns start to re-approach each other. The three counter-ions centered on the loaded pattern are found to rather lie in the space between the patterns (one has moved from the tip of the molecule to this region), so that a high density of counter-ions is found in this region. Consequently, the Fe^{2+}/Fe^{3+} interaction is screened by this higher density of negative charge, allowing the bending of the carbon chain. This conformation is found to be the one having the lowest energy: the system prefers to decrease the strong 2+/3+ electrostatic interaction by screening them instead of continuing to expel them at maximum by adopting the straight conformation. Quite certainly $-1/-1$ interactions between the counter ions are unfavorable, but this penalty energy is mainly compensated by the gain of energy caused by the screening. For $n = 2$, the location of the counter-ions is only piloted by the optimization of the overall electrostatic interaction (a network of -1, 2+ and 3+ charges) given that the size and the poor flexibility of the two carbon chains do not allow such a screening.

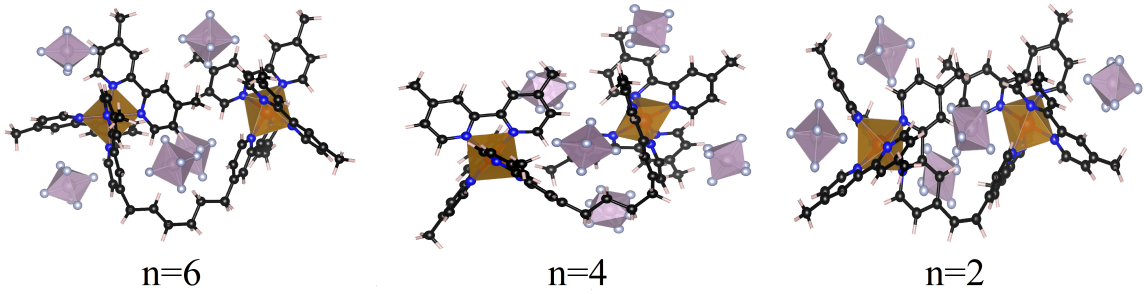

Figure 3.3: Minimized structure of Fe Half loaded (HL) complex for alkyl chain $-(CH_2)_n-$ of length n for $n = 6$, 4 and 2 at the PBE0/Def2SVP level of theory.

Finally, in Figure 3.4, the conformations of the fully loaded compounds are displayed. They are not pretty different from the half-loaded case and rely on the same phenomena. We can eventually indicate a larger folding of the molecule for the six carbons chain due to its larger flexibility.

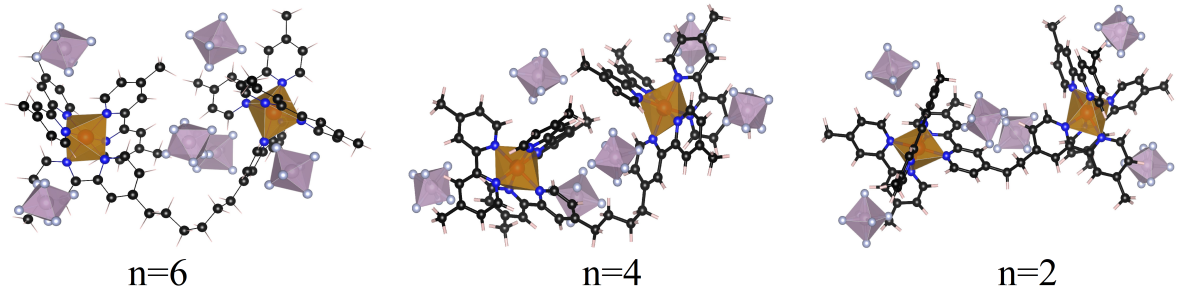

Figure 3.4: Minimized structure of Fe Full loaded (FL) complex for alkyl chain $-(CH_2)_n-$ of length n for $n = 6$, 4 and 2 at the PBE0/Def2SVP level of theory.

3.3.3 Ground state properties

To complete this qualitative study we have reported in Table 3.1, properties such as spin multiplicity, Mulliken charge, net spin on metallic sites as well as the distances between both mono-nuclear states. They are, as usual, obtained within the PBE and PBE0 functionals. We observe for a Neutral system that the net spin acquired by the metallic centers and ligands is zero. For the Full loaded system the net spin resides on two metallic centers with the same number of electrons with nearly zero net spins on *dmbpy* and counter-ions. All these results confirm that these properties are not varied during the loading process, showing that the main site-projected features of the electronic structures will not be deeply affected during the charge/discharge process. Such behavior is mandatory if our compounds have to be considered as a valuable candidate for a battery application.

The distance between two Fe centers is surprisingly hardly varied from one alkyl chain to another, with average values ranging from approximately 9 to 11 Å. The $-(CH_2)_6-$ chain presenting three times the length of the $-(CH_2)_2-$ chain, a larger $Fe-Fe$ distance could have been expected for the compound made of $-(CH_2)_6-$. To the opposite, this latest result shows that the bending and folding of the molecule described above is piloted by a very specific arrangement of counter-ions, in common for the three alkyl chains: the alkyl chain is found to adapt its shape in order to satisfy this optimized arrangement: this particular arrangement has to be viewed as the one which minimizes at best the electrostatic interactions. This so-obtained critical distance is large enough to allow us to conclude that the loading process on one site of the molecule will poorly affect the loading process of the second center at the other tip of the molecule.

Table 3.1: Ground state properties of bi-nuclear complex for Neutral *(N)*, Half loaded *(HL)*, and Full loaded *(FL)* system with $-(CH_2)_n-$ alkyl chain for $Ci = PF_6^-$ counter-ion. S is the spin ground state of the system. Net spin and Charge calculated with Mulliken population analysis (MPA) and d_{Fe} is the distance between two Fe sites at PBE0/PBE//Def2SVP level of theory.

			PBE0						PBE			
			N		HL		FL		N		FL	
			Fe^{2+}	Fe^{2+}	Fe^{3+}	Fe^{2+}	Fe^{3+}	Fe^{3+}	Fe^{2+}	Fe^{2+}	Fe^{3+}	Fe^{3+}
2C	MPA	Charge	0.55	0.57	0.56	0.57	0.58	0.58	0.33	0.33	0.36	0.36
		net spin	0	0	1.14	0	1.14	1.14	0	0	1.08	1.083
		d_{Fe}(Å)	9.29		9.69		11.9		10.46		9.71	
		S	0		1/2		1		0		1	
4C	MPA	Charge	0.56	0.55	0.58	0.58	0.56	0.56	0.30	0.34	0.33	0.34
		net spin	0	0	0.00	1.14	1.14	1.14	0	0	1.08	1.08
		d_{Fe}(Å)	11.32		9.32		10.21		11.06		10.16	
		S	0		1/2		1		0		1	
6C	MPA	Charge	0.57	0.54	0.6	0.5	0.57	0.57	0.33	0.33	0.34	0.34
		net spin	0	0	1.14	0	1.14	1.14	0	0	1.082	1.082
		d_{Fe}(Å)	11.82		9.86		10.18		11.84		11.52	
		S	0		1/2		1		0		1	

Finally, Table 3.2 displays the same properties but for the Ru complex the same kind of behavior is observed. However, we have to outline that a sudden shrinkage of the $Ru-Ru$ distance for the 6C full-loaded configuration is obtained. From the Figure 3.5, 3.6, and 3.7 this shortening of distance is attributed to the change of location of the counter-ions.

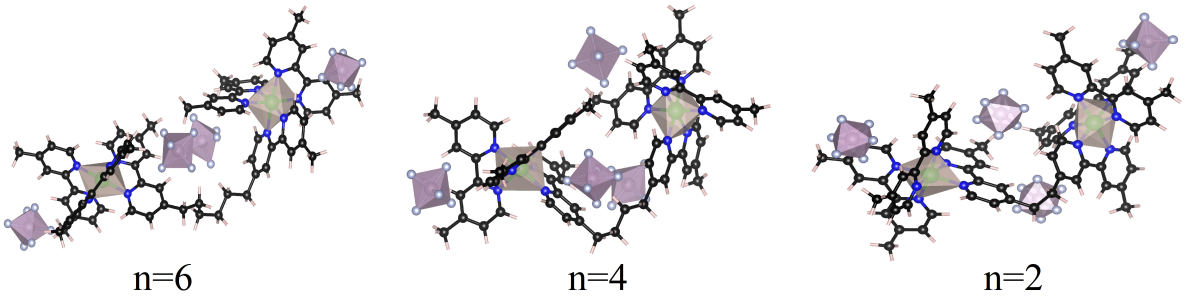

Figure 3.5: Minimized structure of Ru Neutral (N) complex for alkyl chain $-(CH_2)_n-$ of length n for $n = 6$, 4 and 2 at the PBE0/Def2SVP level of theory.

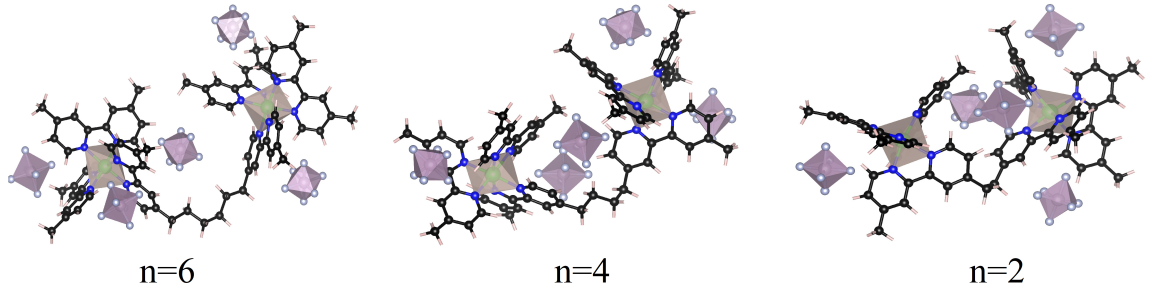

Figure 3.6: Minimized structure of *Ru* Half loaded (HL) complex for alkyl chain $-(CH_2)_n-$ of length n for $n = 6$, 4 and 2 at the PBE0/Def2SVP level of theory.

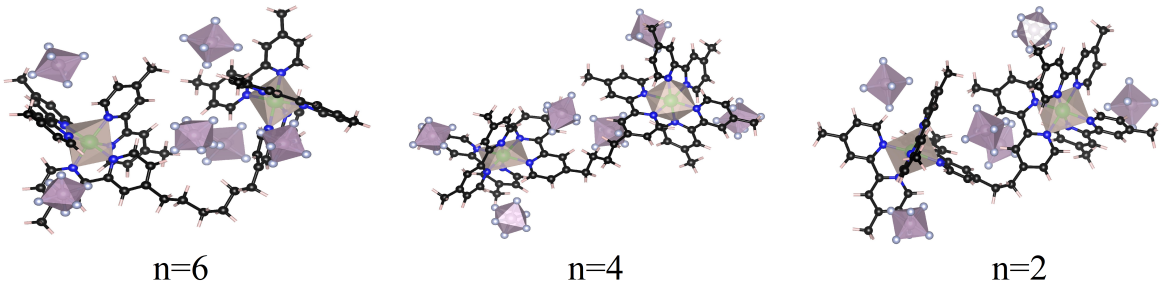

Figure 3.7: Minimized structure of *Ru* Full loaded (FL) complex for alkyl chain $-(CH_2)_n-$ of length n for $n = 6$, 4 and 2 at the PBE0/Def2SVP level of theory.

Table 3.2: Ground state properties of bi-nuclear complex for Neutral *(N)*, Half loaded *(HL)*, and Full loaded *(FL)* system with $-(CH_2)_n-$ alkyl chain for $Ci = PF_6^-$ counter-ion. S is the spin ground state of the system. Net spin and Charge calculated with Mulliken population analysis (MPA) and d_{Ru} is the distance between two Ru atoms.

			PBE0						PBE			
			N		HL		FL		N		FL	
			Ru^{2+}	Ru^{2+}	Ru^{3+}	Ru^{2+}	Ru^{3+}	Ru^{3+}	Ru^{2+}	Ru^{2+}	Ru^{3+}	Ru^{3+}
2C	MPA	Charge	0.33	0.33	0.35	0.52	0.52	0.51	0.14	0.11	0.23	0.26
		net spin	0	0	0	0.9	1.0	1.0	0	0	0.9	0.9
		d_{Ru}(Å)	10.38		10.205		10.85		13.32		12.51	
		S	0		1/2		1		0		1	
4C	MPA	Charge	0.34	0.34	0.33	0.52	0.54	0.53	0.13	0.14	0.26	0.26
		net spin	0	0	0	1.0	1.0	1.0	0	0	0.9	0.9
		d_{Ru}Å)	10.31		10.34		12.74		10.38		12.75	
		S	0		1/2		1		0		1	
6C	MPA	Charge	0.33	0.34	0.52	0.33	0.51	0.52	0.13	0.15	0.24	0.24
		net spin	0	0	0	1.0	1.0	1.0	0	0	0.90	0.91
		d_{Ru}(Å)	13.49		12.98		11.26		13.38		10.98	
		S	0		1/2		1		0		1	

3.4 Local geometries

3.4.1 Bond distances

In Table 3.3, 3.5 and 3.7 average $M-N$ bond lengths for bi-nuclear complex are computed for each alkyl chain with two functionals. Intra-atomic distances resembles nicely to the mono-nuclear complex calculated in previous chapter. On average bond lengths calculated for $d^1 = Fe1-N$ and $d^2 = Fe2-N$ is 1.96 Å and 1.95 Å for PBE functional. Similarly, for PBE0 functional it is 1.98 Å and 1.98 Å respectively. Similarly, for half loaded and full loaded system the bond lengths are in agreement with the experimental results. In all cases, for PBE0 functional it deviates by 0.02 Å. For half loaded system, bond lengths for PBE functional are omitted for above mentioned reasons. Moreover, depending on the counter-ions position interatomic distances are measured with respect to each metallic center. For some ions if they are near to $Fe1$ center the nearby counter-ions are accounted and similarly for $Fe2$ center. On average, the counter-ions distance

are on the order of 5.5 Å which corroborates nicely with the mono-nuclear complex.

Similarly, in Table 3.4, 3.6, and 3.8 the intra-atomic distances are close to those found in the mono-nuclear complex and the interatomic distance between *Ru* center and counter-ion are on the order of 5.5 Å.

Table 3.3: *Fe* bi-nuclear bond lengths computed for Neutral (N), Half loaded (HL), and full loaded (FL) system in the $Ci = PF_6^-$ counter-ion medium for 6C alkyl chain. All bond lengths are given in Å.

	PBE		PBE0				PBE		PBE0		
	N	FL	N	HL	FL		N	FL	N	HL	FL
Fe1-N	1.96	1.97	1.98	1.97	1.97	Fe2-N	1.95	1.97	1.98	1.98	1.97
Fe1-P1	6.014	5.744	5.966	5.479	5.669	Fe2-P1	6.535				
Fe1-P2	6.244		6.197			Fe2-P2		5.658	6.545	5.988	5.664
Fe1-P3				6.017		Fe2-P3	5.818	6.068	5.836		6.025
Fe1-P4		5.775		5.974	5.771	Fe2-P4	5.711		5.703	5.971	
Fe1-P5		5.631		6.670	5.595	Fe2-P5		6.188			6.117
Fe1-P6		6.306			6.302	Fe2-P6					

Table 3.4: *Ru* bi-nuclear bond lengths computed for Neutral (N), Half loaded (HL), and full loaded (FL) system in the $Ci = PF_6^-$ counter-ion medium for 6C alkyl chain. All bond lengths are given in Å.

	PBE		PBE0				PBE		PBE0		
	N	FL	N	HL	FL		N	FL	N	HL	FL
Ru1-N	2.064	2.068	2.062	2.062	2.063	Ru2-N	2.062	2.069	2.063	2.061	2.063
Ru1-P1	6.34	5.72	6.21	5.85	5.60	Ru2-P1					
Ru1-P2	6.25		6.38			Ru2-P2		5.66		6.056	5.69
Ru1-P3				5.66		Ru2-P3	6.40	6.19	6.25		6.093
Ru1-P4		6.24			6.07	Ru2-P4	6.21		6.43	6.292	
Ru1-P5		5.26		5.87	5.43	Ru2-P5		5.75			6.098
Ru1-P6		6.43			6.38	Ru2-P6					

Table 3.5: *Fe* bi-nuclear bond lengths computed for Neutral (N), Half loaded (HL), and full loaded (FL) system in the $Ci = PF_6^-$ counter-ion medium for 4C alkyl chain. All bond lengths are given in Å.

	PBE		PBE0				PBE		PBE0		
	N	FL	N	HL	FL		N	FL	N	HL	FL
Fe1-N	1.95	1.96	1.98	1.98	1.96	Fe2-N	1.96	1.97	1.98	1.97	1.97
Fe1-P1	6.754	6.793			6.676	Fe2-P1	8.046	5.745	7.786	6.091	5.767
Fe1-P2	5.818	5.956	6.004	6.078	5.895	Fe2-P2	6.313				
Fe1-P3	5.833		5.790	6.332		Fe2-P3		5.626		9.179	5.588
Fe1-P4		5.899			5.785	Fe2-P4	6.235	7.911	5.791	5.309	
Fe1-P5						Fe2-P5		5.619			5.576
Fe1-P6		6.292			6.241	Fe2-P6		8.262			

Table 3.6: *Ru* bi-nuclear bond lengths computed for Neutral (N), Half loaded (HL), and full loaded (FL) system in the $Ci = PF_6^-$ counter-ion medium for 4C alkyl chain. All bond lengths are given in Å.

	PBE		PBE0				PBE		PBE0		
	N	FL	N	HL	FL		N	FL	N	HL	FL
Ru1-N	2.061	2.069	2.060	2.063	2.064	Ru2-N	2.063	2.068	2.062	2.059	2.063
Ru1-P1						Ru2-P1	5.94	5.489	5.922	5.534	5.153
Ru1-P2	6.199		6.200	5.889		Ru2-P2		6.299			6.148
Ru1-P3	6.256	6.038	6.168	5.928	5.975	Ru2-P3					
Ru1-P4		6.360		9.192	6.290	Ru2-P4	6.269		6.258		
Ru1-P5		5.461			5.722	Ru2-P5		7.84		5.751	
Ru1-P6						Ru2-P6		5.715			5.925

Table 3.7: *Fe* bi-nuclear bond lengths computed for Neutral (N), Half loaded (HL), and full loaded (FL) system in the $Ci = PF_6^-$ counter-ion medium for 2C alkyl chain. All bond lengths are given in Å.

	PBE		PBE0				PBE		PBE0		
	N	FL	N	HL	FL		N	FL	N	HL	FL
Fe1-N	1.96	1.97	1.98	1.98	1.97	Fe2-N	1.96	1.97	1.98	1.96	1.97
Fe1-P1						Fe2-P1	6.292	5.928	6.250	5.911	5.856
Fe1-P2	5.672		5.619	5.940		Fe2-P2	5.971	5.390	5.949		5.386
Fe1-P3	6.385	5.962	6.313	6.395	5.814	Fe2-P3				6.336	
Fe1-P4	6.025	6.080	6.037	6.420	5.968	Fe2-P4			7.618	6.121	5.657
Fe1-P5		5.453			5.452	Fe2-P5		6.835		5.680	
Fe1-P6						Fe2-P6		6.086			

Table 3.8: *Ru* bi-nuclear bond lengths computed for Neutral (N), Half loaded (HL), and full loaded (FL) system in the $Ci = PF_6^-$ counter-ion medium for 2C alkyl chain. All bond lengths are given in Å.

	PBE		PBE0				PBE		PBE0		
	N	FL	N	HL	FL		N	FL	N	HL	FL
Ru1-N	2.062	2.066	2.061	2.060	2.065	Ru2-N	2.061	2.069	2.062	2.063	2.060
Ru1-P1		5.594				Ru2-P1	6.222		6.342	6.086	5.451
Ru1-P2	6.265		6.210	6.348		Ru2-P2		5.665			5.314
Ru1-P3				6.099	6.005	Ru2-P3	5.844	6.030	6.142		
Ru1-P4	6.584	6.456	5.841	5.436	5.939	Ru2-P4			5.599	6.831	
Ru1-P5				5.638	6.011	Ru2-P5		6.146			
Ru1-P6		5.733			6.494	Ru2-P6					5.841

3.5 Electronic structure of the compounds for 6C alkyl chain

We start our study of the electronic structure by the longest chain. As mentioned above, the distance between both metallic centers appears to be a constant of our problem whatever the length of the alkyl chain may be. Hybridization effects between the *dmbpy* and the alkyl chain will cancel at the middle of the alkyl chain so that this case is expected to present a maximum of similarities with the mono-nuclear case. For the

smallest chains, these hybridization effects will sum up and we will compare in the next sections the changes in their densities of states with respect to the ones of the compounds using this six carbons chain, considered as the new reference.

3.5.1 Results within the PBE0 approximation

Figure 3.8, displays the site-projected DOS (PDOS) for the neutral bi-molecular compound. The first panel corresponds to the first monomer centered on site $Fe1$ and the second panel to the monomer centered on site $Fe2$. We represent the PDOS for the Fe site1, the N (Nitrogen's atom) sites at their immediate vicinity but also the ones of the counter-ions surrounding each monomer. If a chemical bond presenting a covalent character is observed, it will involve these N (Nitrogen's atom) atoms and the Fe sites and states in common will be noticeable (location and shape of the peak of both PDOS of Fe and N will be strongly correlated). As already encountered in the case of the monomer, the ligand field picture is not conserved within this PBE0 approximation with the obtaining of one single peak for the Fe sites. This latter is found to be the HOMO states. No states are developed for Fe in the window of energy ranging from -8 to -15 eV where the nitrogen states are present so that no hybridization is found between the Fe and the N of the *dmbpy* surrounding the Fe site. Thus, we may conclude that the PBE0 approximation leads to a very isolated Fe state for iron, with no covalent character for the chemical bond between Fe and N. No hybridization between the counter-ions peaks and Fe or N peaks are observed counters-ions add an additional electrostatic potential over the Fe site and adapt their geometry when they approach this site but we may in any manner consider that a bond is created between them and the monomer patterns. No major differences are found between both sites: the PDOS only slightly vary from one site to another according to the precise local geometry (precise counter-ion locations all around each pattern in the dimer). This latter remark is true for all the compounds we have studied in this section and we will most of the time present our results for one pattern over both in the dimer in the followings.

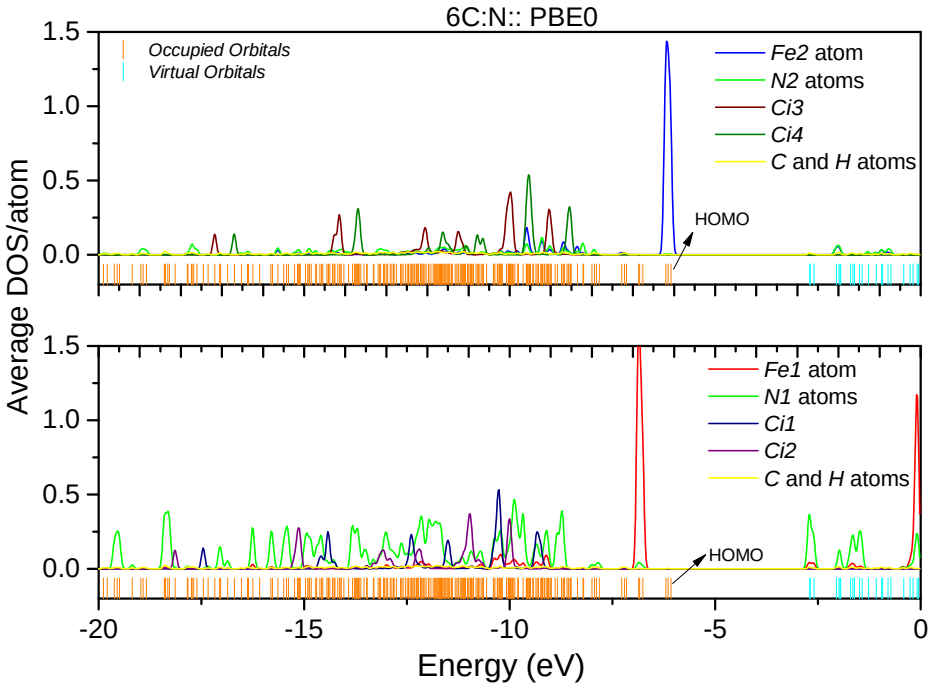

Figure 3.8: Average partial density of states (PDOS) calculated within the PBE0 approximation for the Neutral 6C complex. It is built upon the data of the electronic levels using Hermite-Gaussian smearing method with a smearing parameter of $w_{1/2} = 0.1$ eV. We have added the partial DOS corresponding to Fe's atoms, the sum of carbon and hydrogen contributions in yellow and the N's regions contributions from the *dmbpy* in green. The occupied orbital electronic levels are reported in orange color at the bottom.

Figure 3.9, presents our results for the fully loaded system for which both Fe sites are 3+. The results are shown for one site for both spin-up and spin-down channels. For this degree of oxidation, the PBE0 approximation leads to a complete reshaping of the PDOS of the Fe sites, with a complete vanishing of the HOMO peak observed in the neutral case: here the Fe states are distributed in the energy window ranging from -8 to -14 eV where the peaks of N (Nitrogen's atom) and counter-ions are mainly observed. This approximation drives to the development of very delocalized states that we still consider to be an inappropriate description of the electronic structure of our compounds. If the passage from the degree of oxidation 2+ to 3+ is expected to decrease the number of states in the HOMO state found in the neutral case with some reasonable reshaping of the PDOS, we can hardly imagine that such a drastic effect may occur due to the mere re-approachment of the counter-ions. A neat correlation between the location of the N (Nitrogen's atom) states and the ones of Fe is obtained. We also notice a larger correlation between the peaks of the Fe, N (Nitrogen's atom), and counter-ions than it was the case of the neutral compound, advocating for very long range delocalization

effects of the electrons, leading to a strong polarization of the counter-ions. Moreover, the HOMO state corresponds to states belonging to the carbon chains and not to the Fe sites anymore, outlining the exaggerated ability of this PBE0 approximation to create delocalized states over the whole system.

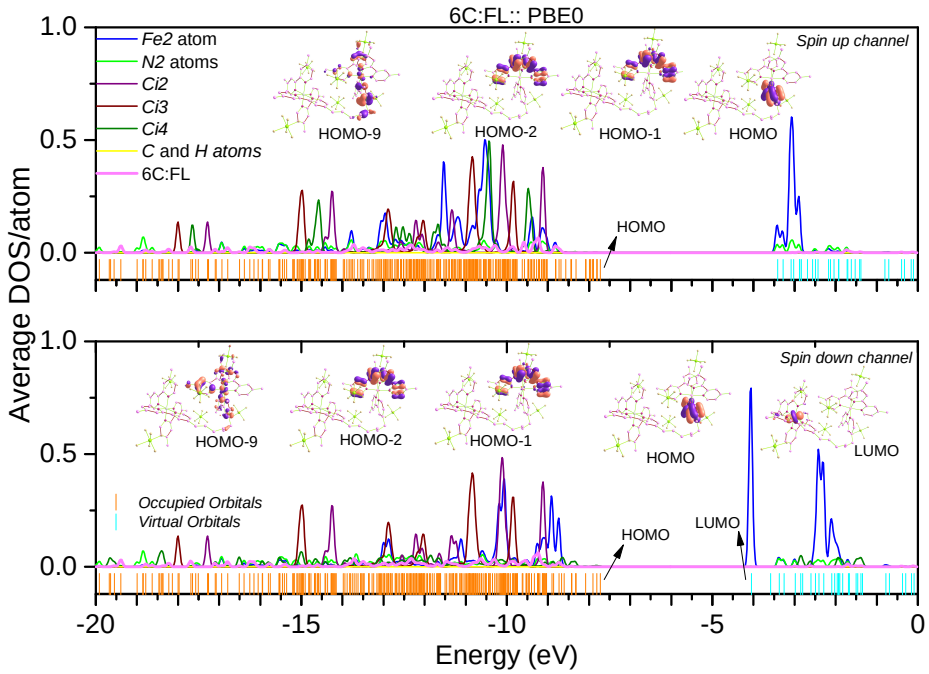

Figure 3.9: Average partial density of states (PDOS) calculated within the PBE0 approximation for the Full loaded 6C complex. It is built upon the data of the electronic levels using Hermite-Gaussian smearing method with a smearing parameter of $w_{1/2} = 0.1$ eV. We have added the partial DOS corresponding to Fe's atoms, the sum of carbon and hydrogen contributions in yellow and the N's regions contributions from the *dmbpy* in green. The occupied orbital electronic levels are reported in orange color at the bottom.

Finally, Figure 3.10 and 3.11 displays our results for the half loaded system. Here $Fe1$ and $Fe2$ sites are not equivalent anymore since one site over both is loaded (degree of oxidation 3+). Site $Fe1$, with its delocalized states, sees its PDOS pretty similar to the case of the fully-loaded compound, while site $Fe2$ displays a deep neutral character with its very localized HOMO Fe peak. However, two remarks have to be done regarding the loaded site:

1. if a large amount of Fe states are still found to be hybridized with the N sites, the Fe peak near the HOMO is more filled than in the fully loaded case. From that, we conclude that the total vanishing of these peaks in the previous case was due to a cumulative effect. The delocalization effects induced by the PBE0 approximation were propagating the information from one site to another leading to a

full hybridization. Here, some more localized peaks remain since the contribution from the other site is of "neutral" type.

2. we have super-impose the PDOS of all the ligands on all the plots in order to show that the PDOS of the fifth one, *i.e.*, the new one involved in the loading process (brown curve), is different from the others (the one already present, involved in the neutral state). It is found shifted with respect to the others. This corresponds to a shift of energy towards the positive energy caused by a slightly different location of this latter with respect to the Fe^{3+} center. The shape of this PDOS is not varied so that we may conclude that the geometry of this additional counter-ion is not fundamentally varied.

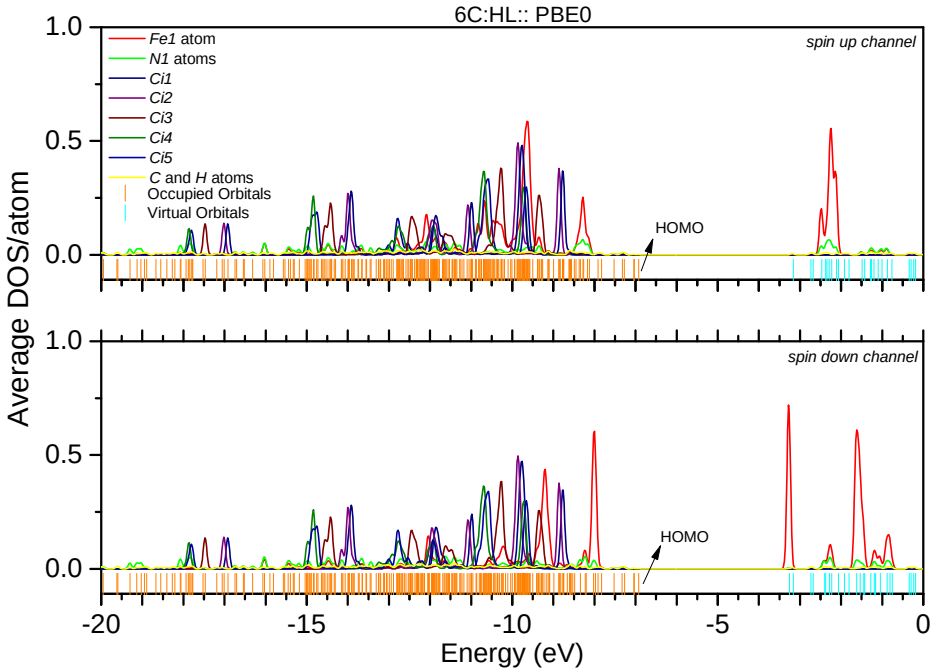

Figure 3.10: Average partial density of states (PDOS) calculated within the PBE0 approximation for the Half loaded 6C complex. It is built upon the data of the electronic levels using Hermite-Gaussian smearing method with a smearing parameter of $w_{1/2} = 0.1$ eV. We have added the partial DOS corresponding to Fe's atoms, the sum of carbon and hydrogen contributions in yellow and the N's regions contributions from the *dmbpy* in green. The occupied orbital electronic levels are reported in orange color at the bottom.

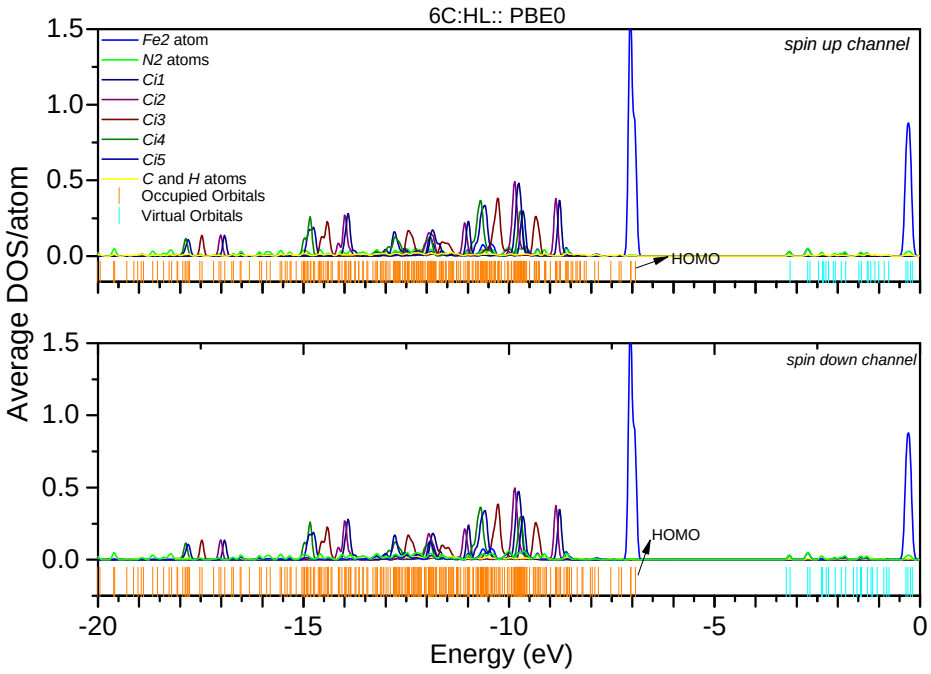

Figure 3.11: Average partial density of states (PDOS) calculated within the PBE0 approximation for the Half loaded 6C complex. It is built upon the data of the electronic levels using Hermite-Gaussian smearing method with a smearing parameter of $w_{1/2} = 0.1$ eV. We have added the partial DOS corresponding to Fe's atoms, the sum of carbon and hydrogen contributions in yellow and the N's regions contributions from the *dmbpy* in green. The occupied orbital electronic levels are reported in orange color at the bottom.

3.5.2 Results within the PBE approximation

Let's now turn to the PBE approximation. For the neutral bi-nuclear compound both the sites obey the expected ligand field scheme with the appearance of neatly separated e_g and t_{2g} peaks, characteristic of the octahedral environment (Figure 3.12). These PDOS are very close to the ones we have presented in the mono-nuclear section and confirm that for this length of alkyl chain, both patterns are found to be totally independent. Figure 3.13 and 3.14 shows the PDOS for the fully-loaded system. The most striking point is the extreme similarity between both the neutral and fully loaded states. Which is in agreement with our intuitive understanding of the electronic structure of these systems when a single counter-ion is brought at the vicinity of each pattern. The only difference comes from the iron peaks: only one over both is occupied due to the change of the degree of oxidation, but this is the expected signature of the oxidization and in total agreement with our ligand field picture. As emptied by an amount of one electron, the occupied Fe peak is shifted towards the negative energy bringing some stabilization

energy. Let us also mention that the PDOS of the counter-ions are all found the same (between each other for one given state (Neutral or Full loaded) but also between the Neutral and Full loaded states, showing a more symmetric distribution of the counter-ions around the monomer patterns but also the pure electrostatic character of their interaction with the monomer patterns. Let us repeat that all these observations are in agreement with our intuitive knowledge of these systems. It was far from being the case within the PBE0 approximation. We argue that this present PBE approximation is a valuable advance in the description of the properties of our bi-nuclear compounds.

No PDOS will be presented for half-loaded systems. As stated earlier, Half loaded the system with PBE functional poses electronic convergence problems, despite our attempts to use different algorithms such as quadrature curvature technique as implemented in Gaussian09 code. We believe that the reason for this failure lies in the inability of the PBE approximation to locate the exact oxidation state in the bi-nuclear complex. This has to be related to the difficulties met by the Experimental group to measure the properties of half loaded system with Cyclic voltammetry (CV) because of the system tunnels quickly. As discussed in previous section hybrid functional (PBE0) distorts the ligand field and states are dispersed. Whereas, PBE functional maintains the ligand field picture but fails to describe the correct spin state for half loaded system. On the other hand, neutral and full loaded system is, to our opinion, properly described.

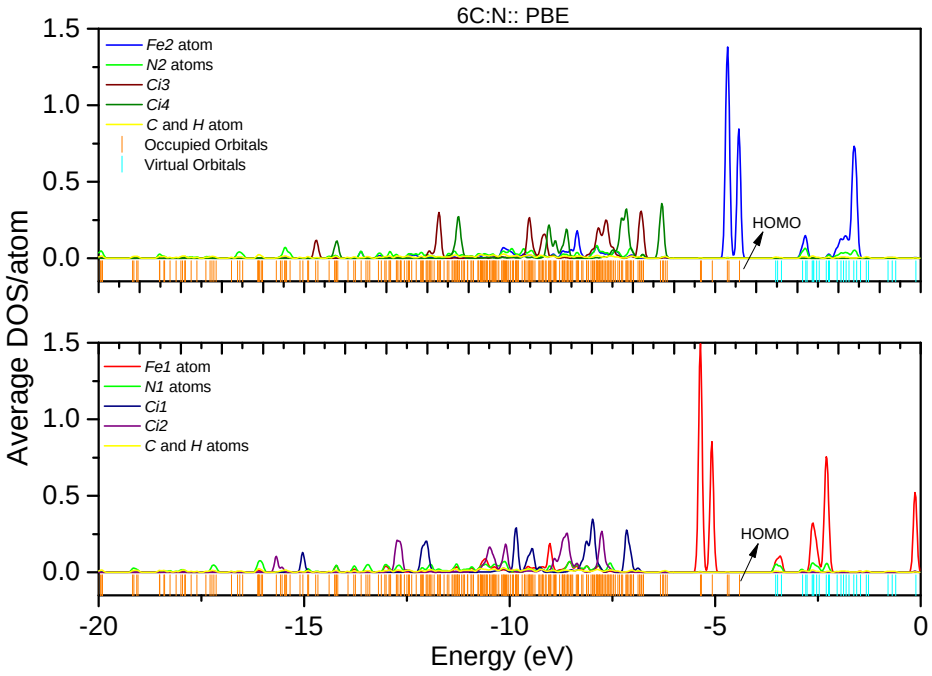

Figure 3.12: Idem as Figure 3.8 but at the PBE/def2SVP level of theory.

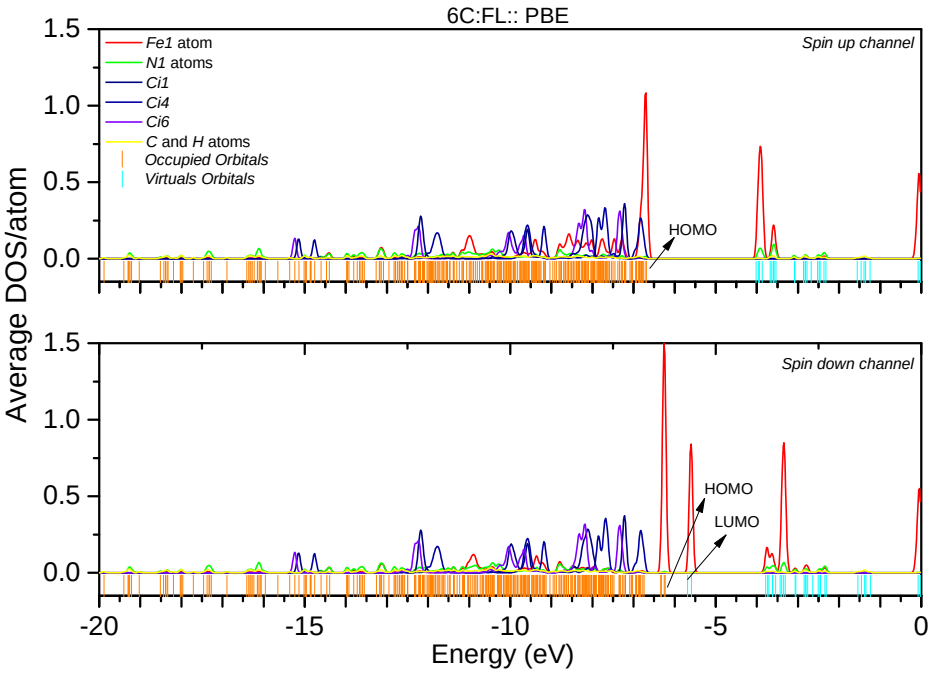

Figure 3.13: Idem as Figure 3.9 but at the PBE/def2SVP level of theory.

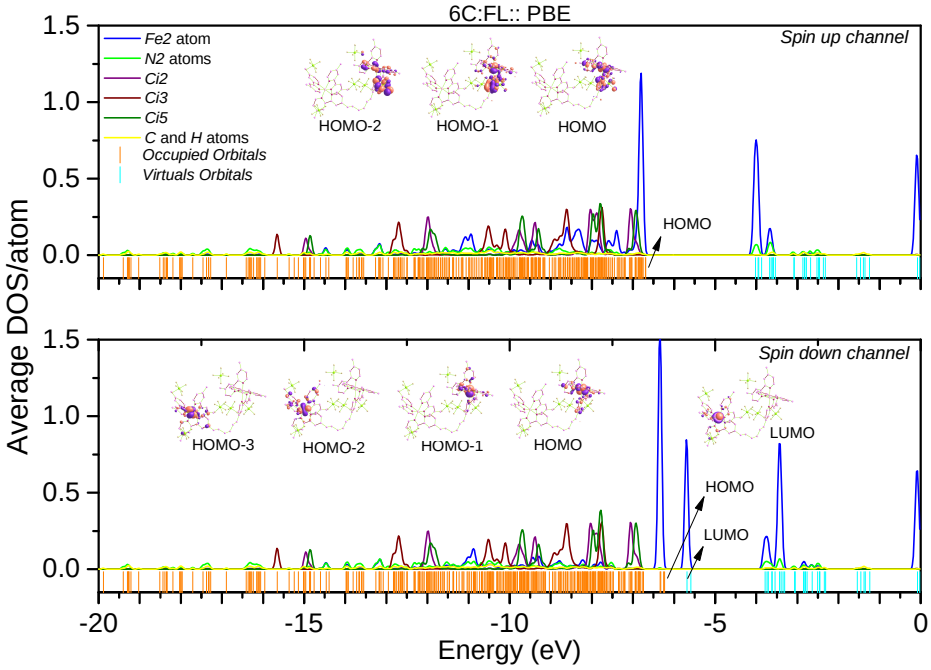

Figure 3.14: Idem as Figure 3.9 but at the PBE/def2SVP level of theory.

3.6 Influence of alkyl chain length

In this section, we are presenting the influence of the length of the alkyl chain (by making a calculation with 4 and 2 carbons chains) on the electronic structure of the compounds considered at first in the neutral state and then in the fully-loaded state. Regarding the half-loaded state, the PDOS were found to be very similar to the case of the 6C chains. Given that they are only accessible within the PBE0 approximation which consider as the poorest representation for our systems and that DFT methods we are using are found quite inadequate to model the tunneling of the electronic hole between both sites, we will not comment these results. They just do not bring new additional valuable information. We, however, provide them in Appendix C. We will actually be very brief in this section since our compound which uses the length of the alkyl chain as a tuning parameter to change the properties of the bi-molecular compounds didn't really meet our hopes. Very minor changes are observed on the density of states

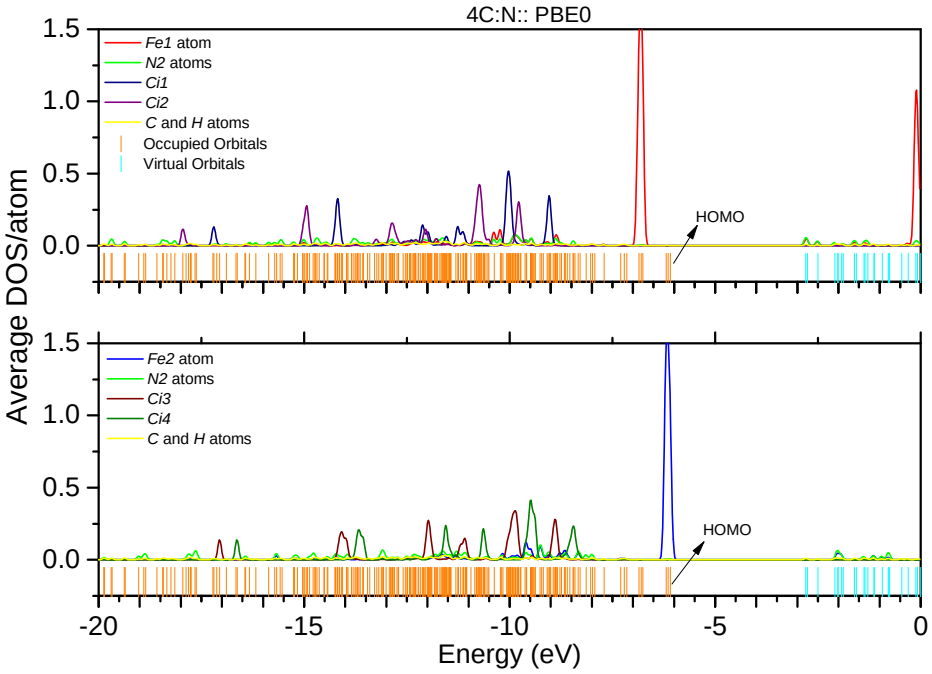

Figure 3.15: Idem as Figure 3.8 but for 4C chain.

For the neutral state no major differences are observed for the 4 and 2 carbons chains with respect to the 6 carbons chain. Within the PBE0 approximation (Figure 3.15 and 3.16), the very isolated character of the Fe site (already discussed in the case of the 6 carbons chain) is conserved when the length of the chain is shrinked, so that the behavior of the three compounds (6C, 4C, and 2C) is found to be the exactly same. The

same observation is made within the PBE approximation (Figure 3.17 and 3.18), since a behavior piloted by the ligand field scheme is found to be independent of the length of the alkyl chain. This is no wonder since the *d*-band of the iron hybridizes very weakly with the Nitrogen atoms, even within the framework of the ligand field scheme, so that the oxidation state of the Fe weakly depends on their environment.

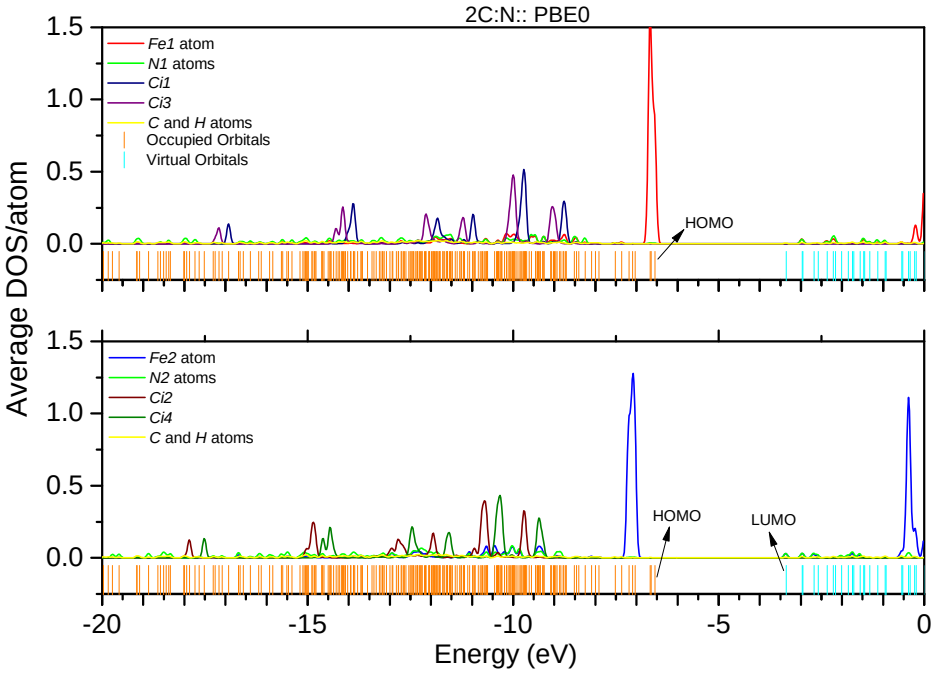

Figure 3.16: Idem as Figure 3.8 but for 2C chain.

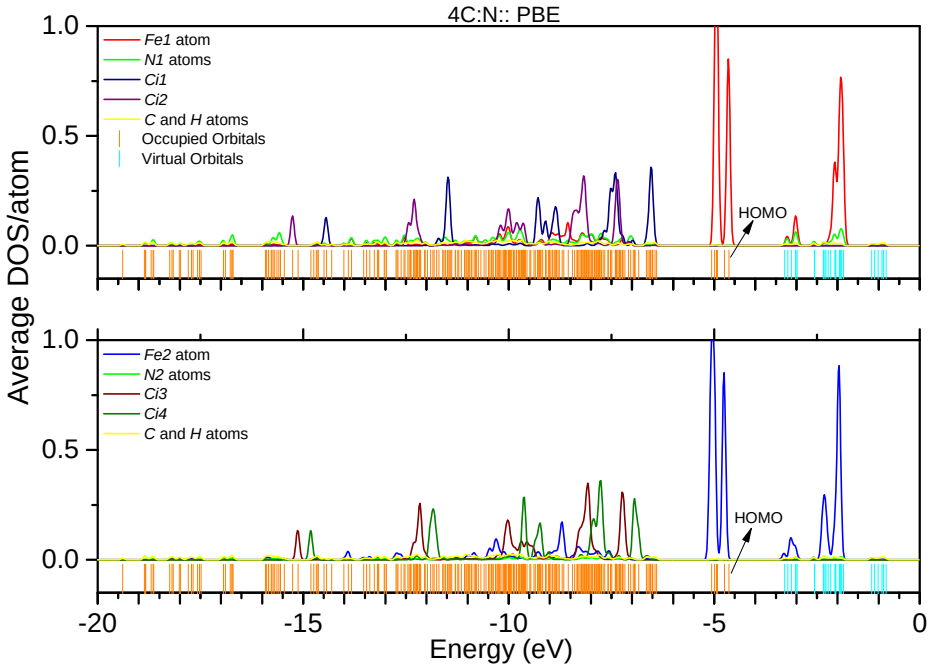

Figure 3.17: Idem as Figure 3.8 but for 4C chain and at PBE/def2SVP level of theory.

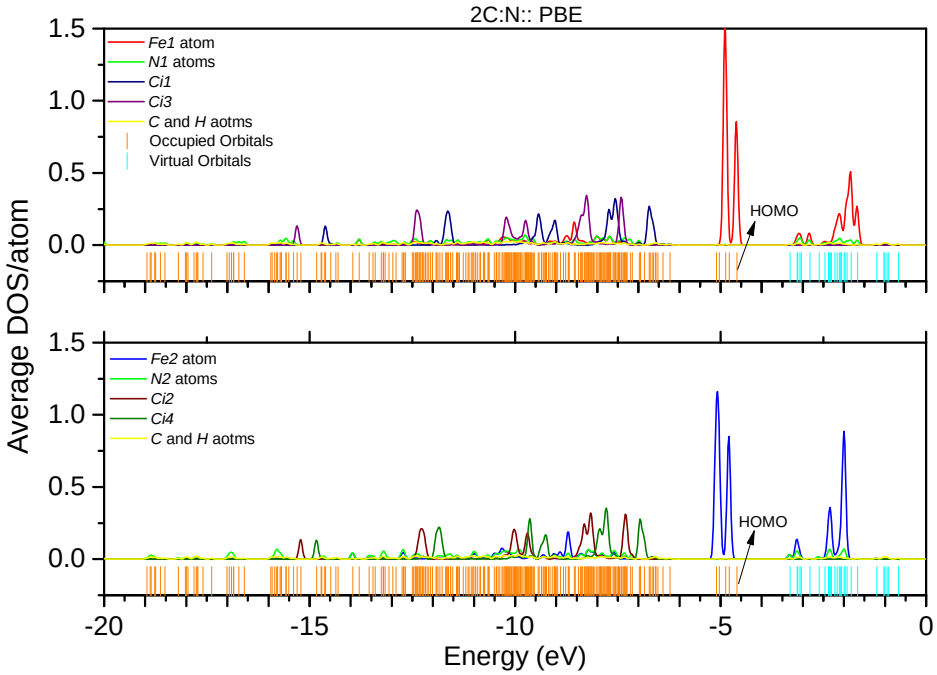

Figure 3.18: Idem as Figure 3.8 but for 2C chain and at the PBE/def2SVP level of theory.

The case of fully-loaded system is a little bit more interesting and makes appear

some slight differences according to the length of the alkyl chain which will be clearly magnified on the calculated voltage as discussed in the next section.

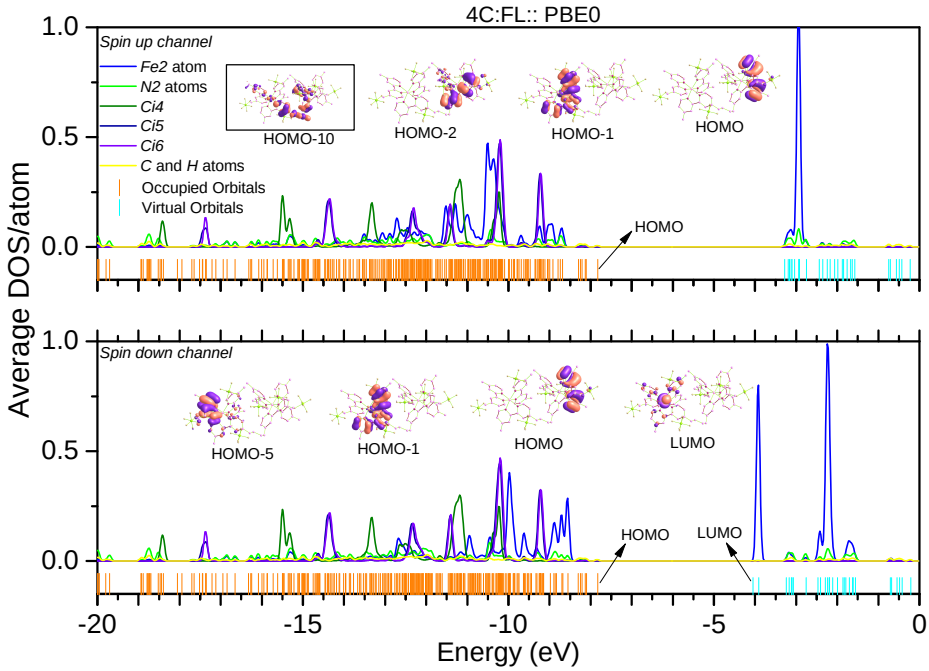

Figure 3.19: Idem as Figure 3.9 but for 4C chain.

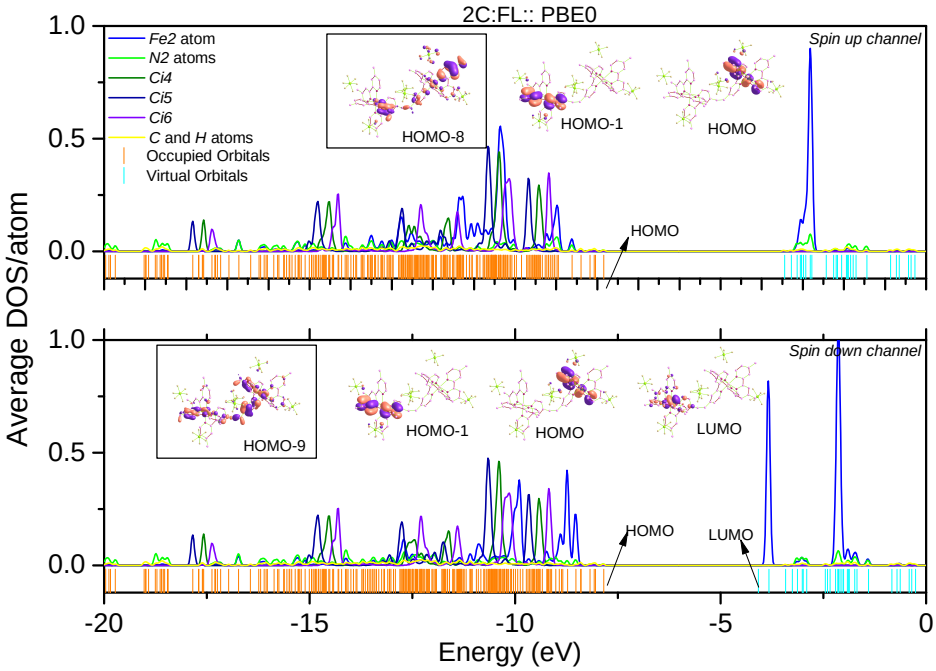

Figure 3.20: Idem as Figure 3.9 but for 2C chain.

3.7 Calculation of the bi-nuclear voltage

Making use of Equation 3.4 and 3.5, we have calculated the voltages of the Fe and Ru dimers for the three alkyl chains within the PBE and PBE0 approximations. They are represented in Figure 3.21. Given that the half-loaded voltage (spotted by the HL tag) calculated within the PBE approximation is not accessible due to the inability of this approximation to model the tunneling effect of the charge (see section 3.3.2), a single point, which actually corresponds to the fully-loaded state, is provided within this approximation. For clarity, we have also reported their numerical values in Table 3.9. The most striking point, appearing in Figure 3.21, is the extreme dependence of the voltage calculated within the PBE0 approximation as a function of both the oxidation state (HL/FL) and the length of the alkyl chain. Although a converged value of the energy of the HL state is obtained, such a dependence is unphysical and in full disagreement with the experiments. The experimental values provided in chapter 1 actually reveal that a variation of about 0.1 V is observed. This result confirms our suspicions regarding the possibility of the PBE0 approximation to model the physico-chemistry of our compounds. If this approximation has been viewed in independent studies as an appropriate patch to recover elementary properties of the complex without counter-ions, it fails to represent our compounds in functional conditions. Such a variation is quite probably the consequence of the excessive delocalization effects introduced by this specific approximation which were found to propagate over the whole alkyl chain. This is no wonder that the energy (and consequently the voltage) depends so much on the length of the alkyl chain given that unphysical molecular orbitals involving the carbon atoms of the chain are introduced.

Table 3.9: Calculated voltages of the Fe and Ru compound for the three $-(CH_2)_n-$ alkyl chains and $Ci = PF_6^-$. We have reported voltages for both fully loaded and half loaded when available (see text) for exchange and correlation potentials. They are given in V.

Fe	PBE0		PBE	
alkyl	V_{HL}	V_{FL}	V_{HL}	V_{FL}
$-(CH_2)_2-$	3.00	3.76	-	4.16
$-(CH_2)_4-$	3.91	4.09	-	4.10
$-(CH_2)_6-$	3.89	3.96	-	4.15

Ru	PBE0		PBE	
alkyl	V_{HL}	V_{FL}	V_{HL}	V_{FL}
$-(CH_2)_2-$	4.24	4.36	-	4.10
$-(CH_2)_4-$	4.00	4.14	-	4.34
$-(CH_2)_6-$	4.81	4.35	-	4.30

To the opposite, the PBE approximation favoring a ligand field picture with more localized d-states does not develop such long-range molecular orbitals, allowing a very

weak dependence of the voltage with respect to the alkyl chain (see Table 3.9). Moreover, this latest approximation provides an excellent absolute value for the voltages in full agreement with the experiments and the value obtained for the monomer (dashed line in Figure 3.21). The same behavior is obtained for the *Ru* compounds.

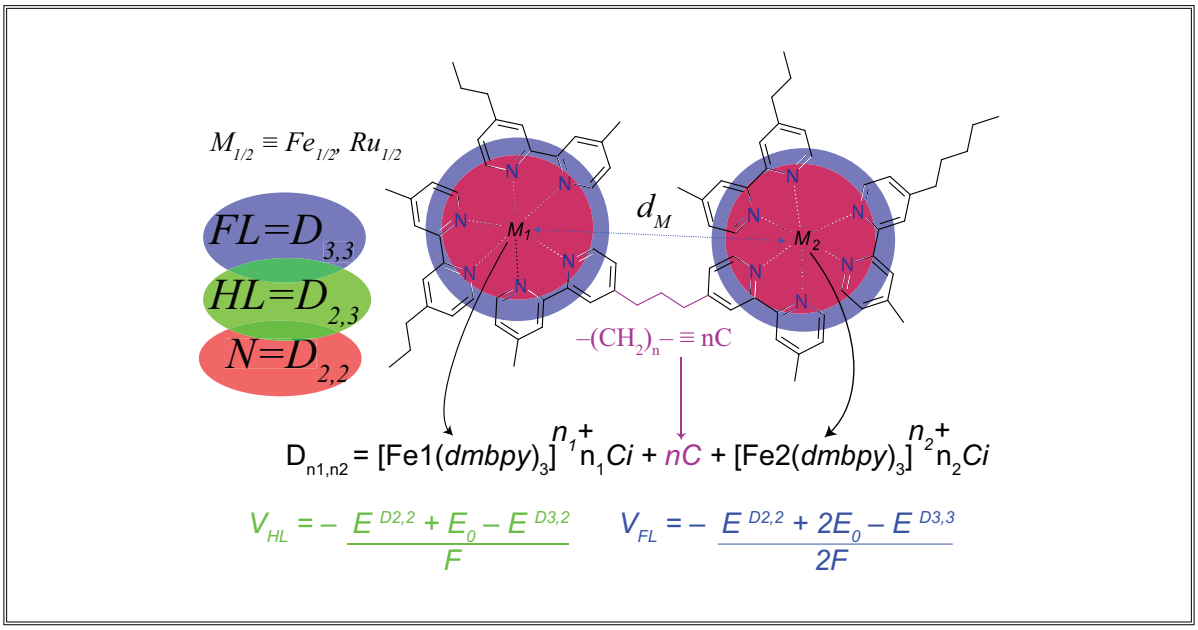

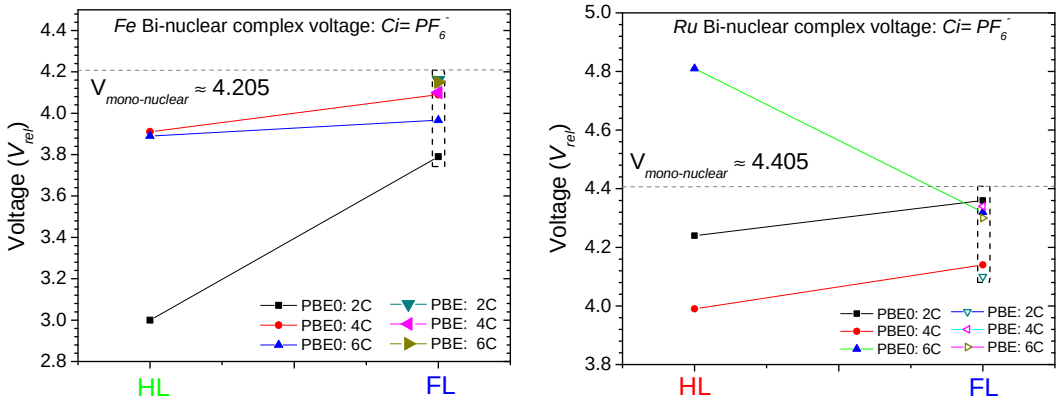

(a) (b)

Figure 3.21: Bi-nuclear relative voltage computed for (a) *Fe* and (b) *Ru* Half loaded and Full loaded complex at the PBE0/PBE//Def2SVP level of theory in the PF_6^- electrolytic medium. The dashed line shows the mono-nuclear voltage computed in the previous chapter.

At this stage, given our definitive choice in favor of the PBE approximation, few words have to be said about the inability of this approximation to converge any calculations devoted to the half-loaded state within acceptable accuracy. We do not think that this problem sheds suspicions on the ability of the PBE approximation to model in a correct manner our systems. As we already suggested in section 3.3.2, in the half-loaded state, a specific center cannot be clearly identified as the oxidized one: an electron will perpetually tunnel from one center to the other, rendering both sites equivalent. Given its trend to localize, the PBE approximation will select one site and freeze the electronic hole on that specific site. A better description for the half-loaded state is to consider that, when the electronic hole lies on one site, this pattern behaves as it does in the mono-nuclear case (the other mono-nuclear site is unseen) and symmetrically when it jumps on the other site. In other words, the voltage of the half-loaded state is one of the mono-nuclear compound calculated in chapter 2 and this in close agreement with the experimental trend.

3.8 Conclusion

From the above discussion, we can conclude that PBE functional provides a better description of the properties of the bi-nuclear systems in working conditions. On average PBE functional produces voltages in close agreement with experiments whatever the length of the alkyl chain maybe. The PBE0 approximation was found to induce unphysical voltage changes for full and half loaded systems. As discussed earlier hybrid functional was designed to localize states. However, we observe that it delocalizes the states over the chain. Thus, PBE0 functional relaxes the structure with all bond lengths whereas, within the PBE approximation, each mono-nuclear pattern is relaxed independently. The alkyl chain does not excessively propagate the hybridization effects, leaving the localization of d-states of the Fe intact. This convinces us that PBE functional is the best approximation we have for this system.

■

Chapter 4

A model for high-dimensional polymers and development of the potential

In the second part of this thesis, we will focus on the development of the force field parameters for the modeling of the active Iron sites in the mono-nuclear complex. In this Chapter, our strategy consisted in constructing the potential for this smallest system and in refining it, making use of DFT calculations. We validate the potential by comparing the geometry obtained during the equilibration phase of the compounds to the one obtained from DFT calculations. Then we move on to calculate the dynamic properties.

4.1 Modeling strategy from low to high dimensional

Our approach for constructing the high dimensional polymer consists in making a linear chain of our units, making use of a linker between them. The linker, in our study case, is alkyl chain of length n, $-(CH_2)_n-$. We have chosen to terminate the chain by a mono-nuclear unit: one mono-nuclear unit is the head and the other is the tail of the chain. At first, all the carbon sites of the *bpy* molecules that can be plugged (six sites for each monomer) are connected to a methyl fragment. Then, two methyl groups are removed for each mono-nuclear (excepted for the head and tail patterns for which a single one is removed) and replaced by an alkyl chain to link the units between each other. In this way, a linear polymer is constructed. In Figure 4.1, a simple model for the n-nuclear linear chain is shown. Here, the main unit is the mono-nuclear unit which repeats its pattern in three different axes with boundary capped by the methylated complex. In

Chapter 2, we studied the complex in three perturbation counter-ions field and did not observe significant changes in geometry and voltages. Here, we have opted to model the complex with the $TFSI^-$ counter-ions and use the default generalized Amber force field (GAFF) atom types and parameters.

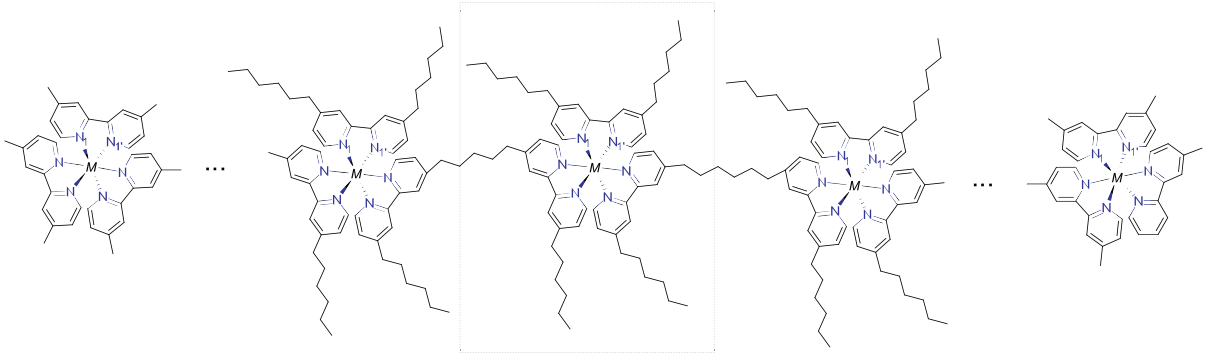

Figure 4.1: Schematic representation of modeling the high dimensional chain with capping on both terminals.

4.2 Parameterization of the Model

In this section, we will describe the procedure for constructing the potential for the mono-nuclear complex. Our complex consists of non-standard residues and we have to build the structure by deconstructing the complex obtained from DFT and then combining each residue to get a whole complex. The residues in the complex will allow us to identify what parameters are already in the database. Most of the parameters for organic molecules have been developed in the context of biological systems (*i.e.*, proteins and nuclear acids). For some missing or inaccurate parameters, they are obtained using experimental or from ab-initio theory. Generally, for transition metal systems, Amber does not provide parameters because the system under study are highly specific and vary according to the ligand interaction. The form of the potential used by Amber (version 18) code [132] reads (neglecting implicit solvent or polarization terms),

$$V(r_N) = \sum_{bonds} k_b(l-l_0)^2 + \sum_{angles} k_a(\theta-\theta_0)^2 + \left(\sum_{i}^{n_{dihedrals}} \sum_{n}^{n_{i,max}} \frac{1}{2} V_{i,n}[1+\cos(n\omega_i - \gamma_{i,n})]\right) + \sum_{j=1}^{N-1}\sum_{i=j+1}^{N}\left[\varepsilon_{ij}\left(\frac{A_{ij}}{R_{ij}^{12}} - \frac{B_{ij}}{R_{ij}^{6}}\right) + \frac{q_i q_j}{R_{ij}}\right] \tag{4.1}$$

The above potential comprises of five contributions. The bonded part models the

interaction between the ion and its surrounding residues via the bond, angle, and torsion. Because of the harmonic approximation used in the bonded model, it does not simulate the processes involving chemical bond formation and dissociation. On the other hand, the non-bonded part puts the charge on the metal ion and use the Coulombic and vdW terms to represent the intermolecular interactions. This simplification can result in a notable underestimation for modeling systems with strong covalent bonds [133]. Even though more accurate models exist such as polarizable force fields but they are highly system specific and are not transferable. The 12-6 Lennard-Jones model is used widely due to its simplistic mathematical form, computational efficiency, and excellent transferability characteristics. We will adopt this form of potential and develop the potential for the polymer chain made of a repetition of the following mono-nuclear units and we will try to use at maximum the parameters already developed if compatible with our system. If some interactions are missing or poorly represented, we will modify with DFT calculations.

4.2.1 Alkyl chain: Linker $(-L-)$

From the DFT results, we observe the alkyl chain of length six was optimum to represent the independent sites inside the bi-nuclear compound. Here, we parameterize the chain by using the default values in Amber18 GAFF database. In Figure 4.2, GAFF force field atom types are shown and in Table 4.1 geometry parameters are compared with respect to the DFT ones. We obtained a good adequacy between the bond lengths calculated using the GAFF parameters and the DFT calculations. The angle θ_{ijk}, displays a slight discrepancy by an amount three degrees. The parameters holds for any chain of length n.

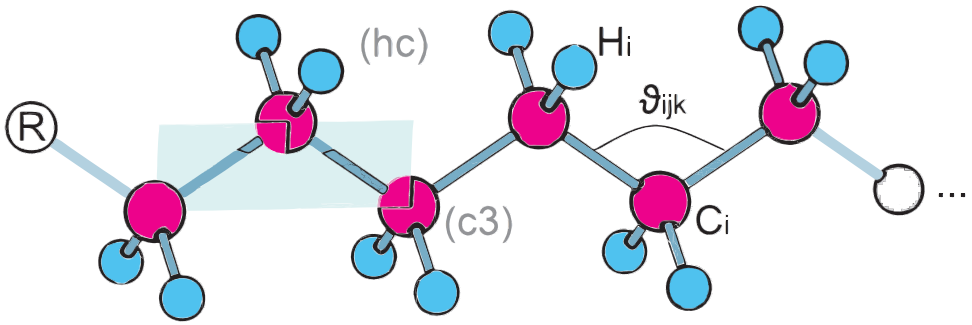

Figure 4.2: Alkyl chain of length $n = 6$. Atom types are shown in light grey color.

Table 4.1: Comparison of parameters obtained at DFT:PBE/Def2SVP level of theory with those already in GAFF database. The naming convention used is GAFF Atomic Types (GAT) and GAFF Parameters Database (GPD).

	GAT	GPD	DFT
$C_i - C_j$ (Å)	c3-c3	1.538	1.530
$C_i - H_j$ (Å)	c3-hc	1.097	1.112
θ_{ijk} (ř)		111.510	114.1
φ_{ijkl} (ř)		180	180

4.2.2 Dimethyl-bipyridine

For *dmbpy*, the atoms types and parameters were used from GAFF database. In Figure 4.3, atom numbering and appropriate atom types names corresponding to neighboring interaction are shown. We tested the default parameters from the Amber database. In Table 4.2, parameters of a geometry of the *dmbpy* are shown in the gas phase and compared. As it can be seen, the GAFF parameters are in agreement with the DFT and experimental. We have also added our calculations using the other set of parameters (param10) that is commonly used. Both sets of parameters lead to similar results, but for some specific bonds. Typically, for cp-cp, it varies by 0.087 Å and for cp-nb by 0.02 Å.

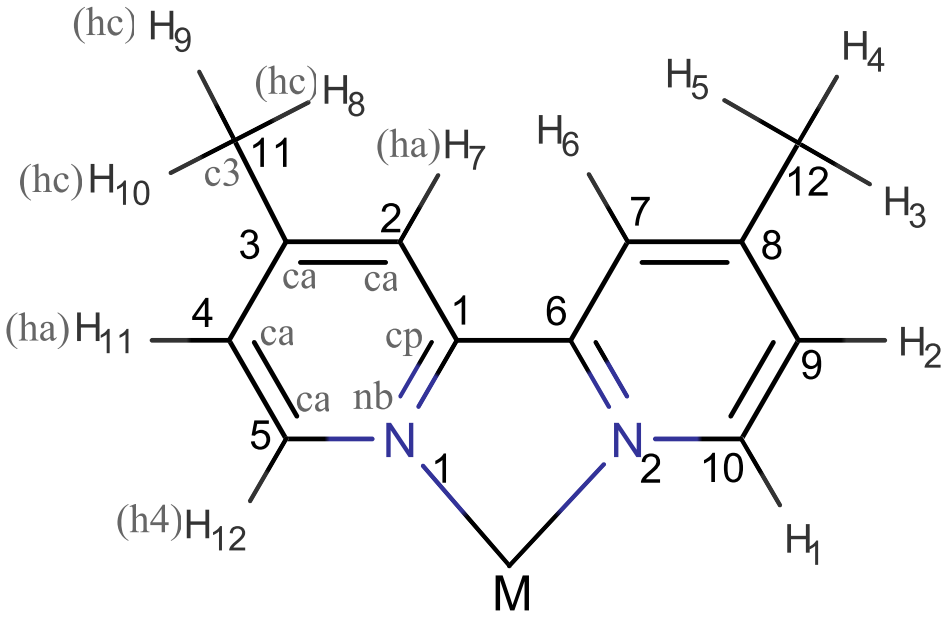

Figure 4.3: Gaff atom types are shown in grey color for each of the *dmbpy* molecules.

These latter remains small and comparable to the errors observed between the DFT calculations and the experiments (0.01 Å). We have selected the GAFF parameters which provides values in better agreement with the DFT calculations.

Table 4.2: Comparison of parameters obtained at DFT:PBE/Def2SVP level of theory with those already in Amber database. The naming convention used is GAFF Atomic Types (GAT) and GAFF Parameters Database (GPD). parm10 is another database for selecting parameters.

bonds (Å)	GAT	amber/parm10	GPD	Exp [134]	DFT
C1-C2	cp-ca	1.398	1.406	1.394	1.414
C2-C3	ca-ca	1.398	1.398	1.385	1.406
C3-C4	ca-ca	1.398	1.398	1.383	1.409
C4-C5	ca-ca	1.398	1.398	1.384	1.403
C5-N1	ca-nb	1.352	1.339	1.341	1.339
C1-N1	cp-nb	1.352	1.339	1.346	1.348
C1-C6	cp-cp	1.398	1.485	1.490	1.499
C3-C11	ca-c3		1.516		
C11-H{8,9,10}	c3-hc		1.097		
C{2,4}-H{7,11}	ca-h4		1.089		

4.3 Vibrational analysis

To obtain Metal-Ligand parameters, we need to perform the calculation of the vibrational frequencies of our compounds, these latter being requisite into the fitting procedure of the parameters of the Metal-ligands potential. Experimentally, vibrational spectroscopy can directly help us to gain information about the molecular structure by identifying the adsorption of ad-atoms on a surface, the strength of intra-molecular bonds and particular geometry associated with a conformation. Theoretically, we calculate these vibrational modes to help us to understand the nature of the compounds and modes associated when external adsorbate are added [135–138]. These modes can be calculated with most of the Computational chemistry codes along with Infrared (IR) intensities. They all rely on a harmonic approximation for which the potential energy surface is developed into a Taylor series and truncated up to the second order around the minimum. The coordinates are then transformed from Cartesian to internal following the convention of [135]. These vibrational frequencies can be calculated analytically. We start with the Hessian matrix $f_{ij}^{cartesian}$, which holds the second partial derivatives of the potential V

with respect to the displacement of the atoms in cartesian coordinates,

$$f_{ij}^{cartesian} = \left(\frac{\partial^2 V}{\partial \eta_i \partial \eta_j}\right)_0 \tag{4.2}$$

Where $f_{ij}^{cartesian}$ is a 3N $\times$ 3N matrix (N is the number of atoms), and η_1, η_2, $\eta_3 \cdots \eta_{3N}$ are the displacement of atoms in Δx_1, Δy_1, Δz_1, $\cdots$, Δz_N cartesian coordinates. The $()_0$ refers to the equilibrium positions of the atoms, that is when first derivatives is zero. Than we convert these force constants to mass weighted cartesian coordinates (MWC),

$$f_{ij}^{MWC} = \frac{1}{\sqrt{m_i m_j}}\left(\frac{\partial^2 V}{\partial q_i \partial q_j}\right)_0 \tag{4.3}$$

where $q_1 = \sqrt{m_1}\eta_1 = \sqrt{m_1}\Delta x_1$, $q_2 = \sqrt{m_2}\eta_2 = \sqrt{m_2}\Delta x_2$ and so on, are the mass weighted cartesian coordinates. Next, the center of mass coordinates is shifted to the origin by the center of mass ($\boldsymbol{R}_{COM}$) equation, to filter out the translational and rotational modes,

$$\boldsymbol{R}_{COM} = \frac{\sum_\alpha m_\alpha \boldsymbol{r}_\alpha}{\sum_\alpha m_\alpha} \tag{4.4}$$

with

$$\boldsymbol{r}_{COM\alpha} = \boldsymbol{r}_\alpha - \boldsymbol{R}_{COM} \tag{4.5}$$

The sum, α is run over all the atoms. Next, the moments of inertia (the diagonal elements) and the products of inertia (off diagonal elements) of the moment of inertia tensor (I) are calculated.

$$\boldsymbol{I} = \begin{pmatrix} \boldsymbol{I_{xx}} & \boldsymbol{I_{xy}} & \boldsymbol{I_{xz}} \\ \boldsymbol{I_{yx}} & \boldsymbol{I_{yy}} & \boldsymbol{I_{yz}} \\ \boldsymbol{I_{zx}} & \boldsymbol{I_{zy}} & \boldsymbol{I_{zz}} \end{pmatrix} = \begin{pmatrix} \sum_\alpha m_\alpha (y_\alpha^2 + z_\alpha^2) & -\sum_\alpha m_\alpha (x_\alpha y_\alpha) & -\sum_\alpha m_\alpha (x_\alpha z_\alpha) \\ -\sum_\alpha m_\alpha (y_\alpha x_\alpha) & \sum_\alpha m_\alpha (x + z_\alpha^2) & -\sum_\alpha m_\alpha (y_\alpha z_\alpha) \\ -\sum_\alpha m_\alpha (z_\alpha x_\alpha) & -\sum_\alpha m_\alpha (z_\alpha y_\alpha) & \sum_\alpha m_\alpha (x_\alpha^2 + y_\alpha^2) \end{pmatrix} \tag{4.6}$$

This symmetric matrix is diagonalized, yielding the principal moments (the eigenvalues $\boldsymbol{I'}$) and a 3×3 matrix ($\boldsymbol{X}$), made up of the normalized eigenvectors of $\boldsymbol{I}$. The eigenvectors of the moment of inertia tensor are used to generate the vectors corresponding to translation and infinitesimal rotation of the molecule $\boldsymbol{I'} = \boldsymbol{X}^\dagger \boldsymbol{I} \boldsymbol{X}$. Once these vectors are known, the rest of the normal modes are vibrations, so we can distinguish low frequency vibrational modes from rotational and translational modes.

Generating coordinates in the rotating and translating frame

From the Eckart conditions the three vectors ($\boldsymbol{D_1}$, $\boldsymbol{D_2}$, $\boldsymbol{D_3}$) of length 3N corresponding to translation in cartesian coordinates is generated by $\sqrt{m_i}$ times the corresponding coordinate axis. Vectors corresponding to rotational motion of the atoms in cartesian coordinates is a little bit more complicated to generate [135]. The normalized vectors for these are defined this way,

$$\begin{aligned} D_{4j,i} &= ((P_y)_i X_{j,3} - (P_z)_i X_{j,2})/\sqrt{m_i} \\ D_{5j,i} &= ((P_z)_i X_{j,1} - (P_x)_i X_{j,3})/\sqrt{m_i} \\ D_{6j,i} &= ((P_x)_i X_{j,2} - (P_y)_i X_{j,1})/\sqrt{m_i} \end{aligned} \tag{4.7}$$

where $j = x, y, z$; i is over all atoms and P is the dot product of $\mathbf{R}$ (the coordinates of the atoms with respect to the center of mass) and the corresponding row of $\mathbf{X}$ (the matrix used to diagonalize the moment of inertia tensor $\boldsymbol{I}$). From the Schmidt orthogonalization we generate $N_{vib} = 3\text{N} - 6$ (or $3\text{N} - 5$) remaining vectors, which are orthogonal to the five or six rotational and translational vectors. This result in a transformation matrix $\boldsymbol{D}$ from the mass weighted Cartesian coordinates $\boldsymbol{q}$ to internal coordinates $\boldsymbol{S} = \boldsymbol{Dq}$, where rotation and translation have been separated out. Now that we have coordinates in the rotating and translating frame, we transform the Hessian, $\boldsymbol{f}^{MWC}$ (still in mass weighted Cartesian coordinates), to these new internal coordinates (internal). Only the N_{vib} coordinates corresponding to internal coordinates will be diagonalized, although the full 3N coordinates are used to transform the Hessian. The transformation is:

$$\boldsymbol{f}^{internal} = \boldsymbol{D}^{\dagger} \boldsymbol{f}^{MWC} \boldsymbol{D} \tag{4.8}$$

The $N_{vib} \times N_{vib}$ submatrix of $\boldsymbol{f}^{internal}$, which represents the force constants internal coordinates, is diagonalized yielding N_{vib} eigenvalues $\lambda = 4\pi^2\nu^2$, and N_{vib} eigenvectors. We call the transformation matrix composed of the eigenvectors $\mathbf{L}$, then we have

$$\boldsymbol{L}^{\dagger} \boldsymbol{f}^{MWC} \boldsymbol{L} = \boldsymbol{\Lambda} \tag{4.9}$$

where $\boldsymbol{\Lambda}$ is the diagonal matrix with eigenvalues λ_i. Than these are converted to frequencies in units of reciprocal centimeters $\widetilde{\nu}_i = \sqrt{\lambda_i / 4\pi^2 c^2}$. Moreover, Infrared Intensities (IR) can be computed with the Equation 4.10. The details of this derivation is given in the paper [139]. Over here we will provide the general meaning of terms used to calculate the intensities (and it is beyond the scope of this thesis) that are observed

in the IR plots.

$$\frac{\partial^2 E_{SCF}}{\partial f \partial a} = 2\sum_{i}^{occ} h_{ii}^{fa} + 4\sum_{i}^{occ}\sum_{j}^{all} U_{ji}^{a} h_{ij}^{f} \tag{4.10}$$

where $h_{ii}^{fa} = \sum_{\mu\nu}^{AO} C_{\mu}^{i0} C_{\nu}^{i0} \left(\frac{\partial^2 h_{\mu\nu}}{\partial f \partial a}\right)$, E_{SCF} is the self-consistent field energy, f is the electric field, a is a nuclear coordinate, $h_{\mu\nu}$ is the one-electron atomic orbital integral, U^a is related to the derivative of the molecular orbital coefficients with respect to a by $\left(\frac{\partial C_{\mu}^{i}}{\partial a}\right) = \sum_{m}^{all} U_{mi}^{a} C_{\mu}^{m0}$. The term *all* in the above summations refers to all occupied and virtual molecular orbitals and *occ* refers to doubly occupied orbitals (closed-shell system) [137, 138]. Terms such as C_{μ}^{i0} refer to the coefficients of the atomic orbital m in the ith unperturbed molecular orbital. IR calculated intensities are generally less accurate than the computed frequencies, but the relative estimates of IR active are usually reliable to identify which peaks will be observed. The relevant details are given in the reference [135].

4.3.1 Vibrational analysis of a loaded and unloaded complex

As typical examples, in the Figure 4.4, 4.5, and 4.6, IR spectra for loaded systems are shown for PBE functionals. The rest of the IR spectra with and without counter-ions for both functionals are given in Appendix D. Our purpose is not to study the IR spectra; nevertheless, we present them here for the sake of completeness, since we lack experimental results to which we can compare. Thus, these calculations represent the first study to analyze the active modes during the loading process. Moreover, from this analysis, we are able to extract constants for metal-ligand interaction (as it will be described in the next section). Here, we are interested in the frequencies corresponding to the ground structure and the peaks corresponding to modes during the loading. The addition of counter-ions amplified the spectra with additional peaks in the regions 100-3500 cm^{-1}. At higher frequency, the modes correspond to C-H stretching bonds, whereas low frequency region belongs to the collective mode of the complex.

From the spectrum, we notice that no imaginary frequencies are found. Consequently, we have the opportunity to demonstrate that the structure that we obtained in Chapter 2 does not possess any saddle or transition state: the structure does not correspond to any metastable state and confirm that the optimized geometries we obtained in chapter 2 correspond to the ground state.

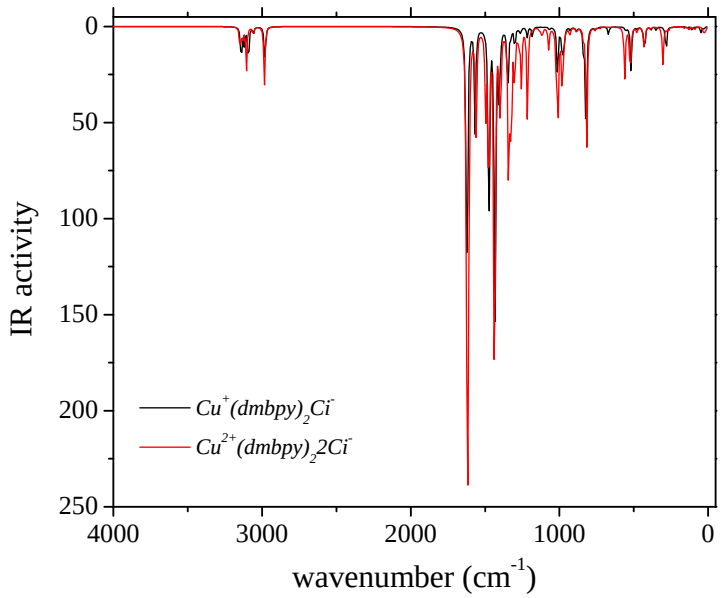

Figure 4.4: Computed IR spectra of Cu complex at PBE/Def2SVP level of theory. The red curves refer to the system when loaded with counter-ions. Black curve is taken as neutral reference.

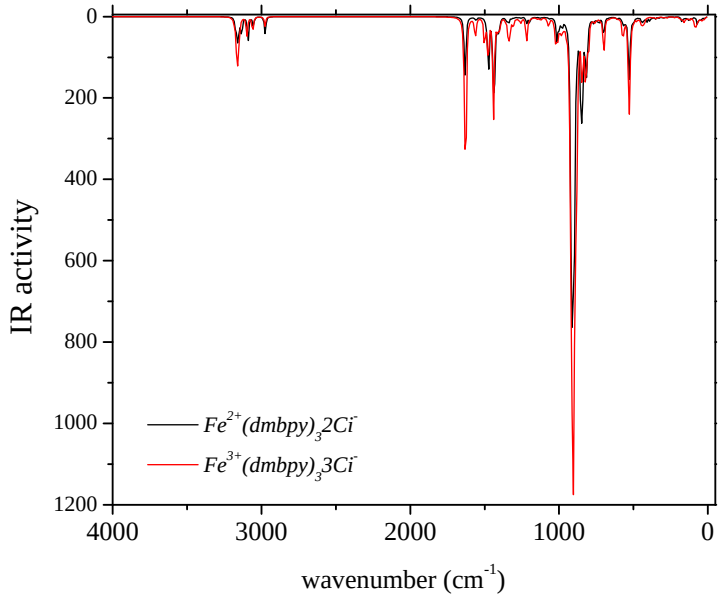

Figure 4.5: Computed IR spectra of Fe complex at PBE/Def2SVP level of theory. The red curves refer to the system when loaded with counter-ions. Black curve is taken as neutral reference.

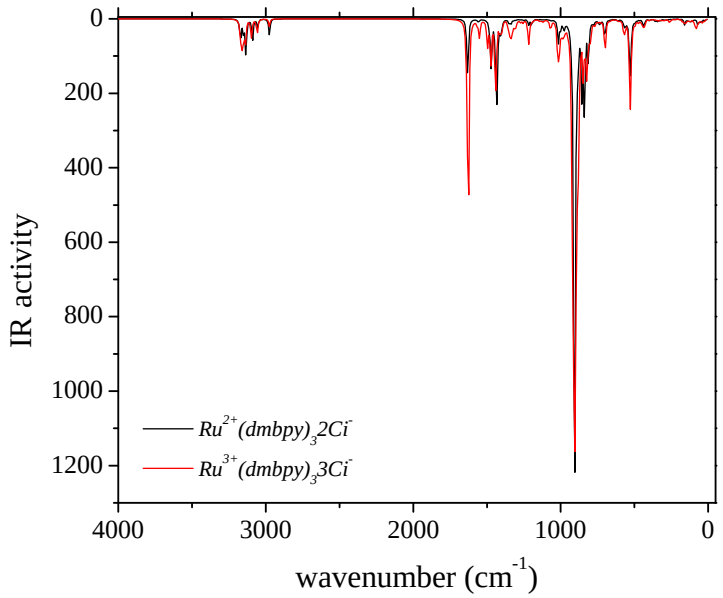

Figure 4.6: Computed IR spectra of Ru complex at PBE/Def2SVP level of theory. The red curves refer to the system when loaded with counter-ions. Black curve is taken as neutral reference.

4.4 Derivation of Fe potential

After an extensive search, we concluded that there are no parameters related to Fe in either gaff or Amber database. Since no parameters exist for this complex, we have to be careful in considering the technical details and integrate all we know on our system from our DFT calculations, such as spin state ordering, ligands types, counter-ions, and geometrical parameters [140]. Moreover, the constraint is that all these essential details have to be captured by a simple potential function. At the same time, we aim to develop the potential for Fe complex such that it is compatible with the Amber potential. The potential energy function used by Amber is given in Eq. 4.1. As it can be seen, these five terms essentially capture the details that DFT could provide us. This study has to be considered as the first one in developing the potential for battery applications. We have chosen to work on the Fe system. Our approach could be easily transferred to the Ru and Cu compounds.

To obtain the force constants of bond stretching and angle bending, we use the method proposed by Seminario *et al.*, [141]. Here, we will parameterize the first two terms of the potential whereas the torsion term derived from this method is not compatible with the Fourier form of the torsion energy term in the current AMBER force field. Therefore, we did not extract the parameters for Fe complex which is coordinated

to six Nitrogen atoms. We assume that ignoring this additional contribution will not pose any problem in describing the dynamics of the system: if we look carefully at the Fe-coordination structure obtained from DFT, we can see that the structure is quite rigid. There are insignificant torsional degrees of freedom so that we can finally assume that the bonded model captures the overall rigidity of this system. However, this kind of approximation cannot be retained if there is some significant torsion as in the case of the Cu complex. To derive the force constants of bond stretching and angle bending, we have to consider the Hessian matrix for a system of N atoms, namely

$$[\delta \boldsymbol{F}_{3N}] = -[k] \times [\delta \boldsymbol{x}_{3N}] \tag{4.11}$$

Where $[k] = k_{ij} = \frac{\partial^2 E}{\partial x_i \partial x_j}$ is the Hessian of tensor rank 2 and dimension $3N \times 3N$, $\delta \boldsymbol{x}_{3N}$ the displacements vector in cartesian coordinates, and $\delta \boldsymbol{F}_{3N}$ resulting reaction forces. From the Seminario's method, the bond-stretching force constant of bond A-B in a system can be derived from the Hessian matrix as a 3×3 matrix, i.e. k_{AB}

$$\delta \boldsymbol{F}_A = -[k_{AB}] \times [\delta \boldsymbol{x}_B] \tag{4.12}$$

or

$$\begin{bmatrix} \delta \boldsymbol{F}_{Ax} \\ \delta \boldsymbol{F}_{Ay} \\ \delta \boldsymbol{F}_{Az} \end{bmatrix} = - \begin{bmatrix} \frac{\partial^2 E}{\partial x_A \partial x_B} & \frac{\partial^2 E}{\partial x_A \partial y_B} & \frac{\partial^2 E}{\partial x_A \partial z_B} \\ \frac{\partial^2 E}{\partial y_A \partial x_B} & \frac{\partial^2 E}{\partial y_A \partial y_B} & \frac{\partial^2 E}{\partial y_A \partial z_B} \\ \frac{\partial^2 E}{\partial z_A \partial x_B} & \frac{\partial^2 E}{\partial z_A \partial y_B} & \frac{\partial^2 E}{\partial z_A \partial z_B} \end{bmatrix} \times \begin{bmatrix} \delta \boldsymbol{x}_B \\ \delta \boldsymbol{y}_B \\ \delta \boldsymbol{z}_B \end{bmatrix} \tag{4.13}$$

Usually, Hessian matrix in Cartesian coordinates is extracted from the frequency analysis. Eq. 4.13, in three component form shows the force experienced by an atom A due to the displacement of the atom B. Diagonalization of the k_{AB} matrix gives the eigenvalues λ_i^{AB} and the corresponding eigenvectors υ_i^{AB},

$$k_{AB} = \sum_i^3 \lambda_i^{AB} |u^{AB}.\upsilon_i^{AB}| \tag{4.14}$$

Here, k_{AB} is the harmonic bond stretching force constant for bond A-B; u^{AB} is the normalized vector pointing from atoms A to B. It should be noted that $k_{AB} = 2k_b$ (k_b is the force constant of bond stretching used in Eq. 4.1). Similarly, the angle-bending force constant k_θ for angle $\angle ABC$ can be derived by considering the responding forces

on atoms A and C due to a displacement in the coordinates of atom B,

$$\begin{bmatrix} \delta \boldsymbol{F}_{Ax} \\ \delta \boldsymbol{F}_{Ay} \\ \delta \boldsymbol{F}_{Az} \end{bmatrix} = - \begin{bmatrix} \frac{\partial^2 E}{\partial x_A \partial x_B} & \frac{\partial^2 E}{\partial x_A \partial y_B} & \frac{\partial^2 E}{\partial x_A \partial z_B} \\ \frac{\partial^2 E}{\partial y_A \partial x_B} & \frac{\partial^2 E}{\partial y_A \partial y_B} & \frac{\partial^2 E}{\partial y_A \partial z_B} \\ \frac{\partial^2 E}{\partial z_A \partial x_B} & \frac{\partial^2 E}{\partial z_A \partial y_B} & \frac{\partial^2 E}{\partial z_A \partial z_B} \end{bmatrix} \times \begin{bmatrix} \delta \boldsymbol{x}_B \\ \delta \boldsymbol{y}_B \\ \delta \boldsymbol{z}_B \end{bmatrix} \tag{4.15}$$

and

$$\begin{bmatrix} \delta \boldsymbol{F}_{Cx} \\ \delta \boldsymbol{F}_{Cy} \\ \delta \boldsymbol{F}_{Cz} \end{bmatrix} = - \begin{bmatrix} \frac{\partial^2 E}{\partial x_C \partial x_B} & \frac{\partial^2 E}{\partial x_C \partial y_B} & \frac{\partial^2 E}{\partial x_C \partial z_B} \\ \frac{\partial^2 E}{\partial y_C \partial x_B} & \frac{\partial^2 E}{\partial y_C \partial y_B} & \frac{\partial^2 E}{\partial y_C \partial z_B} \\ \frac{\partial^2 E}{\partial z_C \partial x_B} & \frac{\partial^2 E}{\partial z_C \partial y_B} & \frac{\partial^2 E}{\partial z_C \partial z_B} \end{bmatrix} \times \begin{bmatrix} \delta \boldsymbol{x}_B \\ \delta \boldsymbol{y}_B \\ \delta \boldsymbol{z}_B \end{bmatrix} \tag{4.16}$$

Then, the angle-bending force constant can be derived as,

$$\frac{1}{k_\theta} = \frac{1}{d_{AB}^2 \sum_i^3 \lambda_i^{AB} |u^{PA}.\upsilon_i^{AB}|} + \frac{1}{d_{CB}^2 \sum_i^3 \lambda_i^{CB} |u^{PC}.\upsilon_i^{CB}|} \tag{4.17}$$

Here, d_{AB} and d_{CB} are the distances between atoms A-B and C-B, respectively and the unit vectors perpendicular to the bonds AB and CB on the plane ABC are $u^{PA} = u_N \times u^{AB}$; $u^{PC} = u^{CB} \times u_N$. They are the direction of small displacements of atoms A and C that result from opening or closing the angle ABC. Let u_N be a unit vector perpendicular to the plane ABC: Then $u_N = (u^{CB} \times u^{AB})/(|u^{CB} \times u^{AB}|)$ where u^{AB}, u^{CB}, λ_i^{AB}, λ_i^{CB}, υ_i^{AB}, and υ_i^{CB} have the same meaning. Note that $k_\theta = 2k_a$ (k_a is the angle-bending force constant in Eq. 4.1). With all the ingredients available in the next section we will describe the implementation part that uses this method to produce specific constants.

4.5 Restrained electrostatic potential charge derivation

As regards to non-bonded interactions, atomic charges play a crucial role in understanding the chemical reaction and the physical properties. Since the distribution of electrons in a molecule is not just a set of punctual charges but, instead of a distributed density around the nucleus, we have to devise a way to represent this distribution as accurately as possible within the framework of this atomistic model. As accurately this charge representation is the more qualitatively and quantitatively we can study the system with Atomistic simulation. There are many ways to generate partial charges some of them are Mulliken, Merz-Kollman (MK), Gasteiger-Marsili, ChelpG [142], and NBO methods. The drawback of Mulliken method is that it is sensitive to the choice of basis sets, while

for MK, ChelpG, and NBO methods they are less sensitive with respect to this choice and the predicted charges significantly vary less. Moreover, Mulliken charges do not reproduce the electrostatic potential of a molecule very well due to the projection of same basis function on different atoms. The simplest case where Mulliken comes up was by partitioning the density onto each atom and calculating the charges, which, physically speaking, lacks the true description of the system.

The one we will use is the method given by Kollman. Amber potential does not really use explicit charges in its writing, it rather uses a restrained electrostatic potential (RESP) [143, 144] method to represent non-bonded interaction. The rationale for our usage of this method relies on a number of points: (i) prior to RESP method, the electrostatic potential (ESP) method was used. The problem with it was that it assigns unrealistically high charges on the charge center and that the charges were varying with the different orientations. Moreover, numerical instability was also the source of poor fitting to the original ESP. (ii) With the RESP method, these sources of limitations were overcome: the numerical instability error is eliminated and the model is found independent of the conformation. RESP method also ensures that rotationally degenerate atoms, such as methyl and methylene hydrogens, have equivalent charges. The fitted potential is obtained from a set of point charges q_c centered at atom c according to,

$$V_{RESP}\left(\boldsymbol{r}_k\right) = \sum_c \frac{q_c}{\left|\boldsymbol{R}_c - \boldsymbol{r}_k\right|} \tag{4.18}$$

than a least squares fitting procedure at defined grid points $\boldsymbol{r}_k$ is carried out,

$$R_{ESP} = \frac{1}{N}\sum_k^N \left(V_{QM}\left(\boldsymbol{r}_k\right) - V_{RESP}\left(\boldsymbol{r}_k\right)\right)^2 \tag{4.19}$$

where V_{QM} is the QM potential and V_{RESP} the potential generated by the RESP charges. N is the number of selected fit points. To avoid unphysical values for the fitted charges, restraints can be set. The restraints in *antechamber* uses a simple harmonic penalty functions,

$$R_{RSTR} = \alpha \sum_i^N \left(q_i - t_i\right)^2 \tag{4.20}$$

where t_i is the target value for charge q_i and α is the strength of the restraint. By default, in the *antechamber* program, all elements, except hydrogen, are weakly restrained to zero. With this added restraint $R{=}R_{ESP} + R_{RSTR}$, the function is minimized using a least square procedure. Overall, to derive RESP charge first we perform the Merz-Kollman (MK) population analysis (ESP charges are determined by Gaussian09 code

at the PBE/Def2SVP level of theory using ultra-fine integration grid) which uses the molecular electrostatic potential produced by the DFT electronic density. Then, a fit to the ESP is made to derive partial charge and, finally, a minimization of the error between the true ESP and the ESP given by the point charges located on the suitable chosen surface is made. This modified scheme also ensures that rotationally degenerate atoms, such as methyl and methylene hydrogens have equivalent charges. For charge derivation, the original paper uses HF/6-31G* level of theory without accounting the electron correlation part and they analyze the error accounted by this method is the same as would be obtained by the difference in the gas and solution phase. Our choice for a specific level of theory for obtaining the RESP charges was driven by the worry to be consistent with our previous calculations, we have used the same basis and functional as we used to find the local minima for the mono-nuclear complex.

4.6 Iron ligand parameterization

Now, we turn to the derivation of the Iron parameters. At first, let's discuss our naming conventions for nonstandard residues uniquely. To define the parameters each nitrogen, N, sites is labeled with Yi, $\forall\, i \,\epsilon\, \{1 \ldots 6\}$ and Fe by $M1$ respectively to differentiate from the gaff database (or in case of nFe atoms they are labeled as Mn).

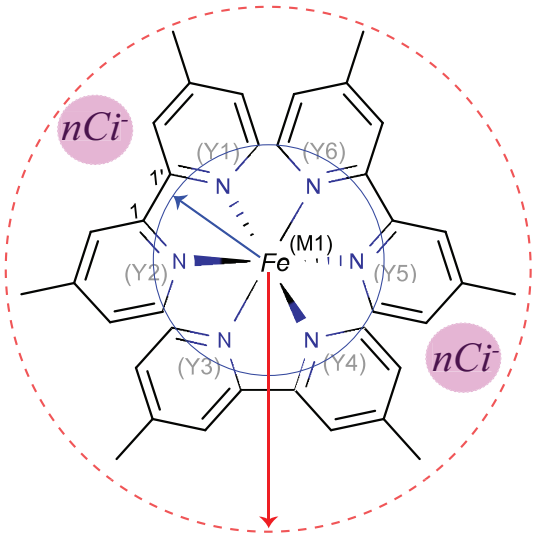

Figure 4.7: Atom types (AT) labels for the $[Fe(dmbpy)_3]^{n+}$ nCi^- complex. First coordination shell is shown in blue and second shell in red color. Atom type are shown in grey color.

Ambiguous naming convention was found as the main cause of errors when extracting

parameters and has to be considered carefully. In Figure 4.7, naming convention is shown in grey color. All the angle and dihedral are thus declared with respect to *dmbpy* atom types. In Table 4.3, bonds length parameters are compared to the experiments. Here, we have reported the parameters which are important for establishing the oxidation level of our complex. For $Fe - N$, the potential is parameterized with the above procedure and the rest using the same procedure as described in the previous section. All other force field parameters are given in Appendix E.

Specific tools in Amber18 code exist and we did not feel the need to implement them again. Metal-ligand parameters extraction is done with Metal Center Parameter Builder (MCPB: version 3) [145] tool which uses the Seminario method and is compatible with Amber forcefield. The names have to be defined uniquely so that the MCPB tool can assign without confusing with existing elemental assignments in Amber database. The Hessian is calculated at PBE/Def2SVP level of theory. In this case, we have ignored the improper and dihedrals angles for the reasons mentioned above. We have parameterize the ligand atoms, which are in direct coordination with a chosen arbitrary cutoff radius of 2.8 Å centered at the Metal site (blue circle). So, surrounding the Metal sites, six Nitrogen with adjacent carbon sites are recognized in describing the force constants of bonds and angles. Within this radius, the angles with nearby Carbon and Nitrogen atoms are measured (which is necessary to maintain the octahedral environment).

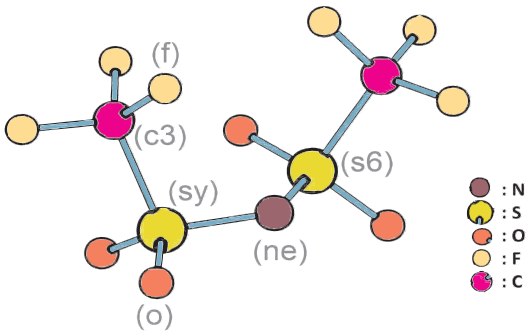

Figure 4.8: Atom types are shown in grey color for $TFSI^-$ counter-ions.

Table 4.3: Comparison of parameters obtained at DFT:PBE/Def2SVP level of theory with those already in Amber. Here AT means Atom Types. All bond lengths are given in **Å**.

Bonds	AT	Exp [24, 115]	DFT	Amber/parm10	Gaff/gaff
$Fe - N$	M1-Yi	1.965(3)	1.96	-	-
$C1 - C1'$	cp-cp	1.472(6) [25]	1.470	1.400	1.485
$N - C1$	Yi-cp	1.350(0)	1.363	1.339	1.339

A first coordination shell (shown in blue color in Figure 4.7) treats the Nitrogen

atoms, while $TFSI^-$ counter-ions are treated in a second coordination shell (shown in red color in Figure 4.7) to avoid nonphysical interactions with the metal sites because of large distance. This will avoid such interactions in our model and is justified by our analysis of the PDOS in chapter 2 which has shown that the counter-ions do not coordinate directly to the metal site but indirectly through *dmbpy* molecules (from DFT calculations they are at a distance of 5.5 Å).

Now, let's turn to the counter-ions. As discussed in the context of DFT calculations (chapter 2), we did not observe any localization of charges on the Nitrogen atoms, but dispersed ones over all atoms, entailing the flexibility of the molecules. The initial atomic positions and optimized conformation are taken from the DFT calculations as shown in Figure 4.8 The RESP charges are determined by considering the whole structure, including counter-ions, so that the charge is allowed to be transferred from the ligands to counter-ions (as we are using the static non-bonded model). These RESP charges have to be viewed as effective ones and do not correspond to an integer number (of an electron). They are fixed so that the electrostatic interactions of our model mimic at best the DFT behavior. This effective charge ensures the neutrality of the system and renders it more realistic for incorporating the effect of polarization in the complex.

In Table 4.4, the bond lengths we obtained with our model are compared to DFT ones. They are in excellent agreement. The ones for which a noticeable change is observed (c3-s6) actually corresponds to a bending of the molecule.

Table 4.4: Comparison of parameters obtained at DFT:PBE/Def2SVP level of theory with those already in Amber database. All bond lengths are given in **Å**.

Bonds	Gaff	DFT
ne-s6	1.672	1.632
ne-sy	1.672	1.624
c3-f	1.350	1.340
c3-sy	1.809	1.895
c3-s6	1.808	1.895
o-s6	1.453	1.483
o-sy	1.466	1.486

4.7 Acetonitrile (ACN) solvent box setting

Before the system can be simulated in explicit solvent, we need to create a model of solvation using the ACN molecules. Since this solvent does not exist in Amber package we created a box (*packmol* program [146] was used to create a box) full of 125 Acetonitrile (ACN) molecules with a rectangular box of dimensions 23.15 Å by 23.11 Å by 23.10 Å. After preparation, the entire system is minimized using steepest descent method for 20000 steps. Then it is heated from 0 K to 300 K in 50 ps using Langevin thermostat with a collision frequency of 2 ps^{-1} in canonical (NVT) ensemble. After heating, a 500 ps simulation under isothermal-isobaric (NPT) ensemble was conducted for the ACN system to ensure density of the box agrees with the experimental value of 0.78 g/cm^3 under constant temperature (300 K) and pressure (1 atm). All bonds involving hydrogen were unrestrained and the time step for numerical integration was 0.5 fs (0.0005 ps). A cutoff of 8 Å was used for non-bonded interactions and long-range electrostatic interactions were treated using the Particle Mesh Ewald (PME) method.

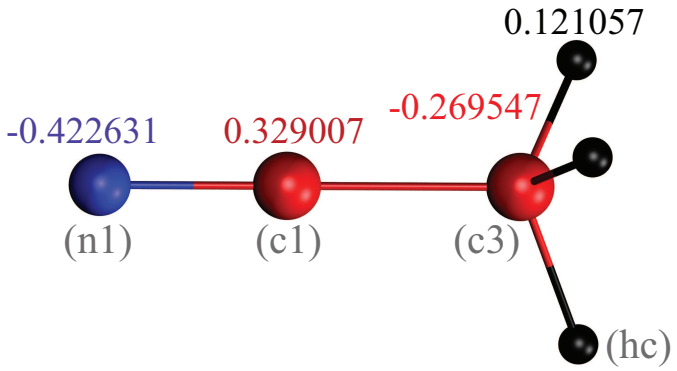

Figure 4.9: Atom types for the ACN molecule shown in grey color and corresponding RESP charges (e) are calculated at PBE/Def2SVP level of theory.

We employ the Gaff atom types and parameters (shown in Table 4.5) and RESP charges were determined with the *antechamber* program at PBE/Def2SVP level of theory. The RESP charges are shown in Figure 4.9. We have used the same level of theory without charge scaling for all the units in the complex. To check if the system is equilibrated, we analyzed the NVT plus NPT simulation data. We used an initial NVT simulation in order to help the system to reach at 300 K (within 50 ps) before running the main NPT simulation. NPT simulation at a low temperature gives inaccurate pressure results due to large over corrections by the barostat and may explode the system.

So, the strategy that is commonly adopted is to run for a few seconds the NVT ensemble to the desired temperature and quickly switch to NPT ensemble to correct the density.

Table 4.5: Comparison of parameters obtained at DFT:PBE/Def2SVP level of theory with those GAFF. All bond lengths are given in **Å**.

Bonds	GPD	DFT
c3-hc	1.097	1.108
c1-c3	1.467	1.458
c1-n1	1.153	1.171

Figure 4.10 (a), shows the energetics of our simulations. During the first 50 ps, we notice the increase corresponding to the gradual increment of the temperature from 0 K to 300 K. After 50 ps kinetic energy (shown in black color) is constant showing the temperature thermostat worked correctly. The potential energy is decreased from 50 ps to 100 ps during the constant pressure simulation and then flattened off at $t = 100$ ps and remained constant for the remainder of the simulation (100 to 550 ps) indicating that the relaxation was completed and that we reached an equilibrium. Figure 4.10 (b) inset shows the volume of the system decreases during the first 50 ps and the average volume of the system remain constant during the NPT simulation. After the equilibration, we computed the average density it is well equilibrated around 0.77 g/cm^3 at 300 K. The difference of 0.01 g/cm^3 is observed with respect to the value found in literature[1]. Moreover, the temperature remained more or less constant for the remainder of the simulation, indicating the use of Langevin dynamics for temperature regulation was successful. From the pressure plot, we note that the pressure is zero during the first 50 ps. This was expected since we were running a constant volume simulation in which the pressure wasn't evaluated. At about 50 ps, when we switched to constant pressure, the pressure drops sharply becoming negative indicating the volume of the box starts to change. The negative pressures mean the force is acting to decrease the box size while positive force mean to increase the box size. From the graph, it might seem the fluctuations are larger but the mean pressure is stabilized around 1 atm after 200 ps of simulation. This is sufficient to indicate successful equilibration.

[1]https://en.wikipedia.org/wiki/Acetonitrile

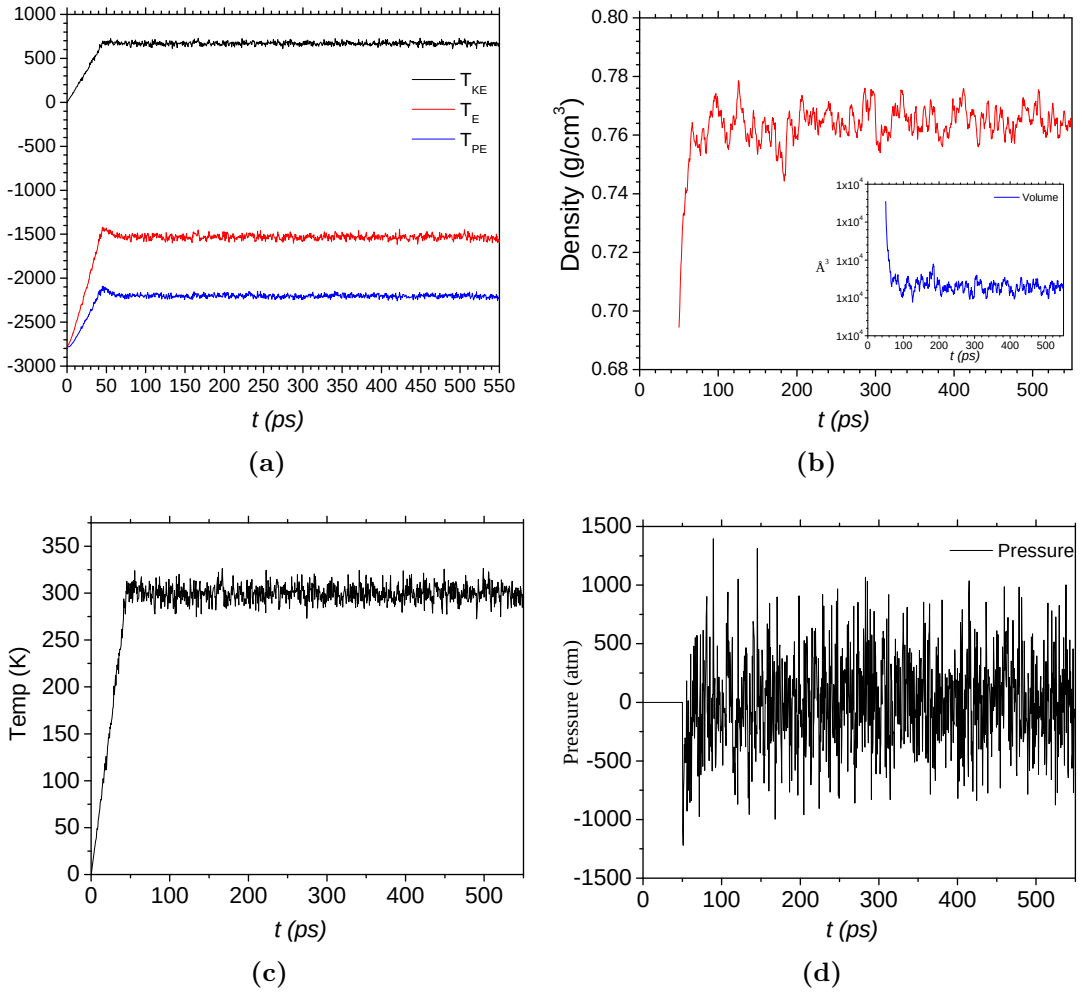

Figure 4.10: Analysis of ACN solvent box. The simulation data are plotted for (a) Energy (b) Density (c) Temperature, and (d) Pressure with respect to simulation time.

4.8 Validation of the force field

Having all the ingredients available, we validate the potential using the bi-nuclear complex in the field of the counter-ions as well as solvents molecules, such as Acetonitrile (ACN), and study their dynamic properties. The RESP charges for bi-nuclear were determined with the *antechamber* program distributed with the Amber18 package. The charge for this structure is discussed in the next chapter. For the sake of convenience, we are presenting the simulation results for a low dimensional system in this section.

4.8.1 System setting and MD simulations

All simulations were carried out using the Amber18 Molecular Dynamics package[132]. The van der Waals (vdW) interaction part uses a 12-6 Lennard-Jones (LJ) potential and for unlike atoms, ε_{ij} and $R_{min,ij}$, are obtained using the Lorentz-Berthelot combining rule (arithmetic mean for the $R_{min,ij}$ and geometric mean for ε_{ij}). The vdW radius parameter for Fe^{2+} and Fe^{3+} atoms are fixed with 1.409 Å and 1.386 Å respectively. These values are taken from the paper by Li *et al.*, [133, 147]. They have calculated these values in TIP3P water model. We are using these values in case of ACN solvents.

The initial structure was obtained from the DFT calculation. Geometrical parameter for the bi-nuclear complex (Neutral and Full loaded) were determined according to the total spin of the system. With the lowest energy structure, we calculated the RESP charges (*discussed in Chapter 5*). The initial structure was setup symmetrical along the longer axis and the obtained RESP charge on each mono-nuclear center were symmetrical around the alkyl chain. This symmetrical charge distribution creates the homogeneous field where the counter-ion during the dynamics can diffuse and finds the minimum position corresponding to Iron center. Here counter-ions acts as a neutralizing agent.

After the construction of the bi-nuclear state, we embed the system in explicit ACN solvents environment. The octahedral box is chosen with the minimum distance between the system atoms and the edge box set to 12 Å. The minimization was subjected to 10000 steps of steepest descent over the whole of the system. Then we heated the system from 0 K to the target temperature of 300 K for a period of 100 ps under constant volume periodic boundary conditions (NVT). After heating the system to 300 K, NPT ensemble run was conducted to equilibrate the box. Average pressure of 1 atm was maintained by using isotropic position scaling with a relaxation time of 2 ps. The temperature was controlled via a Langevin thermostat with a collision frequency of 2 ps^{-1}. Then we switch to NVE ensemble and run over a period of 500 ps for calculating the dynamic properties. A cutoff of 10 Å was used for non-bonded interactions and long-range electrostatic interactions were treated using the Particle Mesh Ewald (PME) method. All bonds involving hydrogen were unrestrained and the time step for numerical integration was 0.5 fs (0.0005 ps). All molecular dynamics (MD) simulations were run using the SANDER module. The steps are summarized in Figure 4.11. The simulation results were analyzed using the *cpptraj* program distributed with the Amber18 package and geometry was analyzed with VMD/Chimera software. Relevant details of other force field parameters are presented in the Appendix E.

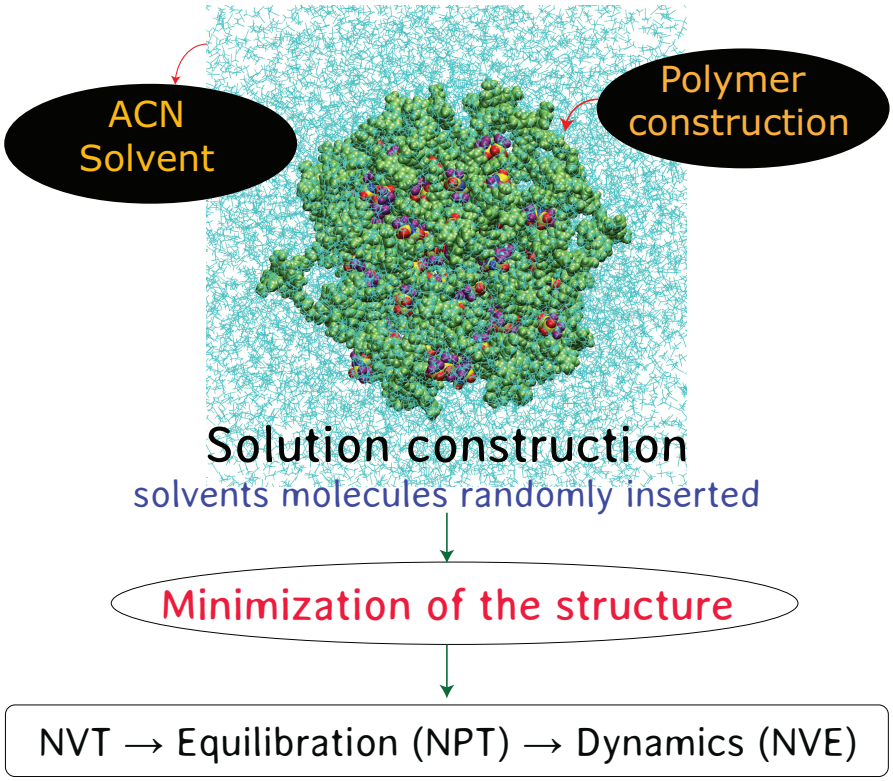

Figure 4.11: Steps involved for simulating a polymer system.

4.8.2 Bi-nuclear solvation

Next we solvate the system with the equilibrated ACN solvents with a box radius of 12 Å with a *LEaP* tool (distributed with Amber18) resulting in a truncated octahedral box of dimensions $a = b = c = 56.926$ Å with $\alpha = \beta = \gamma = 109.47°$. We choose this box rather than rectangular because during rotation (*by self-diffusion*) the long axis of the bi-nuclear complex will be along the short side of the box. Since the box is tiled infinitely in space by the periodic boundary method, there is a possibility that the end of bi-nuclear will interact with its periodic image. To avoid this one solution is to enlarge the box but it will create more solvent molecules. However, it will increase the computational time. The use of truncated octahedral box reduces the requirement of solvents and solves the rotation problem.

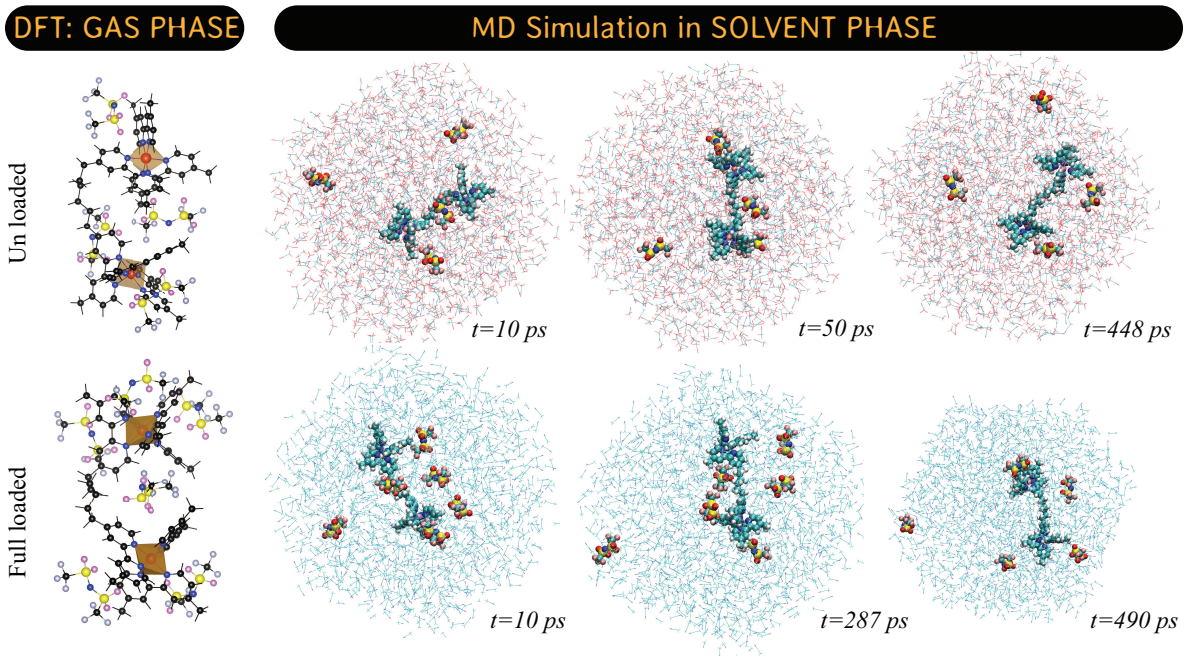

Figure 4.12: Comparison of DFT structure in gas phase, and MD Bi-nuclear in solvent phase.

Table 4.6: Metal Ligand distances for the selected parameters and the effective diffusion constant D_{eff} for the counter-ions. N mean *Neutral* and FL means *Full Loaded*. All distances are given in Å.

	MD Simulation		Exp	
	N	FL	N [24, 115]	FL [116]
M1-nb	2.0 ± 0.04	2.0 ± 0.03	1.965(3)	1.96(3)
cp-cp	1.50 ± 0.02	1.50 ± 0.03	1.472(6) [25]	1.473(6)
nb-cp	1.35 ± 0.01	1.35 ± 0.02	1.350(0)	1.350(0)
D_{eff} $(10^{-5} cm^2/s)$	0.6520	0.525	-	-

We will study two models Neutral and the Fully loaded (*see Chapter 2 for notational scheme*) to verify the potential. The simulation box for Neutral and Full loaded contain 6756, and 7188 atoms respectively. Without loss of generality, we initiated our simulations using only the alkyl chain of length $n = 6$. In Figure 4.13, equilibrated state in NPT ensemble for two systems are shown. The density is well equilibrated at 0.78 g/cm^3 around 200 ps on average. Similar, analysis with energy graph shows the kinetic energy is constant which indicates the thermostat worked correctly in stabilizing the temperature. The potential energy (shown in red color) decreases during the 50-100

ps and then flattened showing the system is relaxed. The temperature curve remains constant during the rest of the simulation. From pressure graph it seems to fluctuate wildly but the mean pressure is stabilized around 1 atm after 200 ps of simulation. This is sufficient to indicate successful equilibration.

For both charging and discharging process, we are most interested in the diffusion of counter-ions. For a quick charging, the diffusion of counter-ion should be high. In chapter 1, experimental kinetic rates have been shown for three counter-ions. Here, we have chosen $TFSI^-$ molecule but for future studies, we will hope to study other counter-ions and compare their diffusion constants. However, for a demonstration of the potential, we will go with this $TFSI^-$ and measure its diffusivity in the presence of structure and solvents. If we look at other counter-ions, they have less degree of freedom for internal movement as compared to $TFSI^-$ and this makes it attractive to study.

The NVE ensemble is run after the NPT ensemble and resume the simulation at fixed energy obtained via the constant pressure from the restart file. From the Table 4.6, we see M1-nb ($Fe - N$) distance on average varies between 2.0 $\pm$ 0.04 at 300 K. Self-diffusion coefficients are calculated from the slope of the mean-square displacement averaged over the trajectories of individual particles. The diffusion constant D_{eff} is calculated from the Einstein relation [148],

$$6D_{eff} = \lim_{t\to\infty} \frac{\partial}{\partial t} < [\boldsymbol{r}_i(t) - \boldsymbol{r}_i(0)]^2 > \tag{4.21}$$

where $\boldsymbol{r}_i(t)$ denotes particle trajectories that are continuous in cartesian space. These diffusion values for counter-ions are quite high (it will be demonstrated in the next Chapter 5 this values reduces considerably in the presence of 3D structure) as it shows they can diffuse freely if the structure is not extended in three dimensions. Our trend also shows that, when fully loaded, the diffusion constant decreases on the order of 0.1 $\times 10^{-5} cm^2/s$.

The solvation effect is also crucial. If we compare to the geometry obtained from DFT as shown in Figure 4.12, we observe, in gas phase, that the bi-nuclear unit closes itself due to electrostatic or steric effect. Whereas, from MD simulation this effect is screened by the solvent molecules. Hence this screened effect aid in stabilizing the structure and allow the ions to move freely without trapping into the specific region. To get the real picture of how the ions diffuse, we have constructed 3D polymer and it will be discussed in the next chapter.

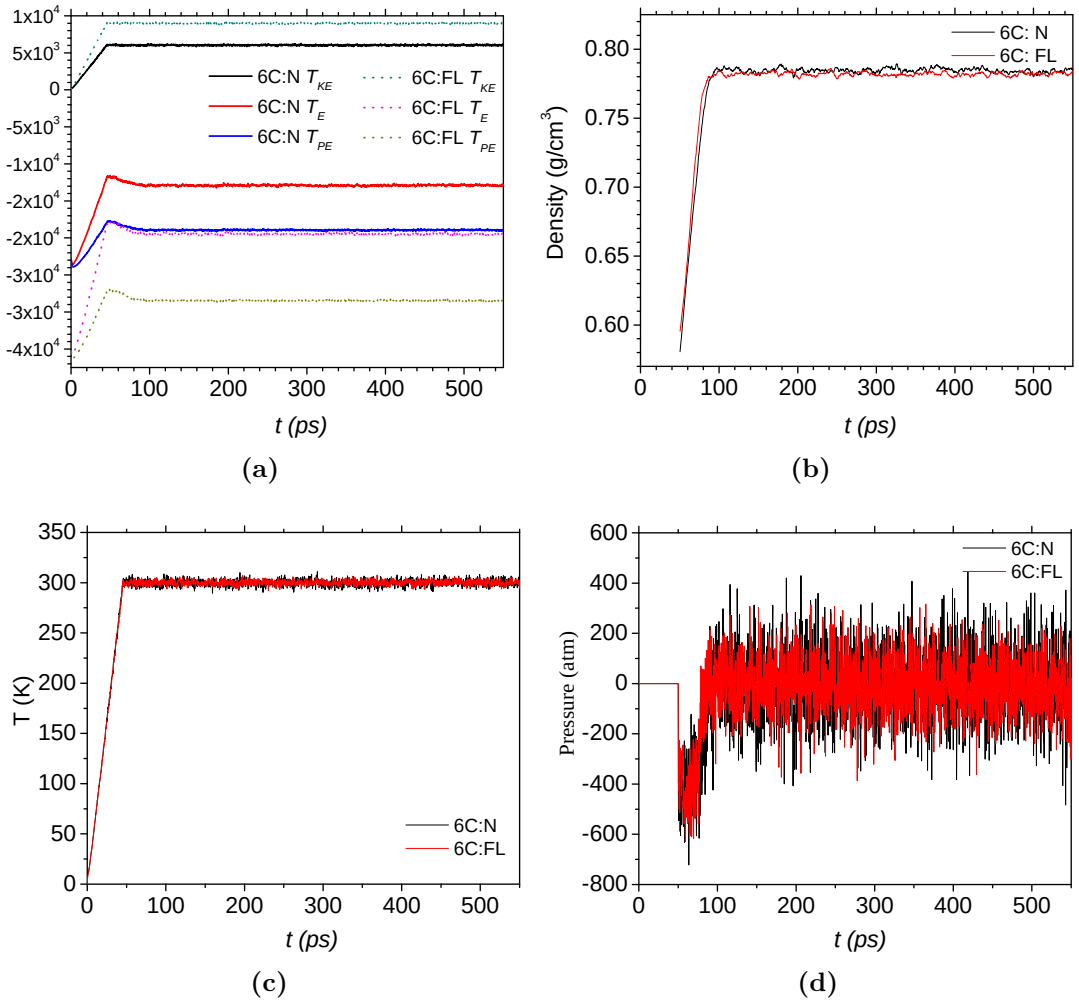

Figure 4.13: Analysis of bi-nuclear complex. (a) Energy (b) Density (c) Temperature and (d) Pressure plots with respect to simulation time.

4.9 Conclusion

This chapter was essentially devoted to the development of an efficient atomistic model for the Fe compound, allowing us to perform calculations on polymers of higher dimensions and about the dynamical aspects of the problem. We have shown that the developed potential behaves in accordance with the DFT results. The ACN solvents are found to screen the counter-ions interaction with the central unit. As a result, the bi-nuclear chains does not collapse, showing that solvent molecules are essential to fix the overall shape and mechanical stability of long chains of the polymer. At 300 K, we did not observe any breakage of bonds. The structure of the compound is maintained

and the counter-ions vibrate around a mean value.

■

Chapter 5

Porous polymer chains in realistic cathode materials

5.1 Introduction

The previous chapter has established the potential developed for the mono-nuclear complex. In this chapter, we will develop the full-scale model of the Iron poly-nuclear complex. This realistic model of the Fe poly-nuclear complex, with explicit solvents and counter-ions, will enable us to study the dynamic properties as a function of the alkyl chains.

In literature many algorithms are designed for constructing structure specific topology but none are universal. In one of many references Luis Martin *et al.*, [149], has devised a scheme for constructing Crystalline Porous Polymers (CPP). Their approach follows in building from the basic specific topology structure and generating the 3D crystal structure. Here we will describe our mathematical approach in constructing 3D poly-nuclear structure. We have used a different concept because the generation of octahedral geometry requires the specific position of *bpy* Nitrogen's atoms, the Linker chain, and methyl groups. The octahedral geometry is translated and rotated along with the position of counter-ions. The Linker positions are minimized in accordance to obtain the correct connecting units between mono-nuclear. In this chapter, we have developed an in-house python code that allows in quick assembling of 3D structure and assigning RESP charges to specific atoms obtained from mono-nuclear studies. We have to remind that the work described in this chapter is quite original. To our knowledge, no literature data exist and we rely mostly on the experimental LEPMI team for their inputs.

5.2 3D porous polymer construction

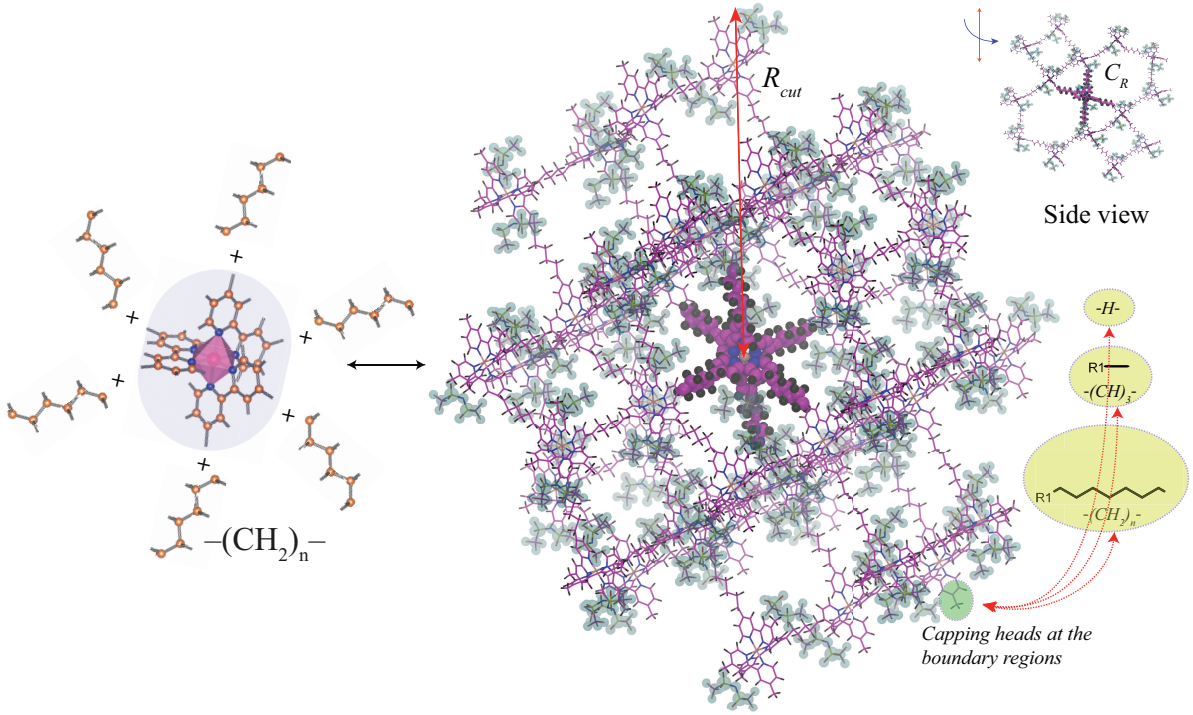

Figure 5.1: Schematic representation of the 3D poly-nuclear complex centered at the mono-nuclear unit with counter-ions to mimic the working battery condition. Three ways to cap boundary regions are shown in yellow color. Solvent molecules have been omitted for reasons of clarity.

In the previous chapter, we constructed the mono-nuclear unit and started building the bi-nuclear unit. Now we will extend this construction to a large spatial scale. Let M be a space of poly-nuclear with boundary. Each mono-nuclear is topologically path connected with alkyl chains of length n. Locally the interior of M, $\mathrm{Int}(M)$, is symmetric and the boundary methylated. We constructed this initial nontrivial poly-nuclear configuration with the spherical symmetry of radius R_{cut}. The algorithm provides a gateway for generating the structure from the mono-nuclear unit and varying alkyl length chain. In Figure 5.1, the 3D neutral system is shown and from the inset side view it can be seen it generates a large cavity region, C_R, as a function of chain length when rotated around the red axis. The phase shows the initial structure obtained consists in the realm between amorphous and condensed phases. This way of generating structure is one of the many possible ways. Here we have adopted this configuration because we assume every path in a structure should be connected as suggested by the experiments. Similarly, this

approach can be extended to the fully loaded system and creating defects to mimic the standard realistic materials (which will be the topic of further research).

Addressing the issue at the periphery is a complicated part of this modeling process. By construction, we can repeat mono-nuclear unit infinitely in 3D space but at one point we have to truncate this construction in such a way that the dynamics should be the same as it is in the interior. In the Figure 5.1, three yellow circles have been shown to explain the various options we have to perform the capping. Either, we cap up with hydrogen atoms, or with $n\,(CH_3)$ methyl fragments or with free alkyl chains. The last solution is quite probably the most inadequate. Such a long fragment seeing one of its tips left free to move, will sweep away the molecules of solvent and the counter-ions. Thus, the counter-ions will fly away and the statistics will be different than in the core of the compound and the dynamics of the system will be deeply affected.

The other solution is to cap with hydrogen atoms but with this option, the chemical bond is drastically changed with respect to a CH_3 or alkyl fragment. As suggested by the experimental studies we have capped with $n\,(CH_3)$ fragments as this capping provide the stability and mimics the condition in the interior near the alkyl chain (start of the reticulation process). However, we will discuss this point in more detail in the next section. With this assumption, we will concentrate our dynamics in the interior of the region, $l_{cut} < R_{cut}$, and exclude the effects at the boundary. All the patterns outside this region, where the methylation is operated, have to be viewed as an effective medium.

5.3 Generating effective charges for Iron porous polymer

In this section, we will lay out the method to derive fixed charges. The computational methodology adopted for this large structure follows the same recipe as mentioned in Chapter 4. However, the direct obtaining of the partial charges for this huge structure is impossible via quantum mechanical calculations (such a calculation cannot be performed for cells containing 10000 atoms). We have to proceed by modules: RESP charges are actually calculated from a series of DFT calculations addressing selected patterns found in the 3D compound. We represent a selection of them in Figure 5.2 (a), (b), (c), and (d). They correspond to the various types of connections that mono-nuclear encounter in the 3D structure. In Figure 5.2 (a), the pattern is said fully reticulated: all the six "plugging" carbons are connected to an alkyl chain. This pattern is found everywhere in the core of our 3D compound. A specific DFT calculation on this pattern allows

awarding the RESP charges for all the atoms of the *bpy* molecules, the Fe sites, the surrounding $TFSI^-$, molecules but also the carbon and hydrogen atoms of the alkyl chains for this specific geometry. However, let's mention immediately that some of the so-obtained charges of the alkyl chains will have to be modified: the ones corresponding to the free tip of the chain since, in our 3D compound, this tip is not left free, but is also connected to a mono-nuclear. In Figure 5.2 (b), (c), and (d), we present some other types of local arrangement in our 3D compounds. They correspond to the various cases that we can encounter at the periphery of our compounds, for which a methylation has been operated to terminate the 3D polymer. As the local geometry is different, the RESP charges on the *bpy* molecules and Fe sites are different from the fully-reticulated case. These calculations also provide a first guess for the RESP charges of the methyl fragments.

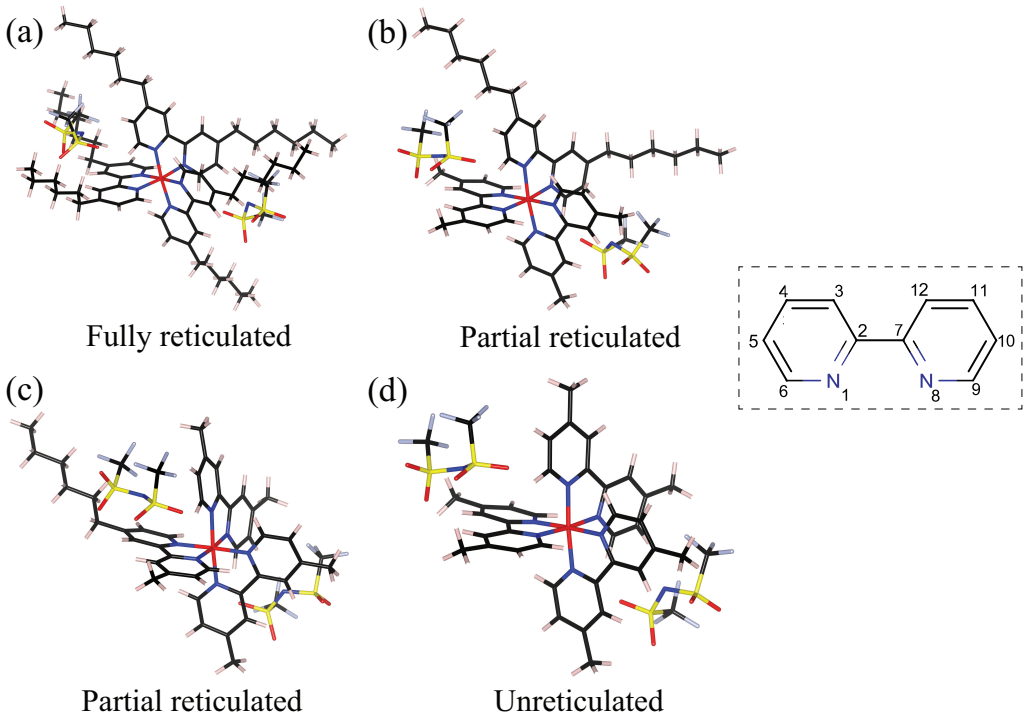

Figure 5.2: RESP sub units charge scheme (a), (b), (c), and (d) configuration in a poly-nuclear structure optimized at PBE/Def2SVP level of theory.

Now, let's turn to the final operation which consists into assembling these modules within the constraint to render compatible between each other all the RESP charges of the fragments in the 3D structure. To do that, we introduce an extended mono-nuclear

unit, made of the three *bpy*, Fe sites, the $TFSI$ molecules and half the atoms of the six alkyl chains (see Figure 5.3). These latter are now attached to one specific mono-nuclear unit, the other half of the six alkyl chains will be attached to the neighboring mono-nuclear units. We realize that this extended pattern is neutral: the summation of the charges within the dotted circle in the Figure 5.3 gives zero. The other half alkyl chains contribute to bringing neutrality to the neighboring patterns.

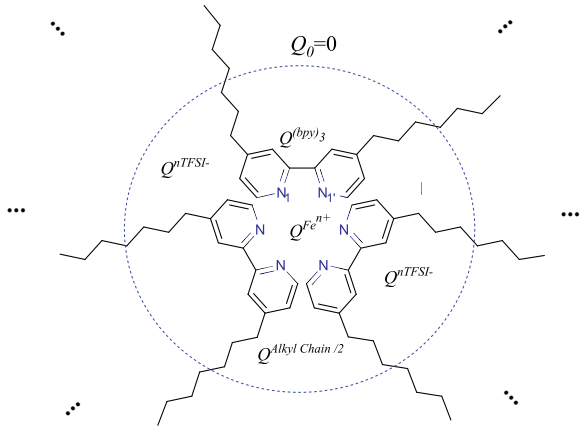

Figure 5.3: Pictorial representation of the mono-nuclear unit inside a 3D structure where the individual charge unit is assumed. The regions inside a dotted circle shows the total charge is zero including counter-ions.

In the case of the patterns contributing at the periphery of the cell (let say presenting α alkyl chains and β methyl fragments), some new adjustments of charges have to be made when we connect them to form the 3D structure. To maintain neutrality for these bounding patterns, the following equation (Eq. 5.1), putting in relation to the charges of the various fragments, has to be satisfied:

$$\alpha \times Q^{\frac{Alkyl\,Chain}{2}} + Q^{(bpy)_3} + Q^{Fe^{n+}} + Q^{n(TFSI^-)} + \beta \times Q^{n(CH_3)} = 0 \tag{5.1}$$

Let us mention that $\alpha + \beta = 6$ since there are six plugging carbons, either connected to an alkyl chain, either by a methyl fragment. Deep internal redistribution of charge is observed when methyl fragments come in replacement of the alkyl chains to ensure the boundary conditions. If both rings of the *bpy* are concerned by a CH_3 plug, these modifications are operated on both pyridine rings. If only one is concerned, they are operated only on this ring, while its neighboring ring adopts a behavior close to the one when both sites are connected to the alkyl chain. In other words, the usage of CH_3 instead of an alkyl chain of length n deeply affects the first carbon neighbors but does not propagate up to the neighboring ring. To conclude, let us also mention that

these peripheral mono-nuclear are not the ones we are interested in, they are boundary conditions, our primary analysis of trajectories will be dedicated to the core of the compound for which RESP charges are exact.

Thus, if we start replicating this unit in all directions, the system observes an overall neutrality. In Figure 5.5, the numerical values of the RESP charges are displayed. These RESP charges are shown in a minimalist way to avoid confusion because the structure is symmetrical around the Iron atom and the rest of the charges can be generated thanks to symmetry. They are presented for both the neutral and full loaded state (values under parenthesis for this latter). The RESP charges are strongly dependent on the degree of oxidation of the metal centers. If the sign of the effective charges remain the same on Fe and *bpy* atoms during the loading process, their amplitude is deeply affected. Polarization effects are developed on a long-range distance, and any simplification consisting to only vary the RESP charge on the Fe site, leaving the RESP charges of the *bpy* unchanged during the loading process, is out of question.

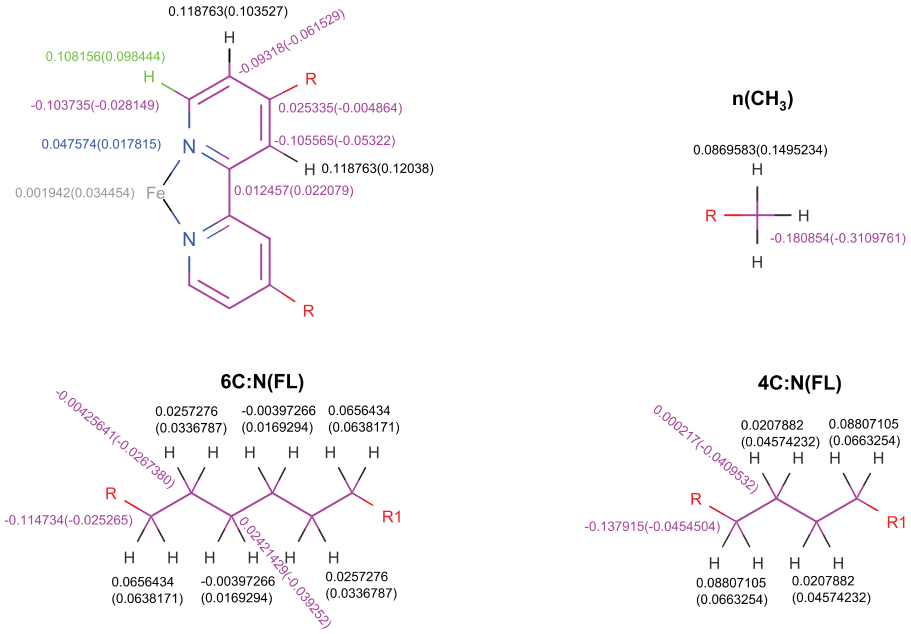

Figure 5.4: RESP charges calculated at PBE/Def2SVP level of theory. 4C:N(FL) mean alkyl chain of length 4 (4C) for Neutral (N) and Full loaded (FL) complex. Similarly, 6C:N(FL) mean alkyl chain of length 6 (6C) for Neutral (N) and Full loaded complex (FL). The charge in the bracket are shown for FL. The charges are represented for Fe *dmbpy* molecule corresponding to 4C and 6C chain. Two connection are possible (R) for each *bpy*. If there is no boundary the alkyl chain is connected (4C or 6C) and if boundary is present methyl group is attached.

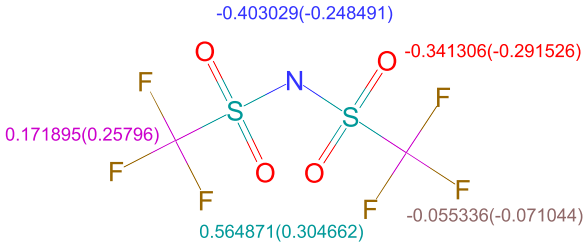

Figure 5.5: Fixed charge on counter-ions for both chains. The charge in the bracket stands for FL state, the other one is for neutral.

In Figure 5.5, we present the calculated RESP charges[1] for the counter-ions embedded in the complex in both the neutral and fully loaded cases. They represent the effective charges of the counter-ions at the neighboring of the mono-nuclear considered in the degree of oxidation 2 and 3. The charges are -0.403 for N (Nitrogen atoms), 0.172 for all C, -0.056 for all F, -0.341 for all O and 0.565 for both S. These values for $nTFSI^-$ molecules will be kept to represent all the counter-ions in the compound, even if they are at the vicinity of a mono-nuclear that is not fully reticulated (*i.e.*, mono-nuclear at the periphery for which $n\,(CH_3)$ fragments replace alkyl chains, the choice we made for boundary conditions in the preparation of large structure for simulation). The exact calculation of the RESP charges on the $nTFSI^-$ molecules at the vicinity of these modified mono-nuclear centers actually reveals that they do not exactly correspond to the ones obtained at the vicinity of the fully reticulated monomers. To conclude on $nTFSI^-$, let's notice that the overall charge on these molecules (whatever the ratio between alkyl chain and $n\,(CH_3)$ fragments maybe) is close to –0.7 for the four molecular configurations (Figure 5.2 (a), (b), (c), and (d)) we have investigated. We argue that this feature is the most important in the treatment of the electrostatic terms and that the inner distribution of charge in the counter-ion molecules is less important so that our choice of one single set of RESP charges for the $nTFSI^-$ is fully justified.

5.4 Selection of box size

Let's now turn to our study aiming at fixing the size of the box of simulation for our 3D poly-nuclear system. Our goal is to determine the optimal size, namely the smallest cell leading to converging properties, being understood that larger box length brings additional computational cost, that we want to avoid. As a typical example, Souza *et*

[1]We have used the naming convention to represent the alkyl chain of length. 4C and 6C denotes the alkyl chain of length $-(CH_2)_4-$ and $-(CH_2)_6-$ respectively.

al., have performed similar studies, but with DNA dodecamer [150]. They solvated the structure with water molecules, using a box length of size 5, 10 and 15Å and analyzed the effects of the size of the box on the mean square displacements of the molecules. Their observation reveals that such a criterium is not sensitive enough to assess what is the best choice for the size of the box. Alternatively, Yeh *et al.*, [151] discuss with more success, the dependence of the properties of water molecules with respect to box size by following their finite diffusion coefficient corrections. Our approach will be similar. The parameter we have decided to analyze is the coefficients of diffusion of the counter-ions embedded in solvent molecules in the cavity regions (Figure 5.1).

We had our study on the Neutral complex only, with the $-(CH_2)_6-$ fragment for the alkyl chain: We built 3D structures containing 5606, 10847, and 18133 atoms. Then, we solvated the system with equilibrated ACN solvent molecules with an octahedral radius of 15Å.With the help of the LEaP tool (program distributed with Amber18) we have truncated the square box in order to form an octahedral box of dimensions $a = b = c = 111.188$ Å, $a = b = c = 122.947$ Å, and $a = b = c = 142.250$ Å with $\alpha = \beta = \gamma = 109.47^o$ respectively. The so-obtained final boxes contain 54458, 72077, and 112837 atoms, respectively (including solvent molecules).

In Figure 5.6, we present the NPT simulations for the three sizes of the cell. It can be seen that the kinetic energy for the three systems remains constant, which shows that the thermostat was successful in achieving the desired temperature. In this analysis, we have ignored the first 100 ps of the NVT simulation so that to eliminate the first steps corresponding to a very rough picture of our compound, far from the equilibrated state. We observed a similar behavior as the one we met in the case of bi-nuclear compounds in chapter 4. The potential energy decreased during the first 200 ps and then flattened, showing that during this phase, the system relaxes and equilibrate its volume, to finally remains constant for the remainder of the simulation. Temperature is more or less constant and pressure graph shows that, on average, it is regulated at 1 atm. Similar, behavior for a fully loaded system was also observed but we have not reported here. We can already notice on the plot of the density (5.6 (b)) that the density corresponding to the 10847, and 18133 atoms cell are in close agreement, while the density corresponding to the 5606 atoms cell is underestimated. From that, we can already state that this latter cell seems too small to achieve our statistics.

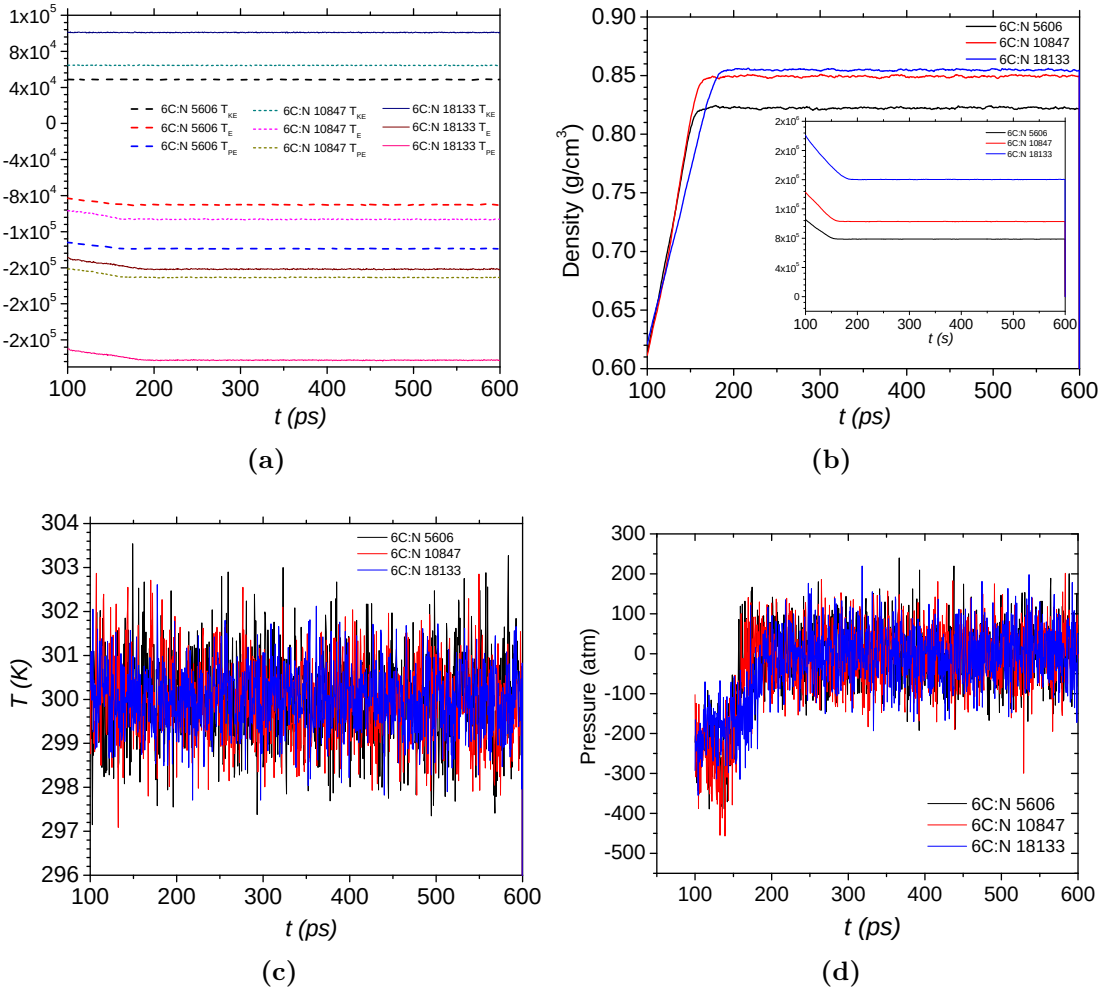

Figure 5.6: System equilibration analysis of neutral system size. The graph shows (a) Energy (b) Density (c) Temperature, and (d) Pressure plots with respect to simulation time.

To calculate the dynamic properties, we switched off the thermostat/barostat and ran NVE (purely Newtonian dynamics) simulation for further 550 ps. By using the *cpptraj* tool (program distributed with Amber18), we strip out the boundary and retain the interior part with a cutoff radius, l_{cut}, of 20 Å. The diffusion is calculated for the counter-ions in the vicinity of the complex and the solvent molecules. The numerical values are given in Table 5.1, and mean square displacement (MSD) plots are shown in Figure 5.7. The MSD curve for complexes of 5606, 10847, and 18133 atoms are shown in black, red and blue, respectively. As for the density, a convergence seems to be reached as far as unless 10000 atoms are considered. This trend is confirmed by the calculation

of the coefficient of diffusion reported in Table 5.1. From that, we decided to use the 10847 atoms cell to carry out our future calculations.

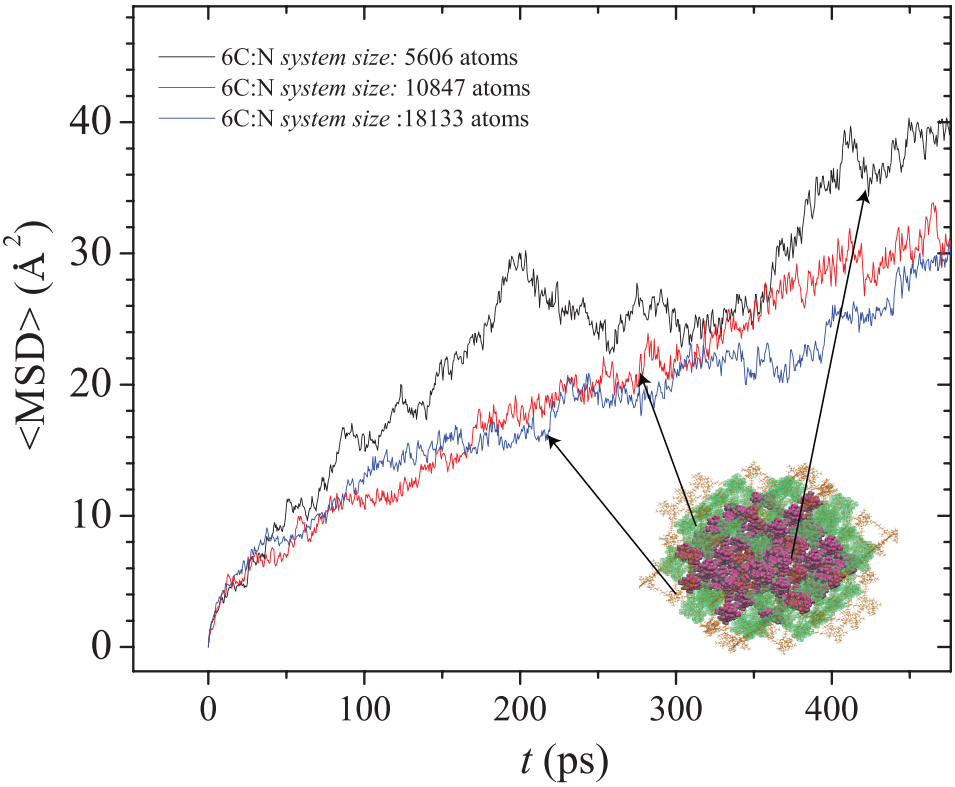

Figure 5.7: MSD plot of counter-ions with respect to simulation time t at 300 K. The MSD is plotted for three Neutral complexes for chain 6C (6C:N).

Since the above system typically behaves like a crowded system (as usually seen in biological systems) with its cavity regions filled with solvent molecules, we decided to determine in which regime the dynamics of the system falls [152]. One relevant parameter is given by,

$$\beta(t) = \frac{d \log MSD}{d \log t} \tag{5.2}$$

where MSD is the mean square displacement curve of the $TFSI^-$ molecules. Typically, $\beta(t) = 1$ corresponds to a linear function of time, $\beta(t) > 1$ to a super-diffusive regime, and for $\beta(t) < 1$, the dynamics is in subdiffusive regime. Calculation for $TFSI^-$ at 300 K for our three cells, after 400 ps, led to $\beta(t)$ values of $\approx$ 0.59, 0.55, and 0.53, respectively. These values indicate they all fall in the subdiffusive regime. Here again,

the very close value obtained for the 10847, and 18133 atoms cells advocates for a final choice of 10847 atoms box of simulation.

Table 5.1: Calculated diffusion constant of counter-ions in three Neutral cell size of chain length 6C (6C:N) at 300 K.

Poly-nuclear size	D_{eff} $(10^{-5}cm^2/s)$	l_{cut} (Å)	ρ (g/cm^3)
5606	0.10	20	0.82
10847	0.091	20	0.84
18133	0.085	20	0.86

5.5 Dynamic properties of counter-ions

In the literature and to our knowledge, no molecular dynamics (MD) simulations are available for the calculation of the diffusion coefficients of this complex immersed in ACN solvent. We have decided to carry out a comprehensive study of the diffusion constants of the 3D fully-reticulated complexes in ACN solvent molecules over the range of temperatures relevant to industrial and technological applications. The primary objective of the current study is to report an extensive series of MD simulations for the diffusion coefficients of counter-ions for Neutral and Full loaded in ACN for a wide range of temperatures (up to 500 K).

5.5.1 Effect due to chain length size

The minimum size of the system is obtained, we continue our study for both the neutral and fully loaded systems, with alkyl chains of varying length (4C and 6C). To be consistent, the spatial extent of the poly-nuclear compounds will vary according to the length of the alkyl chain, but a solvated box with a dimension of 15Å is kept constant. The cavity region, C_R, is particularly interesting to study since this region sees its size reduced together with the chain length. This is expected to affect the counter-ion diffusion and the density. During the loading process, free counter-ions present in these cavities move through the medium made of the ACN solvent molecules (which actually fill the cavities) to come and surround the active centers. To perform this study, we fixed the temperature at 300 K.

Table 5.2: Bond lengths and the effective diffusion constant of the counter-ions reported at 300 K. All bond lengths are given in **Å**.

	MD Simulation			
	N		FL	
$Fe-N$	2.0 ± 0.02		2.0 ± 0.04	
$C1-C1'$	1.50 ± 0.02		1.50 ± 0.03	
$N-C1$	1.35 ± 0.01		1.35 ± 0.02	
	4C	6C	4C	6C
D_{eff} $(10^{-5}cm^2/s)$	0.047	0.095	0.029	0.077

In Table 5.2, we report the diffusion constants for 4C and 6C alkyl chains, as well as selected bond lengths. These latter corroborate nicely with the DFT results. Figure 5.8, displays the mean square displacements.

Our first remark will address the difference of behavior between the 4C and 6C neutral compounds: MSD curve for 6C chain shows a larger diffusivity than the one of the 4C chain. This is also true for the fully-loaded system. We explain this phenomenon by the larger size of the cavities in the case of the 6C chain, allowing a larger displacement of the counter-ions: they diffuse more freely than in the 4C chain.

Our second remark emphasizes that, for both 4C and 6C chains, the diffusivity systematically lowers when the system is loaded. With a degree of oxidation passing from 2+ to 3+, counter-ions are seen more efficiently trapped all around the active centers. Consequently, the diffusivity is lowered.

Finally, If we compare all these values to ones of bi-nuclear compounds (which were studied in the previous chapter) they are lowered by a factor of ≈10 for both neutral and fully loaded case. The enclosure of the $TFSI^-$ ions inside the cavities limits the diffusivity of these latter.

As a comparison, Ebadi *et al.*, simulated the system ($PEO/LiTFSI$) in the presence of Li slab presenting a wall and calculate the diffusion of $TFSI^-$ anions in the bulk and close to the surface region. Their finding revealed that the dynamics of the $TFSI^-$ were not connected to PEO and Li and displayed a low diffusion constant (≈ 0.0020 $10^{-5}cm^2/s$) [153]. In the present study, our calculated diffusion coefficient is higher than what they have computed, the reason being that their system is bounded by the walls, while our system is in an amorphous polymer state, with cavity regions across each mono-nuclear unit. Overall, this finding reveals that large cavity is preferred for fast diffusion with, in addition, the benefit that it allows accumulating more Li/Na and counter-ions, hence increasing the energy density of the system. From the above Eq. 5.2,

after 500 ps at 300 K, $\beta(t)$ for 4C and 6C Neutral system is 0.46 and 0.56, respectively whereas, for fully loaded it is 0.40 and 0.48, respectively. Which shows they all fall in the subdiffusive regimes.

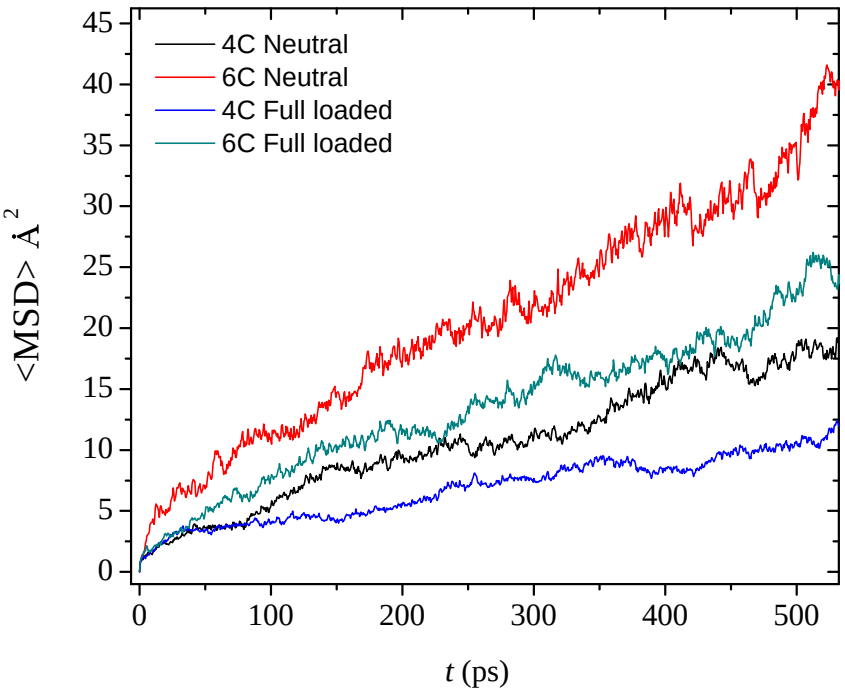

Figure 5.8: MSD plot of counter-ions for chain 4C and 6C with respect to simulation time t at 300 K.

5.5.2 Effect of temperature

Next, we consider the effect of temperature on the diffusivity of counter-ions. For this study, we have considered the fully loaded system with the 6C chain, which means that the cavity region is vast compared to the 4C chain. With current fixed atomic charges, the density is 0.86 g/cm^3 at 300 K. After we have equilibrated the system at 300 K, the temperature of the system is increased stepwise to 500 K, a little bit higher than the boiling point of ACN[2]. From Figures 5.9 (a) and (b), it is seen that, with increasing temperature the diffusion increases gradually and $\beta(t)$ also. After 400 ps the values for $\beta(t)$ for temperature T = 300, 350, 375, 400, and 500 K are 0.44, 0.60, 0.73, 0.78, and 0.85, respectively. Looking at the Figure 5.9 (b), the simulated diffusion constant almost

[2]https://en.wikipedia.org/wiki/Acetonitrile

follows the Arrhenius function, $D = Ae^{-E_a/RT}$ with an activation energy, E_a, estimated from our plot, found to be 18.652 kJ/mol over the temperature range of 300 K to 500 K. If the behavior is found exactly Arrhenius for low temperature values, the values for higher temperatures deviate slightly from the Arrhenius function. We believe this deviation could be a result of a too-brief simulation run since we have simulated our system for only 1000 ps: at higher temperatures, the number of paths of diffusion is sense to increase and a larger time of simulation can be necessary to investigate all of them. Karu *et. al.*, have investigated the activation energy of various ionic liquids for electrochemical application [48]. For $[TFSI]^-$ $[BMIm]^+$ ionic pair, they have reported the experimental activation energy of 27.50 kJ/mol in temperature range of 278.15 – 373.15 K. If a direct comparison to our data is not possible, (the obtained values depend too much on the choice of the system), the order of magnitude remains correct. Tsuzuki *et al.*, have also reported the diffusion of these ions in NPT ensemble and they have deduced that longer simulations give different diffusion values as compared to briefer simulation [154]. They have calculated the diffusion of coefficient from the data of 12 ns simulation for $[TFSI]^-$ $[BMIm]^+$ and found 0.59 $\times 10^{-7} cm^2/s$ at 350 K, whereas, the experimental value is known to be 12 $\times 10^{-7} cm^2/s$. Similar, studies done at 4 ns simulation gives a value of 9.7 $\times 10^{-7} cm^2/s$. As suggested by the authors, these discrepancies could be reduced by carefully refining their force field model. We hope our model does not induce such a deviant behavior.

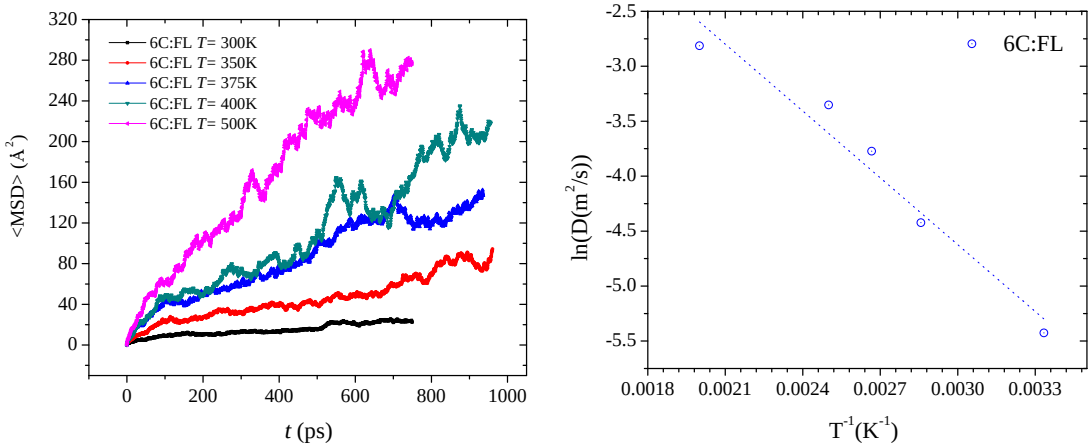

Figure 5.9: (a) MSD plot of counter-ions for chain 6C for full loaded system with respect to simulation time *t*. (b) Plot of diffusion constant of counter-ions with respect to temperature.

In Figure 5.10, we have plotted the calculated density as a function of temperature. This plot reveals that, with increasing temperature, the density of the system, for both 4C and 6C chains, decreases. Whatever the temperature may be, the density of the compound using 4C chains is found higher than the density of the compound using the 6C chains. This has to be related to the denser packing imposed by the smaller 4C cavity regions. By comparing with the coefficients of diffusion that we have calculated in Table 5.2, it follows that the diffusion coefficient entertains an inverse relation, $D_{eff} \approx 1/\rho$, with the density, which can be considered as a useful parameter for designing this material for cathode application.

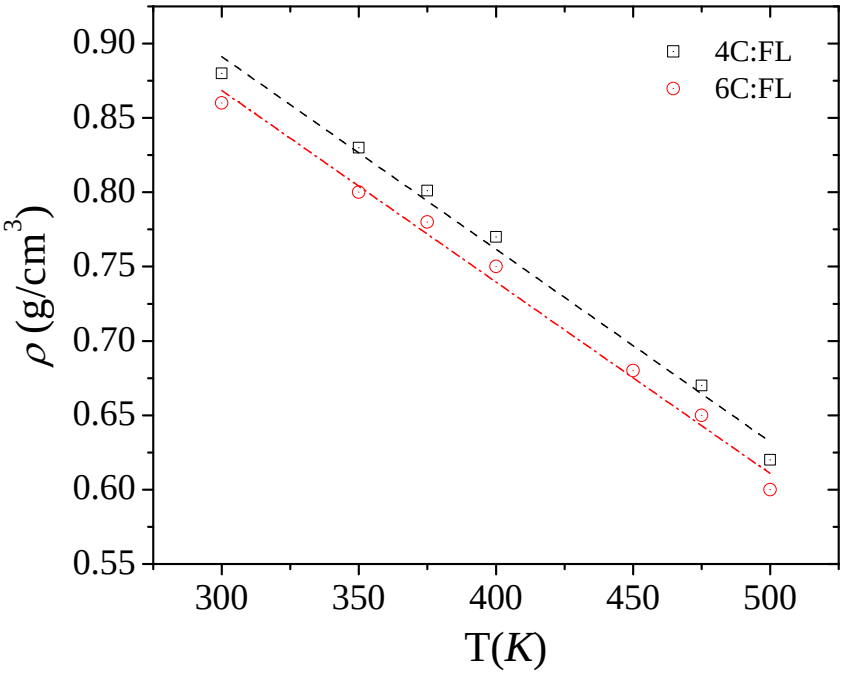

Figure 5.10: Variation of Full loaded complex density for two chains as a function of temperature.

5.6 Transient state

Let's consider the simplest model that can be considered in tackling the gradual build-up of the loading process. We have termed this intermediate state as mixed or transient state. In Figure 5.11, a schematic sketch of the model is shown. In this model, we

approximate our setup with the loaded complex in the center of the Neutral complex. The corresponding charges are fixed according to the neutral and loaded states, which we have already obtained. In the center of the complex, near the loaded region, the location of the counter-ions are initialized far away from the active centers, deep inside the cavity regions.

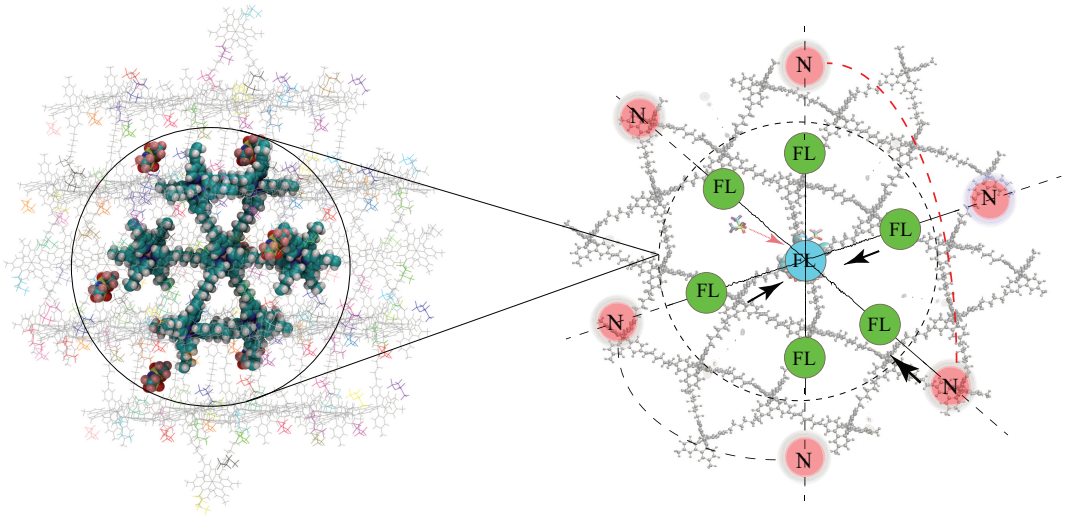

Figure 5.11: Schematic representation for a full loaded (FL) with counter-ions in the vicinity of neutral (N) complex. The green color shows the initiation of the loading process.

To calculate the diffusion constant we have followed the same procedure as described in the previous sections but now for a longer duration that is for 2.5 ns. In Figure 5.12, MSD plot for the transient state is shown. This plot is interesting because the diffusion pattern is a typical characteristic of a biological system, in particular, the diffusion of proteins in a cell. From the plot we see up to 400 ps the displacement is linear resembling the random walk. After that, it is flattened out for further 600 ps. During this time frame, the motion is confined. This pattern is repeated but confined time frame is shortened from 1500 to 1750 ps. This motion we have termed as *walking confined diffusion*. The interpretation of the motion, what we observed from the MD run, can be understood in the following way. During the simulation run, these counter-ions are drifted towards the loaded state and during this time frame they have to overcome some barriers, meanwhile they are wondering and this motion is reflected on the graph as flattened out. Eventually, we see this flattened out curve decrease in size over the

long run. The diffusion constant for these counter-ions is 0.09 $\times 10^{-5} cm^2/s$ which by the previous studies resembles the loaded state.

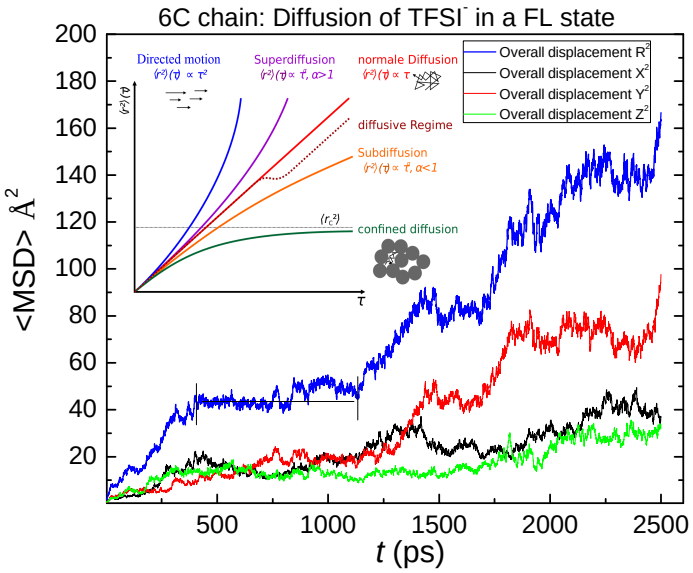

Figure 5.12: MSD plot of counter-ions for chain 6C with respect to simulation time t at 300 K. The Blue curve shows the overall displacement of the counter-ions during the loading process. Other color shows the displacement in each coordinates axis.

5.7 Conclusion

We successfully created the 3D reticulated poly-nuclear structure and showed it is the one of the possible structure that could be conceived with the information provided by the experimental group by exploiting the connected unit structure property. The cavity regions also impact the diffusion of the ions and the trend shows with a large cavity the ions have more freedom to roam.

■

Chapter 6

Conclusions and perspectives

At the turn of this thesis, we outline the main results that resulted from this work by contributing new advancement in the field of modeling polymer batteries.

If electrochemical properties of the polymer batteries are usually (in the literature) derived from calculations involving the mono-nuclear considered in various degrees of oxidation in empty medium, our approach has rather consisted to mimic the best functioning conditions of these polymers when used as battery devices. Charged positively as loaded, the main parameters affecting the geometries and energies of the polymers are the negatively charged counter-ions of the electrolyte which penetrate the cathode material during the loading process. Introducing these counter-ions in the calculation is not common place, but we considered that their effects be crucial to model our batteries in working conditions and that it constitutes one step further to model such systems. However, the huge number of degrees of freedom associated with the introduction of the counter-ions has considerably complicated our research of the ground state properties of both the mono-nuclear and bi-nuclear compounds formed from our TM complexes (a considerable amount of time were devoted to this part in this thesis) and we can understand why such a study is hardly met in literature. But, we managed to succeed in our goals as the comparison of our calculated voltages with the experiments proved it (any metastable state arising from an inappropriate geometry, electronic structure convergence failure or wrong spin-state preparation were leading to a very poor description of the voltages). We did not introduce the ions (Li^+ or Na^+) in our calculations, which are expelled far away from the positively charged centers and whose influence is screened by the solvent molecules. Both ions and solvent molecules belong to the second sphere of influence compared to the counter-ions that are found in close location to the complexes.

To carry out this first study, we used First Principles methods. The case of bi-

nuclear compounds was the very limit study case for these compounds given the CPU time needed and memory requested to obtain the ground state in a quite reasonable lapse of time. The reliability of these methods as well as their power of prediction has not to be proven anymore, but the choice of the most adequate exchange and correlation potential used in the functional of the density still remains a delicate problem. In the literature, the PBE0 approximation was found to be the best match; this functional was chosen to be the best to represent the properties of mono-nuclear in empty space, without the surrounding counter-ions. Our calculations using this approximation corroborates these results, but we rapidly realized its inability to cope with the compounds in the field of counter-ions. Moreover, its unexplained ability to create delocalized states in our systems (in agreement with independent calculations) sheds suspicions on its usage. Actually this functional is known to produce the opposite behavior. Thus, we had to undertake a series of calculations using numerous exchange and correlation functionals in order to discover an alternative to this functional. The PBE functional was finally found the most valuable to represent in a correct manner all the properties of the compounds (let's say in agreement with our intuitive knowledge of these systems). This PBE functional were perfectly capable of keeping the expected ligand field picture for the d orbitals of the TM but also providing accurate interatomic distances, conformations, and voltages. For the loaded system, the ligand field completely vanishes within the PBE0 approximation and the d-bands are seen dispersed in deeper levels. This rehabilitation of the PBE approximation, only able to cope with our polymerized polymers in working conditions, is an important and fundamental point of this work.

Regarding the results (Fe and Ru complex), we report that the counter-ions affect the TM complexes in a large manner during the loading process. According to their size and conformation, their exact location with respect to the complex will vary. But they all produce the same effects on the TM and *dmbpy* arrangements: they do not create chemical bonds and they adapt their location in order to optimize the electrostatic interactions with the active centers. Thus, no major influence is noticed on the voltages. Great expectations were formulated regarding the role played by the length of the alkyl chain in the bi-nuclear compounds to tune the properties of the batteries. This study has actually revealed that very negligible effects have to be declared on the electronic structure but also, as a consequence, on the voltages. The only noticeable point is the general conformation of the bi-nuclear compound since, for the largest length of alkyl chain, this latter is found to bend in order to optimize the inner electrostatic interactions. This is due to the very localized character of the d-orbitals of the TM within the ligand field scheme. Regarding the Cu based complex, our results show

that large structural deformations are observed upon loading, making it less effective for the battery application. To complete this part, let us mention that the voltages corroborate nicely with the experimental results under the external perturbations we apply (counter-ions).

In the second part of the thesis, we have developed an atomistic potential relying on the Force Field scheme for the Iron complex in order to study the dynamic properties of this compound at larger simulation scale. If many parameters entering the writing of the empirical potential were already available in the literature, the ones corresponding to the charged Fe with its surrounding *dmbpy* were not. To specifically develop them, we made an intensive use of the DFT data (energies, geometries, spin-state configurations and calculated vibrational properties). We used the Seminario method to obtain these parameters within the framework of the Amber code. Let's mention that we have ignored the improper and dihedral terms and retain the angle and bond parameters which are sufficient to maintain the octahedral geometry of the complex. However, it should be pointed out that these neglected parameters in the case of the Cu complex might be important for which an important relative displacement of the *dmbpy* planes is observed (DFT calculations). This development was also the occasion to provide theoretical IR spectra for the polymers since the vibrational frequencies of the molecules had to be calculated to achieve the determination of our parameters. Our potential was validated on the bi-nuclear compounds for which the properties are known from our DFT calculations and independent experiments.

Last chapter was devoted to the exploitation of the potential. Here, we investigate more realistic cathode materials by building a fully reticulated polymer presenting a 3D structure. Building such a cell was a challenge by itself. Computational techniques (written in *python* language) were developed specifically to create a 3D structure of transition metal complexes satisfying the condition to be fully reticulated; the location of each mono-nuclear in space had to be determined so that every six "plugging" carbons of the three *dmbpy* molecules surrounding the Fe ion be connected to an alkyl chain, all these alkyl chains being plugged to a complex. For this purpose, starting from a central complex, we added the alkyl chain on that pattern with a complex pattern at their other tip. We wrote an algorithm capable to rotating and shifting these latter so that this new layer of the pattern be able to connect between each other, and continue the job, layer per layer so that to obtain a spherical cluster made of fully connected complexes. Bounding conditions had also to be fixed. We used methyl fragments to connect the remaining unplugged carbon sites of the *dmbpy* at the external surface of the cluster. Our building makes appear that large cavity regions are compulsory to

allow the full reticulation. They have also to be seen as diffusion channels. A procedure aiming at fixing reliable and physical effective charges on each atom of the simulation cell (compatible with DFT results) has been developed. These charges are obtained at 0 K from various adequate configurations by means of DFT calculations.

A series of molecular dynamics simulation using these initial cells was undertaken to calculate the diffusion constants as well as the equilibrium geometries of our compounds at room temperature. We saw in the large cavity regions the counter-ions drift, diffuse, and flip around their axis. This cavity region is particularly important to study the transport properties of the counter-ions. As already encountered in the DFT calculations for which the bi-nuclear units were collapsing/bending during the optimization of its geometry, the 3D compound tends to collapse as we do not introduce solvent molecules. When we solvate our complex with ACN molecules, the compound acquires a stabilization state which avoids this collapse while maintaining an overall density close one of the ACN solvents. Consequently, we observed that the diffusivity of the counter-ions is considerably lower with respect to the case where no solvent is used. Moreover, our initial MD results show for 6C chain the diffusivity is large as compared to the 4C chain. Which shows for battery application the large cavity region is more preferred for the ions movement. This result, however, in terms of diffusivity also reinforces the choice for this chain length. Further, the diffusivity of counter-ions in the porous structure resembles the biological system, like proteins diffusion in a cell, where diffusion is not linear rather it follows the confined diffusion path.

Future research lies in exploring high dimensional polymers for Cu based complex with different ligands. Since we observed *bpy* ligands during oxidation brings about a large conformation change which renders it inapplicable for practical use. One solution is to use other ligands to curb the large conformation yet observing the same electrochemical properties. With regards to the macromolecular structure, we hope to study the transport properties of counter-ions in the presence of some defect. The defects we assume are the absence of alkyl chains. Our hope is to construct the potential, RESP charge scheme and study the structural effects and transport properties.

■

References

[1] Novák, P.; Müller, K.; Santhanam, K. S. V.; Haas, O. *Chemical Reviews* **1997**, *97*, 207–282.

[2] Liang, Y.; Tao, Z.; Chen, J.; *Organic electrode materials for rechargeable lithium batteries*; 2012.

[3] Nakahara, K.; Iwasa, S.; Satoh, M.; Morioka, Y.; Iriyama, J.; Suguro, M.; Hasegawa, E. *Chemical Physics Letters* **2002**, *359*, 351–354.

[4] Nishide, H.; Iwasa, S.; Pu, Y. J.; Suga, T.; Nakahara, K.; Satoh, M. In *Electrochimica Acta*; Pergamon; pp 827–831.

[5] Burkhardt, S. E.; Bois, J.; Tarascon, J. M.; Hennig, R. G.; Abruña, H. D. *Chemistry of Materials* **2013**, *25*, 132–141.

[6] Li, Q.; Chen, J.; Fan, L.; Kong, X.; Lu, Y. *Green Energy Environment* **2016**, *1*, 18–42.

[7] Armand, M.; Grugeon, S.; Vezin, H.; Laruelle, S.; Ribière, P.; Poizot, P.; Tarascon, J. M. *Nature Materials* **2009**, *8*, 120–125.

[8] Chen, H.; Armand, M.; Demailly, G.; Dolhem, F.; Poizot, P.; Tarascon, J. M.; *From biomass to a renewable LiXC6O6 organic electrode for sustainable li-ion batteries*; 2008.

[9] Liang, Y.; Tao, Z.; Chen, J.; *Organic electrode materials for rechargeable lithium batteries*; 2012.

[10] Dai, G.; Wang, X.; Qian, Y.; Niu, Z.; Zhu, X.; Ye, J.; Zhao, Y.; Zhang, X. *Energy Storage Materials* **2018**, *16*, 236–242.

[11] Singh, V. K.; Rao, O. S.; Singh, R. A. *Indian Journal of Engineering and Materials Sciences* **1996**, *3*, 201–206.

[12] Manuel, J.; Kim, J. K.; Matic, A.; Jacobsson, P.; Chauhan, G. S.; Ha, J. K.; Cho, K. K.; Ahn, J. H. In *Materials Research Bulletin*; Pergamon; pp 2815–2818.

[13] Nyholm, L.; Nyström, G.; Mihranyan, A.; Strømme, M. *Advanced Materials* **2011**, *23*.

[14] Nyström, G.; Razaq, A.; Strømme, M.; Nyholm, L.; Mihranyan, A. *Nano Letters* **2009**, *9*, 3635–3639.

[15] Muench, S.; Wild, A.; Friebe, C.; Häupler, B.; Janoschka, T.; Schubert, U. S. *Chemical Reviews* **2016**, *116*, 9438–9484.

[16] Kim, J.; Kim, J. H.; Ariga, K. *Joule* **2017**, *1*, 739–768.

[17] Nakahara, K.; Oyaizu, K.; Nishide, H. *Chemistry Letters* **2011**, *40*, 222–227.

[18] Suguro, M.; Iwasa, S.; Kusachi, Y.; Morioka, Y.; Nakahara, K. *Macromolecular Rapid Communications* **2007**, *28*, 1929–1933.

[19] Liang, Y.; Jing, Y.; Gheytani, S.; Lee, K.-Y.; Liu, P.; Facchetti, A.; Yao, Y. *Nature Materials* **2017**, *16*, 841–848.

[20] Lepretre, J. C.; Bar, B.; Chauvin, J.; Deronzier, A.; Lefebvre, B. *Inorganic Chemistry Communications* **2004**, *7*, 47–50.

[21] Guilmin, R.; Alloin, F.; Molton, F.; Leprêtre, J.-C. *Electrochimica Acta* **2017**, *232*, 182–191.

[22] Mun, J.; Lee, M.-J.; Park, J.-W.; Oh, D.-J.; Lee, D.-Y.; Doo, S.-G. *Electrochemical and Solid-State Letters* **2012**, *15*, A80.

[23] Emmenegger, F.; Williams, M. E.; Murray, R. W. *Inorganic Chemistry* **1997**, *36*, 3146–3151.

[24] England, J.; Scarborough, C. C.; Weyhermüller, T.; Sproules, S.; Wieghardt, K. *European Journal of Inorganic Chemistry* **2012**, *2012*, 4605–4621.

[25] Scarborough, C. C.; Wieghardt, K. *Inorganic Chemistry* **2011**, *50*, 9773–9793.

[26] Swart, M. *Journal of Chemical Theory and Computation* **2008**, *4*, 2057–2066.

[27] Goel, S.; Ph.D. thesis; 2005.

[28] Goj, L. A.; Blue, E. D.; Delp, S. A.; Gunnoe, T. B.; Cundari, T. R.; Pierpont, A. W.; Petersen, J. L.; Boyle, P. D. *Inorganic Chemistry* **2006**, *45*, 9032–9045.

[29] Hathaway, B.; Billing, D. *Coordination Chemistry Reviews* **1970**, *5*, 143–207.

[30] Kulik, H. J.; Marzari, N. *Journal of Chemical Physics* **2010**, *133*, 114103–124303.

[31] Johnson, P. S.; Cook, P. L.; Zegkinoglou, I.; García-Lastra, J. M.; Rubio, A.; Ruther, R. E.; Hamers, R. J.; Himpsel, F. J. *Journal of Chemical Physics* **2013**, *138*.

[32] Balzani, V.; Juris, A.; Venturi, M.; Campagna, S.; Serroni, S. *Chemical Reviews* **1996**, *96*, 759–834.

[33] Cabrera, P. J.; Yang, X.; Suttil, J. A.; Brooner, R. E. M.; Thompson, L. T.; Sanford, M. S. *Inorganic Chemistry* **2015**, *54*, 10214–10223.

[34] Constable, E. C.; John Wiley Sons. *Metals and ligand reactivity : an introduction to the organic chemistry of metal complexes*; VCH, 1996.

[35] Liska, P.; Vlachopoulos, N.; Nazeeruddin, M. K.; Comte, P.; Graetzel, M. *Journal of the American Chemical Society* **1988**, *110*, 3686–3687.

[36] Parkins, A. W. *Applied Organometallic Chemistry* **1998**, *12*, 294–294.

[37] Rong, D.; Anson, F. C. *Journal of Electroanalytical Chemistry* **1996**, *404*, 171–177.

[38] Kaes, C.; Katz, A.; Hosseini, M. W. *Chemical Reviews* **2000**, *100*, 3553–3590.

[39] Zhang, Z.; Awaga, K. *MRS Bulletin* **2016**, *41*, 883–889.

[40] Xu, G.; Nie, P.; Dou, H.; Ding, B.; Li, L.; Zhang, X. *Materials Today* **2017**, *20*, 191–209.

[41] Wang, Z.; Wang, S.; Wang, A.; Liu, X.; Chen, J.; Zeng, Q.; Zhang, L.; Liu, W.; Zhang, L. **2018**.

[42] Batten, S. R.; Champness, N. R.; Chen, X.-M.; Garcia-Martinez, J.; Kitagawa, S.; Öhrström, L.; O'Keeffe, M.; Paik Suh, M.; Reedijk, J. *Pure and Applied Chemistry* **2013**, *85*, 1715–1724.

[43] Fromm, K. M.; *Coordination polymer networks with s-block metal ions*; 2008.

[44] Zheng, Q.; Niu, Z.; Ye, J.; Zhang, S.; Zhang, L.; Li, L.; Zhao, Y.; Zhang, X. *Advanced Functional Materials* **2017**, *27*, 1604299.

[45] Baik, M.-H.; Friesner, R. A. *The Journal of Physical Chemistry A* **2002**, *106*, 7407–7412.

[46] Tavernelli, I.; Vuilleumier, R.; Sprik, M. *Physical Review Letters* **2002**, *88*, 213002.

[47] Krossing, I.; Raabe, I.; *Noncoordinating anions - Fact or fiction? A survey of likely candidates*; 2004.

[48] Karu, K.; Ruzanov, A.; Ers, H.; Ivaništšev, V.; Lage-Estebanez, I.; García de la Vega, J. *Computation* **2016**, *4*, 25.

[49] Ue, M.; Sasaki, Y.; Tanaka, Y.; Morita, M. In *Modern Aspects of Electrochemistry*, 2014; Vol. 58, pp 93–165.

[50] Xu, K. *Chemical Reviews* **2004**, *104*, 4303–4418.

[51] Park, M.; Zhang, X.; Chung, M.; Less, G. B.; Sastry, A. M. *Journal of Power Sources* **2010**, *195*, 7904–7929.

[52] Tarascon, J.-M. M.; Armand, M. *Nature* **2001**, *414*, 359–367.

[53] Cheng, X.-B. B.; Zhang, R.; Zhao, C.-Z. Z.; Wei, F.; Zhang, J.-G. G.; Zhang, Q. *Advanced Science* **2016**, *3*, 1500213.

[54] Beck, F.; Rüetschi, P. *Electrochimica Acta* **2000**, *45*, 2467–2482.

[55] Stephan, A. M.; *Review on gel polymer electrolytes for lithium batteries*; 2006.

[56] Fenton, D. E.; Parker, J. M.; Wright, P. V. *Polymer* **1973**, *14*, 589.

[57] Croce, F.; Appetecchi, G. B.; Persi, L.; Scrosati, B. *Nature* **1998**, *394*, 456–458.

[58] Li, Q.; Itoh, T.; Imanishi, N.; Hirano, A.; Takeda, Y.; Yamamoto, O. *Solid State Ionics* **2003**, *159*, 97–109.

[59] Appetecchi, G. B.; Hassoun, J.; Scrosati, B.; Croce, F.; Cassel, F.; Salomon, M. *Journal of Power Sources* **2003**, *124*, 246–253.

[60] Dai, Y.; Wang, Y.; Greenbaum, S.; Bajue, S.; Golodnitsky, D.; Ardel, G.; Strauss, E.; Peled, E. *Electrochimica Acta* **1998**, *43*, 1557–1561.

[61] Golodnitsky, D. *Journal of The Electrochemical Society* **1997**, *144*, 3484.

[62] Wieczorek, W.; Raducha, D.; Zalewska, A.; Stevens, J. R. *The Journal of Physical Chemistry B* **1998**, *102*, 8725–8731.

[63] Weston, J.; Steele, B. *Solid State Ionics* **1982**, *7*, 75–79.

[64] Sequeira, C.; Santos, D. *Polymer electrolytes*; Woodhead Publishing Limited, 2010.

[65] Smyrl, W. H.; Lien, M. *Applications of Electroactive Polymers* **1993**, 29–74.

[66] Dudley, J. T.; Wilkinson, D. P.; Thomas, G.; LeVae, R.; Woo, S.; Blom, H.; Horvath, C.; Juzkow, M. W.; Denis, B.; Juric, P.; Aghakian, P.; Dahn, J. R. *Journal of Power Sources* **1991**, *35*, 59–82.

[67] Freemantle, M. *Focus on Catalysts* **2010**, *2010*, 8.

[68] Watanabe, M.; Thomas, M. L.; Zhang, S.; Ueno, K.; Yasuda, T.; Dokko, K. *Chemical Reviews* **2017**, *117*, 7190–7239.

[69] Macfarlane, D. R.; Tachikawa, N.; Forsyth, M.; Pringle, J. M.; Howlett, P. C.; Elliott, G. D.; Davis, J. H.; Watanabe, M.; Simon, P.; Angell, C. A. *Energy Environmental Science Royal Society of Chemistry* **2014**, *7*, 232–250.

[70] Kerner, M.; Plylahan, N.; Scheers, J.; Johansson, P. *Physical Chemistry Chemical Physics* **2015**, *17*, 19569–19581.

[71] Moreno, M.; Simonetti, E.; Appetecchi, G. B.; Carewska, M.; Montanino, M.; Kim, G.-T.; Loeffler, N.; Passerini, S. *Journal of The Electrochemical Society* **2017**, *164*, A6026–A6031.

[72] Armand, M.; Endres, F.; MacFarlane, D. R.; Ohno, H.; Scrosati, B. *Nature Materials* **2009**, *8*, 621–629.

[73] Osada, I.; De Vries, H.; Scrosati, B.; Passerini, S.; *Ionic-Liquid-Based Polymer Electrolytes for Battery Applications*; 2016.

[74] Pokhodenko, V.; Koshechko, V.; Krylov, V. *Journal of Power Sources* **1993**, *45*, 1–5.

[75] Meyer, W. H. *Advanced Materials* **1998**, *10*, 439–448.

[76] Yamagata, M.; Tanaka, K.; Tsuruda, Y.; Sone, Y. *Electrochemistry* **2015**, *83*, 918–924.

[77] Kim, J.-K.; Scheers, J.; Park, T. J.; Kim, Y. *ChemSusChem* **2015**, *8*, 636–41.

[78] Ue, M. *Journal of The Electrochemical Society* **1994**, *141*, 3336.

[79] Dahn, J. R.; von Sacken, U.; Juzkow, M. W.; Aljanaby, H. *Journal of the Electrochemical Society* **1991**, *138*, 2207–2211.

[80] Newman, G.H., Francis, R. W., Gaines, L. H., Rao, B. M. *J. Electrochem. Soc.* **1980**, *127*, 2025.

[81] Sloop, S. E.; Pugh, J. K.; Wang, S.; Kerr, J. B.; Kinoshita, K. *Electrochemical and Solid-State Letters* **2001**, *4*, A42.

[82] Walker, C. W.; Cox, J. D.; Salomon, M. *Journal of The Electrochemical Society* **1996**, *143*, L80–L82.

[83] Ue, M.; Murakami, A.; Nakamura, S. *Journal of The Electrochemical Society* **2002**, *149*, A1572.

[84] Younesi, R.; Veith, G. M.; Johansson, P.; Edström, K.; Vegge, T. *Energy Environ. Sci.* **2015**, *8*, 1905–1922.

[85] Krause, L. J.; Lamanna, W.; Summerfield, J.; Engle, M.; Korba, G.; Loch, R.; Atanasoski, R. *Journal of Power Sources* **1997**, *68*, 320–325.

[86] Foropoulos, J.; DesMarteau, D. D. *Inorganic Chemistry* **1984**, *23*, 3720–3723.

[87] Shkrob, I. A.; Marin, T. W.; Zhu, Y.; Abraham, D. P. *Journal of Physical Chemistry C* **2014**, *118*, 19661–19671.

[88] Dominey, L. A.; Koch, V. R.; Blakley, T. J. *Electrochimica Acta* **1992**, *37*, 1551–1554.

[89] Naoi, K. *Journal of The Electrochemical Society* **1999**, *146*, 462.

[90] Wang, X.; Yasukawa, E.; Kasuya, S. *Journal of The Electrochemical Society* **2000**, *147*, 2421.

[91] Yang, H.; Kwon, K.; Devine, T. M.; Evans, J. W. *Journal of The Electrochemical Society* **2000**, *147*, 4399.

[92] Hathaway, B. J.; Billing, D. E. *The electronic properties and stereochemistry of mono-nuclear complexes of the copper(II) ion*; Elsevler Publishmg Company, Ed.; Amsterdam, 1969.

[93] Chaurin, V.; Constable, E. C.; Housecroft, C. E. **2006**.

[94] McCleverty, J. A.; Meyer, T. J. *Comprehensive coordination chemistry II : from biology to nanotechnology*; Elsevier Pergamon, 2004.

[95] Cohen, A. J.; Mori-Sánchez, P.; Yang, W. *Chemical Reviews* **2012**, *112*, 289–320.

[96] Jones, R. O. *Reviews of Modern Physics* **2015**, *87*, 897–923.

[97] Kohn, W.; Sham, L. J. *Physical Review* **1965**, *140*, A1133–A1138.

[98] Hohenberg, P.; Kohn, W. *Phys. Rev.* **1964**, *136*, B864–B871.

[99] Perdew, J. P.; Burke, K.; Ernzerhof, M. *Physical Review Letters* **1996**, *77*, 3865–3868.

[100] Ernzerhof, M.; Scuseria, G. E. *Journal of Chemical Physics* **1999**, *110*, 5029–5036.

[101] Furche, F.; Perdew, J. P. *The Journal of Chemical Physics* **2013**, *044103*, 44103–154104.

[102] Becke, A. D. *The Journal of Chemical Physics* **1993**, *98*, 5648–5652.

[103] Adamo, C.; Barone, V. *The Journal of Chemical Physics* **1999**, *110*, 6158–6170.

[104] Tran, F.; Blaha, P.; Schwarz, K.; Novák, P. *Physical Review B - Condensed Matter and Materials Physics* **2006**, *74*, 155108.

[105] Tao, J.; Perdew, J. P.; Staroverov, V. N.; Scuseria, G. E. *Physical Review Letters* **2003**, *91*, 146401.

[106] Jensen, K. P.; Roos, B. O.; Ryde, U. *Journal of Chemical Physics* **2007**, *126*, 014103.

[107] Ioannidis, E. I.; Kulik, H. J. *Journal of Chemical Physics* **2015**, *143*, 034104.

[108] Ioannidis, E. I.; Kulik, H. J. *Journal of Physical Chemistry A* **2017**, *121*, 874–884.

[109] Frenkel, D.; Smit, B. *Understanding Molecular Simulation, Second Edition: From Algorithms to Applications*, 2001.

[110] Suter, J. L.; Anderson, R. L.; Greenwell, H. C.; Coveney, P. V. **2009**.

[111] Frisch; et al.; *Gaussian 09, Revision D.01*; 2016.

[112] Weigend, F.; Ahlrichs, R. *Physical Chemistry Chemical Physics* **2005**, *7*, 3297.

[113] Weigend, F. *Physical Chemistry Chemical Physics* **2006**, *8*, 1057.

[114] O;Boyle, N. M.; Tenderholt, A. L.; Langner, K. M. *Journal of Computational Chemistry* **2008**, *29*, 839–845.

[115] Batten, S. R.; Murray, K. S.; Sinclair, N. J. *Acta Crystallographica Section C Crystal Structure Communications* **2000**, *56*, e320–e320.

[116] Figgis, B.; Skelton, B.; White, A. *Australian Journal of Chemistry* **1978**, *31*, 57.

[117] Biner, M.; Buergi, H. B.; Ludi, A.; Roehr, C. *Journal of the American Chemical Society* **1992**, *114*, 5197–5203.

[118] Rillema, D. P.; Jones, D. S. *J. Chem. Soc., Chem. Commun.* **1979**, *0*, 849–851.

[119] Young, D. C. *Chemistry computational chemistry A Practical Guide for Applying Techniques to Real-World Problems*; Wiley, 2001; Vol. 9.

[120] Bowman, D. N.; Jakubikova, E. *Inorganic Chemistry* **2012**, *51*, 6011–6019.

[121] Pierloot, K.; Vancoillie, S. *The Journal of Chemical Physics* **2006**, *1251*, 124303–124303.

[122] Johansson, P.; Gejji, S. P.; Tegenfeldt, J.; Lindgren, J.; Johansson Patrik; Gejji Shridhar P.; Tegenfeldta JoÈrgen; Lindgrena Jan *Electrochimica Acta* **1998**, *43*, 1375–1379.

[123] Herstedt, M.; Smirnov, M.; Johansson, P.; Chami, M.; Grondin, J.; Servant, L.; Lassègues, J. C.; Lass??gues, J. C. *Journal of Raman Spectroscopy* **2005**, *36*, 762–770.

[124] Watkins, T.; Buttry, D. A. *The Journal of Physical Chemistry B* **2015**, *119*, 7003–7014.

[125] Mootz, D.; Oellers, E.-J.; Wiebcke, M. *J. Am. Chem. Soc* **1987**, *109*, 1200–1202.

[126] Watkins, T.; Buttry, D. A. *The Journal of Physical Chemistry B* **2015**, *119*, 7003–7014.

[127] Furche, F.; Perdew, J. P. *Journal of Chemical Physics* **2006**, *124*, 114103–124303.

[128] Wang, M.; England, J.; Weyhermüller, T.; Wieghardt, K. *European Journal of Inorganic Chemistry* **2015**, *2015*, 1511–1523.

[129] O'Sullivan, C.; Murphy, G.; Murphy, B.; Hathaway, B. *Journal of the Chemical Society, Dalton Transactions* **1999**, *0*, 1835–1844.

[130] Murphy, G.; Nagle, P.; Murphy, B.; Hathaway, B. *Journal of the Chemical Society, Dalton Transactions* **1997**, *2*, 2645–2652.

[131] Foley, J.; Tyagi, S.; Hathaway, B. J. *Journal of the Chemical Society, Dalton Transactions* **1984**, *2*, 1–5.

[132] Ross C Walker UCSD, A. . R. M.

[133] Li, P.; Roberts, B. P.; Chakravorty, D. K.; Merz, K. M. *Journal of Chemical Theory and Computation* **2013**, *9*, 2733–2748.

[134] Chisholm, M. H.; Huffman, J. C.; Rothwell, I. P.; Bradley, P. G.; Kress, N.; Woddruff, W. H. *Journal of the American Chemical Society* **1981**, *103*, 4945–4947.

[135] Wilson, E. B. E. B.; Decius, J. C.; Cross, P. C. *Molecular vibrations : the theory of infrared and Raman vibrational spectra*; Dover Publications, 1980.

[136] Arnolds, H. *Progress in Surface Science* **2011**, *86*, 1–40.

[137] Grunenberg, J. *Computational Spectroscopy: Methods, Experiments and Applications*; Grunenberg, J., Ed.; Wiley-VCH Verlag GmbH Co. KGaA: Weinheim, Germany, 2010.

[138] Barone, V.; Wiley InterScience (Online service) *Computational spectroscopy : status and perspectives*; Wiley-Blackwell, 2010.

[139] Yamaguchi, Y.; Frisch, M.; Gaw, J.; Schaefer, H. F.; Stephen Binkley, J.; Schaefer III, H. F. *Citation: The Journal of Chemical Physics* **1986**, *84*, 2150.

[140] Lin, F.; Wang, R. *Journal of Chemical Theory and Computation* **2010**, *6*, 1852–1870.

[141] Seminario, J. M. *International Journal of Quantum Chemistry* **1996**, *60*, 1271–1277.

[142] Breneman, C. M.; Wiberg, K. B. *Journal of Computational Chemistry* **1990**, *11*, 361–373.

[143] Bayly, C. I.; Cieplak, P.; Cornell, W.; Kollman, P. A. *The Journal of Physical Chemistry* **1993**, *97*, 10269–10280.

[144] Cornell, W. D.; Cieplak, P.; Christopher, .; Bayly, I.; Kollman, P. A.; *Application of RESP Charges To Calculate Conformational Energies, Hydrogen Bond Energies, and Free Energies of Solvation*; Tech. Rep.; 1993.

[145] Li, P.; Merz, K. M. *Journal of Chemical Information and Modeling* **2016**, *56*, 599–604.

[146] Martínez, L.; Andrade, R.; Birgin, E. G.; Martínez, J. M. *Journal of Computational Chemistry* **2009**, *30*, 2157–2164.

[147] Li, P.; Song, L. F.; Merz, K. M. *The Journal of Physical Chemistry B* **2015**, *119*, 883–895.

[148] Einstein, A. *Annalen der Physik* **1905**, *322*, 549–560.

[149] Martin, R. L.; Haranczyk, M. *Crystal Growth Design* **2014**, *14*, 2431–2440.

[150] Norberto de Souza, O.; Ornstein, R. L.; *Effect of Periodic Box Size on Aqueous Molecular Dynamics Simulation of a DNA Dodecamer with Particle-Mesh Ewald Method*; Tech. Rep.; 1997.

[151] Yeh, I.-C.; Hummer, G. *The Journal of Physical Chemistry B* **2004**, *108*, 15873–15879.

[152] Hadi Ghatee, M.; Moosavi, F.; Reza Zolghadr, A. *Journal of Molecular Liquids* **2012**, *167*, 5–13.

[153] Ebadi, M.; Costa, L. T.; Araujo, C. M.; Brandell, D. *Electrochimica Acta* **2017**, *234*, 43–51.

[154] Tsuzuki, S.; Shinoda, W.; Saito, H.; Mikami, M.; Tokuda, H.; Watanabe, M. *The Journal of Physical Chemistry B* **2009**, *113*, 10641–10649.

Appendix A

DFT: Thermodynamic properties without methylation

A.1 Voltage without methylation

For comparison purpose, we have included non-methylation effect on a mono-nuclear center. In Figure A.1, energy difference for two $TFSI^-$ configuration embedded in a Metal complex is shown. The energy difference between *cis* and *trans* is $0.14eV$ for PBE and 0.3 eV for PBE0 functional. In Table A.1, voltages calculated with different functionals are shown. We could not report the V_{Ru} voltage for PBE functional due to electronic convergence problem specifically for ClO_4^- counter-ion. Different algorithms implemented in Gaussion09 code were tested with different geometry, but it fails. We also try to read the charge density with PBE0 functional and run at PBE level of theory yet it still fails to converge. It could be that the algorithm is lost in localizing on the metal center.

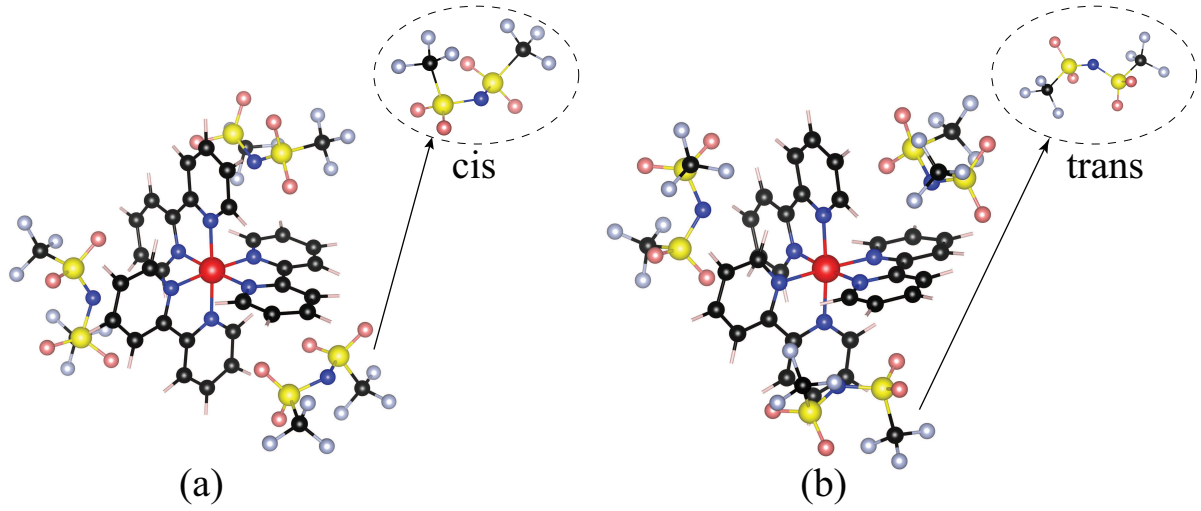

Figure A.1: Ground state structure for $[Fe(bpy)_3]^{3+}3TFSI$ complex without methylation. Two complexes are optimized with $TFSI^-$ (a) *cis* and (b) *trans*.

Table A.1: Relative voltages calculated for mono-nuclear complex in different electrolyte without methylation.

	PBE		PBE0	
Ci^-	$V_{Ru-Fe}(V)$	$V_{Cu-Fe}(V)$	$V_{Ru-Fe}(V)$	$V_{Cu-Fe}(V)$
ClO_4^-	-	-0.91	0.35	-1.20
PF_6^-	+0.16	-0.63	0.29	-1.07
$TFSI^-$	0.37	-0.74	0.4	-0.89

	APFD		B3PW91	
Ci^-	$V_{Ru-Fe}(V)$	$V_{Cu-Fe}(V)$	$V_{Ru-Fe}(V)$	$V_{Cu-Fe}(V)$
ClO_4^-	-	-	-	-
PF_6^-	0.04	-1.4	0.3	-0.9
$TFSI^-$	0.21	-1.13	0.24	-0.97

A.2 DOS and PDOS curve using GaussSum

The density of states (DOS) spectrum is convoluted using Gaussian curves of unit height and the specified full width at half-maximum (FWHM) in eV. Here full width at half-maximum controls the width of the Gaussian curves to convolute the DOS spectra. Next, the percentage contribution of a group of atoms or each atom to each molecular

orbital is calculated based on Mulliken Population Analysis (MPA). As it is known in literature MPA has some well-known deficiencies which can lead to unphysical values such as negative percentage contributions. So, in this case, we are not interested in the exact figures but the trend across a group of compounds. Partial density of states spectra (PDOS) is plotted with each one stacked on top of the previous one, which means the line at the greatest height is equal to the sum of all of the partial density of states, and hence equal to the total density of states spectrum.

Appendix B

DFT: Basis sets analysis

B.1 Basis set effect without counter-ions

In choosing an exchange correlational (XC), functional other important factors to consider is the choice of basis sets to describe the approximate wavefunction accurately. Here we are going to set the criterion for establishing the suitable basis set to describe our systems. This choice always involves a balance between accuracy and computational cost. In this thesis, we have studied two basis sets; Def2SVP and Def2TZVP with added "polarization functions" which enhances the flexibility of atoms to form chemical bonds in any direction and improve system description. We measure the three parameters as shown in Table B.1 and B.2. For both functional, we observe $C1-C1'$ bond lengths decrease by 0.005 Å and $N-C$ by 0.004 Å. No much variation is observed for $M-N$ bond lengths. From this analysis it is seen using more accurate basis sets does not improve system description further. Generally, we calculated the voltage with these two basis sets and found the voltage is nearly the same. Since we are computing the relative voltage the error in one system translate to other overall, there is a cancellation. With anions in our complex, it is recommended to use diffusive functions, however, above family of basis sets with diffusive is not implemented in Gaussian code. There are other basis sets which include the diffusivity properties, but they are not available for the second-row transition metal. From this section, we will use the def2SVP basis set for the reason of computational cost and memory moreover, the qualitative and quantitative description of the system is described by this set adequately.

Table B.1: Selected average experimental bond lengths parameters for $[M(bpy^0)_3]^{2+}$ (*Neutral*: *N*)and $[M(bpy^0)_3]^{3+}$ (*Full Loaded*: *FL*) complex are compared to the minimized structure obtained at PBE/PBE0//Def2SVP/Def2TZVP level of theory. For *Fe*: experimental parameters for *N* are given for methylation and *FL* without methylation. The bond lengths are given in **Å**.

	$[Fe^{II}(dmbpy)_3]^{2+}$					$[Fe^{III}(dmbpy)_3]^{3+}$				
	Opt				Exp [24, 115]	Opt				Exp [116]
	Def2SVP		Def2TZVP			Def2SVP		Def2TZVP		
	PBE	PBE0	PBE	PBE0		PBE	PBE0	PBE	PBE0	
$Fe-N$	1.96	1.99	1.97	1.99	1.965(3)	1.98	1.97	1.98	1.98	1.96(3)
$C1-C1'$	1.470	1.474	1.465	1.469	1.473(3)	1.471	1.471	1.466	1.466	1.472(6)
$N-C_1$	1.363	1.344	1.359	1.341	1.350(0)	1.370	1.354	1.366	1.350	1.350(0)

Table B.2: Selected average experimental bond lengths parameters for $[M(bpy^0)_3]^{2+}$ (*Neutral*: *N*) and $[M(bpy^0)_3]^{3+}$ (*Full Loaded*: *FL*) complex are compared to the minimized structure obtained at PBE/PBE0//Def2SVP/Def2TZVP level of theory. For *Ru*: experimental parameters for *N* and *FL* system are given without methylation, respectively. The lengths are given in **Å**.

	$[Ru^{II}(dmbpy)_3]^{2+}$					$[Ru^{III}(dmbpy)_3]^{3+}$				
	Opt				Exp	Opt				Exp [117]
	Def2SVP		Def2TZVP			Def2SVP		Def2TZVP		
	PBE	PBE0	PBE	PBE0		PBE	PBE0	PBE	PBE0	
$Ru-N$	2.066	2.065	2.067	2.065	2.054 [117, 118]	2.077	2.071	2.067	2.070	2.056
$C1-C1'$	1.473	1.473	1.467	1.467	1.474(7) [25]	1.475	1.473	1.468	1.465	1.450
$N-C_1$	1.365	1.348	1.361	1.344	1.351	1.375	1.357	1.370	1.353	

B.1.1 Basis set voltage analysis

First, we study the effect of using accurate basis sets (Def2TZVP) on the voltages. In Table B.3, relative voltage for methyl complex are shown. Comparison of basis sets for each functional shows the variation on the order of 0.05 V for Ru/Fe complex and 0.01 V for Cu/Fe complex. Cu/Fe shows no variation when using larger basis sets. However, this shows for Ru/Fe complex larger basis sets does improve the voltage. In Table B.4, ground state multiplicity *S* along with Mulliken net spin (NS) on Metal sites are shown. Our system consists of open and closed shell system. For closed shell system, the number

of up and down spins is same, so no need to perform spin polarize calculation and net Mulliken spin polarization is zero. Even we tried different multiplicities, $S = 0$ was the lowest in energy. For open shell system, an unpaired electron could reside on metal or ligands? Our calculation shows with or without methylation the net spin on metal sites are same irrespective of the functional use and for open shell system oxidation is taking place at metallic center with no net spin residing on the *dmbpy* ligands.

Table B.3: Relative voltages calculated for mono-nuclear complex with methylation and comparison of basis sets.

	Methyl				
	Def2SVP		Def2TZVP		
	PBE	PBE0	PBE	PBE0	Exp
$V_{Ru-Fe}(V)$	+0.25	+0.31	+0.20	+0.26	+0.20 [24]
$V_{Cu-Fe}(V)$	-2.51	-2.61	-2.50	-2.60	-1.03

Table B.4: Calculated properties of the mono-nuclear complex with and without methylation. S is the spin ground state of the system, and Q is total charge on a system and NS is the net Mulliken spin polarization on transition metal site in a cluster obtained at Def2SVP level of theory.

	Net spin (NS)					
	Non-methyl		Methyl			
	PBE	PBE0	PBE	PBE0	Q	S
$[Ru(dmbpy)_3]^{2+}$	0	0	0	0	2+	0
$[Ru(dmbpy)_3]^{3+}$	0.91	1.01	0.91	1.01	3+	1/2
$[Fe(dmbpy)_3]^{2+}$	0	0	0	0	2+	0
$[Fe(dmbpy)_3]^{3+}$	1.08	1.14	1.08	1.14	3+	1/2

B.2 Basis set effect with counter-ions

Here we will do the same analysis as it is done in the previous section to find out the effect of using larger basis sets in the field of external perturbations. For convenience reason, we have chosen PF_6^- counter-ion. Comparison of optimized geometry are shown in Figure B.1. Table B.5 and B.6, shows on average, using triple zeta valence polarization basis sets (Def2TZVP) the bond lengths distance between $M - N$ atom reduced

by 0.003 Å for $[Fe\,(dmbpy)_3]^{2+}\,2PF_6^-$ and 0.002 Å for $[Fe\,(dmbpy)_3]^{3+}\,3PF_6^-$. Others parameters also vary in that range which by experimental results does not show much variation. Similarly, for *Ru* complex distance between $M-N$ remains invariant and other parameters vary on the order of 0.004 Å. For this reason, we have employed smaller Def2SVP basis sets which suffice for the qualitative description of the system moreover in calculating relative voltages the error get canceled.

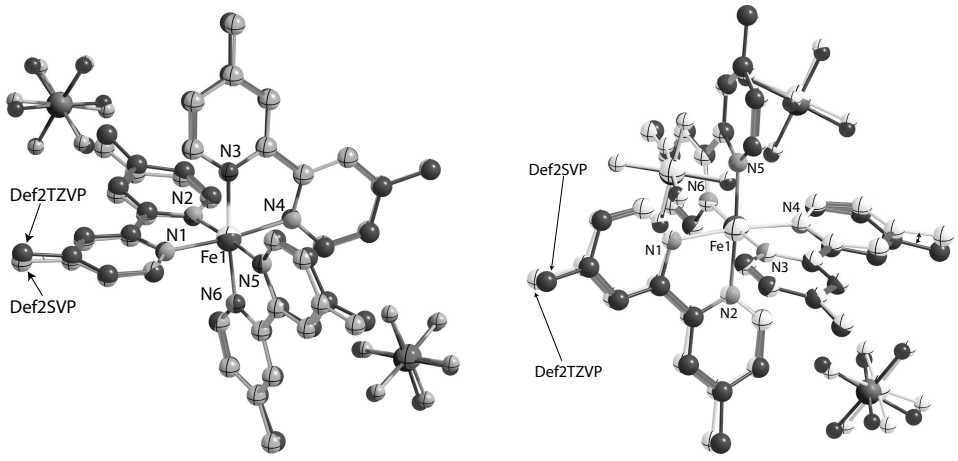

(a) **(b)**

Figure B.1: Comparison of geometry observed for (a) $[Fe\,(dmbpy)_3]^{2+}\,2PF_6^-$ and (b) $[Fe\,(dmbpy)_3]^{3+}\,3PF_6^-$ mono-nuclear complex at PBE0 level of theory using Def2SVP and Def2TZVP basis sets. Here we superimpose one of *dmbpy* and see the effect on geometry.

Table B.5: Selected Experimental bond lengths (averaged) parameters for (*Neutral: N*) and (*Full Loaded*: *FL*) complex compared to the minimized structure obtained at PBE/PBE0//Def2SVP/Def2TZVP level of theory. For *Fe*: experimental parameters for *N* are given for methylation and for *FL* without methylation. The lengths are given in **Å**.

	$[Fe(dmbpy)_3]^{2+}2PF_6^-$					$[Fe(dmbpy)_3]^{3+}3PF_6^-$				
	Opt				Exp [24, 115]	Opt				Exp [116]
	Def2SVP		Def2TZVP			Def2SVP		Def2TZVP		
	PBE	PBE0	PBE	PBE0		PBE	PBE0	PBE	PBE0	
$Fe-N$	1.960	1.986		1.989	1.965(3)	1.971	1.971		1.973	1.96(3)
$C1-C1'$	1.468	1.471		1.467	1.472(6) [25]	1.465	1.467		1.462	1.473(6)
$N-C_1$	1.371	1.351		1.348	1.350(0)	1.369	1.356		1.350	1.350(0)

Table B.6: Selected Experimental bond lengths (averaged) parameters for (*Neutral: N*) and (*Full Loaded*: *FL*) complex compared to the minimized structure obtained at PBE/PBE0//Def2SVP/Def2TZVP level of theory. For *Ru*: *N* and *FL* are without methylation. The lengths are given in **Å**.

	$[Ru(dmbpy)_3]^{2+}2PF_6^-$					$[Ru(dmbpy)_3]^{3+}3PF_6^-$				
	Opt				Exp	Opt				Exp [117]
	Def2SVP		Def2TZVP			Def2SVP		Def2TZVP		
	PBE	PBE0	PBE	PBE0		PBE	PBE0	PBE	PBE0	
$Ru-N$	2.064	2.063		2.063	2.054 [117, 118]	2.069	2.063		2.063	2.056
$C1-C1'$	1.471	1.471		1.466	1.474(7) [25]	1.469	1.467		1.463	1.450
$N-C_1$	1.372	1.355		1.351	1.354 [25]	1.372	1.357		1.351	

Appendix C

DFT: Half loaded PDOS plots

C.1 Electronic structure within PBE0 approximation for 4C alkyl chain

Similarly, for half loaded system, we observe the same effect as for 6C chain. It can be seen from the Figure C.1 and C.2 for one particular Iron site in a bi-nuclear complex we see the oxidation is taking place that is one electron leaves the system. The same observation is for the 2C chain. The DOS plot also shows the site from which the electrons oxidizes there is a deep distribution of bands and hybridization with counter-ions and Nitrogen regions. However, C and H elements in *dmbpy* contribute very little to the hybridization with the Iron d-orbitals. Moreover, for PBE0 functional the signature of the DOS plot shows there is an influence of chain length in the energy window –8 to –13 eV.

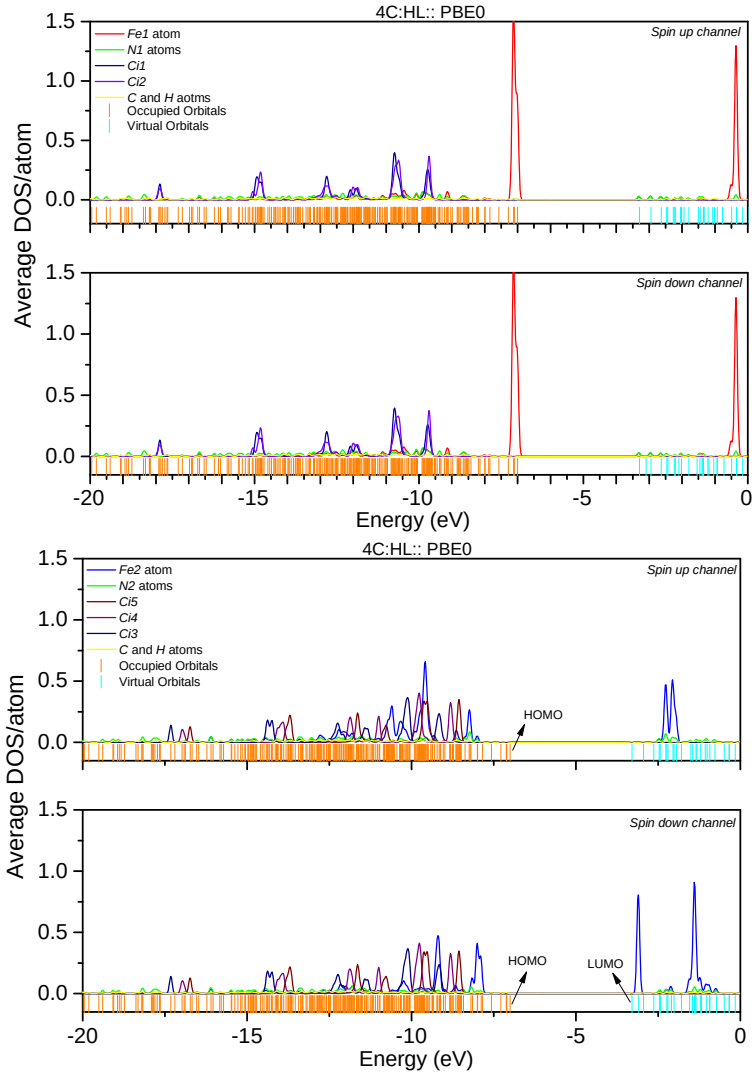

Figure C.1: Average DOS per atom calculated within the PBE0 approximation for the 4C:HL complex. We have added the partial DOS corresponding to $Fe1$ and $Fe2$ atoms, the sum of carbon and hydrogen contributions in yellow and the N's regions contributions from the *dmbpy* in green. The occupied orbital electronic levels are reported in orange color at the bottom.

C.2 Electronic structure within PBE0 approximation for 2C alkyl chain

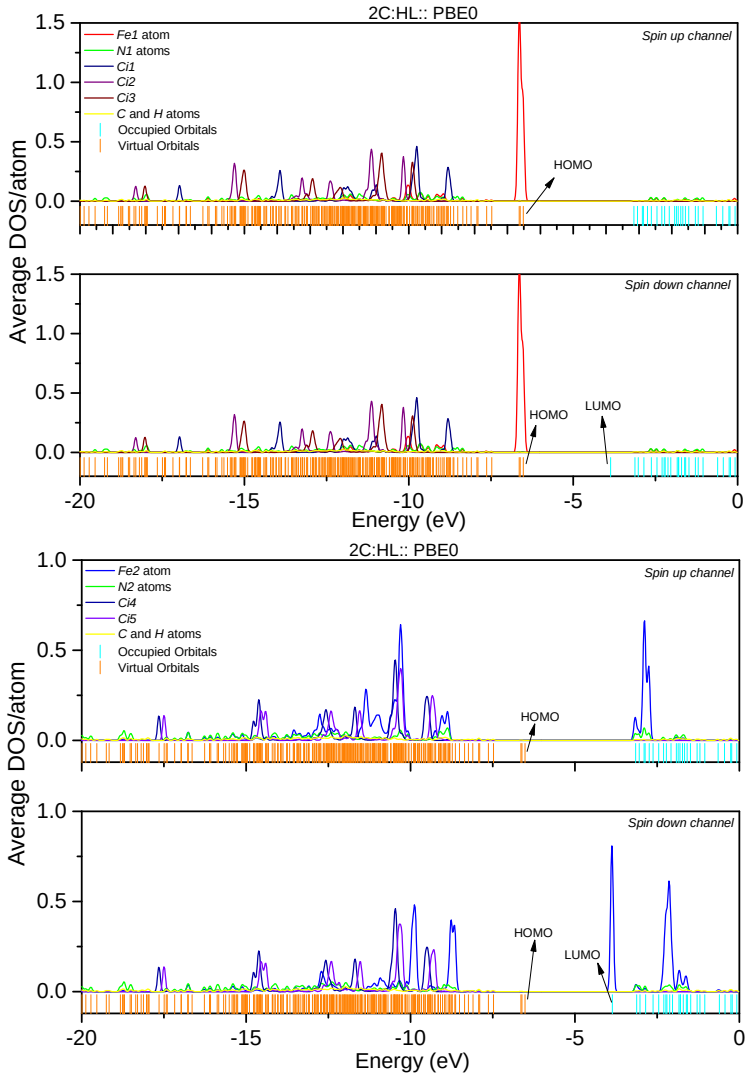

Figure C.2: Average DOS per atom calculated within the PBE0 approximation for the 2C:HL complex. We have added the partial DOS corresponding to $Fe1$ and $Fe2$ atoms, the sum of carbon and hydrogen contributions in yellow and the N's regions contributions from the *dmbpy* in green. The occupied orbital electronic levels are reported in orange color at the bottom.

C.3 Demonstration of delocalization of states over the chain

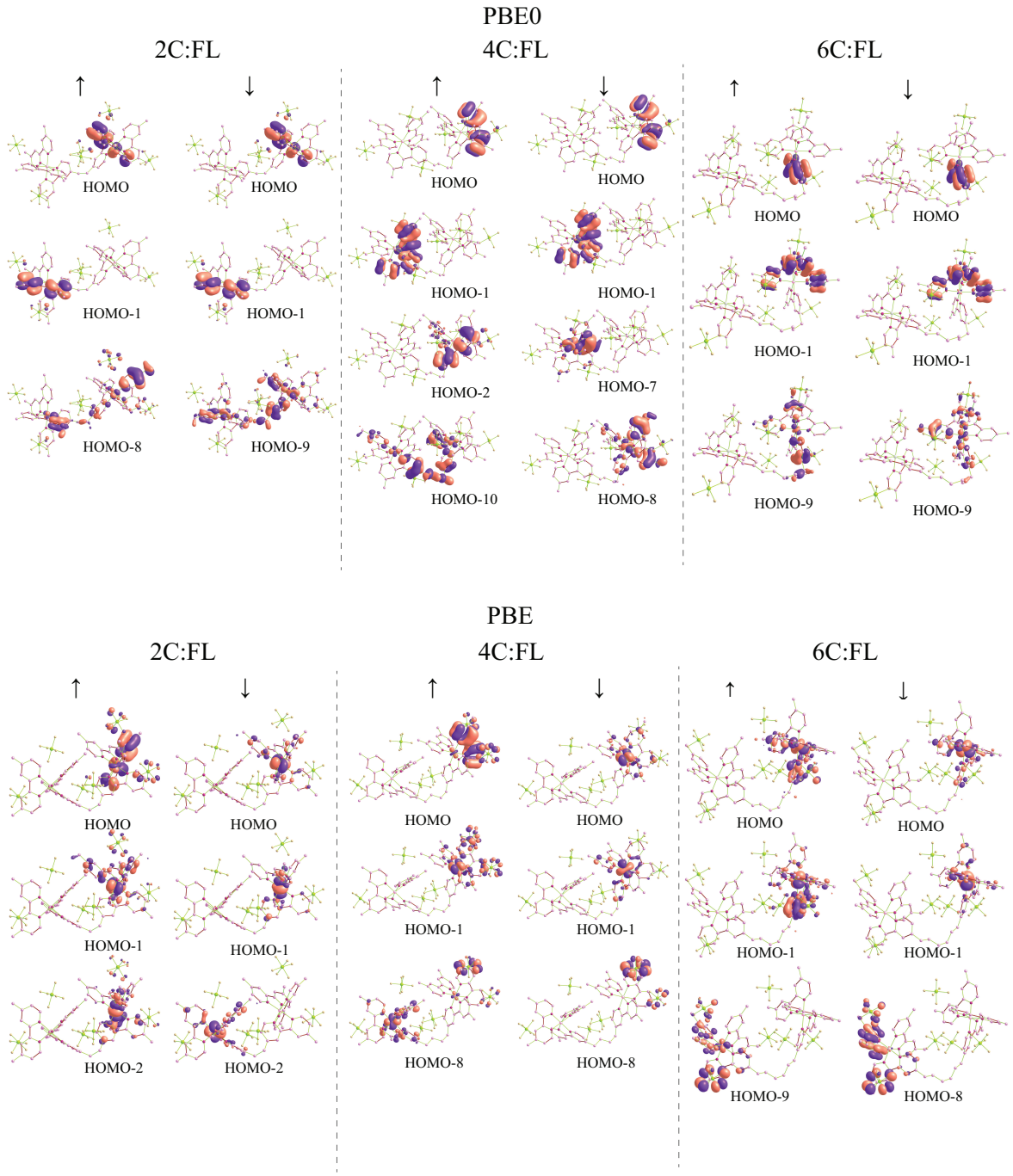

Appendix D

DFT: Vibrational Analysis

D.1 IR spectra of complexes with and with counter-ions

The vibrational analysis shows the obtained structure is at the local minima on a potential energy surface (PES). In the Figure D.2, D.3, and D.1 IR spectra with and without counter-ions are shown for PBE and PBE0 functionals. From the spectrum, it can be seen no imaginary frequency is found. The addition of counter-ions modified the spectrum in the regions 200-3500 cm^{-1}. Higher frequency modes corresponds to C-H bonds. Whereas, low frequency region we see the collective mode of the complex. No much difference is observed between two functional corresponding to the IR active modes in the whole regions. The curve has been generated with GaussSum program.

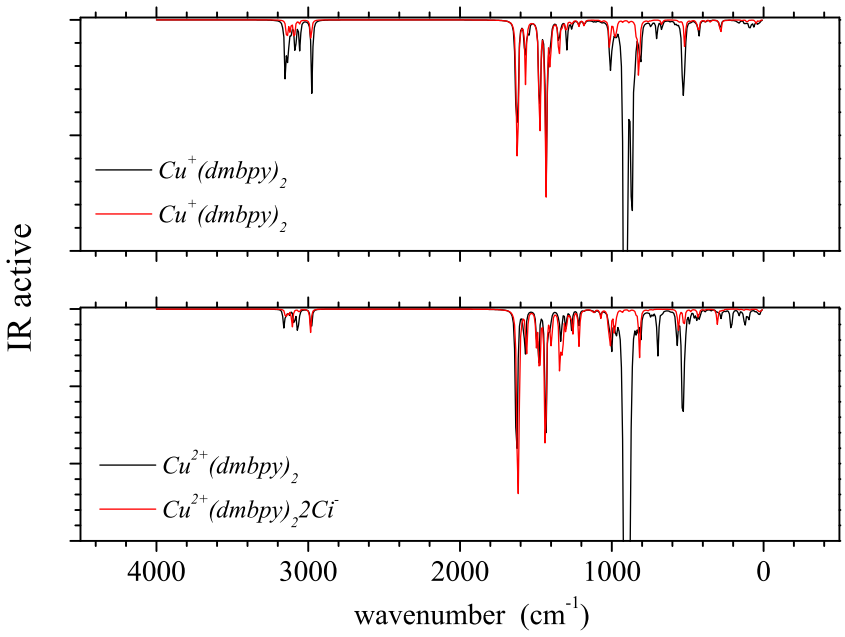

(a)

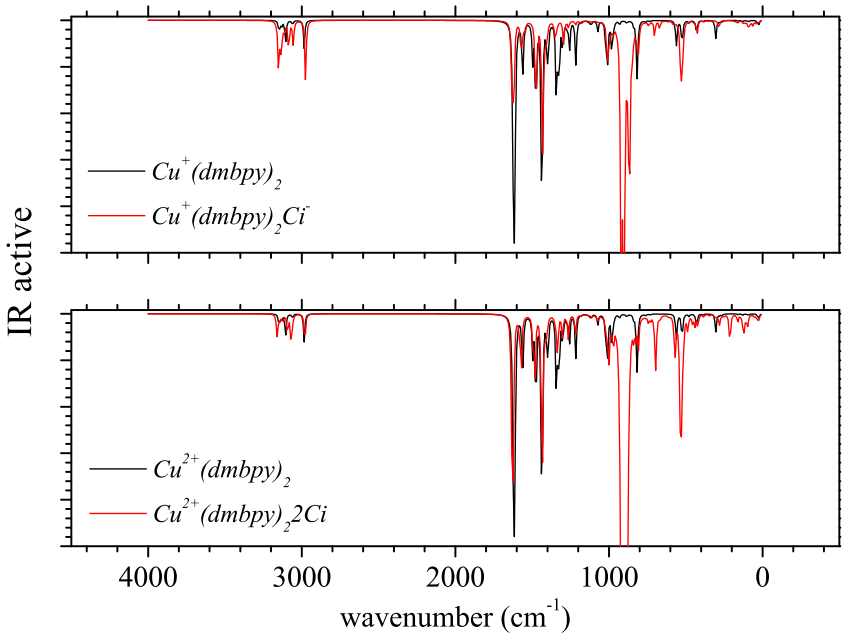

(b)

Figure D.1: Computed IR spectra of Cu complex at (a) PBE, and (b) PBE0/Def2SVP level of theory. The red and black dashed curves refer to the system with and without counter-ions, respectively.

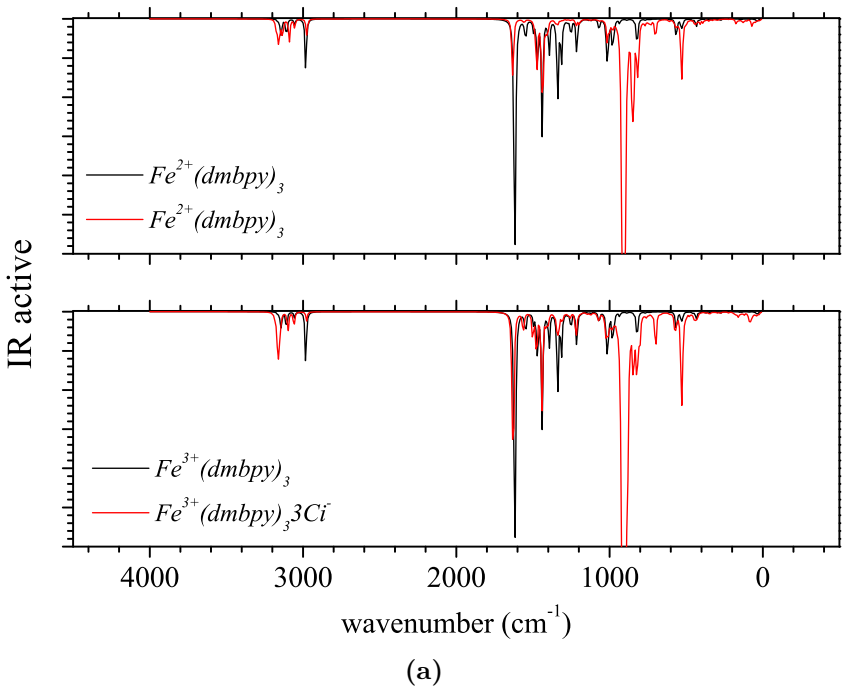

(a)

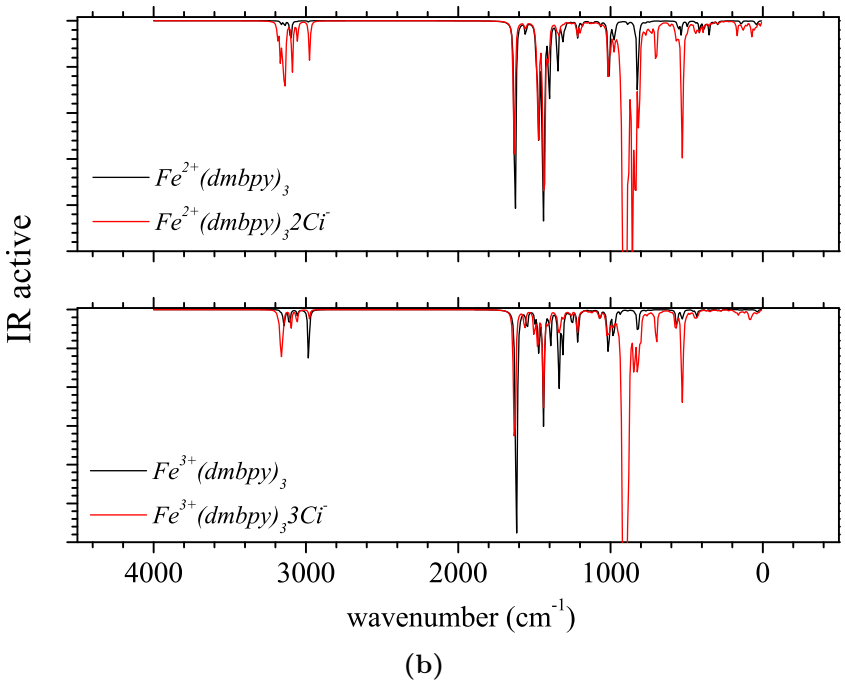

(b)

Figure D.2: Computed IR spectra of Cu complex at (a) PBE, and (b) PBE0/Def2SVP level of theory. The red and black dashed curves refer to the system with and without counter-ions, respectively.

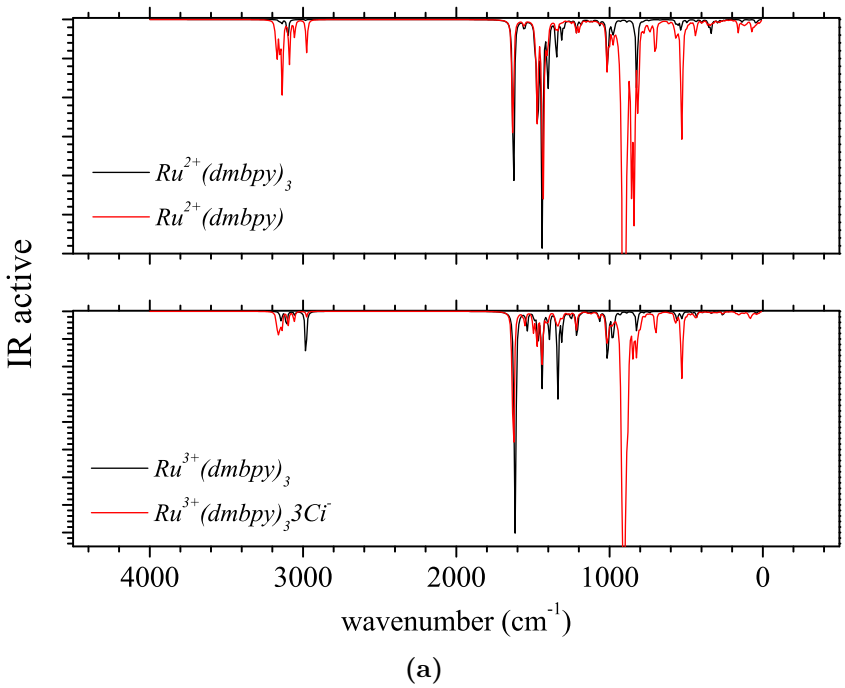

(a)

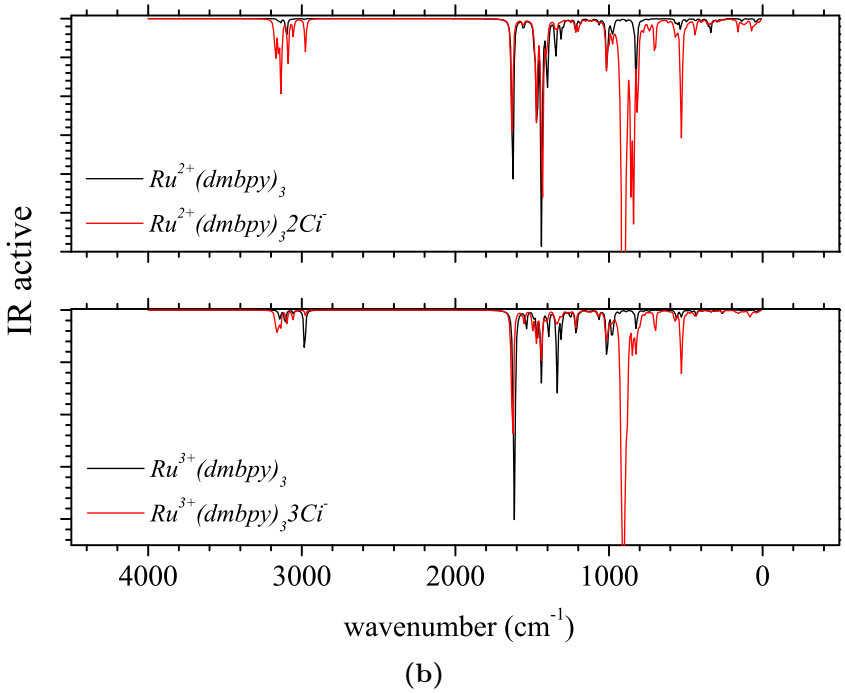

(b)

Figure D.3: Computed IR spectra of Cu complex at (a) PBE, and (b) PBE0/Def2SVP level of theory. The red and black dashed curves refer to the system with and without counter-ions, respectively.

Appendix E

MD: Force field parameters

E.1 Parameters for ACN solvent

Table E.1: Parameters for ACN (a) bonds (b) angles.

(a)

Bonds	$kcal/(mol\text{Å}^2)$	Å
c3-hc	330.60	1.097
c1-c3	371.60	1.467
c1-n1	954.60	1.153

(b)

Angle	$kcal/(mol\text{rad}^2)$	Å
hc-c3-hc	39.400	107.580
c1-c3-hc	48.400	109.410
c3-c1-n1	58.000	178.580

Table E.2: Parameters for ACN dihedrals.

Dihedral	divider	$kcal/(mol)$	ψ	n
n1-c1-c3-hc	3	0.000	180.000	2.000

Table E.3: Non-bonded parameters for ACN.

Non-bonded	R_{min}	ϵ
hc	1.4870	0.0157
c3	1.9080	0.1094
c1	1.9080	0.2100
n1	1.8240	0.1700

E.2 Parameter for Counter-ions ($TFSI^-$)

Table E.4: Parameters for $TFSI^-$ bonds.

Bonds	$kcal/(mol\text{Å}^2)$	Å
ne-s6	317.10	1.672
ne-s6	317.10	1.672
c3-f	356.90	1.350
c3-sy	232.80	1.809
c3-s6	233.50	1.808
o-s6	512.70	1.453
o-sy	493.00	1.466

Table E.5: Parameters for $TFSI^-$ angles.

Angle	$kcal/(mol\text{rad}^2)$	Å
c3-s6-ne	16.300	108.190
ne-s6-o	70.800	119.100
c3-sy-ne	64.100	102.190
ne-sy-o	70.300	109.650
c3-sy-o	65.400	107.850
c3-s6-o	65.400	108.610
f -c3-f	70.900	107.360
f -c3-s6	63.100	109.680
f -c3-sy	63.100	109.680
o -s6-o	73.600	120.050
o -sy-o	72.500	121.410
s6-ne-sy	65.900	119.630

Table E.6: Parameters for $TFSI^-$ dihedrals.

Dihedral	divider	$kcal/(mol)$	ψ	n
f -c3-s6-ne	9	1.3	0	3.0
f -c3-sy-ne	9	1.3	0	3.0
s6-ne-sy-c3	3	1.5	180	-3.0
s6-ne-sy-c3	3	20.4	180	1.0
sy-ne-s6-c3	3	20.0	180	2.0
f -c3-s6-o	3	1.3	0	3.0
f -c3-sy-o	9	1.3	0	3.0
sy-ne-s6-o	9	20.0	180	2.0
s6-ne-sy-o	3	1.5	180	-3.0
s6-ne-sy-o	3	20.4	180	1.0

Table E.7: Non-bonded parameters for $TFSI^-$.

Non-bonded	R_{min}	ϵ
ne	1.8240	0.17
c3	1.9080	0.109
f	1.75	0.0610
p	1.6612	0.21
s6	2.0	0.25
sy	2.0	0.25

E.3 Parameters for Neutral unit

Table E.8: Bond parameters for Neutral system.

Bonds	$kcal/(mol\text{Å}^2)$	Å
M2-Y9	62.9	1.9672
M2-Z1	60.9	1.9716
M2-Z2	64.6	1.9667
M2-Z3	65.9	1.9629
Y7-M2	56.5	1.9626
Y8-M2	49.9	1.9645
Y9-ca	488.00	1.339
Y9-cp	488.50	1.339
Z1-ca	488.00	1.339
Z1-cp	488.50	1.339
Z2-ca	488.00	1.339
Z2-cp	488.50	1.339
Z3-ca	488.00	1.339
Z3-cp	488.50	1.339
ca-Y7	488.00	1.339
ca-Y8	488.00	1.339
cp-Y8	488.50	1.339

Table E.9: Angle parameters for Neutral system.

Angle	$kcal/(mol\text{rad}^2)$	Å	Angle	$kcal/(mol\text{rad}^2)$	Å
M2-Y9-ca	144.36	126.79	Y8-ca-ca	68.800	122.940
M2-Y9-cp	134.74	115.45	Y8-ca-h4	51.900	116.030
M2-Z1-ca	146.67	126.94	Y8-cp-cp	68.200	116.610
M2-Z1-cp	136.66	115.33	Y9-ca-ca	68.800	122.940
M2-Z2-ca	137.53	126.84	Y9-ca-h4	51.900	116.030
M2-Z2-cp	130.33	115.28	Y9-cp-ca	69.000	121.620
M2-Z3-ca	148.83	126.74	Y9-cp-cp	68.200	116.610
M2-Z3-cp	137.61	115.45	Z1-ca-ca	68.800	122.940
Y7-M2-Y8	141.96	81.80	Z1-ca-h4	51.900	116.030
Y7-M2-Y9	125.42	88.57	Z1-cp-ca	69.000	121.620
Y7-M2-Z1	136.22	94.74	Z1-cp-cp	68.200	116.610
Y7-M2-Z2	127.28	176.04	Z2-ca-ca	68.800	122.940
Y7-M2-Z3	134.04	95.25	Z2-ca-h4	51.900	116.030
Y8-M2-Y9	134.78	95.20	Z2-cp-ca	69.000	121.620
Y8-M2-Z1	139.24	175.40	Z2-cp-cp	68.200	116.610
Y8-M2-Z2	126.52	95.54	Z3-ca-ca	68.800	122.940
Y8-M2-Z3	142.78	89.28	Z3-ca-h4	51.900	116.030
Z1-M2-Y9	145.47	81.63	Z3-cp-ca	69.000	121.620
Z2-M2-Y9	132.55	94.61	Z3-cp-cp	68.200	116.610
Z2-M2-Z1	125.56	88.07	ca-Z1-cp	68.100	118.050
Z3-M2-Y9	151.36	174.49	ca-Z2-cp	68.100	118.050
Z3-M2-Z1	146.17	94.08	ca-Z3-cp	68.100	118.050
Z3-M2-Z2	149.26	81.75	ca-ca-Y7	68.800	122.940
ca-Y7-M2	141.55	126.67	ca-cp-Y8	69.000	121.620
ca-Y8-M2	136.22	127.10	cp-Y7-ca	68.100	118.050
cp-Y7-M2	133.12	115.53	cp-Y8-ca	68.100	118.050
cp-Y8-M2	128.16	115.32	cp-Y9-ca	68.100	118.050
Y7-ca-h4	51.900	116.030	cp-cp-Y7	68.200	116.610
Y7-cp-ca	69.000	121.620			

Table E.10: Dihedrals angles parameters for Neutral complex. Angles with respect to Metal sites have been omitted because MCPB code assumes them to be zero.

Dihedral	divider	$kcal/(mol)$	ψ	n
Y7-ca-ca-ha	4	14.5	180.0	2.0
Y7-cp-ca-ca	4	14.5	180.0	2.0
Y7-cp-ca-ha	4	14.5	180.0	2.0
Y8-ca-ca-ha	4	14.5	180.0	2.0
Y8-cp-ca-ha	4	14.5	180.0	2.0
Y8-cp-cp-Y7	4	4.0	180.0	2.0
Y8-cp-cp-ca	4	4.0	180.0	2.0
Y9-ca-ca-ca	4	14.5	180.0	2.0
Y9-ca-ca-ha	4	14.5	180.0	2.0
Y9-cp-ca-ca	4	14.5	180.0	2.0
Y9-cp-ca-ha	4	14.5	180.0	2.0
Y9-cp-cp-Z1	4	4.0	180.0	2.0
Y9-cp-cp-ca	4	4.0	180.0	2.0
Z1-ca-ca-ca	4	14.5	180.0	2.0
Z1-ca-ca-ha	4	14.5	180.0	2.0
Z1-cp-ca-ca	4	14.5	180.0	2.0
Z1-cp-ca-ha	4	14.5	180.0	2.0
Z1-cp-cp-ca	4	4.0	180.0	2.0
Z2-ca-ca-ca	4	14.5	180.0	2.0
Z2-ca-ca-ha	4	14.5	180.0	2.0
Z2-cp-ca-ca	4	14.5	180.0	2.0
Z2-cp-ca-ha	4	14.5	180.0	2.0
Z2-cp-cp-Z3	4	4.0	180.0	2.0
Z2-cp-cp-ca	4	4.0	180.0	2.0
Z3-ca-ca-ca	4	14.5	180.0	2.0
Z3-ca-ca-ha	4	14.5	180.0	2.0
Z3-cp-ca-ca	4	14.5	180.0	2.0
Z3-cp-ca-ha	4	14.5	180.0	2.0
Z3-cp-cp-ca	4	14.5	180.0	2.0

Dihedral	divider	$kcal/(mol)$	ψ	n
ca-Y7-cp-ca	2	9.6	180.0	2.0
ca-Y8-cp-cp	2	9.6	180.0	2.0
ca-Z1-cp-ca	2	9.6	180.0	2.0
ca-Z1-cp-cp	2	9.6	180.0	2.0
ca-Z2-cp-ca	2	9.6	180.0	2.0
ca-Z2-cp-cp	2	9.6	180.0	2.0
ca-Z3-cp-ca	2	9.6	180.0	2.0
ca-Z3-cp-cp	2	9.6	180.0	2.0
ca-ca-Z1-cp	2	9.6	180.0	2.0
ca-ca-Z2-cp	2	9.6	180.0	2.0
ca-ca-Z3-cp	2	9.6	180.0	2.0
ca-ca-ca-Y7	4	14.5	180.0	2.0
ca-ca-ca-Y8	4	14.5	180.0	2.0
ca-ca-cp-Y8	4	14.5	180.0	2.0
ca-cp-Y8-ca	2	9.6	180.0	2.0
ca-cp-Y9-ca	2	9.6	180.0	2.0
ca-cp-cp-Y7	4	4.0	180.0	2.0
cp-Y7-ca-ca	2	9.6	180.0	2.0
cp-Y7-ca-h4	2	9.6	180.0	2.0
cp-Y8-ca-ca	2	9.6	180.0	2.0
cp-Y8-ca-h4	2	9.6	180.0	2.0
cp-Y9-ca-ca	2	9.6	180.0	2.0
cp-Y9-ca-h4	2	9.6	180.0	2.0
cp-cp-Y9-ca	2	9.6	180.0	2.0
h4-ca-Z1-cp	2	9.6	180.0	2.0
h4-ca-Z2-cp	2	9.6	180.0	2.0
h4-ca-Z3-cp	2	9.6	180.0	2.02.0

Table E.11: Improper angles parameters for Neutral complex. Angles with respect to Metal sites have been omitted because MCPB code assumes them to be zero.

Improper	$kcal/(mol)$	ψ	n
Y9-ca-cp-cp	1.1	180	2
Y6-ca-cp-cp	1.1	180	2
Y9-ca-ca-h4	1.1	180	2
Z1-ca-cp-cp	1.1	180	2
Y7-ca-ca-h4	1.1	180	2
Y5-ca-ca-h4	1.1	180	2
Y3-ca-ca-h4	1.1	180	2
Y7-ca-cp-cp	1.1	180	2
Y6-ca-ca-h4	1.1	180	2
Y4-ca-ca-h4	1.1	180	2
Y2-ca-ca-h4	1.1	180	2
Y5-ca-cp-cp	1.1	180	2
Y8-ca-cp-cp	1.1	180	2
Y2-ca-cp-cp	1.1	180	2
Y8-ca-ca-h4	1.1	180	2
Z3-ca-cp-cp	1.1	180	2
Y4-ca-cp-cp	1.1	180	2
Z2-ca-ca-h4	1.1	180	2
Y3-ca-cp-cp	1.1	180	2
Z2-ca-cp-cp	1.1	180	2
Z3-ca-ca-h4	1.1	180	2
Y1-ca-cp-cp	1.1	180	2
Z1-ca-ca-h4	1.1	180	2
Y1-ca-ca-h4	1.1	180	2

Table E.12: Non-bonded parameters for neutral system.

Non-bonded	R_{min}	ϵ
M2	1.4090	0.0172100000
Y7/Y8/Y9/Z1/Z2/Z3	1.8240	0.1700

E.4 Parameter for Full loaded unit

Table E.13: Bonds parameters for Fully loaded.

Bonds	$kcal/(mol\text{Å}^2)$	Å
M1-Y1	79.4	1.9702
M1-Y2	84.9	1.9653
M1-Y3	79.8	1.9699
M1-Y4	84.6	1.9656
M1-Y5	85.3	1.9655
M1-Y6	78.9	1.9701
Y1-ca	488.00	1.339
Y1-cp	488.50	1.339
Y2-ca	488.00	1.339
Y2-cp	488.50	1.339
Y3-ca	488.00	1.339
Y3-cp	488.50	1.339
Y4-ca	488.00	1.339
Y4-cp	488.50	1.339
Y5-ca	488.00	1.339
Y5-cp	488.50	1.339
Y6-cp	488.50	1.339

Table E.14: Angle parameters for Fully loaded.

Angle	$kcal/(mol\text{rad}^2)$	Å
M1-Y1-ca	137.59	126.27
M1-Y1-cp	130.25	114.63
M1-Y2-ca	145.16	126.43
M1-Y2-cp	130.32	114.60
M1-Y3-ca	137.41	126.25
M1-Y3-cp	130.18	114.66
M1-Y4-ca	144.50	126.44
M1-Y4-cp	129.78	114.60
M1-Y5-ca	144.07	126.44
M1-Y5-cp	129.61	114.60
M1-Y6-ca	136.84	126.26
M1-Y6-cp	129.40	114.64
Y2-M1-Y1	164.22	82.28
Y3-M1-Y1	120.32	95.61
Y3-M1-Y2	136.03	176.46
Y4-M1-Y1	106.80	87.34
Y4-M1-Y2	137.42	94.75
Y4-M1-Y3	164.18	82.28
Y5-M1-Y1	136.05	176.54
Y5-M1-Y2	139.30	94.81
Y5-M1-Y3	109.38	87.39
Y5-M1-Y4	137.03	94.79
Y6-M1-Y1	119.14	95.68
Y6-M1-Y2	107.03	87.32
Y6-M1-Y3	120.72	95.74
Y6-M1-Y4	135.63	176.55
Y6-M1-Y5	163.22	82.28

Angle	$kcal/(mol\text{rad}^2)$	Å
Y1-ca-ca	68.800	122.940
Y1-ca-h4	51.900	116.030
Y1-cp-ca	69.000	121.620
Y1-cp-cp	68.200	116.610
Y2-ca-ca	68.800	122.940
Y2-ca-h4	51.900	116.030
Y2-cp-ca	69.000	121.620
Y2-cp-cp	68.200	116.610
Y3-ca-ca	68.800	122.940
Y3-ca-h4	51.900	116.030
Y3-cp-ca	69.000	121.620
Y3-cp-cp	68.200	116.610
Y4-ca-ca	68.800	122.940
Y4-ca-h4	51.900	116.030
Y4-cp-ca	69.000	121.620
Y4-cp-cp	68.200	116.610
Y5-ca-ca	68.800	122.940
Y5-ca-h4	51.900	116.030
Y5-cp-ca	69.000	121.620
Y5-cp-cp	68.200	116.610
Y6-ca-ca	68.800	122.940
Y6-ca-h4	51.900	116.030
Y6-cp-ca	69.000	121.620
Y6-cp-cp	68.200	116.610
ca-Y2-cp	68.100	118.050
ca-Y6-cp	68.100	118.050
cp-Y1-ca	68.100	118.050
cp-Y3-ca	68.100	118.050
cp-Y4-ca	68.100	118.050
cp-Y5-ca	68.100	118.050

Table E.15: Dihedrals angles parameters for Fully loaded complex. Angles with respect to Metal sites have been omitted because MCPB code assumes them to be zero.

Dihedral	divider	$kcal/(mol)$	ψ	n
Y1-ca-ca-ca	4	14.5	180.0	2.0
Y1-ca-ca-ha	4	14.5	180.0	2.0
Y1-cp-ca-ca	4	14.5	180.0	2.0
Y1-cp-ca-ha	4	14.5	180.0	2.0
Y1-cp-cp-Y2	4	4.0	180.0	2.0
Y1-cp-cp-ca	4	4.0	180.0	2.0
Y2-ca-ca-ca	4	14.5	180.0	2.0
Y2-ca-ca-ha	4	14.5	180.0	2.0
Y2-cp-ca-ca	4	14.5	180.0	2.0
Y2-cp-ca-ha	4	14.5	180.0	2.0
Y2-cp-cp-ca	4	4.0	180.0	2.0
Y3-ca-ca-ca	4	14.5	180.0	2.0
Y3-ca-ca-ha	4	14.5	180.0	2.0
Y3-cp-ca-ca	4	14.5	180.0	2.0
Y3-cp-ca-ha	4	14.5	180.0	2.0
Y3-cp-cp-Y4	4	4.0	180.0	2.0
Y3-cp-cp-ca	4	4.0	180.0	2.0
Y4-ca-ca-ca	4	14.5	180.0	2.0
Y4-ca-ca-ha	4	14.5	180.0	2.0
Y4-cp-ca-ca	4	14.5	180.0	2.0
Y4-cp-ca-ha	4	14.5	180.0	2.0
Y4-cp-cp-ca	4	4.0	180.0	2.0
Y5-ca-ca-ca	4	14.5	180.0	2.0
Y5-ca-ca-ha	4	14.5	180.0	2.0
Y5-cp-ca-ca	4	14.5	180.0	2.0
Y5-cp-ca-ha	4	14.5	180.0	2.0
Y5-cp-cp-Y6	4	4.0	180.0	2.0
Y5-cp-cp-ca	4	4.0	180.0	2.0
Y6-ca-ca-ca	4	14.5	180.0	2.0
Y6-ca-ca-ha	4	14.5	180.0	2.0
Y6-cp-ca-ca	4	14.5	180.0	2.0
Y6-cp-ca-ha	4	14.5	180.0	2.0
Y6-cp-cp-ca	4	4.0	180.0	2.0

Dihedral	divider	$kcal/(mol)$	ψ	n
ca-Y2-cp-ca	2	9.6	180.0	2.0
ca-Y2-cp-cp	2	9.6	180.0	2.0
ca-Y6-cp-ca	2	9.6	180.0	2.0
ca-Y6-cp-cp	2	9.6	180.0	2.0
ca-ca-Y2-cp	2	9.6	180.0	2.0
ca-ca-Y6-cp	2	9.6	180.0	2.0
ca-cp-Y1-ca	2	9.6	180.0	2.0
ca-cp-Y3-ca	2	9.6	180.0	2.0
ca-cp-Y4-ca	2	9.6	180.0	2.0
ca-cp-Y5-ca	2	9.6	180.0	2.0
cp-Y1-ca-ca	2	9.6	180.0	2.0
cp-Y1-ca-h4	2	9.6	180.0	2.0
cp-Y3-ca-ca	2	9.6	180.0	2.0
cp-Y3-ca-h4	2	9.6	180.0	2.0
cp-Y4-ca-ca	2	9.6	180.0	2.0
cp-Y4-ca-h4	2	9.6	180.0	2.0
cp-Y5-ca-ca	2	9.6	180.0	2.0
cp-Y5-ca-h4	2	9.6	180.0	2.0
cp-cp-Y1-ca	2	9.6	180.0	2.0
cp-cp-Y3-ca	2	9.6	180.0	2.0
cp-cp-Y4-ca	2	9.6	180.0	2.0
cp-cp-Y5-ca	2	9.6	180.0	2.0
h4-ca-Y2-cp	2	9.6	180.0	2.0
h4-ca-Y6-cp	2	9.6	180.0	2.0

E.5 Charge analysis for Counter-ions ($TFSI^-$)

In Table E.16, we have analyzed the charge fitting scheme at various level of theory. To be consistent with our choice of functional and basis sets we compare at other levels of theory to see if they are consistent and how much they vary. The counter-ions charges were fitted independently from the main Metal center. Compared to RESP scheme Mulliken charges depends highly on the choice of functional and basis sets. It can be seen charges calculated using the Merz Kollman (MK) scheme show a similarly small dependence on the computational method and are thus considered better to Mulliken charges. The following results calculated for NCF_3SO_2 in its gas phase structure are shown for one triflic groups. The MK charges are much less variable (between -0.523 and -0.707 for N atoms). Moreover, the MK charges are practically constant at the PBE1PBE and PBE level of theory. While the Mulliken charges differ widely with theoretical method and basis set choice. Here we opted the RESP scheme which is also recommended by the Amber for the potential it was developed for.

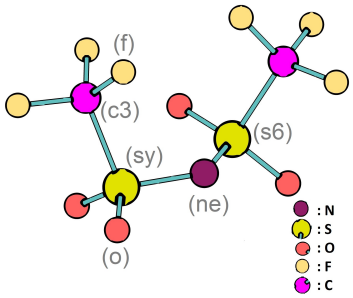

Figure E.1: Atom types naming convention for the $TFSI^-$ counter-ions.

Table E.16: Comparison of RESP charge fitting to MK scheme and Mulliken charges calculated at various level of theory.

Atom	AT	PBE/Def2SVP		PBE/Def2TZVP	PBE1PBE/Def2SVP		PBE1PBE/Def2TZVP
		RESP	Mull	Mull	RESP	Mull	Mull
N1	ne	-0.616751	-0.506487	-0.523198	-0.678912	-0.581365	-0.571487
C1	c3	0.09419	0.381822	0.111771	0.141772	0.529116	0.114859
F1	f	-0.085046	-0.146818	-0.092643	-0.100045	-0.190665	-0.094708
F2	f	-0.085046	-0.146525	-0.092643	-0.100045	-0.191128	-0.094708
F3	f	-0.085046	-0.160977	-0.092643	-0.100045	-0.204720	-0.094708
S1	sy/s6	0.933038	0.698345	0.831914	1.04837	0.809806	0.931005
O1	o	-0.481856	-0.436407	-0.452079	-0.525275	-0.488061	-0.487998
O2	o	-0.481856	-0.423712	-0.452079	-0.525275	-0.474766	-0.487998